UNIVERSITÀ DEGLI STUDI DI NAPOLI "FEDERICO II"
FACOLTÀ DI SCIENZE MM.FF.NN.

Ph.D. thesis in Fundamental and Applied Physics
XXIV Doctoral Cycle

Measurement of single top t-channel production cross section through the $t \rightarrow Wb \rightarrow \mu\nu b$ decay in 7 TeV proton-proton collisions with the Compact Muon Solenoid detector at the Large Hadron Collider

Supervisor:
Chiar.mo Prof. C. Sciacca
Chiar.mo Dr. L. Lista

Ph.D. Candidate:
Alberto Orso Maria Iorio

"However much I study, it is never enough."

Takamatsu Toshitsugu

"O frati," dissi, "che per cento milia
perigli siete giunti a l'occidente,
a questa tanto picciola vigilia

d'i nostri sensi ch'è del rimanente
non vogliate negar l'esperïenza,
di retro al sol, del mondo sanza gente.

Considerate la vostra semenza:
fatti non foste a viver come bruti,
ma per seguir virtute e canoscenza."

Dante Alighieri, Inferno, Canto XXVI, 112-120.

A Bianca Fagnani

Abstract

In my PhD I actively participated the Compact Muon Solenoid (CMS) experiment at the Large Hadron Collider (LHC) of CERN. My work over the three years of the PhD encompassed several aspects of the experiment, including participation to data taking activities, performance studies of the detector and data analysis finalized to the measurement of single top quark production. During the first year of my Ph.D. program I had the chance to participate in the commissioning effort of the CMS Muon System, studying the performances of the Resistive Plate Chambers detectors using cosmic ray data collected in 2008-2009 and early collision data taken in 2010. The second and third years of my Ph.D. program were devoted to the study of the production of single-top events in proton-proton collisions at LHC. The LHC has been successfully running since the end of 2009 and is providing 7 TeV center of mass proton-proton collision data since March 2010, collecting data corresponding to an integrated luminosity of $36.1 \ pb^{-1}$. With the data taking of 2011, the instantaneous luminosity of the machine was constantly upgraded, allowing to collect $5.73 \ fb^{-1}$ of integrated luminosity. The CMS detector has successfully collected collision data through 2010 and 2011, collecting a total integrated luminosity of $5.22 \ fb^{-1}$. The LHC is often considered to be a "top quark factory", allowing for a production of top quarks through several mechanisms: $t\bar{t}$ pair production, mainly occurring through processes which involve the strong interaction, and single top quark production, which occurs through electroweak interactions and has been object of study of my thesis. There are three mechanisms of production of single top, known as t,s, and tW channels. The study of single top processes provides the unique opportunity to explore the electroweak sector of top quark physics, allowing for example a direct measurement of V_{tb} as well as the study of Flavour Changing Neutral Currents. On the other hand single top channels offer a window for searches for physics beyond standard model, being for instance sensitive to W' resonances. Amongst the three channels, I focused my work on the t channel, which yields a production cross section of 64.6 pb, the highest amongst the single top processes. I developed and deployed an analysis which focused on the top quark decay channel $t \rightarrow Wb \rightarrow \mu\nu b$ aiming at early observation of single top events with the 2010 dataset. I was successful in achieving the first experimental evidence of single top at the LHC, which resulted in a paper published on PRL . With 2011 data incoming, I developed and deployed a new analysis, adapting the strategy to a different goal: the new analysis should have minimized the systematic uncertainty and at the same time be model-independent to allow for further studies of single top polarization and beyond standard model physics searches. The results have been updated with a luminosity of $1299 \ pb^{-1}$, and a combination with the electron channel results has been performed to increase the precision of the measurement.

Contents

List of Figures

List of Tables

Chapter 1

Introduction

The efforts undergone through the last century by the world-wide scientific community on both the experimental and theoretical sides to understand the world of particle physics led to a coherent, yet not by all means exhaustive, picture within a very successful relativistic quantum field theory known as the standard model (SM). The standard model [6][7][8] [11] allowed for sa everal predictions which over the course of the years could be experimentally verified, at the same time confirming the model and giving more insight of it thanks to increasingly precise measurements on the SM free parameters. Much of the history of particle physics revolved around the chase between the experiments and the theoretical predictions both in terms of precision and energy scale. At the current stage, our understanding of particle physics is nevertheless far from complete. First of all, the standard model does require the introduction of an ad-hoc mechanism for the generation of the mass, the Higgs mechanism, forseeing the presence of an extra particle, said the Higgs boson, which to the day stays the only standard model particle which has not been experimentally observed. Besides, there are other issues that cannot be solved within the boundaries of the standard model. Examples include cosmological observations of dark energy and mass, quantum gravity, etc. Finally, the current experiments have already explored most of the standard model looking for confirmation of its validity, but not all sectors have been equally covered and no experiment was able to fully probe the energy scale at which the standard model assumptions are expected to break down, namely the TeV scale. To address the open questions of standard model and to search for the Higgs boson as well as for evidences of new physics beyond the standard model, to make a step forward to either close the deal with the standard model or find solid indications of a new model that replaces it, a machine able to explore the TeV frontier is necessary. The Large Hadron Collider (LHC) has been specifically built for the purpose: to be a discovery machine with multi-TeV center of mass energies for particle generation and a high luminosity of the beams to gather the necessary statistics for discovery in a few years. The proportions of the experimental challenges that this ambitious project poses are reflected in the design and sheer numbers of LHC: located about 100 meters underground in the tunnel which previously hosted the Lage Electron Positron (LEP) collider, with its 26.7 km length it is nowadays the greatest active experiment ever realized by mankind. It took two decades of planning, developing and building and the collaboration of about 10 000 physicists from more than 30 different countries. The Large Hadron Collider (LHC) is a two-ring-superconducting-hadron accelerator and collider which is currently active and providing collisions since the last months of 2009. In correspondence of its four interaction points four big experiments are placed: ATLAS [31], CMS [32], ALICE [33] and LHCb [34].

The Compact Muon Solenoid experiment at the LHC is designed to perform standard model measurements at the LHC energy as well as to search for the Higgs boson and for

hints of new physics. There is great interest in standard model physics measurements at LHC. The first reason is that no machine has ever tested the standard model at such energy scale. The second reason is that there are some sectors of the SM physics where the measurements of SM parameters at LHC can surpass the precision of the ones at previous accelerators. There are even SM processes which where not observable at all in previous accelerators. This is the case for the physics of the top quark.

One of the most remarkable successes of the SM is the prediction of three quark families in association to three leptons families. At the same time, it is remarkable that amongst the quark families, the last family presents the widest gap in the mass of its constituents, namely the beauty b and top t quarks. For such reason, the top quark is the latest particle of the standard model to have been discovered. Althought the Tevatron accelerator at Fermilab has already measured the top quark production and properties in a different energy range, the production cross section of top quarks at LHC is much higher. In fact, this results into a huge array of possibilities for physics measurements in such sector, both for standard model precision measurements as well as for new physics searches having decay modes involving top quarks.

Amongst the top quark production mechanisms, the electroweak processes are the most recently observed and the ones where the LHC can exploit its full potential. Since in those processes the top quark is produced in association quarks much lighter than it, they are named single-top processes, in contrast with $t\bar{t}$ pair production processes. Three such processes are in the LHC energy reach named s, t, and tW channels. All three of them are directly related to the Cabibbo Kobayashi Maskawa matrix element V_{tb}; they can be used to probe several standard model properties to indirectly search for new physics; moreover they are also windows for the direct search for new physics processes.

The $t-$channel has the highest cross section of the three single top processes, and has also the highest potential for early, low statistics studies. The precision measurement of the $t-$channel cross section is a crucial check of the standard model at the LHC energy scale, and through that it is possible to measure V_{tb}. Also the SM predicts a consistent asymmetry in top-antitop pair production from proton-proton collisions, which can be measured to constrain the distribution functions of the LHC protons constituents (partons).

This thesis work focuses on the study of the $t-$channel production throug the decay chain $t \to Wb \to \mu\nu b$, which provides the cleanest signature for this process.

This thesis is organized as follows

- Chapter 2 gives an overview of the current picture of particle physics at the accelerators, describing the standard model and the electroweak symmetry breaking mechanism, as well as the beyond standard model possible scenarios.

- Chapter 3 describes the workings LHC accelerator and the detail of the CMS detector.

- Chapter 4 gives an overview of the CMS event reconstruction chain, describing the physics objects used in the analysis, showing the performances of the detector on data taken in 2010 and 2011.

- Chapter 5 describes the Resistive Plate Chambers (RPC) detector at CMS and the workings of the RPC Level-1 trigger, and include my performance studies on the RPC detector and trigger system.

- Chapter 6 describes in the detail the physics prospect at the LHC, with particular attention to the top quark sector. The chapter concludes describing the phenomenology of single top events.

- Chapter 7 describes in the detail the physics of single top at the CMS, the topology of single top events reconstructed in the CMS detector and the analysis performed on

2010 data to achieve early evidence of single top t-channel production

- Chapter 8 describes the analysis adapted to minimize systematics uncertainties and model-dependent assumptions which has ben developed and deployed on 1299 pb^{-1} of collision data taken by CMS in 2011.

- Chapter 9 summarizes the results, describes the combination to get the final result, the V_{tb} extraction a and draws the conclusions.

Chapter 2

Particle physics at the TeV scale and beyond

2.1 The Standard Model

The purpose of particle physics is to identify the fundamental components matter and to understand the interactions between them. The most accurate model that describes particle physics is known as the Standard Model [14] [13] [12]. The Standard Model is a quantum field theory that treats both matter and force fields with the same formalism, since interactions are themselves regarded as mediated by particles. Fundamental matter particles in Standard Model are categorized as either quarks or leptons, which are grouped in three generations each. A generation (or family) is a doublet of particles associated to an isospin quantum number. All quark generations contain a particle with $+2/3$ charge and a particle with charge $-1/3$, while lepton generations include a particle with charge -1 (e.g. the electron) and a neutral particle, named neutrino. The quantum numbers of all quarks and leptons are listed in table 2.1. The Standard Model describes three fundamental interactions: electromagnetic, weak and strong interaction. Each interaction is associated to a boson multiplet, whose components are referred to as mediators for the interaction, and to an absolutely conserved quantum number, which is the charge in the case of electromagnetism. Mediator bosons are listed in Table 2.2. The dynamics equations for the Standard Model are obtained from a gauge principle: the free particle lagrangian is requested to be invariant under a local (gauge) transformation from the symmetry group:

$$SU(3)_{col} \otimes SU(2)_{is} \otimes U(1)_y \tag{2.1}$$

the free particle lagrangian is requested to be invariant under a local (gauge) transformation from the symmetry group:

$$SU(3)_{col} \otimes SU(2)_{is} \otimes U(1)_y \tag{2.2}$$

The number of the mediator bosons for an interaction is determined by the symmetry group associated with it. The $SU(3)_{col}$ group is the symmetry that generates the strong interaction.

Particle				Spin	Charge
Leptons	$\begin{pmatrix}\nu_e\\e\end{pmatrix}$	$\begin{pmatrix}\nu_\mu\\\mu\end{pmatrix}$	$\begin{pmatrix}\nu_\tau\\\tau\end{pmatrix}$	$1/2$	0 -1
Quarks	$\begin{pmatrix}\nu_e\\e\end{pmatrix}$	$\begin{pmatrix}\nu_\mu\\\mu\end{pmatrix}$	$\begin{pmatrix}\nu_\tau\\\tau\end{pmatrix}$	$1/2$	$2/3$ $-1/3$

Table 2.1: Standard model fermions.

Interaction	Particle	Spin	Charge
Electromagnetic	γ	1	0
Weak	W^+, W^-, Z	1	$1, -1, 0$
Strong	8 gluons (g)	1	0

Table 2.2: Standard model mediator bosons and fundamental interactions.

Its conserved quantum number is the color, which is the equivalent of electromagnetic charge for strong interactions, with the dierence that three possible colors are present. Strong interaction is mediated by an octet of vector bosons, the gluons. Those gluons are colored particles themselves, while the photon, for instance, doesn't carry electromagnetic charge. The $SU(2)_{is} \otimes U(1)_y$ group is the symmetry that generates both the Electromagnetic and Weak interactions into an unified theory known as th e Glashow-Salam-Weinberg model [6] [8] [7]. The mediators generated by this symmetry are the vector bosons $W^\pm, Z$, and γ. It is noteworthy that while the photon is massless, all mediators from weak interactions are massive particles. In order to produce a mass term for $W^\pm$ and Z Z that does not destroy the gauge invariance for the Standard Model lagrangian, the spontaneous symmetry breaking mechanism is introduced. This mechanism predicts the presence of a scalar particle, the Higgs boson [15] [16], whose couplings with the vector bosons allow the presence of the required mass term. At present state, no experimental evidence of the Higgs boson has been found.

2.2   Quantum electrodynamics

The Quantum Electrodynamics is the simplest example of a realistic quantum field theory obtained from the imposition of a gauge invariance. The symmetry group involved in this case is $U(1)_q$, where the subscript charge indicates the conserved quantum number, interpreted as the charge of the particles. The lagrangian density for the Dirac equation describing a spin 1/2 fermion can be written as:

$$\mathcal{L}_D = i\bar{\psi}\gamma^\mu\partial_\mu\psi - m\psi\bar{\psi} \tag{2.3}$$

which comprises a kinetic term and a mass term, where m is the fermion mass parameter, γ^μ are the Dirac gamma matrices and $\psi(\bar{\psi})$ is the spinor field for the fermions (its adjoint), namely:

$$\psi = \begin{pmatrix} \psi_R \\ \psi_L \end{pmatrix} \tag{2.4}$$

The kinematic lagrangian term for a photon is introduced as:

$$\mathcal{L}_\gamma = -\frac{1}{4}F^{\mu\nu}F_{\mu\nu} \tag{2.5}$$

where $F^{\mu\nu}$ is the tensor field constructed starting from the 4-vector electromagnetic field A_μ in the following way:

$$F_{\mu\nu} = \partial_\mu A_\nu - \partial_\nu A_\mu \tag{2.6}$$

So, the free (non interacting) lagrangian for a fermion field and an electromagnetic field is:

$$\mathcal{L}_D + \mathcal{L}_\gamma = i\bar{\psi}\gamma^\mu\partial_\mu\psi - m\psi\bar{\psi} - \frac{1}{4}F^{\mu\nu}F_{\mu\nu} \tag{2.7}$$

The dynamics equations obtained from Eq. 2.7 do not couple the fermion field ψ and the electromagnetic field A_μ, so that an additional interaction term is needed in which both the

fermion and the photon fields are involved. This term is obtained using a gauge invariance principle. As a first step, one can notice that the lagrangian of Eq. 2.7 is invariant under a global $U(1)_q$ gauge transformation:

$$\psi \to \psi' = e^{i\theta}\psi \tag{2.8}$$

where θ is a real constant number. This kind of invariance does not extend however to local $U(1)_y$ transformations, which are of the type:

$$\psi \to \psi' = e^{i\theta(x)}\psi \tag{2.9}$$

where $\theta(x)$ has a dependence for the space-time point. The gauge principle consists in imposing this local $U(1)_y$ invariance. The covariant derivative operator is defined:

$$D_\mu = \partial_\mu + iqA_\mu \tag{2.10}$$

where A_μ transforms under $U(1)_y$ according to the rule:

$$A_\mu \to A'_\mu = A_\mu - \frac{1}{q}\partial_\mu\theta \tag{2.11}$$

By replacing the usual derivative operator with the covariant derivative in Eq. 2.7 one obtains the Quantum Electrodynamics (QED) lagrangian:

$$\mathcal{L}_{QED} = i\bar{\psi}\gamma^\mu\partial_\mu\psi - m\psi\bar{\psi} - \frac{1}{4}F^{\mu\nu}F_{\mu\nu} - q\bar{\psi}\gamma^\mu A_\mu\psi \tag{2.12}$$

The additional term that represents the electromagnetic interaction is:

$$\mathcal{L}_{int} = -q\bar{\psi}\gamma^\mu A_\mu\psi = -J^\mu A_\mu \tag{2.13}$$

where q is the charge of the particle and represents the strength of the coupling. The quantity J^μ is interpreted as the charge current, that is the probability current of the particle multiplied by its charge. The interaction term is then used to obtain the amplitude for all electromagnetic processes; it is also possible define a diagram for any electromagnetic process that is associated with its amplitude. Those diagrams are also known as Feynman diagrams. The crucial point of this procedure is the necessity to introduce a covariant derivative term Eq. 2.10in order to make the lagrangian gauge invariant.
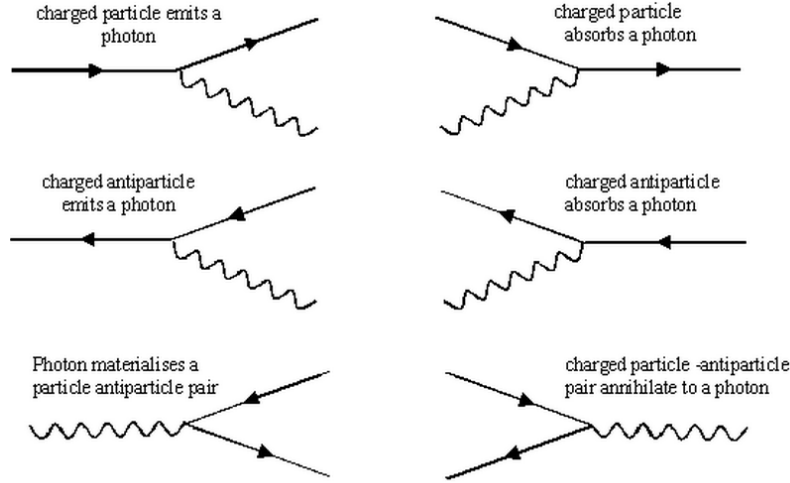
Figure 2.1: Electromagnetic interaction vertices, coupling two fermion fields and one photon field.

2.3 The electroweak theory

2.3.1 The GSW model

The relevant symmetry group for Weak interactions is $SU(2)_L$, where the L, subscript means that only the left-handed chiral components of the fields are involved in the interaction. The choice of this group is suggested by the kind of transitions this interaction produces: six families (doublets) of weak isospin can be identified and weak interactions produce a transition between the members of those doublets. Since the fundamental representation of $SU(2)$ is generated by Pauli matrices, it is possible to adopt the usual formalism of the angular momentum for weak isospin. By naming t the weak isospin quantum number and t_3 its observed component one can define

$$\begin{aligned} t_3 &= +1/2 \\ t_3 &= -1/2 \end{aligned} \begin{pmatrix} \nu_e \\ e \end{pmatrix}_L \begin{pmatrix} \nu_\mu \\ \mu \end{pmatrix}_L \begin{pmatrix} \nu_\tau \\ \tau \end{pmatrix}_L \tag{2.14}$$

for lepton pairs, and:

$$\begin{aligned} t_3 &= +1/2 \\ t_3 &= -1/2 \end{aligned} \begin{pmatrix} u \\ d' \end{pmatrix}_L \begin{pmatrix} c \\ s' \end{pmatrix}_L \begin{pmatrix} t \\ b' \end{pmatrix}_L \tag{2.15}$$

for quark pairs, where the d', s',and b' quarks are quantum mechanical superpositions of d, s and b which are classiifed by their strong quantum numbers. A local $SU(2)_L$ transformation acting on the isospin doublets will therefore take the form:

$$\begin{pmatrix} \nu_l \\ l^- \end{pmatrix}_L' = e^{-\frac{i}{2}\vec{\alpha}(x)\cdot\vec{\tau}} \begin{pmatrix} \nu_l \\ l^- \end{pmatrix}_L \tag{2.16}$$

where $\vec{\tau}$ is the vector of Pauli matrices and $\vec{\alpha}(x)$ is a vector of three real parameters and it depends from the space-time point. The right-handed chiral component of the particles does not enter the interaction, so it has the properties of an $SU(2)_L$ singlet. By imposing the gauge invariance one can obtain three vector fields: namely W^1, W^2, W^3.

In this naive model for weak interactions the boson fields do not correspond to the actual physical fields. This model is therefore completed and expanded adding the requirement of the $U(1)_y$ invariance and therefore defining the group of transformations:

$$SU(2)_{is} \otimes U(1)_y \tag{2.17}$$

This symmetry group therefore requires the presence of 3 + 1 gauge fields The relevant quantum numbers, and the conserved quantities of the interaction are the hypercharge y and the weak isospin T. The following relation allows to define the electromagnetic charge of a particle from the electroweak quantum numbers:

$$eQ = e\left(t_3 + y/2\right) \tag{2.18}$$

where t_3 is the third component of weak isospin. The covariant derivative operator that makes the free lagrangian invariant under an $SU(2)_{is} \otimes U(1)_y$ transformation takes the following form:

$$D_\mu = \partial_\mu + ig\frac{\vec{\tau}}{2}W_\mu + ig'yB_\mu \tag{2.19}$$

The mass terms for fermions and bosons will be discussed later in this chapter. Not considering the mass terms for now, the lagrangian for electroweak interactions will include a Dirac term for the fermions modified with the covariant derivative:

$$\mathcal{L}_{fermions} = \sum_f \bar{\psi}\gamma^\mu D_\mu \psi \tag{2.20}$$

and a term for the dynamics of the gauge boson fields

$$\mathcal{L}_{gauge} = -\frac{1}{4}W_i^{\mu\nu}W_{\mu\nu}^i - \frac{1}{4}B^{\mu\nu}B_{\mu\nu} \tag{2.21}$$

where $W_i^{\mu\nu}$ and $B_{\mu\nu}$ are the tensor fields:

$$W_i^{\mu\nu} = \partial^\mu W_i^\nu - \partial^\nu W_i^\mu \tag{2.22}$$
$$B_i^{\mu\nu} = \partial^\mu B^\nu - \partial^\nu B^\mu \tag{2.23}$$
$$\tag{2.24}$$

and W_μ is a three component vector field. The complete lagrangian for the electroweak processes will therefore be:

$$\begin{aligned}
\mathcal{L}_{EW} = &-i\psi_L\left(\partial_\mu + ig\frac{\vec{\tau}}{2}\cdot W_\mu + ig'yB_m u\right)\psi_L+ \\
&-i\psi_R\left(\partial_\mu + ig'yB_m u\right)\psi_R+ \\
&-\frac{1}{4}W_i^{\mu\nu}W_{\mu\nu}^i - \frac{1}{4}B^{\mu\nu}B_{\mu\nu}+ \\
&+\mathcal{L}_{WWV} + \mathcal{L}_{WWVV}
\end{aligned} \tag{2.25}$$

where ψ_L and ψ_R are the left and right handed chiral components of the particles, and the $\mathcal{L}_{WWV}$, and $\mathcal{L}_{WWVV}$ terms describe the three- and four- point self interactions of the vector bosonsthat arise because of the non-Abelian nature of the $SU(2)_{is}$ group. The four gauge fields can be combined to produce the physical vector fields for the $W^\pm, Z$ bosons and the photon:

$$\begin{aligned}
W_\mu^\pm &= \sqrt{\frac{1}{2}}\left(W_\mu^1 \mp W_\mu^2\right) \\
A_\mu &= B_\mu\cos\theta_W + W_\mu^3\sin\theta_W \\
Z_\mu &= -B_\mu\sin\theta_W + W_\mu^3
\end{aligned} \tag{2.26}$$

$$cos\theta_W$$

where θ_W is the Weinberg angle, or weak mixing angle, defined as:

$$\cos\theta_W = \frac{g}{\sqrt{g^2 + g'^2}}, \quad \text{and} \quad \sin\theta_W = \frac{g'}{\sqrt{g^2 + g'^2}} \tag{2.27}$$

The electromagnetic charge is therefore:

$$q = g' \cos \theta_W = g \sin \theta_W \qquad (2.28)$$

2.3.2 Spontaneous symmetry breaking and the Higgs boson

The gauge principle allows to successfully describe the interactions between particles; however, all fields produced by imposing the gauge invariance are strictly massless. A mass term of the form $mA^\mu A_\mu$ for a boson field is not invariant under an $SU(2)_{is} \otimes U(1)_y$ transformation, nevertheless it is established that the vector bosons $W^\pm$ and Z have a consistently non zero mass, which gives weak interactions their short-range characteristics. $W^\pm$, Z masses have been measured in 1983 thanks to the $UA1$ [17] and $UA2$ [18] collaborations. It is therefore necessary to introduce a new term that coherently represents the masses of the particles, while at the same time it must preserve the gauge principle. The spontaneous symmetry breaking mechanism allows to generate such terms by postulating the existence of a new scalar particle: the Higgs boson. The Higgs boson field is written as a $SU(2)_{is}$doublet with two scalar components:

$$\begin{pmatrix} \phi^+ \\ \phi^0 \end{pmatrix} = \begin{pmatrix} \phi_1 + i\phi_2 \\ \phi_3 + i\phi_4 \end{pmatrix} \qquad (2.29)$$

The lagrangian for such boson includes a potential which is responsible of the symmetry breaking mechanism:

$$\begin{aligned}
\mathcal{L}_H &= (D^\mu \Phi)^\dagger D_\mu \Phi - V(\Phi) = \\
&= (D^\mu \Phi)^\dagger D_\mu \Phi - \mu^2 \Phi^\dagger \Phi - \lambda \left(\Phi^\dagger \Phi \right)^2
\end{aligned} \qquad (2.30)$$

By requiring that $\mu^2 < 0$ and $\lambda > 0$ the minimum of the potential is not unique anymore, but its located on a continuous ring on a complex plane (see Fig.2.2). There is therefore a
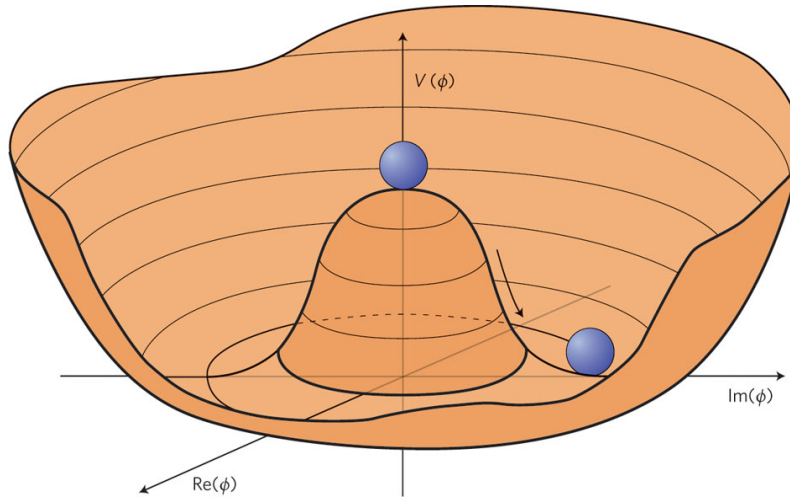
Figure 2.2: Higgs potential described from the last two terms of Equation 2.30 with $\mu^2 < 0$ and $\lambda > 0$. The potential minimum is located on a continuous ring.

degree of freedom for the choice of higgs vacuum state. Writing the higgs field so theat only one of its components is non-zero we obtain:

$$\begin{pmatrix} 0 \\ v + h(x) \end{pmatrix} \qquad (2.31)$$

where

$$v = -\sqrt{-\mu^2/\lambda} \tag{2.32}$$

In an $SU(2)_{is} \otimes U(1)_y$ theory the kinetic term of Higgs lagrangian can therefore be written by imposing the form of the covariant derivative from Eq. 2.19, so to obtain:

$$
\begin{aligned}
(D^\mu \Phi)^\dagger D_\mu \Phi =& \frac{1}{2}\partial_\mu h \partial^\mu h + \\
& \frac{1}{8}(v+h)^2 g^2 (W_\mu^1 + iW_\mu^2)(W^{1\mu} - W^{2\mu}) + \\
& \frac{1}{8}(v+h)^2 (g'B_\mu - gW_\mu^3)(g'B^\mu - gW^{3\mu})
\end{aligned} \tag{2.33}
$$

The lagrangian of the sector consisting of the gauge fields and the Higgs is:

$$
\begin{aligned}
\mathcal{L}_{G\Phi} = \mathcal{L}_{gauge} + \mathcal{L}_H = &+\mathcal{L}_{gauge} = \\
(D^\mu \Phi)^\dagger D_\mu \Phi - V(\Phi) &- \frac{1}{4}W_i^{\mu\nu}W_{\mu\nu}^i - \frac{1}{4}B^{\mu\nu}B_{\mu\nu}
\end{aligned} \tag{2.34}
$$

Switching to the physical Z and A fields, and keeping only the quadratic terms, Eq. 2.34 can be written as:

$$
\begin{aligned}
\mathcal{L}_{G\Phi} =& \frac{1}{2}\partial_\mu h \partial^\mu h - \mu^2 h^2 + \\
& -\frac{1}{4}(\partial_\mu W_\nu^1 - \partial_\nu W_\mu^1)(\partial^\mu W^{1\nu} - \partial^\nu W^{1\mu}) + \frac{1}{8}g^2 v^2 W_\nu^1 W^{1\nu} \\
& -\frac{1}{4}(\partial_\mu W_\nu^2 - \partial_\nu W_\mu^2)(\partial^\mu W^{2\nu} - \partial^\nu W^{2\mu}) + \frac{1}{8}g^2 v^2 W_\nu^2 W^{2\nu} \\
& -\frac{1}{4}(\partial_\mu Z_\nu - \partial_\nu Z_\mu)(\partial^\mu Z^\nu - \partial^\nu Z^\mu) + \frac{1}{8}(g^2 + g'^2)v^2 Z_\nu Z^\nu \\
& -\frac{1}{4}F^{\mu\nu}F_{\mu\nu}
\end{aligned} \tag{2.35}
$$

where the latter raw is the tensor field for the photon as in Eq 2.6, the second term in the second and third rows has exactly the form of a mass term for the $W^{1(2)}$ fields and one therefore can define the W mass as:

$$m_W = \frac{1}{2}vg \tag{2.36}$$

while from the fourth row of Eq 2.35 one gets the Z boson mass term:

$$m_Z = \frac{1}{2}v\sqrt{g^2 + g'^2} = \frac{m_W}{\cos\theta_W} \tag{2.37}$$

2.3.3 The fermions masses

The fermion mass term $-m\bar{\psi}\psi$ introduced in Eq 2.3 can be written in terms of left and right-handed spinors, e.g. for the electron:

$$m_e \bar{\psi}\psi = m_e(\bar{e}_R e_L + \bar{e}_L e_R) \tag{2.38}$$

However, this term is not gauge invariant because e_L is a component of an $SU(2)_{is}$ doublet while e_R is an $SU(2)_{is}$ singlet. It is possible to produce a gauge invariant mass term by introducing a Yukawa coupling between the fermions and the higgs field:

$$\mathcal{L}_Y = g_f(\bar{\psi}_L \Phi \psi_R - \bar{\psi}_R \Phi^\dagger \psi_L) \tag{2.39}$$

where ψ_L and ψ_R are the left $SU(2)_{is}$ doublet and the right $SU(2)_{is}$ singlet, g_f is the Yukawa coupling constant. At $\Phi = \Phi^0$, Eq 2.39 becomes (e.g. for leptons):

$$\frac{g_f}{\sqrt{2}}\left[(\nu_l \ l)\begin{pmatrix} 0 \\ v+h(x) \end{pmatrix} l_R + l_R(0 \ v+h)\begin{pmatrix} \nu_l \\ l \end{pmatrix}\right] =$$
$$\frac{g_f}{\sqrt{2}}(v+h)(l_L l_R + l_R l_L) \tag{2.40}$$

so that the constant coefficient of $(l_L l_R + l_R l_L)$ is the mass term for the leptons:

$$m_f = \frac{g_f \cdot v}{\sqrt{2}} \tag{2.41}$$

Analogously one can write for the quarks:

$$\frac{1}{\sqrt{2}}\left[g_{d,i}(u_{i,L} \ d_{i,L})\begin{pmatrix} 0 \\ v+h(x) \end{pmatrix} d_{i,R} + g_{u,i}(u_{i,L} \ d_{i,L})\begin{pmatrix} -(v+h)* \\ 0 \end{pmatrix} u_{i,R} + hc\right] =$$
$$\frac{1}{\sqrt{2}}(v+h)[g_{u,i}(u_{i,L}u_{i,R} + u_{i,R}u_{i,L}) + g_{d,i}(d_{i,L}d_{i,R} + d_{i,R}d_{i,L})+] \tag{2.42}$$

where $u_i = (u; c; t)$ and $d_i = (d; s; b)$ and the mass term has the same form as in Eq. 2.41. Even if this kind of Yukawa coupling solves the problem of fermions' masses, it does not arise from a gauge principle and it is purely phenomenological. In order for it to be justified an important step would be the discovery of the Higgs boson and the measurement of its branching fractions.

2.4   Quantum Chromodynamics

Quantum Chromodynamics (QCD) is the theory of strong interactions. As for electromagnetic and weak interactions it is formulated thanks to the imposition of a gauge principle, with the dierence that now the symmetry group is $SU(3)_{col}$, where the C subscript refers to a new degree of freedom called color. Strong interactions only involve quarks, which are present in three color eigenstates. The free quark lagrangian is now:

$$\mathcal{L}_{Free} = \bar{\psi}_\alpha \gamma_\mu \partial^\mu \psi_\alpha - m\bar{\psi}_j \psi_j \tag{2.43}$$

where $\alpha = 1,2,3(B,R,G)$ is the color index. The $SU(3)_{col}$ transformation takes the form:

$$\psi \rightarrow \psi' = e^{-\frac{i}{2}g_s \theta_\alpha(x)\lambda_\alpha}\psi \tag{2.44}$$

where λ_α are the eight Gell Mann matrices and are generators of $SU(3)_{col}$, $g_s = \sqrt{4\pi\alpha_s}$, and α_s is is the coupling constant for strong interactions. The commutation rules of λ_α are:

$$\left[\frac{\lambda_a}{2}, \frac{\lambda_b}{2}\right] = if_{abc}\frac{\lambda_c}{2} \tag{2.45}$$

where f_{abc} are the structure constants of the groups and the indices run from 1 to 8. Gauge invariance under transformations in Eq 2.44 requires a covariant derivative such as:

$$D_\mu = \partial_\mu + ig_s \frac{\lambda_a}{2}G_\mu^a \tag{2.46}$$

where G_μ^a are the 8 gluon fields that transform as:

$$G_\mu^a \rightarrow G_\mu'^a = G_\mu^a + ig_s f^{abc}\theta_b(x)G_{c,\mu} \tag{2.47}$$

The complete QCD lagrangian then becomes:

$$\mathcal{L}_{QCD} = \bar{\psi}\gamma^\mu\partial_\mu\psi - m\bar{\psi}\psi - igs\bar{\psi}\gamma^\mu\lambda_a\psi G_\mu^a - \frac{1}{4}G^{\mu\nu}G_{\mu\nu}^a \qquad (2.48)$$

with $G_a^{\mu\nu}$ the tensor field defined as

$$G_a^{\mu\nu} = \partial^\mu G_a^\nu - \partial^\nu G_a^\mu - g_s f_{abc}G^{b,\mu}G^{c,\nu} \qquad (2.49)$$

The last term in Eq. 2.49 is quadratic in the gluon fields and produces a self-interaction between the gluon fields themselves. Such a term does not arise in QED and is due to the non-Abelian character of the $SU(3)_{col}$symmetry group
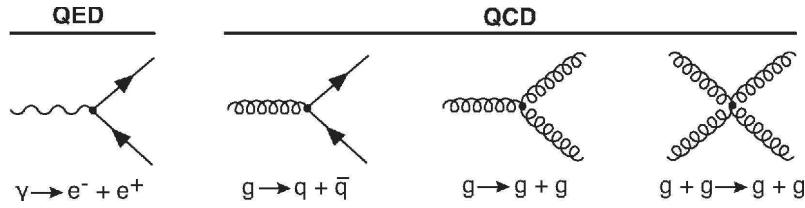
Figure 2.3: Electromagnetic interaction vertex (left) vs QCD interaction vertices (right). The last two diagrams represent a gluon-gluon tree-level interaction which has no counterpart in QED

2.4.1 Asymptotic freedom and color confinement

Quantum Chromodynamics as the theory for strong interactions has to explain its fundamental characteristics. Strong force is responsible for the inter-quark interactions that bind them together, forming hadrons. However, no color multiplicity of mass degenerate hadrons is observed, so stable states can only be color singlets. This property is known as color confinement. The study of bound states in QCD presents several difficulties, due to the strength of the coupling that makes a perturbative approach to calculations impossible at energies of $O(200)$ MeV, that is the energy scale of quarks and gluons in a proton at rest and in general of colored particles composing an hadron. Still all experimental results show that, for sufficiently high energy processes, quarks inside protons behave as free particles. This property is known as asymptotic freedom and it can be qualitatively explained thanks to the renormalization of QCD theory. The renormalization process starts from the fact that the physical coupling constant is not actually the gs that appears in the lagrangian, but the real parameter takes into the account all the loop corrections of the theory at any perturbative order. This happens because in nature particles are cannot be separated from interactions even when they are propagating in the void, meaning that the physic lagrangian is the one that includes the interaction terms. Thus a particle at any space-time point produces virtual couples that modify the charge distribution around the particle itself. This causes the actual coupling constant in any process to assume a dependance from the transferred 4-momentum q:

$$\alpha_s(|q^2|) = \frac{\alpha_s(\mu^2)}{\left[1 + \alpha_s(\mu^2)\frac{(33-2N_f)}{12\pi}ln(|q^2|/\mu^2)\right]} \qquad (2.50)$$

where $N_f = 6$ is the number of fermions capable of strong interactions (6 quarks) and μ is a scale parameter for the strength of the coupling. So the value of the coupling constant decreases as the transferred 4-momentum increases, making it possible to apply perturbative calculation. Equivalently, α_s is a growing function of the distance between the two interacting particles, and the critical value set by the μ scale is approximately 1 fm,

which is also the approximate proton radius. This result shows that QCD is consistent with the fact that no calculation can be made at perturbative level for hadronic states; on the other hand, progresses have been made for studies of bound states thanks to Lattice Field Theories. Figure 2.4 shows α_s as a function of the transferred four momentum module Q.
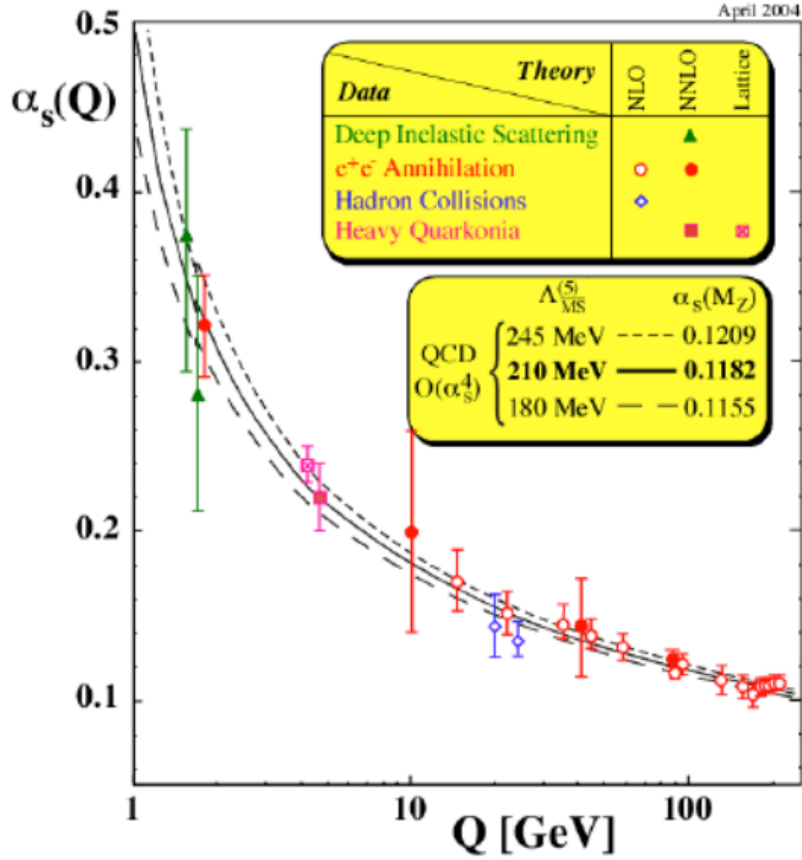
Figure 2.4: QCD coupling constant α_s as a function of the module of the transferred momentum Q from theory and experiment.

2.5 The quark parton model and hadron-hadron interactions

The properties of QCD described in Section 2.4.1, in particular the running of α_s as an decreasing function of the transverse four momentum, imply that while high energy collisions of quarks and gluons can be treated with perturbative methods, low-energy QCD interactions, e.g. processes with transferred four momentum $q^2 \sim 200 GeV$, cannot be treated in any perturbative theory. Therefore, we cannot predict what is the exact structure of the proton or neutron (inclusively called nucleons). Nevertheless it is possible to realize a model of the internal structure of a nucleon as an incoherent superposition of quarks and gluons, called partons [19] [20]. Each parton carries a fraction x of the nucleon momentum, and the probability distributions of this variable is called Parton Distribution Function (PDF). Therefore we write this as:

$$p_i^\mu = xp^\mu \tag{2.51}$$

where p and p_i are the proton and the ith parton 4-momenta respectively, and x is distributed as $f_i(x)$, with:

$$\sum_{i=partons} \int x f_i(x) dx = 1 \tag{2.52}$$

which means that the partons 4-momenta must add up to the proton momentum. If we interpret proton-proton interactions in term of partons collisions and in a first step neglect any dependence of f_i from the energy scale Q^2, we can write the cross section $\sigma_{pp \to cd}$ of a generic proton-proton process leading to a final state with particles c, d as:

$$\frac{d\sigma_{pp \to cd}}{dx_1 dx_2 d\Omega} = \sum_a \sum_b f_a(x_1) f_b(x_2) \frac{d\sigma_{ab \to cd}}{d\Omega} \qquad (2.53)$$

where the sums are intended over all partons which can give a proccess such as $ab \to cd$, $\sigma_{ab \to cd}$ is the cross section of the elementary process, Ω is the solid angle. With this model in mind it is possible to probe the internal structure of the proton at diffetent energies exploiting known processes. A first simple model the assumption that protons and neutrons are color singlets composed of three quarks each, respectively uud and udd. Nevertheless, nonperturbative strong interactions allow gluon and quark-antiquark pairs to continuously form and annihilate. Such quarks and gluons are often referred as "sea" partons, while the original three quarks composing the color singlet are named "valence" partons. It is not possible to derive the PDFs from theory due to the impossibility to perform calculations, yet it was poossible to measure them with several processes of deep inelastic scattering (HERA). PDFs actually do depend from the transferred momentum Q^2: their values tend to be shifted at low values of x as Q^2 increases. This introduces a further complication in Eq. 2.53, which however can be treated since the scale dependence of the parton distributions is calculable in QCD perturbation theory. Figures 2.5 show the parton distribution functions extrapolated at the energy of the LHC. The PDF modeling is one of
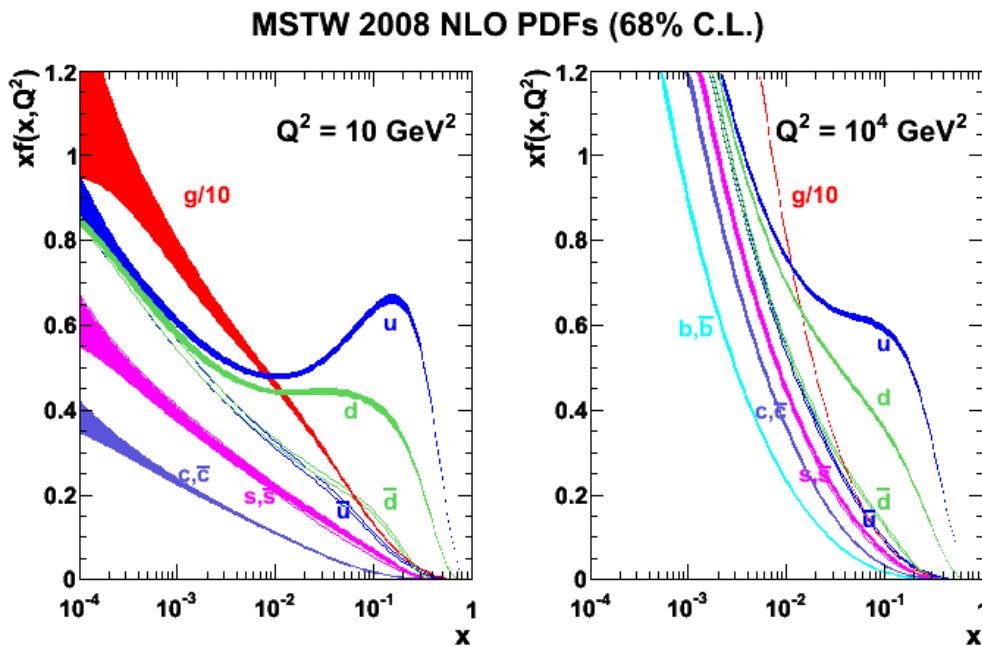
Figure 2.5: Partons pdfs examples at 10 and $10^4 GeV^2$ Q^2.

the sources of uncertainty for precision measurements of most physical processes at the LHC, and becomes crucial when dealing with measurements of charge asymmetries which in general depend on the flavour of the initial parton.

2.5.1 Phenomenology of proton-proton interactions

Proton-proton interactions at the colliders like the LHC can be therefore described as Standard Model processes involving partons which compose the original protons. The final

state of the a proton-proton collision will therefore be constituted of particles originated in the physics process of interest, which will have a significant momentum in the transverse plane with respect to the direction of the colliding protons (p_T), and the proton fragment which remain after the interaction and whose momentum is mostly parallel to the original momentum of the protons.

The physics process of QCD after the collision involve both the high p_T particles produced in the scattering process, and the hadronic fragments proceeding along the proton momentum. The scale of energy at which the parton collisions happen is sufficiently high that the processes can be treated in the framework of perturbative Standard Model even for QCD processes. Nevertheless as the colored particles in the final state, either from the hard interaction or the proton remnants, reach a distance of $O(1fm)$ between each other, non perturbative QCD interactions start to produce colored particles from the void up to the point where only color-neutral hadrons are present. To model this process one can make use of the QCD factorization theorem, which essentially ensures that the the different stages constituted by the hard process, the parton showering, and the hadronization can essentially be factorized. Figure 2.6 shows a pictorial representation of the different stages of hadron formation. *Parton showering* represents the phase where partons and
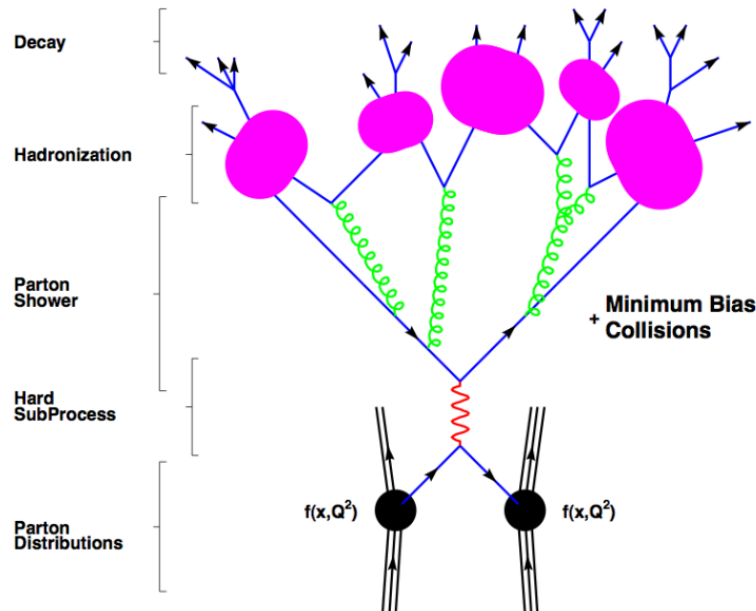
Figure 2.6: Summary of the different stages of hadron production.

gluons are emitted by the naked color charges due to the increase of the strength of the interaction. This is not modeled within the hard scattering, yet within the so called shower approach, where a parton decays into another parton and usually a gluon, and the splitting is regulated through the Altarelli splitting function [21]. The successive phase is the *hadronization*, where quarks and gluons are grouped together to form color-neutral hadrons. Two approach to hadronization modeling are usually adopted: the *Lund string* [100] [24] hadronization which models the strong interaction as 1 dimensional string between color-charged partons. The string breaks after a sufficient energy has been gathered for two partons to join in a color singlet. The leftovers of the string proceed until the next breaking point is reached. This gives an iterative procedure that can proceed up to the complete hadronization of colored particles. The second approach is the so called *Cluster Model*: [25] is based on the observation that the final quanta can be ordered and colour-singlet pairs end up close in phase space. Therefore, partons are "Preconfined": gluons of a given momentum Q_0 are split to $q\bar{q}$ pair, giving birth to high mass $q\bar{q}$ clusters. Figures

2.7 up, down show respectively a pictorical representation of the Lung string and cluster hadronization models.
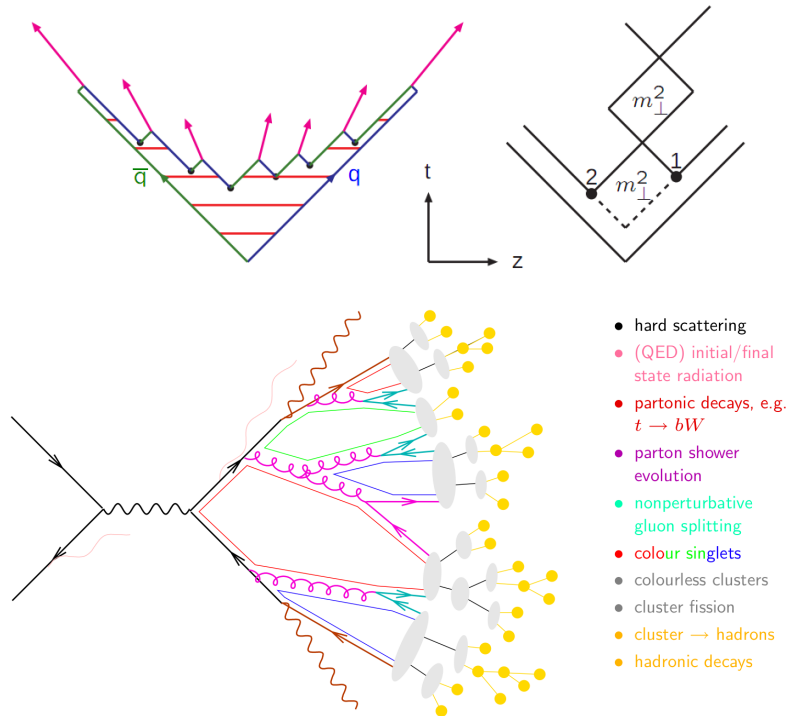
Figure 2.7: (up) Lund String model: when strings reach a given energy, they break and the remnant formes another string. (down) Cluster Model: the gluons with a momentum Q_0 are forced to split in $q\bar{q}$ pairs, giving an universal spectra for all hadronization processes.

The clusters of hadrons and particles stemming from hadronization of the partons are called *jets*. There are several algorithms for jet clustering and reconstruction, whose properties will be discussed in the detail in Chapter 4. Also, it is clear how hadronization of the proton remnants contaminates the final state of the high p_T phyiscs process, constituting the so called *underlying event*.

2.6 Open issues of the Standard Model

The Standard Model has been a successful theory, in so far it provided accurate predictions which have been verified experimentally over the last half century. Nevertheless, while the confidence in the validity of the Standard Model to describe particle physics at the electroweak scale increased as it was getting confirmed by always improving precision experiments, many motivations rose to believe the Standard Model could not be the exhaustive theory of particle physics. Of course, the stringent experimental verification of most of the Standard Model predictions indicate the validity of such theory at the electroweak scale, suggesting that SM is an effective theory which hints the presence of some underlying physics that manifests at an higher energy scale [26]. In fact, several issues are still open in modern particle physics:

- **The Higgs boson**: First of all, in order to satisfactorily incorporate the mass of the particles without recurring to new physics model, it is necessary that the Standard Model Higgs boson exists. Other mechanisms which generate a non SM higgs boson, like the technicolor, have been purposed. Constraints on the higgs boson mass are

given by imposing the self-consistency of the Standard Model In figure 2.8 these bounds on the SM Higgs boson mass are shown as a function of the cut-off scale Λ which the SM is to be replaced by a higher energy theory. The lower curve is
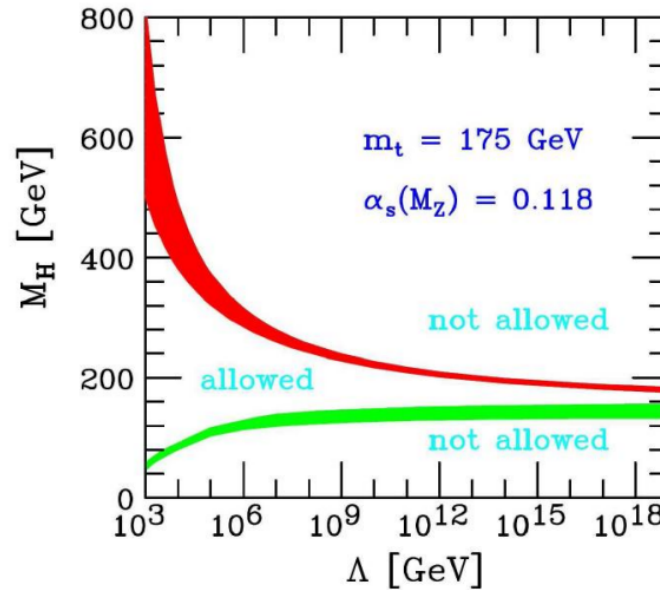
Figure 2.8: Theoretical limits on the Standard Model Higgs boson.

the region at which Higgs quartic potential becomes negative. The upper curve is the region at which Higgs self interactions cause loss of perturbativity of the theory. Observation of an Higgs boson outside the allowed region will indicate the presence of a theory beyond Standard Model (BSM). Stringent experimental constrains have been set by the Large Electron Positron experiment in the past, and recently by the LHC and Tevatron experiments which will be extensively discussed in chapter 6.

- **Forces unification and quantum gravity**: Althought Standard model unifies the electromagnetic and weak coupling constants within a $SU(2)_{is} \otimes U(1)_y$ gauge theory, the electroweak and strong interactions are not unified yet. Many theoretical models have been proposed, amongst which the GUT (Grand Unification Theory), which foresee the unification within more complex gauge groups and the presence of new heavy boson mediators and brand new sets of particles. On the other hand, Standard Model by design does not even incorporate quantum-gravitational interactions. The expected energy at gravitational interactions are expected to be quantized is the so-called Planck scale, which is $O(10^{19} GeV)$. This is related to the huge difference in strength of the interactions, as the electromagnetic coupling costant α at the electroweak $O(100) GeV$ scale is several orders of magnitude greater than the gravitational one α_g, since it yields: $\alpha = 1/137$ while $\alpha_g \sim 10^{-39}$. The reason behind the huge difference between those two scales is itself an issue. Another important issue about gravity is that due to the dimensionality of the gravitational coupling constant, no renormalizable quantum theory can be realized out of it. The incorporation of gravitational interactions could however come in the picture of a completely new physics model.

- **The hierarchy problem**: If the Higgs mechanism is really the responsible of the mass of the particles, then a problem with the naturalness of the theory arises: Higgs boson mass is not UltraViolet safe, but depends on whatever scale new physics presents

itself. Self-interaction terms in fact arise of the type:

$$m_H^2 \approx M_{H,0}^2 + \frac{\lambda}{4\pi^2}\Lambda^2 \tag{2.54}$$

where λ is the strength of the coupling and Λ^2 is the scale of new physics. Since Higgs boson has to couple to every massive particle, one can recalculate the one-loop corrections to Higgs mass as:

$$m_H^2 \approx M_{H,0}^2 + \frac{g_f}{4\pi^2}\left(\Lambda^2 + m_F^2\right) + \frac{g_s}{4\pi^2}\left(\Lambda^2 + m_S^2\right) \tag{2.55}$$

where $f(s)$ is a fermion (scalar) particle and $g_{f(s)}$ and $m_{f(s)}$ are the coupling constant of such particles to the Higgs and the mass term. In order for this divergence to either cancel out or be reduced to a manageble order (logarithmic), a very precise balancement (fine tuning) would be needed between fermions and scalars. This tuning should keeping into account the tight constraints on the higgs mass displayed in Figure 2.8. A possibility to avoid such fine tuning would be an exact symmetry allowing cancellation of boson and fermion terms: this is the very basic idea behind supersymmetric models [27]. Figure 2.9 shows the one loop correction to the Higgs mass term from the top quark and his supersymmetric partner, the stop.

Figure 2.9: One-loop correction to the Higgs mass term from the top quark (a) and his supersymmetric partner, the stop quark (b).

- **Cosmology**: Any theory which purposes itself to give a clear picture of the fundamental constituents of the universe must also be consistent with whatever cosmological observation is made. First, it has been verified that a significant amount of matter in the galaxy which does not emit visible light thus is not observable with normal telescopes, yet it is detectable through gravitational effects and through measurements on the cosmic microwave background. The presence of this "Dark Matter" cannot be reconduced to the particles present in the SM. Another issue is related to baryogenesis: there is an imbalance in the observed universe between matter and anti-matter, where matter patently prevails. To explain this, the CP symmetry is required to be violated at a level far higher than the one allowed by the Standard Model. Also CP violation in the neutrino sector would be needed.

- **The neutrino sector**: The SM neutrino sector is one of the most difficult to explore due to the elusive nature of those chargless, almost massles particles[1]. One still open question is whether or not neutrino anti-particles exist. Neutrinos and anti-neutrinos coincide in the hypothesis it is a Majorana fermion. This scenario leads to a completely different behavior from a Dirac neutrino in term of Lorentz and CPT transformations.

---

[1]Although SM neutrinos are strictly massless, evidence of neutrino oscillation proves they actually have a mass, although several orders of magnitude smaller with respect to the electron, the smallest charged lepton

Chapter 3

The Large Hadron Collider and the Compact Muon Solenoid

The Standard Model validity for energies up to the electroweak scale ($O(100)\ GeV$) has been extensively tested with precision experiments like the Large Electron Positron collider, the b-factories like BaBar [28] or Belle [29], and even the proton-antiproton collider TeVatron at Fermilab, capable of achieving an center of mass energy for collisions of 1.96 TeV, although the actual energy available for elementary collision processes is much smaller and determined by the parton distribution functions of the proton(or anti-proton). However, the current knowledge of particle physics indicates that the most likely energy frontier for the validity of the Standard Model and for hints of new physics is located at the scale of the TeV. Therefore, a new machine was necessary which is able to reach such energy. Another important characteristic for such a machine was to have an instantaneous luminosity high enough to make the search for new physics and for the higgs boson possible even in few years of data taking, so to quickly surpass the discovery phase and to proceed to the studies of any new physics sighted. Moreover, chosing such machine to be an hadronic collider would have allowed for a search in a wide spectrum of energy, automatically scanning the range made available by the parton distribution functions. From this design guidelines, the Large Hadron Collider (LHC) was born. At the same time, the experimental conditions at the LHC require a careful design for the detectors which are to perform physics measurements. Any experiment taking LHC data has to cope with extremely high rates of events due to the high luminosity conditions and the high center of mass energy available for collisions. This causes several important consequences on the design of the experiment: detectors, especially the ones closer to the interaction points, have to be robust against extreme radiation conditions. To select interesting events and to reduce the information produced by detectors to a manageable size, an ad hoc system for *triggering* has to be developed. The data acquisition and transfer systems has to sustain a constant stream of data and transfer it to the storage facilities, ensuring the highest bandwith available to reduce loss of data. Finally, all reconstruction algorithms for the physics objects present an event have to be robust against contamination from the *underlying event* (every detector signature that does not directly stem from the hard elementary process) and from *pileup* (effect of the "piling up" of several collsion events in the same bunch). In this chapter we describe in the the design and main characteristics of the LHC machine and the give the detail of the Compact Muon Solenoid detector, showing how it has been carefully designed in order to cope with the extreme experimental conditions and to acheve maximum performance in the physics measurements of interest at the LHC. Figure 3.3 compares summarizes the evolution of of colliders in term of center of mass energy.
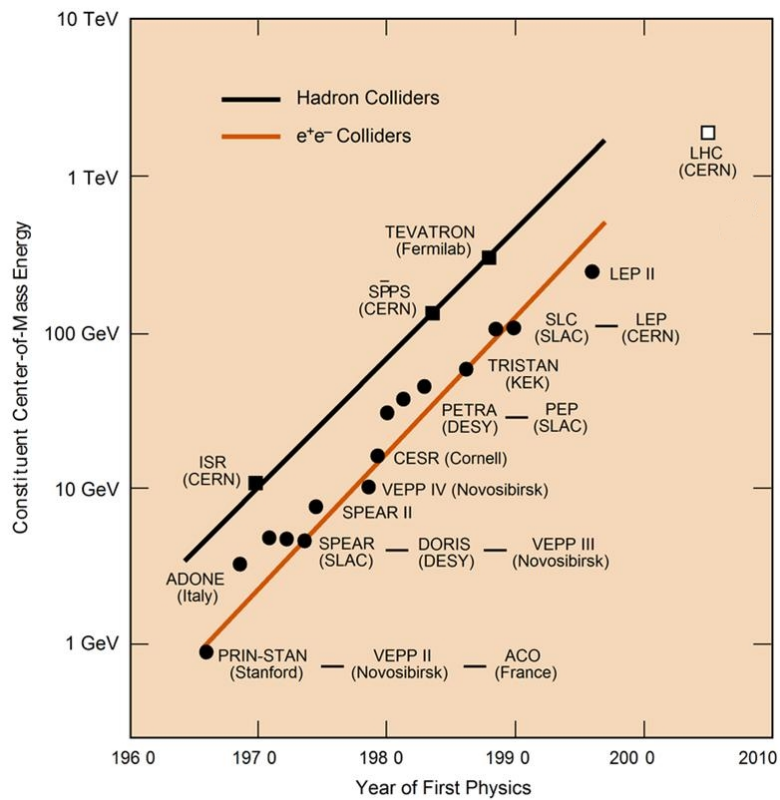
Figure 3.1: Diagram representing several modern colliders' center of mass energy vs date of construction.

3.1   The LHC accelerator

The Large Hadron Collider (LHC) [30] is a two rings superconducting proton accelerator and collider designed to explore TeV scale, probing the Standard Model processes and searching for the Higgs bosons as well as hints of new physics. LHC is designed to accelerate proton beams up to 7 TeV, which result in a center of mass energy available for collisions of 14 TeV. From March 2010 it has started operations accelerating proton beams up to 3.5 TeV each. The LHC is located in an underground 26.7 km long tunnel which was originally built to host the CERN Large Electron Positron (LEP) accelerator. The tunnel is located between 45 and 170 meters below the surface, crossing the border between France and Switzerland, and it is connected to the CERN accelerating complex by two tunnels. Several access points allow to communicate between the ground and the surface. There are four points where the LHC beams LHC, in correspondence of which four great experiments are located: ATLAS (A Toroidal Lhc ApparatuS) [31], ALICE(A Large Ion Collider Experiment) [33], CMS (Compact Muon Solenoid) [32] and LHCb [34]. Figure 3.2 shows the location of the LHC under the French and Swiss border and the four access points corresponding to the aforementioned experiments.
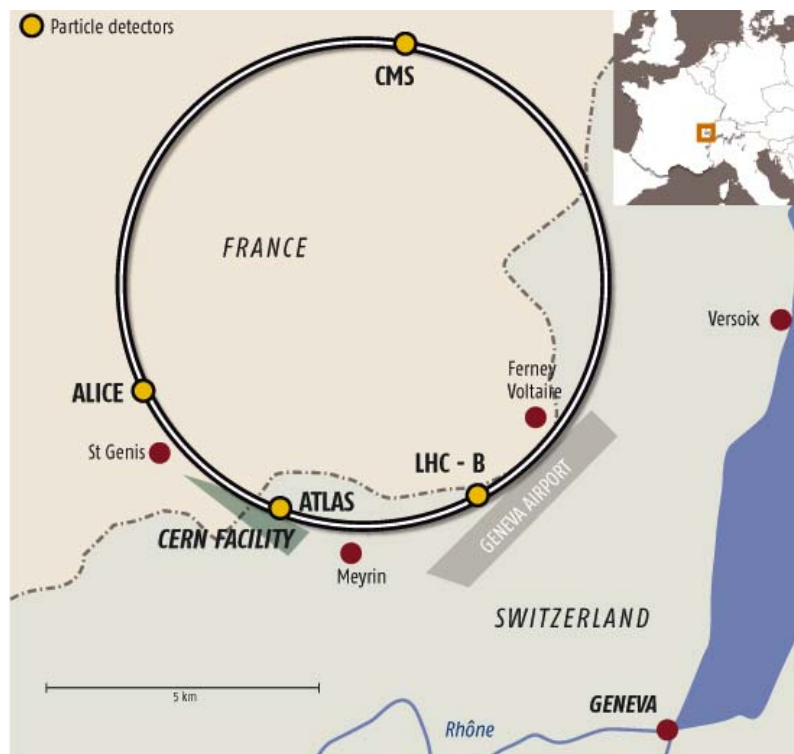
Figure 3.2: Location of the LHC accelerator in the region between France and Switzerland.

3.1.1   Design and main features

The main parameters of interest for physics at the LHC are the center of mass energy and the *instantaneous luminosity* $\mathcal{L}(t)$. The luminosity is a parameter of interest for the colliders which relates the cross section of a given process with the number of events N generated in the collisions per time unit is: $\frac{dN_{event}}{dt} = \mathcal{L}(\sqcup)\sigma$. For a collider where both beams have the same energy, one can write the luminosity as the following functions of the accelerator
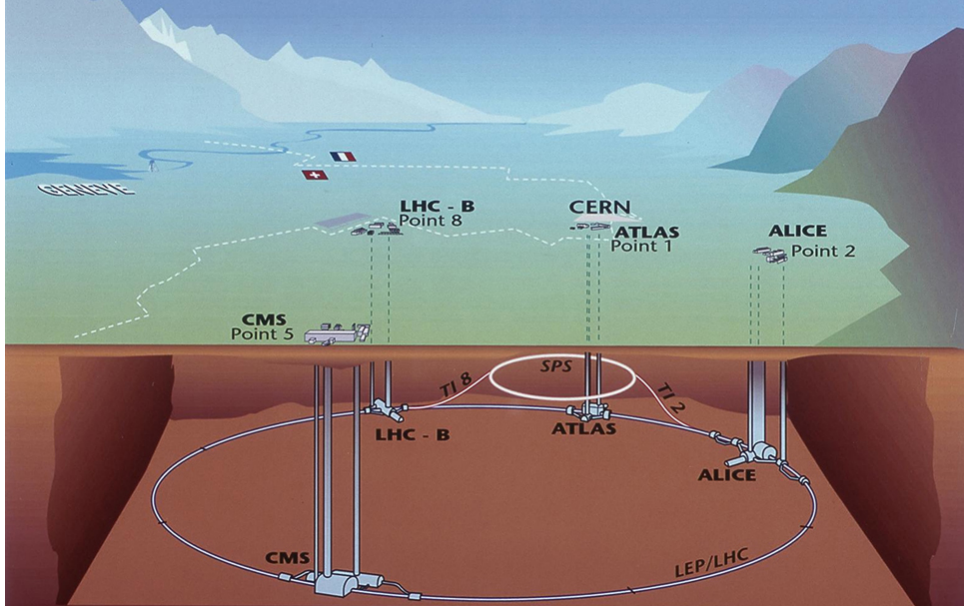
Figure 3.3: LHC pictorical view of the location and the four experiments located at the interaction points.

parameters:

$$\mathcal{L}(\sqcup) = \frac{N_b^2 n_b f_{rev} \gamma_r}{4\pi \epsilon_n \beta*} F \tag{3.1}$$

Where: N_b is the number of particles per bunch, n_b is the number of bunches per beam, f_{rev} the revolution frequency, γ_r the relativistic gamma factor[1], ϵ_r the normalized transverse beam emittance, $\beta*$ the beta function at the collision point, and F the geometric luminosity reduction factor due to the crossing angle at the interaction point:

$$F = \left(1 + \left(\frac{\theta_c \sigma_z}{2\sigma*}\right)^2\right)^{1/2} \tag{3.2}$$

where θ_c is the full crossing angle of the beams at the interaction point, σ_z the RMS of the bunch length, $\sigma*$ the transverse RMS beam size at the interaction point. This holds assuming round beams (cylindrical symmetry around the beam direction), $\sigma_z << \beta*$ and equal beam parameters for both beams. The design luminosity for ATLAS and CMS experiments is $\mathcal{L} = 10^{34} cm^{-2}$. The other two great experiments located at the interaction points of LHC, ALICE and LHCb, have a lower design instantaneous luminosity, namely $\mathcal{L} = 10^{32} cm^{-2}$ for LHCb and $\mathcal{L} = 10^{29} cm^{-2}$ for ALICE [2]. It is noteworthy that this is CMS and ATLAS luminosity the highest ever achieved counting pre-LHC hadron colliding machines. Such high luminosity could not be achieved with proton-antiproton beams, due to the impossibility to produce and store anti-particles in a sufficient amount to reach LHC design luminosity. There is actually an advantage in terms of the increase physical processes cross sections due to $p\bar{p}$ processes in place of pp, but this turned out to be not convenient in the balance with the loss of luminosity. The CMS and ATLAS design luminosity corresponds roughly to $15pb^{-1}$ of luminosity per hour, and $100fb^{-1}$ per year counting approximately an effective operating time of the machine of 250 days with 12 hours of data taking. The LHC design center of mass energy available for proton-proton collision is 14 TeV. Figure 3.4

---

[1]The relativistic factor γ for particle of speed v, momentum p and energy E is $1/\sqrt{1 - \beta^2}$, where $\beta = v/c$ or equivalently $\beta = p/E$.

[2]ALICE is designed as an heavy ion experiment. The design luminosity is referred to lead-ion collisions

shows a scheme of the LHC beam circulation and interaction points. The CERN accelerating
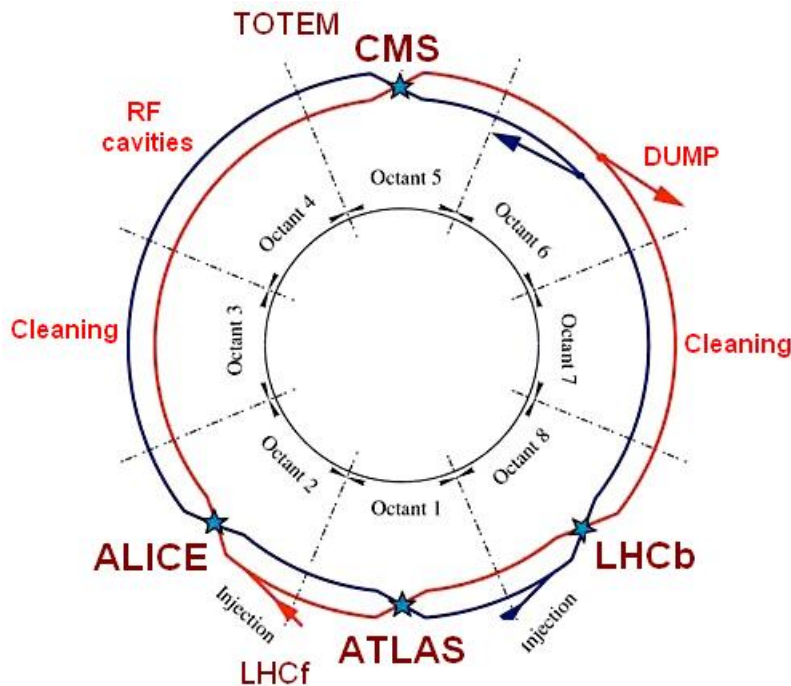
Figure 3.4: LHC beam structure.

complex, which accelerates proton up to the LHC injection energy of 450 GeV through the following chain:

- The protons are produced at 92 keV and introduced in the CERN Linear Accelerator (LINAC2), which accelerates them up to 50 MeV of energy. Protons pass into the Proton Synchrotron Booster (PSB), which accelerates them up to 1.4 GeV and introduces to the Proton Synchrotron (PS).

- Proton Synchrotron accelerates protons up to 25 GeV. Protons come out of PS packed in bunches separated by 25 nanoseconds each. This posed an unprecedented challenge for Proton Synchrotron.

- Super Proton Synchrotron has to accelerate the beams up to the LHC injection energy. Injection kicker rise time of SPS separates two consecutive bunches. Such time is 225 ns and is equivalent to 8 bunches.

- SPS injects porotons in the LHC in groups of 3 and 4 trains of 72 bunches each. The LHC accelerates the bunches up to the energy required for physics (14 TeV by design). LHC injection kicker rise time separates each group of 3/4 train coming from SPS and the following. Such time is 0.975 μs (38 bunches), and rises to 1μs (39 bunches) every three injections, allowing the LHC train to have the characteristic pattern 333 334 334 334 shown in figure 3.6, which displays the LHC bunch train. The LHC beam dump kicker rise time at the end of the train is 3 μs, corresponding to 119 bunches. Therefore an overall LHC train has a length corresponding to 3654, while actual proton bunches are 2808 .

The transverse emittances of the LHC beam have to be maintained at their unusually small size throughout the injector chain, posing serious problems at the regions of transition between the different accelerators. Figure 3.5 shows a scheme of the LHC accelerating complex. Table 3.1 summarizes the most important LHC parameters.

The LHC injection complex
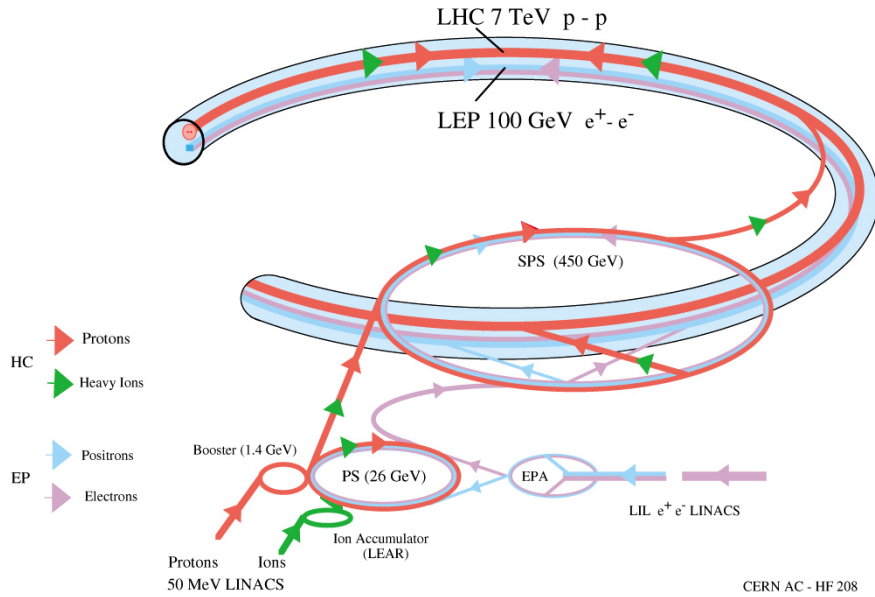
Figure 3.5: LHC accelerating complex.
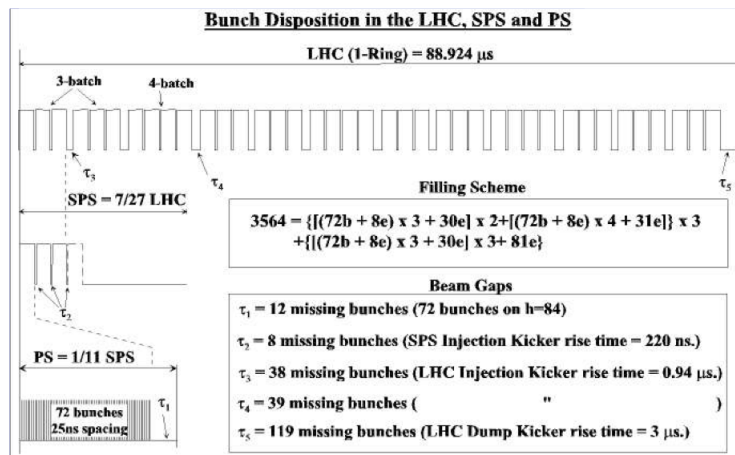
Figure 3.6: LHC beam structure.

Parameter	Current best value	Design value	Units
Center of mass energy	7	14	TeV
Peak instantaneous luminosity (CMS,ATLAS)	$3.54 \cdot 10^{33}$	10^{34}	$cm^{-2}s^{-1}$
Bunch separation	25	25	ns
Number of bunches		2808	
Beam current		0.58	A
Dipole field (7 TeV)	8.33		T
$\beta*$		0.55	m
Beam radius RMS at interaction point $\sigma*$		16.7	μm
Luminosity mean life		15	h
Number of collisions per bunch crossing		~ 20	

Table 3.1: LHC accelerator parameters of interest.

3.1.2 Luminosity lifetime

The LHC luminosity is subject to decay due to degradation of beams intensities and emittance. We can divide the different contributions in the following way:

- beam loss due to collisions. One can write time for the beam to fully decay as:

$$\tau_{nuclear} = \frac{N_{tot,0}}{\mathcal{L}\sigma_{tot}k} \tag{3.3}$$

  where $N_{tot,0}$ is the initial beam intensity, $\mathcal{L}$ the initial luminosity, σ_{tot} the total cross section ($\sigma_{tot} = 10^{25}cm^{-2}$ at 14 TeV) and k the number of interaction points. For ATLAS and CMS, the two high luminosity experiments, considering the design luminosity of $10^{34}cm^{-2}s^{-1}$ Equation 3.3 yields $\tau = 44.85$ h. Therefore we can write the beam intensity and luminosity as functions of time:

$$N_{tot}(t) = \frac{N_{tot,0}}{1 + t/\tau_{nuclear}} \tag{3.4}$$

$$L(t) = \frac{L_0}{1 + t/\tau_{nuclear}} \tag{3.5}$$

  While the time required to reach $1/e$ of the initial luminosity is given by:

$$t_{1/e} = \left(\sqrt{e} - 1\right)\tau \tag{3.6}$$

  yielding a luminosity decay time of $\tau_{nuclear,1/e} = 29$ h.

- beam loss due to Toucheck scattering.

- particle losses due to a slow emittance blow-up. Emittance blow-up can be caused by the scattering of particles on residual gas, the nonlinear force of the beam-beam interaction, RF noise, and IBS scattering effects. One can assume that the radiation damping process just cancels the beam blow up due to the beam-beam interactions and RF noise [35].

This results in a luminosity decay law given by the formula:

$$\frac{1}{\tau} = \frac{1}{\tau_{IBS}} + \frac{1}{\tau_{resgas}} + \frac{1}{\tau_{nuclear,1/e}} \tag{3.7}$$

Assuming IBS time constant of 80 hour and a rest gas time constant of 100 one finds: $\tau_L = 14.9$ h.

3.1.3 Operation during 2010 and 2011

The first injections of beams atcually took place in September 10 2008, but due to an accident due to a faulty resistence of an interconnection between two magnets happened the 19th of the same month, the LHC stopped for more than one year for repairs and for commissioning of further safety measurements. The injections restarted in November 2009 with the first 450 GeV beams circulating through the LHC. Energy of the beams then was raised by steps until in March 2010 it reached 3.5 TeV and the first physics run at the LHC finally started. The data taking proceeded smoothly through the whole 2010, with a slowly yet steadily increase of luminosity which allowed the LHC to deliver a total of 47.03 up to November 2010, when the proton-proton collisions stopped to start one month of Heavy Ions runs. Figure 3.7 (a) shows the total luminosity delievered by LHC and collected by CMS during 2010 and Figure 3.7 (b) shows the intantaneous luminosity collected by CMS.

(a)   (b)
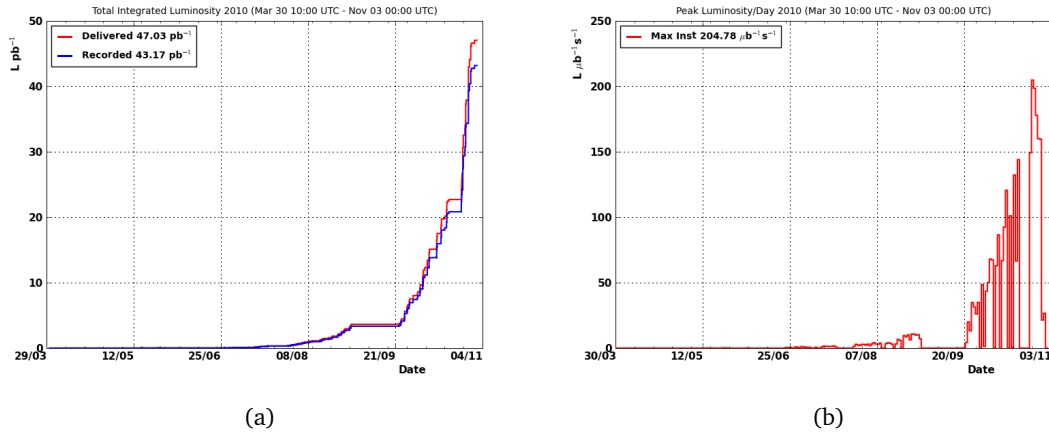
Figure 3.7: (a) Integrated luminosity delievered by LHC (blue) and collected by CMS (red). (b) Instantaneous peak luminosity per day collected by CMS during 2010.

The proton-proton collisions started again in March 2011. The increased knowledge of the machine allowed to increase the instantaneous luminosity, surpassing in few weeks the collected statistics of the whole 2010 and quickly approaching the design luminosity.

Figure 3.8 (a) shows the total luminosity delievered by LHC and collected by CMS during 2011 and Figure 3.8 (b) shows the intantaneous luminosity collected by CMS.

(a)   (b)
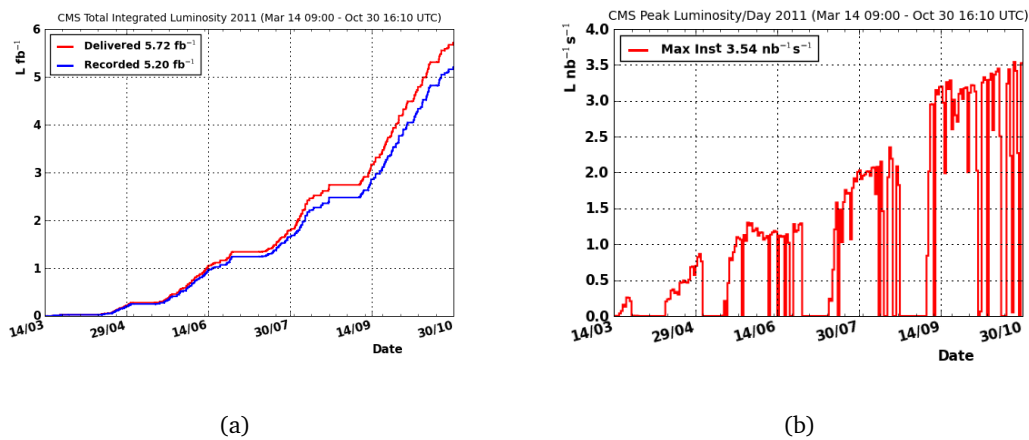
Figure 3.8: (a) Integrated luminosity delievered by LHC (blue) and collected by CMS (red). (b) Instantaneous peak luminosity per day collected by CMS during 2011.

3.2 The Compact Muon Solenoid detector

The Compact Muon Solenoid [32] experiment is one fo the four great experiments at the LHC. It is a so-called "general-purpose" experiment, meaning its research program includes most of the physics at the LHC, from the Standard Model measurements to the Higgs and new physics searches. CMS takes its name from the superconducting solenoid which generates an internal magnetic field of 3.8 Tesla, which allows a compact design of the detector, and from the Muon System located outside the solenoid, which ensures excellent

muon triggering and identification. The total proton-proton cross-section at $\sqrt{s} = 14$ TeV is expected to be roughly 100 mb. At design luminosity the general-purpose detectors will therefore observe an event rate of approximately 10^9 inelastic events/s. This leads to a series of unprecedented experimental challenges that any detector at LHC has to cope with:

- **Rate reduction** The huge event rate has to face physical limitations in the bandwidth at which data can be transferred to the storage facilities: a manageable event rate that can be passed to the storage and subsequent analysis is about 100 events/s, meaning that a reduction of order 10^7 has to be operated by the selection process (*trigger*). The bunch crossing interval of 25 ns implies that it is not possible to transfer this to any offline software to perform such reduction, therefore it has to be performed online with electronics triggering systems. The bunch crossing timing is therefore crucial to design the CMS triggering system.

- **Pile up events** At the design luminosity, a mean of about 20 inelastic collisions will be superimposed on the event of interest. This implies that around 1000 charged particles will emerge from the interaction region every 25 ns. The products of an interaction under study may be confused with those from other interactions in the same bunch crossing. This problem clearly becomes more severe when the response time of a detector element and its electronic signal is longer than 25 ns. The effect of this pile-up can be reduced by using high-granularity detectors with good time resolution, resulting in low occupancy. This requires a large number of detector channels. The resulting millions of detector electronic channels require very good synchronization.

- **Radiation robustness** The high rates have the important consequence that detectors have to sustain a severe amount of radiation, and have to mantain good performances over the course of several years of data taking. This problem affects especially detectors which are closer to the interaction point (any system aiming to measure the vertex at interaction point or the tracks) and the ones at lower angles with respect to the beam pipe.

Different solutions were found by the LHC experiments to those problems, ultimately resulting in different creative designs for the detectors.

The CMS reference frame

Here we introduce some notations on the CMS reference frame to be used in the following part of this thesis. The coordinate frame is centered at the nominal interaction point, the z axis is coaxial with the beam pipe and the $x - y$ plane is therefore orthogonal to the beam, with the x axis pointed towards the center of LHC and the y axis pointing upwards. Since the detector has a cylindrical symmetry around the z axis, a pseudo-angular reference is used: r is the radial distance from the z axis, ϕ is the azimuthal angle measured from the x axis and η is the pseudorapidity, defined as $\eta = -\ln\tan(\theta/2)$, where θ is the polar angle. are indicated.

CMS design requirements

The CMS choices to face the experimental issues at LHC can be summarized as follow:

- Good muon identification and reconstruction: muons are crucial for the trigger, therefore muon momentum resolution has to be excellent in a momentum range as large as possible. Muons must therefore be reconstructed in the range $|\eta|$ ¡ 2.5 with correct charge up to transverse momentum scale of $p_T = TeV/c$. Good resolution on

the invariant mass of muons pairs is also important for several physics processes (1% at $100 GeV/c^2$).

- Good reconstruction of the vertices in the inner region of the detector: combining the high curvature of charged particles due to the 3.8 T magnetic field with an excellent inner tracking system allows for online tagging of b jet and excellent performances of offline τ and b-jets tagging algorithms (see also chapter 4).

- Good resolution of the electromagnetic calorimeter, allowing for photon and electron identification and energy measurement. Excellent energy mesurement is required in a range of $|\eta| < 2.5$. Di-photon mass resolution required to be $O(1\%)$ at 100 GeV/c^2,

- Jets reconstruction requires excellent hadronic calorimeters in a range of $|\eta| < 2.5$. Extra forward calorimeters allow to cover up to a range $|\eta| < 5.2$, both to cover extreme kinematic regions and to ensure hermiticity of the detector. Missing energy reconstruction is crucial for many physics searches and measurements at the LHC, therefore hermiticity is crucial especially on the transverse $x - y$ plane.

The initial design benchmarks for the performances have been met, and actually have been surpassed thanks to improvements in reconstruction algorithms and to the insight of the detector and of experimental effects gained over the years of data taking.

3.2.1   General detector layout

The CMS detector has cylindrical symmetry with respect to the beam axis. It is constituted by several layers of detectors centered on the interaction point. The η coverage of subdetectors change case by case. Each subdetector is divided in a central "*barrel*" region and two "*endcap*" regions covering the extreme $|\eta|$ regions. From the innermost to the outermost CMS detector we have:

- The Pixel detector: silicon pixel detector used for accurate measurement of the vertex.

- The Silicon Strip Tracker: a silicon strip detector which is used for accurate track reconstruction.

- The Electromagnetic Calorimeter (ECAL): an omogeneous lead tungstate electromagnetic calorimeter, for accurate electron and photon energy measurement which also contributes to measure the electromagnetic fraction of jets energy.

- The Hadronic Calorimeter (HCAL): a sampling calorimeter with plastic scintillators as detector region and brass as absorber. It is crucial for energy measurements of jets and missing energy.

- The Superconducting Solenoid: the coil generating an internal constant magnetic field of 3.8 Tesla in the direction of the beam axis.

- The Muon system: constituted of gas detectors for muon identification and triggering: Drift Tube detectors and Resistive Plate Chambers in the barrel region $|\eta| < 1.18$, Cathode Strip Chambers and Resistive Plate Chambers in the endcap region $|\eta| > 1.18$.

- The return yoke: interloped with the Muon System is the return yoke to sustain the structure and studied so to allow magnetic field lines of the solenoid

- The Forward Hadron Calorimeter: a Cherenkov-Based calorimeter for the very forward region covering $|\eta| > 2.5$.

Figures 3.9 show the layout of the CMS detector.
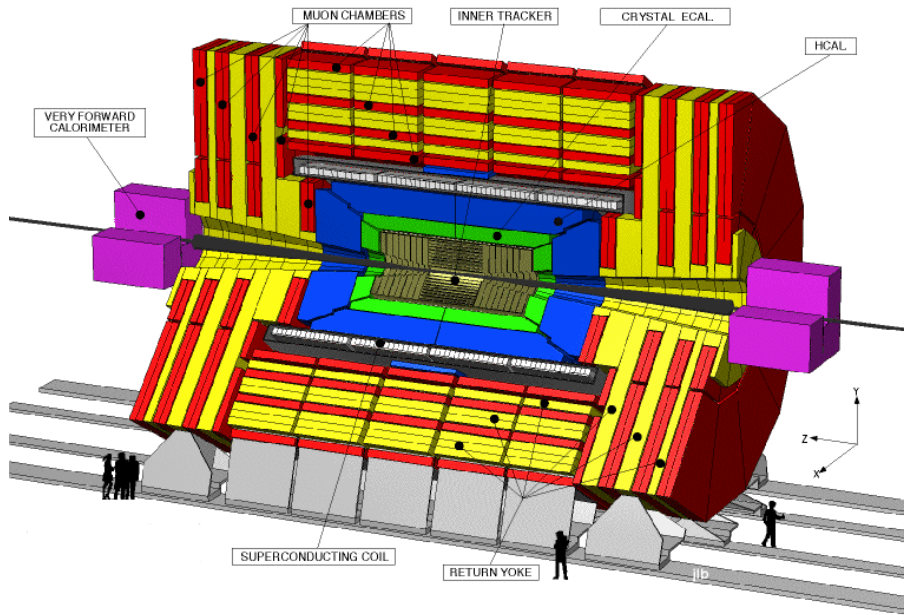
Figure 3.9: Perspective view of the CMS detector.

3.2.2 The superconducting magnet

The CMS superconducting magnet for CMS [36] has been designed to generate a 4-Tesla field in a free bore of 6-m diameter and 12.5-m length with a stored energy of 2.6 GJ at full current. The return yoke returns the flux so that the field lines close outside the magnet and the magnetic field is intense and constant enough to ensure momentum measurement of particles in the outer CMS Muon System (see Section 3.2.5). The return yokes consists of iron, weights 10 000-tons and comprises 5 wheels and 6 disks divided in the two endcaps (figure 3.9). The magnet was fully and successfully tested and commissioned in the hall above CMS (SX5) during autumn 2006 before being laid down in the experimental cavern. Figure 3.10 shows a pictorical view of the CMS solenoid.

3.2.3 The inner tracking system

The CMS inner tracking system [37] [38] has to provide efficient and precise reconstruction of charged particles tracks in a radiation heavy region of the detector over the whole lifetime of the CMS experiment. The precision of track parameters measurement is crucial for the entire physics program of CMS, allowing reconstruction of particles like muons or electrons as well as of more complex objects like interaction vertices, b-tagged jets and τ. In this section we describe the This very challenging task is achieved successfully.

3.2.3.1 Requirements and experimental challenges

The region occupied by the inner tracking system is a cylinder centered around the interaction point, with a length of 5.8 m and a diameter of 2.5 m. A magnetic field of 3.8 Tesla covers this whole region, allowing charged particles to bend sensibly in the volume of the tracker. Assuming the LHC design luminosity of $10^{34}cm^{-2}s^{-1}$ there are more than 20 proton-proton interactions per each bunch crossing. This results in order of 1000 particles crossing the tracker region each 25 ns. This sets the requirements for the tracking system:
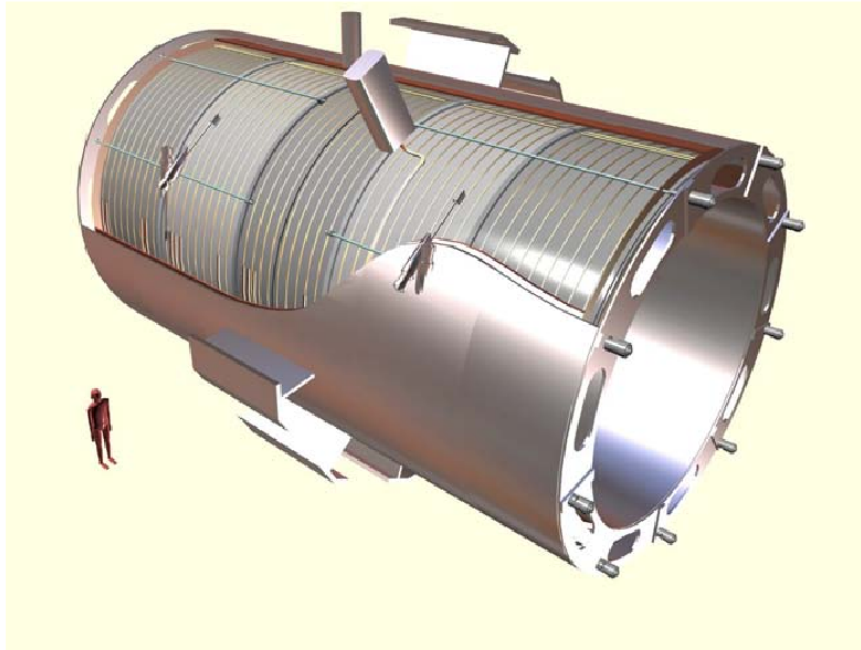
Figure 3.10: Pictorical view of the CMS magnet
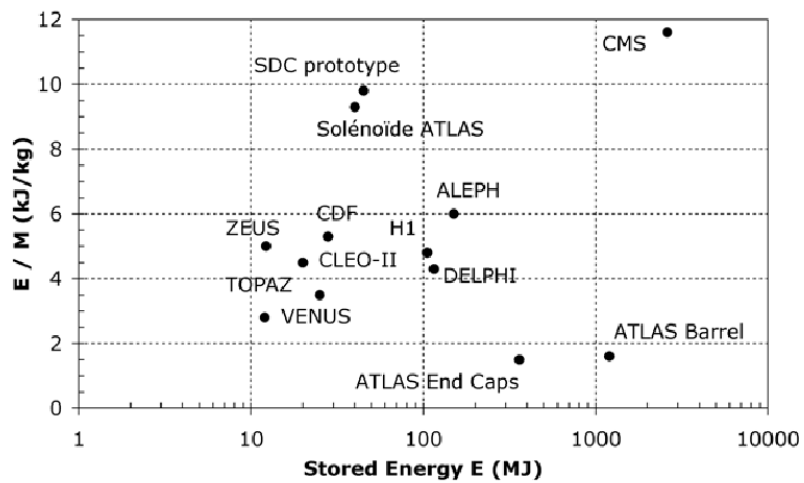
Figure 3.11: The energy-over-mass ratio E/M, for several detector magnets.
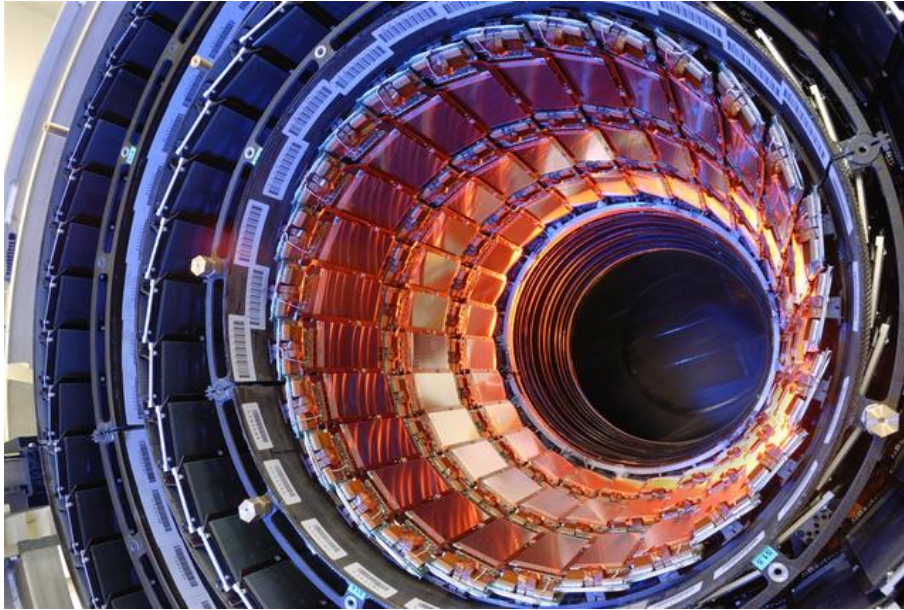
Figure 3.12: View of the tracker silicon strips before being assembled in CMS.

- High granularity in order to discriminate even adjacent trajectories and make ambiguities easily removable at reconstruction level.

- Fast response time, in order to cope with the high bunch crossings frequencies.

- Radiation robustness: the intense particle flux causes damage to the detectors over time, so it was compelling to design a tracking system which could operate under LHC conditions and stay efficient over the entire CMS lifetime.

A consequence of the first two requirements is that a high power density of on-detector electronics is needed, and therefore an efficient cooling system is also necessary. The detector design had to cope with those issues while at the same time keeping at the minimum possible the amount of material present in the tracking volume, so to limit the effect of particle interactions (bremsstrahlung, multiple scattering, photon conversion, nuclear interactions) with the inert portion of the detector. The choice of a tracking system based on silicon detectors was driven by the three aforementioned issues.

3.2.3.2 Tracking system overall design

The CMS inner tracking system consists of two detector technoligies: a pixel detector for the inner region and a silicon strip tracker for the outer region. The pixel has three cylindrical barrel layers between 4.4 cm and 10.2 cm from the beam axis, centered on the interaction point and parallel to the beam axis. The tracker has 10 cylindrical barrel layers up to a distance of 1.1 m from the beam axis and parallel to it. Both pixel and tracker are completed by 2 endcap disks in the pixel detector and 3 (tge so called "TID") plus 9 (so called "TEC") disks in the strip tracker on each side of the barrel, granting full angular coverage in the region $|\eta| <$2.5. For a layout of the pixel and the tracker systems see also Figures 3.15 and 3.13(up). With about 200 m^2 of active silicon area the CMS tracker is the largest silicon tracker ever built The LHC bunch crossing at design luminosity results in about 1000 particles hitting the tracker, leading to a hit rate density of 1 MHz/ mm^2 at a radius of 4 cm, falling to 60 kHz/mm2 at a radius of 22 cm and 3 kHz/mm2 at a radius of 115 cm. The aim for an optimal reconstruction is to keep an occupancy at or below 1% . The subdivision of the tracking system is a consequence of this:

Radius (cm)	Fluence of fast hadrons ($10^{14} cm^{-2}$)	Dose (kGy)	Charged particle flux ($cm^{-2}s^{-1}$)
4	32	840	10^8
11	4.6	190	
22	1.6	70	$6 \cdot ^6$
75	0.3	7	
115	0.2	1.8	$3 \cdot ^5$

Table 3.2: Expected hadron fluence and radiation dose in different radial layers of the CMS tracker (barrel part) for an integrated luminosity of 500 fb^{-1} (~ 10 years). The fast hadron fluence is a good approximation to the 1 MeV neutron equivalent fluence

- Below 10 cm in radius, pixel detectors are necessary. The interaction point vertex resolution drives the pixel size, which is chosen to be 100×150 μm^2 in $r - \phi$ and z. In this region the occupancy is of the order 10^{-4} per pixel per LHC bunch crossing.

- At radii 20 cm < r < 55 cm silicon micro-strip detectors can be used. The typical silicon cells size is 10 cm $\times$ 80 μm. The occupancy in this region is 2–3% per strip per LHC bunch crossing.

- In the outer region (55 cm < r < 110 cm) the strip pitch and strip length are further increased . This becomes necessary to reduce the number of read-out channels and the corresponding electronics to be implemented. Due to the strip capacitance scaling with its length, electronics noise is a linear function of the strip length. Therefore, in order to keep a signal to noise ratio of to an acceptable level (>10) CMS uses 500 μm thick silicon sensors in the outer tracker region, as opposed to the 320 μm thick strips of the inner tracker region. Cell size in the outer tracker goes up to about 25 cm $\times$ 180 μm , yielding an occupancy of about 1%. These occupancy-driven design choices for the strip tracker also satisfy the requirements on position resolution.

Table 3.2 shows the expected fast hadron fluence (flux integrated over time) and radiation dose in the CMS barrel tracker for an integrated luminosity of 500 fb^{-1}. This allows to have an idea of the radiation the tracker has to withstand over about 10 years of full-regime data taking. A substantial contribution to fast hadrons flux is due to neutrons generated in hadronic interactions in the ECAL crystals, and such contribution is particularly important in the outer tracker region.

3.2.3.3 Silicon pixel detector

The pixel detector is the closest to the interaction point amongst all CMS subdetectors, therefore it is essential for the reconstruction of the primary vertex and of secondary vertices from b and tau decays, and forming seed tracks for the outer track reconstruction and high level triggering. The pixel detector barrel consists of three cylindrical layers (BPix) of hybrid pixel detectors at radii of 4.4, 7.3 and 10.2 cm from the beam axis. The pixel endcaps consist of two disks (FPix) of pixel detectors orthogonal to the beam axis on each side of the barrel, covering a pseudorapidity region of $|\eta| < 2.5$, the same as the silicon strip tracker. The FPix disks extend from $\sim$6 to 15 cm in radius, are placed on each side at $z = \pm 34.5$ and $z = \pm 46.5$ cm. BPix (FPix) contain 48 million (18 million) pixels covering a total area of 0.78 (0.28) m^2 . The arrangement of the 3 barrel layers and the forward pixel disks on each side gives 3 tracking points over almost the full η-range. Figure 3.13 (up) shows the geometric arrangement and the hit coverage as a function of pseudorapidity

η. In the high η region the 2 disk points are combined with the lowest possible radius point from the 4.4 cm barrel layer. The pixel detector more than the others is subject to a
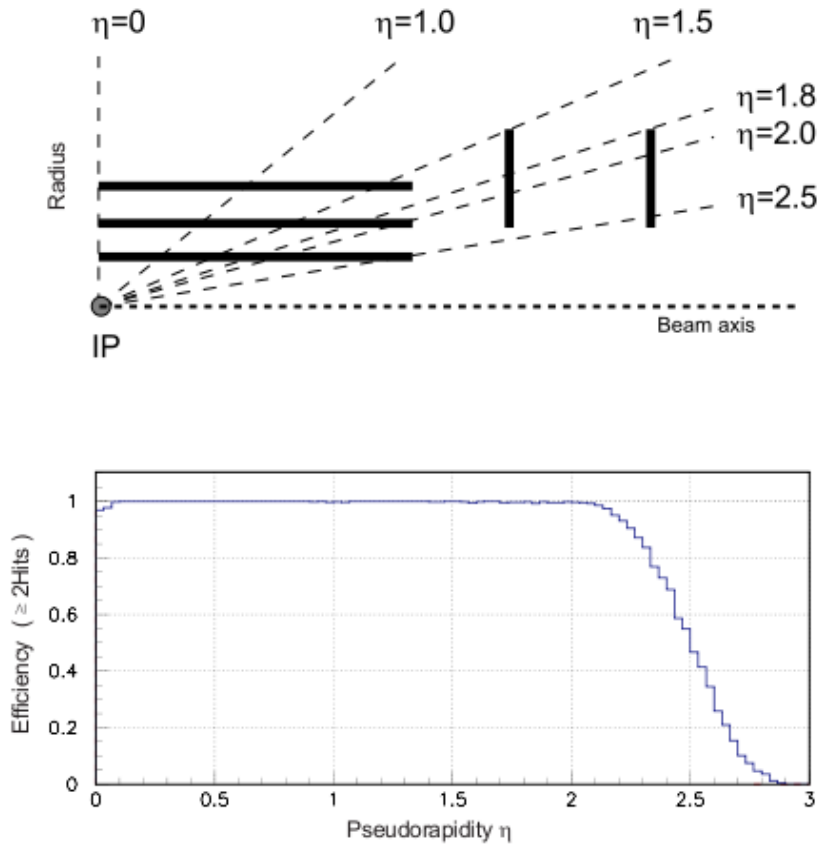
Figure 3.13: Geometrical layout of the pixel detector and hit coverage as a function of pseudorapidity.

very high track rate and particle fluences due to the vicinity to the interaction region. The design has to take this into account properly, both from the sensor and from the electronics point of view. For the barrel layers the drift of the electrons to the collecting pixel implant is perpendicular to the 3.8 T magnetic field of CMS. The resulting Lorentz drift leads to charge spreading of the collected signal charge over more than one pixel. With the analog pulse height being read out a charge interpolation allows to achieve a spatial resolution in the range of 15–20 μm. The forward detectors are tilted at 20°, resulting in a turbine-like geometry. This allows charge sharing, due to the geometric effect of particles entering the detector at an average angle of 20° away from normal incidence, and is also enhanced by the E × B drift. A position resolution of approximately 15 μm can be achieved this way. The reduction in the depletion depth or the increase in bias voltage will lead to a reduction of charge-sharing and therefore a degradation of the spatial resolution with radiation damage. Figure 3.14 shows the vertex reconstruction resolution with the tracking system measured on data.

3.2.3.4 Silicon strip tracker detector

A schematic drawing of the CMS tracker is shown in Figure 3.15. The tracker occupies the radial region between 20 cm and 116 cm. It is composed of three different parts: The
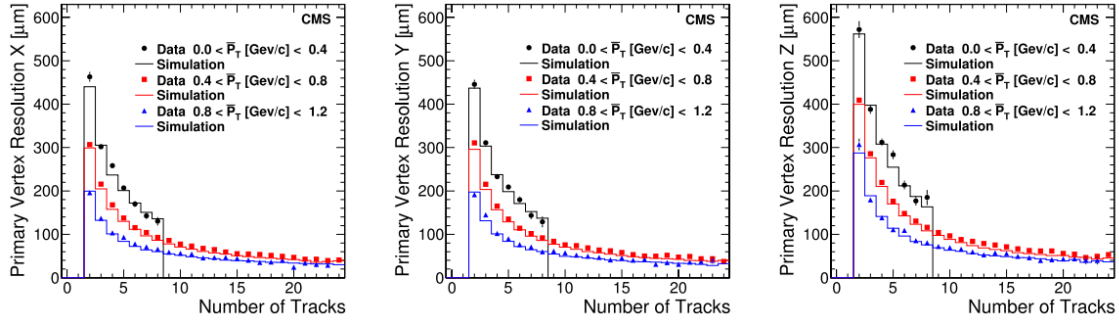
Figure 3.14: Primary vertex resolution distributions in x (left), y (middle), and z (right) versus number of tracks. The three sets of results in each plot show different average p_T ranges and within each p_T range, data and simulation are compared
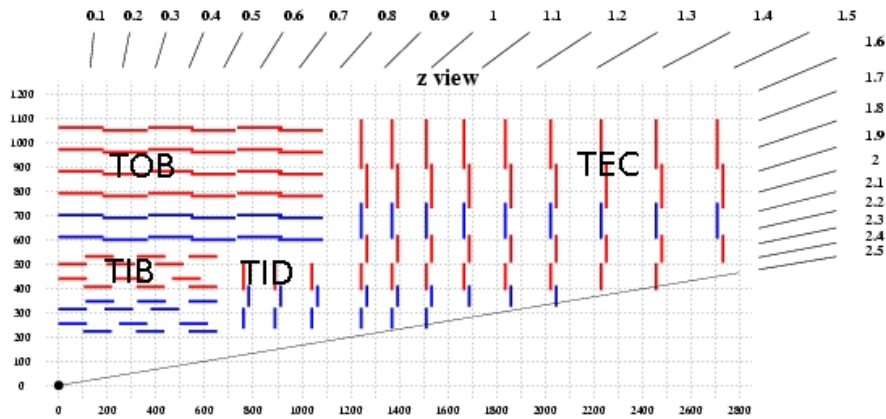
Figure 3.15: Cross section of the CMS tracker.

Tracker Inner Barrel and Disks ("TIB/TID") compose the innermost region of the Tracker. Such region extends in radius up to 55 cm. The TIB consists of 4 barrel layers of silicon strip detectors parallel to the beam axis, allowing to measure up to 4 points on the $r - \phi$ plane. The TID consists of 3 disks at each end of the TIB. In this region strips are 320 μm thick, and the strip pitch is 80 μm on layers 1 and 2 and 120 μm on layers 3 and 4 in the TIB, resulting in a single point resolution of 23 μm and 35 μm, respectively. In the TID the mean pitch varies between 100 μm and 141 μm. The second region outside the TIB/TID is the Tracker Outer Barrel ("TOB"), covering a radius up to 116 cm with 6 barrel layers, and extending in z between $\pm$ 118 cm. In this region strips are 500 μm thick due to increased electronic noise (see Sec 3.2.3.2). The pitches of 183 μm on the first 4 layers and 122 μm on ayers 5 and 6, resulting in $r - \phi$ measurements with single point resolution of 53 μm and 35 μm, respectively. At both ends of the TOB the Tracker EndCaps are located, named TEC+ and TEC− (where the sign indicates the location along the z axis). The TECs cover the region $124\text{cm} < |z| < 282$ cm and $22.5\text{cm} < |r| < 113.5\text{cm}$, corresponding to the $|\eta| < 2.5$ region. Each TEC consists of 9 disks, carrying up to 7 rings of silicon micro-strip detectors (320 μm thick on the inner 4 rings, 500 μm thick on rings 5-7) with radial strips of 97 μm to 184 μm average pitch. Thus, they provide up to 9 ϕ measurements per trajectory. The modules in the first two layers and rings, respectively, of TIB, TID, and TOB as well as rings 1, 2, and 5 of the TECs carry a second micro-strip detector module mounted back-to-back with a stereo angle of 100 mrad in order to provide a measurement of the second co-ordinate (z in the barrel and r on the disks). This allows to achieve a single point resolution of this measurement of 230 μm and 530 μm in TIB and TOB, respectively, and varies with pitch in TID and TEC. This tracker layout ensures at least $\sim$ 9 hits in the silicon strip tracker in the full range of $|\eta| < 2.4$ with a two dimensional measurement of at least $\sim$ 4 of them. The CMS silicon strip tracker has a total of 9.3 million strips and 198 m^2 of active silicon area. Figures 3.16 show the resolution of the tracks p_T, transverse and longitudinal impact parameters, while Figure 3.17 shows the muons and pions tracking efficiency.
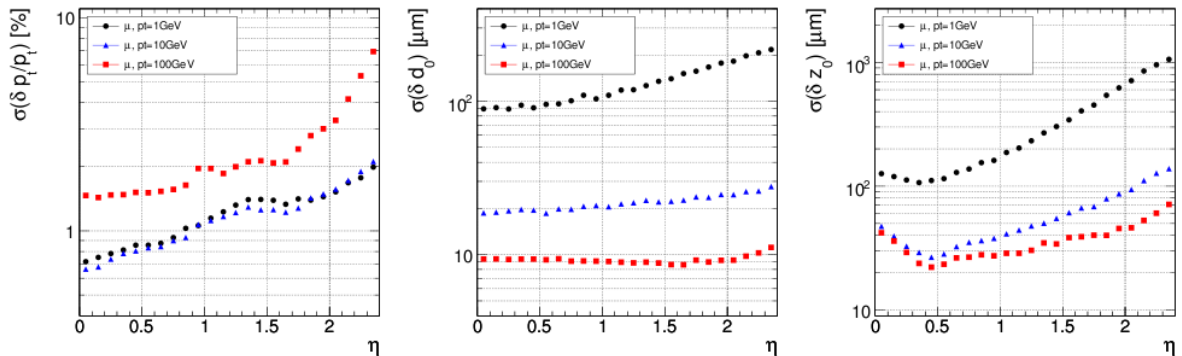
Figure 3.16: Resolution of several track parameters for single muons with transverse momenta of 1, 10 and 100 GeV: transverse momentum (left), transverse impact parameter (middle), and longitudinal impact parameter (right).

3.2.4 The electromagnetic and hadronic calorimeters

An accurate measurement of the electrons, photons and jets energy require a precise and hermetic calorimetric system. CMS uses a lead tungstate Electrmagnetic Calorimeter (ECAL) and a sampling Hadronic Calorimeter (HCAL) for such purpose. Those calorimeters cover
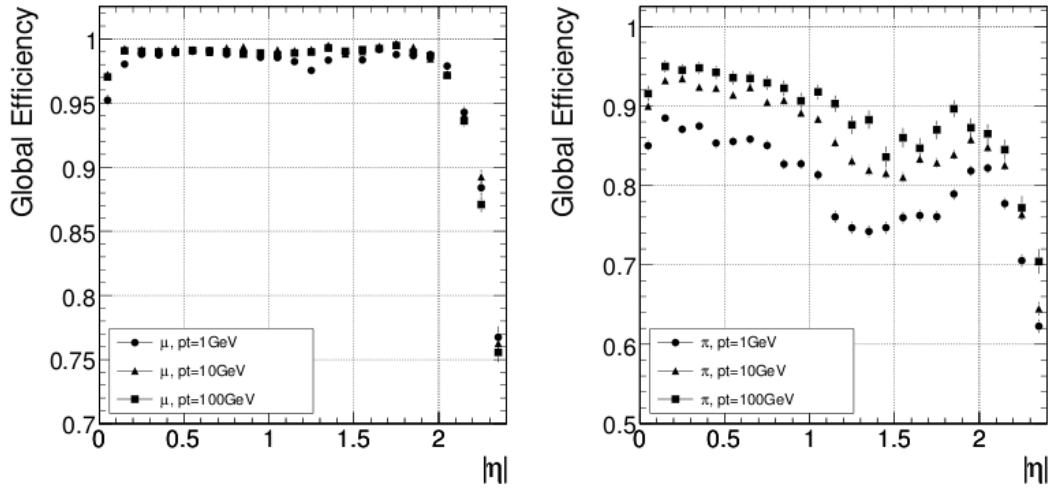
Figure 3.17: Global track reconstruction efficiency for muons (left panel) and pions (right panel) of transverse momenta of 1, 10 and 100 GeV.

up to $|\eta| < 2.5$. The regions at low-angle with respect to the beam axis (corresponding to high $|\eta|$) are important for both luminosity and physics measurements, but due to the much higher radiation conditions different technologies have to be used. CMS uses a Cherenkov Forward Calorimeter.

3.2.4.1   Electromagnetic Calorimeter design and general characteristics

CMS ECAL is a hermetic homogeneous lead tungstate ($PbWO_4$) calorimeter. It consists of a central barrel part closed by two endcaps. A preshower detector is placed in front of the endcap crystals. Avalanche photodiodes (APDs) are used as photodetectors in the barrel and vacuum phototriodes (VPTs) in the endcaps. To obtain high granularity, fast radiation and radiation hardness, high density cristals have been used. The choice of $PbWO_4$ crystals was optimal for this purposes: the high density (8.28 g/cm^3), short radiation length (0.89 cm)[3] and small Molière radius [4] (2.2 cm) result in a fine granularity, compact calorimeter, well suited for the LHC experimental conditions of pile-up, high radiation and rate. The layout of the calorimeter is shown in figure 3.18.

3.2.4.2   ECAL Barrel

The barrel part of the ECAL (EB) is composed of 61 200 crystals, covering the pseudorapidity range $|\eta|$ ¡ 1.479. The barrel has a 360-fold granularity in ϕ and a (2×85)-fold granularity in η. The crystals shape slightly varies with position in η. The crystals axes make an angle of 3° with respect to the vector from the nominal interaction vertex in both the ϕ and η projections in order to avoid cracks aligned with the separation regions between adjacent crystals. A crystal corresponds to a solid angle of approximately 0.0174×0.0174 in $\eta - \phi$

---

[3]By definition, the radiation length (X_0) of a material is the thickness of that material where pair production happens with a probability $1 - e^{-7/9} \sim 54\%$ for high energy photons.

[4]The Molière radius (RM) of a material is defined as the radius of a cylinder containing on average 90% of the shower's energy deposition. It gives the scale cof the transverse dimension of the fully contained electromagnetic showers initiated by an incident high en- ergy electron or photon. A smaller Molière radius means better shower position resolution and better shower separation. X_0 and R_M are related by the following approximated relation: $R_M = 0.0265 \cdot X_0(Z + 1.2)$, where Z is the atomic number of the material.

(the equivalent of 22×22 mm^2 at the front face of crystal, and 26×26 mm^2 at the rear face). The crystal length is 230 mm corresponding to 25.8 X_0.

3.2.4.3 ECAL Endcaps

The endcaps (EE) are composed of 7 324 crystals each and cover the rapidity range 1.479 ¡ $|\eta|$ ¡ 3.0. The longitudinal distance between the interaction point and the endcap envelope is 315.4 cm, taking account of the estimated shift toward the interaction point by 1.6 cm when the 4-T magnetic field is switched on. The endcap crystals are all identically shaped and grouped in mechanical units of 5×5 crystals (supercrystals, or SCs) consisting of a carbon-fibre alveola structure.

Each endcap consists of 2 halves, named Dees (thus 3 662 crystals each), comprehensive of 138 standard SCs and 18 special partial supercrystals on the inner and outer circumference. The crystals and SCs are arranged in a rectangular $x - y$ grid, and the crystals point at a focus 1 300 mm beyond the interaction point, resulting in angles ranging from 2 to 8 degrees off the interaction point. Each crystal has a front face of 28.62×28.62 mm2 and a rear face of 30×30 mm^2 . Crystals have a length of 220 mm, corresponding to 24.7 X_0. The endcaps crystal volume is 2.90 m^3 and the weight is 24.0 t.
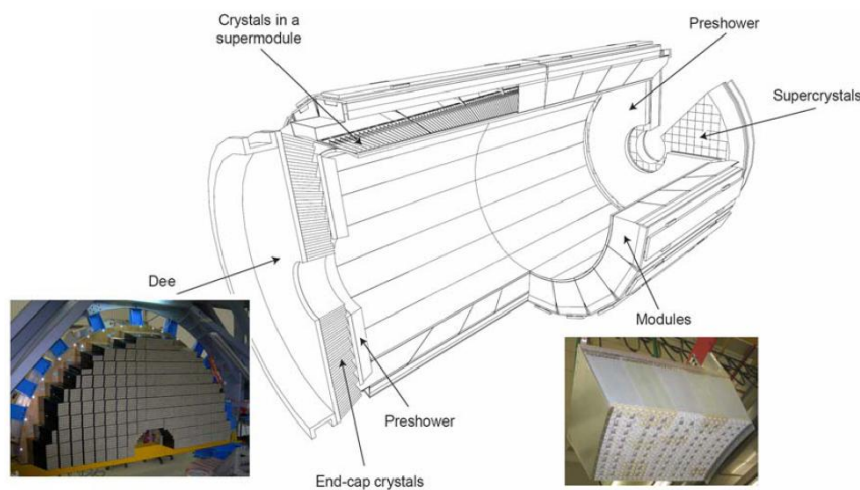
Figure 3.18: Schematic view of the CMS ECAL.

3.2.4.4 ECAL resolution

ECAL energy resolution is the sum of three terms:

- **Stochastic term**: coming from the combination of event-to-event fluctuations in the lateral shower containment, a photostatistics contribution of 2.1%, and fluctuations in the energy deposited in the preshower absorber (where present) with respect to what is measured in the preshower silicon detector.

- **Noise term**: sum of the electronics noise, digitization noise, and pile-up noise.

- **Constant term** stemming from three sources: non-uniformity of the longitudinal light collection, intercalibration errors,leakage of energy from the back of the crystal.

For energies below about 500 GeV, the combination of the stochastic S, noise N and constant C terms can be written as:

$$\left(\frac{\sigma}{E}\right)^2 = \left(\frac{S}{\sqrt{E}}\right)^2 + \left(\frac{N}{E}\right)^2 + C^2 \tag{3.8}$$

In a test beam, reconstructing the energy by summing 3×3 crystals a typical energy resolution was found to be:

$$\left(\frac{\sigma}{E}\right)^2 = \left(\frac{2.8\%}{\sqrt{E}}\right)^2 + \left(\frac{0.12}{E}\right)^2 + (0.30)^2 \tag{3.9}$$

with E expressed in GeV.

3.2.4.5   ECAL calibration

CMS ECAL has been subject to a calibration procedure before installation and on data [40]. Calibration steps can roughly be divided as follow:

- Precalibration: a calibration prior to installation in CMS has been performed. Laboratory measurements of crystal light yield and photo-detector gain have been performed with cosmic rays and test beam electrons.

- Data-driven calibration is performed through different methods. Calibration using $\pi^0 \to \gamma\gamma$ decays, $W \to e\nu$, and $Z \to e^+e^-$ decays have been performed, as well as calibration based on the ϕ symmetry of minimum bias events.

- The crystal light output and transparency is monitored with with a laser-based system [41].

3.2.4.6   Hadronic Calorimeter design and general characteristics

The CMS detector is designed to study a wide range of high-energy processes, resulting in a variety of final state topology involving hadronic jets, neutrinos or also exotic particles manifesting through missing energy in the transverse plane of the detector. It is therefore crucial to have a precise measurement of jets energy and ensure the hermiticity of the detector to reduce the uncertainty on transverse energy lost due to cracks in the detector. The CMS Hadronic Calorimeter (HCAL) [42] is a sampling calorimeter covering the pseudorapidity range $|\eta| < 3$, complemented in the high η region by the Forward Calorimeter and the CASTOR detectors [43]. The HCAL is divided in a Barrel region (HB) and two Endcap regions (HE) 3.19. Figure 3.20 shows a longitudinal cross section of the CMS detector.Proceeding from the interaction point the hadron calorimeter barrel and endcaps is located just outside electromagnetic calorimeter, occupying a radius between R = 1.77 m (the outer border of the ECAL) and R = 2.95 m (the inner extent of the superconducting solenoid). Theis sets a limit for the amount of inert material that can be put in order to absorb the hadronic shower. An outer hadron calorimeter (HO) or tail catcher is placed outside the solenoid complementing the barrel calorimeter. The Forward Calorimeter is located 11.2 m away from the interaction point, allowing to cover the pseudorapidity region to include the $3 < |\eta| < 5.2$ range. The HF uses a Cherenkov-based, radiation-hard technology.
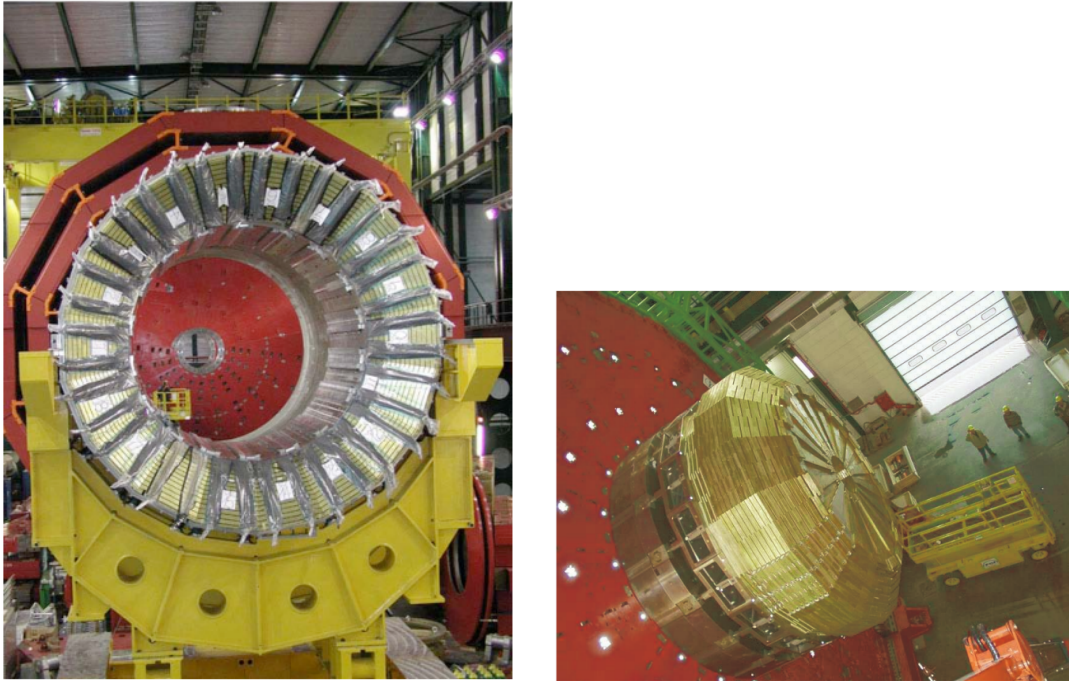
Figure 3.19: View of the CMS Hadron Calorimeter Barrel(a) and Endcap (b)

3.2.4.7   The Hadronic Calorimeter Barrel

The Hadronic Calorimeter Barrel (HB) covers the pseudorapidity range $|\eta|$ ¡ 1.3. The HB is divided into two half-barrel sections, named HB− and HB+ in the verse of the z axis, installed from either side of the barrel and hung from rails in the median plane. The HB is divided in 36 identical azimuthal wedges, made out of flat brass absorber plates ($70\%Cu$, $30\%Zn$, radiation length $X_0 = 1.49$ cm, interaction length[5] 16.42 cm) aligned parallel to the beam axis. Each wedge is segmented into four azimuthal angle (ϕ) sectors. The plates geometrical configuration that contains no projective dead material for the full radial extent of a wedge (figure 3.21). The innermost and outermost plates are made of stainless steel. The plastic scintillator is divided into 16 η sectors, which results in a segmentation ($\Delta\eta, \Delta\phi$) = (0.087, 0.087). The crack between the wedges is less than 2 mm. The active uses tiles with wavelength shifting fibres to capture the light. The HCAL calorimeter consists of a total of about 70 000 tiles. Tiles of belonging to a same ϕ layer are grouped into a single mechanical scintillator tray unit. Figure 3.22 shows a typical tray layout. The scintillators have been constructed tested away from the installation location (this was made possible by the tray geometry). Each HB wedge has four ϕ divisions (ϕ-index = 1-4). Trays with segmentation of ϕ-index 2 and 3 go into the center of a wedge while trays with segmentation of ϕ -index 1 and 4 go into the edge slots in a wedge . Each layer has 108 trays.

3.2.4.8   The Hadron Calorimeter Endcaps

The Hadron Calorimeter Endcaps (HE) cover the rapidity range 1.3 ¡ $|\eta|$ ¡ 3. This region corresponds to corresponds to 13.2% of the solid angle and contains containing about 34%

---

[5]The interaction length (or mean free path) is the mean distance a particle travels through a medium before it interacts with one of the target particles. The general interaction length λ for a nuclear process is given by: $\lambda(E) = \Sigma n_i \sigma (Z_i, E)$ where n_i is the number of atoms per volume unit, σ is the cross section per atomic process, Z_i is the atomic number of the material, and the sum is with i running over all interaction processes.
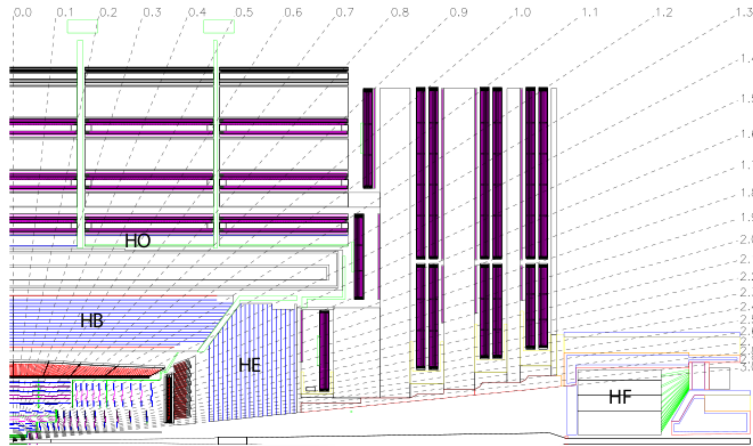
Figure 3.20: Longitudinal view of the CMS detector showing the locations of the hadron barrel (HB), endcap (HE), outer (HO) and forward (HF) calorimeters.
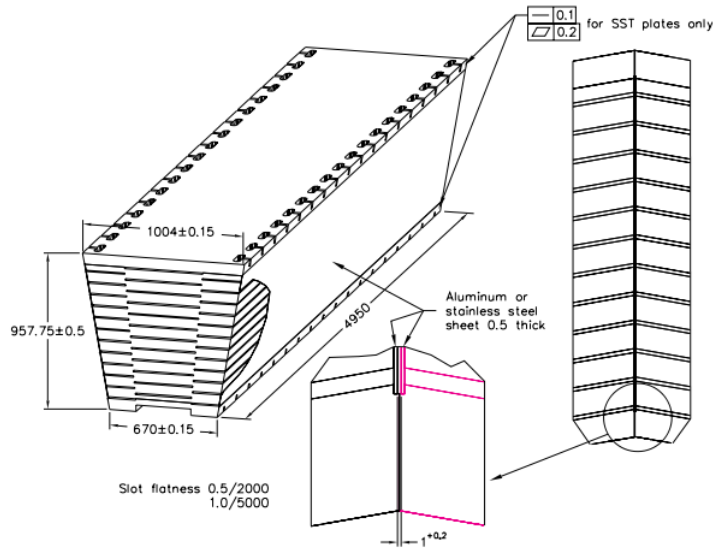
Figure 3.21: View
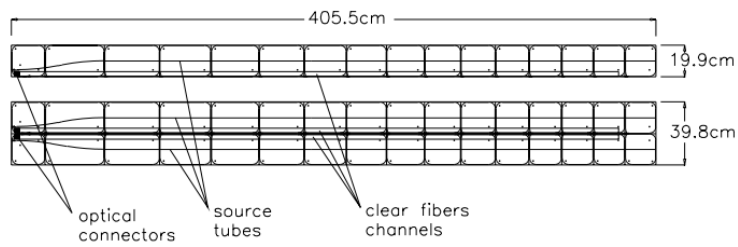
Figure 3.22: (up) Isometric view of the HB wedges, showing the hermetic design of the scintillator sampling. (down) Scintillator trays.

of the particles produced in the final state. The HE design had to keep into account the high rates of particles forseen in this region: at design LHC luminosity of $10^{34}cm^{-2}s^{-1}$) the particle rate is of order of the MHz, so that the required radiation tolerance at $|\eta| <$ 3 os order of 10 MRad after 10 years of operation at design luminosity. Furthermore, ECAL calorimeter is located in the ends of the CMS magnet, therefore imposing the use of a non-magnetic material for the absorber. In order for the absorber to have a sufficient number of radiation lengths to fully extinguish the hadronic showers and good mechanical properties, C26000 cartridge brass was chosen. Single object resolution in HE is strongly limited by magnetic field, pileup, and parton fragmentation effects, so the design of the absorber focused rather on minimizing the cracks between the HB and HE. The geometry of plates is staggered so that no projective "dead" is present.

The brass plates are 79-mm-thick, while the scintillator are located within with 9-mm gaps. An extra layer (-1) is added to tower 18 to compensate the dead material region used for electronics. The optical elements are inserted into the gaps after the absorber is completely assembled; therefore, the optical elements must have a rigid structure to allow insertion from any position. The scintillation light is collected by wavelength shifting fibres. The design minimizes dead zones because the absorber can be made as a solid piece without supporting structures while at the same time the light can be easily routed to the photodetectors. A total of 1368 trays is present in the HE, comprehensive of 20 916 trays. The granularity of the calorimeters is $\Delta\eta \times \Delta\phi = 0.087 \times 0.087$ for $|\eta| < 1.6$ and $\Delta\eta \times \Delta\phi \sim 0.17 \times 0.17$ for $|\eta| \simeq 1.6$. Figure 3.23 shows the η segmentation of HE.
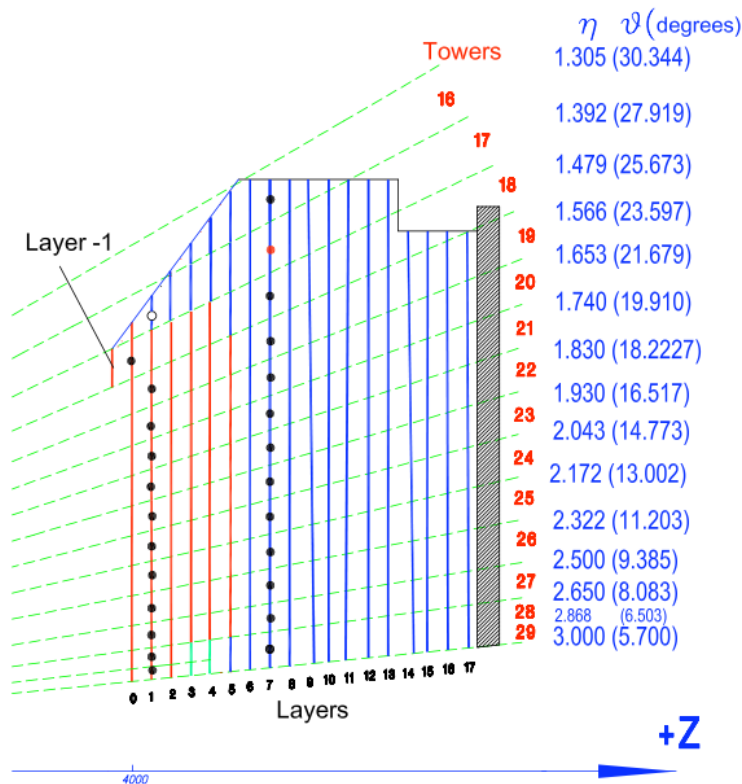
Figure 3.23: η segmentation of the HE.

3.2.4.9   The Outer Hadron Calorimeter

In the central pseudorapidity region, the combined stopping power of EB plus HB does not provide sufficient containment for hard hadron showers. To ensure adequate sampling depth for $|\eta|$ ¡ 1.3, the hadron calorimeter is extended outside the solenoid with a tail catcher called outer calorimeter (HO). The HO utilises the solenoid coil as an additional absorber equal to $1.4\sin\theta$ interaction lengths and is used to identify late starting showers and to measure the shower energy deposited after HB. The HO is placed as the first sensitive layer in each of these five rings. The rings are identified by the numbers -2, -1, 0, $+1$, $+2$, where the numbering follows the direction of the z axis (see also Section 3.2.5).

Figure 3.24 shows the position of HO layers in the CMS detector
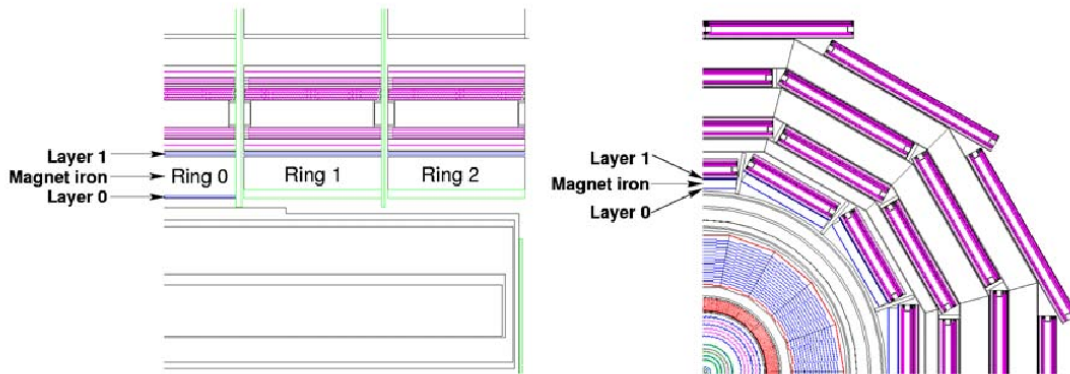
Figure 3.24: Longitudinal and transverse views of the CMS detector showing the position of HO layers.

3.2.4.10   Forward Calorimeter

The forward calorimeter has to experience unprecedented particle fluxes: an average of 760 GeV energy per proton-proton interaction is deposited into the two forward calorimeters, compared to only 100 GeV for the rest of the detector, with a non uniform distribution in terms of rapidity. At $|\eta| = 5$ after an integrated luminosity of $500\ fb^{-1}$ (~ 10 years of LHC operation), the HF will experience ~ 10 MGy. The charged hadron rates will also be extremely high, exceeding 10^{11} Hz per cm^2 [42], inside the HF absorber at 125 cm from the beam-line. The HF calorimeter had to be carefully designed to ensure a lifetime of at least 10 years in such harsh conditions: radiation hardness of the absorbing material was one of the main requirements for this purpo. Quartz fibres were chosen as the active medium because of their radiation hardness. A Cherenkov effect is exploited for signal generation: when charged shower particles above the Cherenkov threshold (E $\geq$ 190 keV for electrons) they generate Cherenkov light, thereby rendering the calorimeter mostly sensitive to the electromagnetic component of showers [44].

The forward calorimeter is essentially a cylindrical steel structure with an outer radius of 130.0 cm. The front face of the calorimeter is located at 11.2 m from the interaction point. There is a cylindrical, hole for the beam pipe is with radius 12.5 cm from the center of the beam line. The HF is divided azimuthally in 36 modular wedges of 20° degrees each, 18 on each side of the interaction point. Figure 3.25 shows a cross section of the HF. The fibres are parallel to the beam line, and are bundled to form 0.175×0.175 ($\Delta\eta \times \Delta\phi$) towers, except for the first and the last which have exceptionally $\Delta\eta = 0.111, 0.300$ respectively. The detector is housed in a hermetic radiation shielding which consists of

layers of 40 cm thick steel, 40 cm of concrete, and 5 cm of polyethylene. A large plug structure in the back of the detector provides additional shielding.
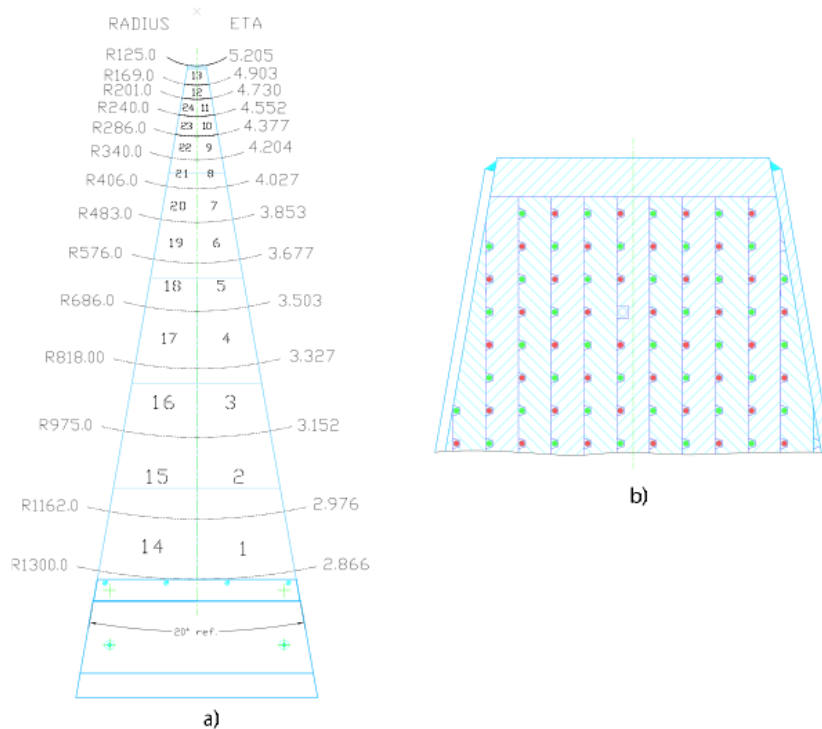
Figure 3.25: (a) Transverse segmentation of the HF towers. (b) An expanded view of the wedge shows the squared out groove holding the radioactive source tube.

3.2.5 The Muon System

Muon play a central role in the LHC physics program: precise identification, triggering and momenutm measurement of muons is therefore crucial. Muons characteristics make them optimal candidates for precision measurements: muons of energies below the scale of O(few TeVs) lose energy mainly due to ionization through the detectors, so that a sufficiently energetic muon ($\sim 5GeV$) can reach the outside of the CMS superconducting coil. Also, since muons are charged particles, precision measurement of their momentum can be performed in the tracking systems. Those features make muon detection a powerful tool for recognizing signatures of interesting processes over the very high background rate expected at the LHC. An example is the predicted decay of the Standard Model Higgs boson into ZZ or ZZ^*, which in turn decay into 4 leptons, has been called "gold plated" for the case in which all the leptons are muons. For this precise case actually the CMS detector was ideally optimized: the characteristic experimental signature of the muons makes them relatively easy to reconstruct and to identify, and allows for the best 4 particle mass resolution. Electrons are in fact more affected by radiative losses in the tracker material. This example, and others from SUSY models, emphasize the discovery potential of muon final states and the necessity for wide angular coverage for muon detection. Therefore, precise and robust muon measurement was one of the primary goals for CMS design, as even the experiment's middle name indicates.

The Muon System (MS) [45] was designed to best exploit the muon features and their potential to provide the cleanest signature amongst all physics objects reconstructed in CMS,

The MS provides muon identification, triggering and momentum reconstruction, which can be used to improve the already excellent tracking system momentum determination of CMS. The MS is located in the region outside the magnet. In this region the return yoke allows for the magnetic field lines to close generating a rougly constant 1.8 Tesla magnetic field in the opposite direction with respect to the one inside the solenoid. Good muon momentum resolution and trigger capability are enabled by the highfield solenoidal magnet and its flux-return yoke. The latter also serves as a hadron absorber for the identification of muons. The CMS muon system is designed to have the capability of reconstructing the momentum and charge of muons over the the entire kinematic range of the LHC. CMS uses 3 types of gaseous particle detectors for muon identification. The Muon System has a cylindrical barrel section around the superconducting solenoid and 2 planar endcap regions. The muon system occupies the largest volume of the detector, and consists of about 25 000 m^2 of detection planes. This implies that the muon chambers had to be inexpensive, reliable, and robust, while on the other hand durability was less influenced by radiation rate with respect to other detectors. In the barrel region the neutron-induced background is small, the muon rate is low, and the magnetic field is reasonably uniform and mostly contained in the steel yoke. Here drift chambers with standard rectangular drift cells are used. The barrel drift tube (DT) chambers cover the pseudorapidity region $|\eta| < 1.2$ and are divided into 4 stations located in between among the layers of iron yoke plates. The first 3 stations each contain 2 layers of 4 chambers which measure the muon coordinate in the $r - \phi$ bending plane, and one layer of 4 chambers measuring the z coordinate. The fourth station does not contain the z-measuring layer. The drift cells of each chamber are offset by a half-cell width with respect to their neighbor to eliminate dead spots in the efficiency. This arrangement also provides a allows to measure muon time with excellent resolution using meantimer circuits. DT can therefore unambiguously identify muons bunch crossing identification. In the CMS endcap both the muons and background rates are higher, and the magnetic field is non uniform. In this region cathode strip chambers (CSC) are chosen due to their fast response time, good segmentation which goes along with a high radiation resistance. The CSCs cover the range $0.9 < |\eta| < 2.4$. CSC chambers are positioned perpendicular to the beam line and interspersed between the iron yoke plates. 4 stations of CSCs are present per endcap. The cathode strips of each chamber run radially from the beam pipe and allow to measure position in the $r - \phi$ bending plane, while the anode wires run approximately perpendicular to the strips and allow to measure η and the beam-crossing time of a muon.To cope with the high bunch crossing frequency at LHC full regime and the high background rate in such conditions, a complementary and independent muon identification and triggering system was implemented with respect to DTs and CSCs: resistive plate chambers (RPC) were added in both the barrel and endcap regions of the CMS Muon System. The RPCs have a fast response, excellent time resolution and allow an highly-segmented trigger with a sharp p_T threshold over a large portion of the rapidity range ($|\eta|$ ¡ 1.6). For the CMS RPCs (see also Chapter 5) to allow operation with hight efficiency at lower applied high voltages and robustness in high rate working conditions, double-gap chambers operated in avalanche mode were chosen. RPCs have with better time resolution than DTs or CSCs, but coarser position resolution. They also help to resolve ambiguities in attempting to make tracks from multiple hits in a chamber. 6 RPC layers are present in the barrel muon system, 2 in each of the first 2 stations, respectively on the top and on the bottom of each DT chamber, and 1 in each of the last 2 stations. The 4 layers located in the first two stations allow the trigger algorithm to work even for low-p_T tracks that may stop before reaching the outer 2 stations. In the endcap region, there is a plane of RPCs in each of the first 3 stations in order for the trigger to use the coincidences between stations to reduce background, to improve the time resolution for bunch crossing identification, and to achieve a good p_T resolution. Figure 3.26 shows a

quarter of the muon system of CMS and figure 3.27 shows a view of the MS in the $x - y$ plane.
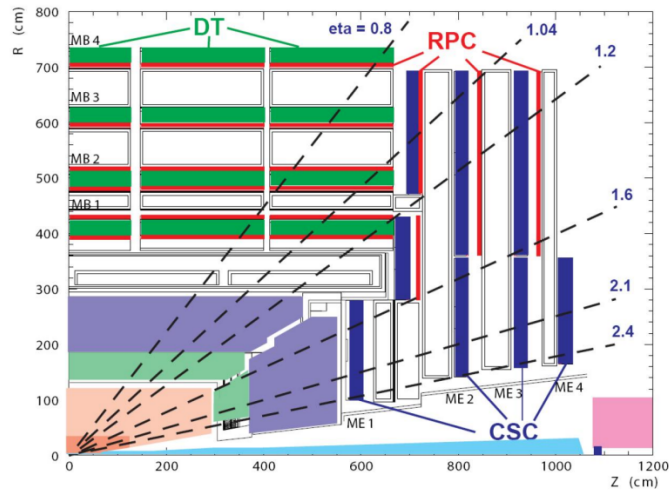
Figure 3.26: Transverse view of the CMS muon system

We describe in the following part the three subsystem in more detail. A further chapter will be dedicated to the performance measurements of the RPC performances which was part of the thesis work.

3.2.5.1 Drift Tubes

The CMS drift tube chambers are located in the Muon System Barrel, covering the $|\eta| < 1.2$ range. There are 4 stations of DTs, forming coaxial cylinders including 60 chambers (first 3) and 70 (outermost cylinder) divided into 5 wheels along the direction of the beam axis (labeled $-2, -1, 0, +1, +2$ in the direction of the z axis), yielding a total of 172 000 sensitive wires. The drift chambers allow for precise position measurements, local track reconstruction and a time resolution sufficient to unambiguously determine muon bunch crossing. The low muon rate and magnetic field intensity make it possible to use drift tubes in the Barrel, while in the endcap a different technology had to be used.

DT cell length is $\sim$ 2.4 m in the $r - \phi$ projection, corresponding moreless to the barrel longitudinal segmentation, while the transverse dimension of the cell, which is also the a maximum drift path, was chosen to be of 21 mm. This corresponds to a maximum drift time of 380 ns in a gas mixture of 85% Ar + 15% CO_2 . This choice results in a negligible cell occupancy while keeping the number of channels under control. The smallest modular unit in the subdetector is the single DT cell, so that it is easier to identify the effects of single malfunctioning DT and to avoid consequences on the entire detector.

Each wheel is segmented in 12 ϕ sectors, with 4 chambers, one per station, named MB1, MB2, MB3, MB4 from the innermost to the outermost. The gaps between sectors are essentially due to the presence of the supports for the iron yoke. A tilted geometry is chosen so that the cracks in different stations do not overlap in ϕ, resulting in a 100% angular coverage.

DT chambers consist of 3 (or 2) superlayers (SL, see Figure 3.30). Each SL is composed of 4 layers of drift cells staggered by half a cell. The wires in the innermost and outermost (along the r cooridinate) SLs of a chamber are parallel to the beam line, providing track measurement in the magnetic bending plane (r-ϕ). In the central SL of the cell, the DT cell wires run orthogonal to the beam line in order to provide measurement of the z coordinate. The third layer is not present in MB4, therefore no z-measuring is performed in
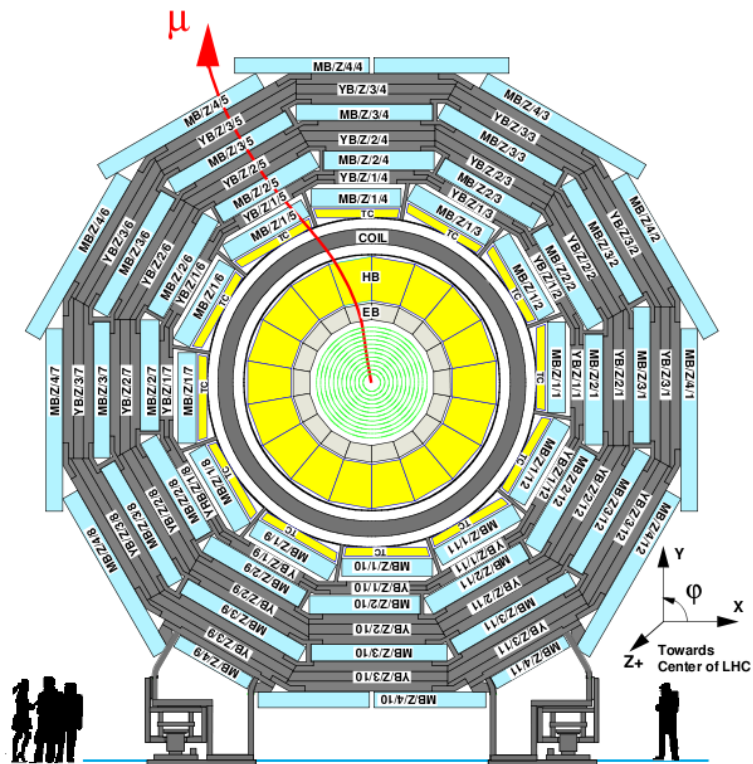
Figure 3.27: Frontal view of the CMS muon system
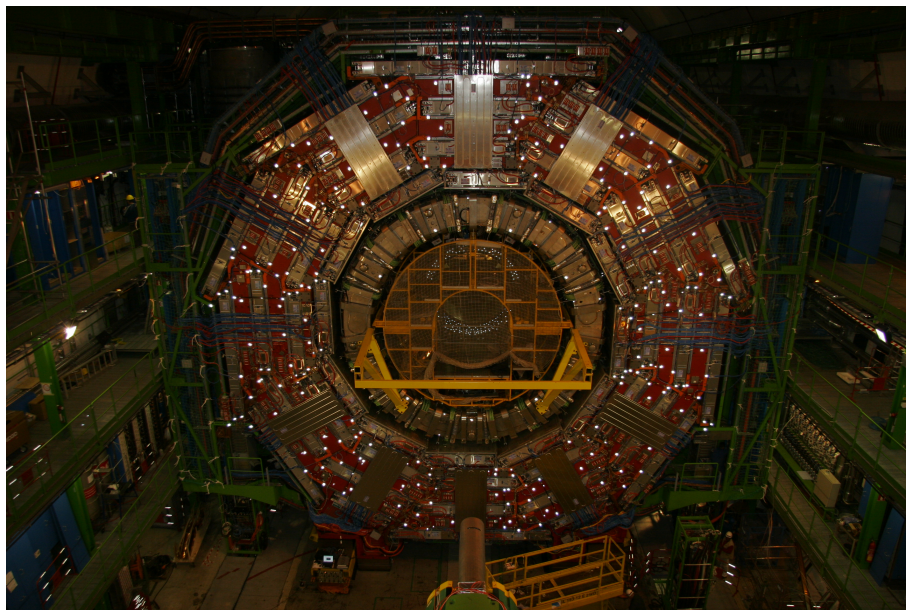
Figure 3.28: Picture of the muon system (left) an open barrel wheel.

such station. A muon coming from the interaction point first encounters a ϕ -measuring SL, passes through the honeycomb plate, then crosses the z- measuring SL and the second ϕ -measuring SL. In this scenario, there still exist limited regions of η in which the combined effect of the ϕ and z discontinuities limits to only 2 (out of 4), the number of stations crossed by a muon. Each cell has an area of 13×4.2 cm^2 where 4.2 cm is the distance between two consecutive anode wires. DT cells have an efficiency above 95% for muon detection in the p_T plateau. The a single wire resolution of 250 μm, while the combined measurement in the 8 $r - \phi$ cells allows to reach the target 100 μm resolution. Figure 3.29 shows the location of drift tube layers with respect to RPC chambers. Figure 3.30 shows a DT chamber section.
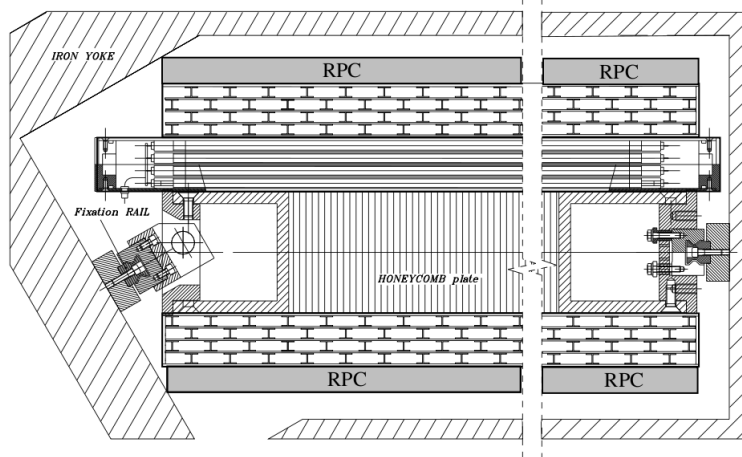
Figure 3.29: A DT chamber in position inside the iron yoke; the view is in the (r-ϕ) plane. One can see the 2 SLs with wires along the beam direction and the other perpendicular to it. In between is a honeycomb plate with supports attached to the iron yoke. Not shown are the RPCs, which are attached to the DT chambers via support plates glued to the bottom and/or top faces, depending on chamber type.
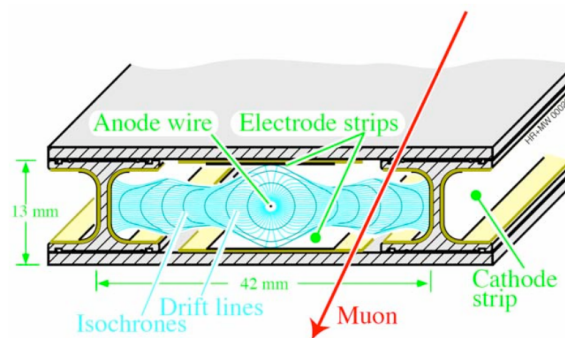
Figure 3.30: Sketch of a DT cell showing drift lines and isochrones. Top and bottom plates are at ground potential, while the a voltage of +3600V is applied on wires, +1800V is applied on the strips, and −1200V on the cathodes.

3.2.5.2 Cathode Strip Chambers

The CMS Cathode Strip Chambers are multiwire proportional chambers [46] located in the Muon System endcap, covering the pseudorapidity range $0.9 < |\eta| < 2.4$. Actually,

there is some overlap between the MS Endcap and the MS Barrel, as it is possible to see in Figure 3.26. In the overlap region, $0.9 < |\eta| < 1.2$, muons are detected by both the barrel drift tubes and endcap CSCs, and measurements from all detectors are used for track reconstruction. A CMS CSC chamber is comprised of 6 anode wire planes interleaved among 7 cathode panels. The wires run azimuthally, allowing precise measurement of the track's radial coordinate. Strips run radially at constant $\Delta\phi$ width. The muon coordinate along the wires is obtained by interpolating charges induced on strips (figure 3.31,right). The nominal gas mixture is ($40\%Ar + 50\%CO2 + 10\%CF4$). The MS Endcap consists of 468 CSCs arranged in groups as follows: 72 ME1/1, 72 ME1/2, 72 ME1/3, 36 ME2/1, 72 ME2/2, 36 ME3/1, 72 ME3/2, and 36 ME4/1, althought the 72 ME4/2are not installed in the current CMS configuration. CSCs have trapezoidal shape, covering 10° or 20° in ϕ. Adjacent chambers overlap providing 100% ϕ coverage. muon in the pseudorapidity range $1.2 < |\eta|$ ¡ 2.4 crosses 3 or 4 CSCs. In the baseline design, muons with $|\eta| < 2.1$ are also detected by resistive plate chambers (RPC); however, in the current initial phase this coverage is reduced to $|\eta| < 1.6$. The CSCs are multiwire proportional chambers comprised of 6 anode wire planes interleaved among 7 cathode panels . Wires run azimuthally and define a track's radial coordinate. Strips are milled on cathode panels and run lengthwise at constant $\Delta\phi$ width. The largest chambers, ME2/2 and ME3/2,are about 3.4×1.5 m^2 in size. The overall area covered by the sensitive planes of all chambers is about 5000 m^2 , the gas volume is >50 m^3 , and the number of wires is about 2 million. There are about 9000 high-voltage channels in the system, about 220 000 cathode strip read-out channels with 12-bit signal digitisation, and about 180 000 anode wire read-out channels. Figure 3.31 (left) shows a layout of a CSC chamber and (right) shows che CSC principle of operation.
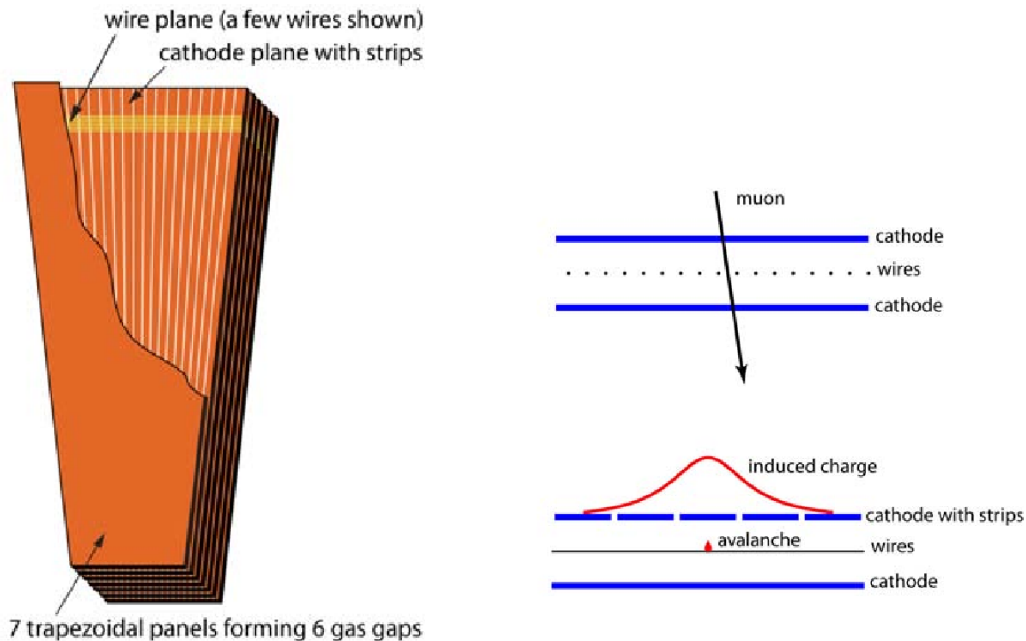
Figure 3.31: Left: Layout of a CSC made of 7 trape- zoidal panels. The panels form 6 gas gaps with- planes of sensitive anode wires. The cut-out in the top panel reveals anode wires and cathode strips. Only a few wires are shown to indicate their azimuthal direction. Strips of constant $\Delta\phi$ run lengthwise (radially). The 144 largest CSCs are 3.4 m long along the strip direction and up to 1.5 m wide along the wire direction. Right: a schematic view of a single gap illustrating the principle of CSC operation. By interpolating charges induced on cathode strips by avalanche positive ions near a wire, one can obtain a precise localisation of an avalanche along the wire direction.

3.2.5.3   Resistive Plate chambers

Resistive Plate Chambers (RPC) are gaseous parallel-plate detectors that combine adequate spatial resolution with a time resolution comparable to that of scintillators . More details about the RPC working principle is described in 5 An RPC time resolution allows to tag the time of a charged particle passing through the detector in in a much shorter time than the 25 ns between 2 consecutive LHC bunch crossings (BX), so that it can easily and unambiguously identify the bunch crossing of a muon, making such detector a well suited candidate for triggering purposes. A dedicated, complementary trigger system was developed for RPCs. The RPC trigger is actually capable of muon identification and p_T measurement even in presence of background sources, thanks to its pattern recognition logics implemented at the level of trigger electroincs, even in presence high rate and background. RPC trigger provides time measurements as well as p_T and position measuremens of the muon on a so-called reference layer. A trigger based on RPCs has to provide the BX assignment to candidate tracks and estimate the transverse momenta with high efficiency in an environment where rates may reach 10^3 Hz/cm2 . The CMS RPC basic double-gap module consists of 2 gaps, hereafter referred as up and down gaps, operated in avalanche mode with common pick-up read-out strips in between (fig- ure 7.66) [47], [48]. The total induced signal is the sum of the 2 single-gap signals. This allows the single-gaps to operate at lower gas gain (lower high voltage) with an effective detector effi- ciency higher than for a single-gap. We proceed to describe the detector in the two regions of Barrel and Endcap.

RPC Barrel

Barrel RPCs are disposed in 6 and roughly cylindrical coaxial layers, revolving around the beam axis.

They are arranged in four stations, as for the DTs, and each station is subdivided in 5 wheels along the z axis, referred to as wheels (-2,-1,0,1,2) with the numbering convention following the verse of the axis. For a cross section of an RPC wheel, see also Figure 3.32. Each wheel is divided in 12 ϕ sectors. The first and second RPC layers (RB1In and RB1Out) are located respectively internally and externally with respect to the first DT station MB1. The third and fourth layers (RB2In and RB2Out) are positioned in the second station and have the same configuration around the second DT station MB2. The third and fourth stations contain 2 RPC chambers each, both located on the inner side of the DT layer (named RB3+ and RB3–, RB4+ and RB4–). A special case is RB4 in sector 4, which consists of 4 chambers: RB4++, RB4+, RB4–, and RB4—. Finally, in sectors 9 and 11 there is only 1 RB4 chamber, because in those sectors the CMS supports are located. There is a total of 480 rectangular barrel RPC chambers, 2455 mm long in the beam direction, with the exceptions of chambers in sector 3 of wheel −1 and sector 4 of wheel +1, which are shorter (2055 mm) to allow passage of the magnet cooling chimney. Chambers width varies from sation to station: RB1, RB2, and RB3 have widths 2080, 2500, and 1500 mm, respectively. Strips always run along the beam direction, providing measurement in the $r - \phi$ plane. Strips are divided into 2 parts for chambers RB1, RB3, and RB4. For the RB2 chambers, special requirements are made on the strip length in order to have an advantageous η segmentation for the trigger algorithm: strips are divided into 2 parts in RB2in for wheels +2 and –2 and RB2out for wheels +1, 0, and –1, and into 3 parts in RB2out for wheels +2 and –2 and in RB2in for wheels +1, 0, and –1 (more detail is given in chapter 5 on the RPC trigger algorithm).

RPC Endcap

The RPCs extend in the forward giving an alternative and independent muon triggering and identification system to CSC . The RPCs are arranged in 3 disks supported by the iron yoke. RPCs are mounted on both faces of the disks forming 3 RPC stations (RE1 - 3). The chambers overlap in ϕ as to avoid dead space at chamber edges. Each endcap RPC chamber consists of a double-gap structure enclosed in a flat trapezoidal shaped box made of 2 aluminium honeycomb panels of 6 mm thickness each and a 16×16 mm^2 section spacer frame The strip panel, sandwiched in between the gas gaps, has copper strip sections on a G10 support. Strips run radially and are radially segmented into 3 trigger sections for the REn/2 and REn/3 chambers (n = 1–3). Figure 3.33 shows the lateral section of endcap RPCs
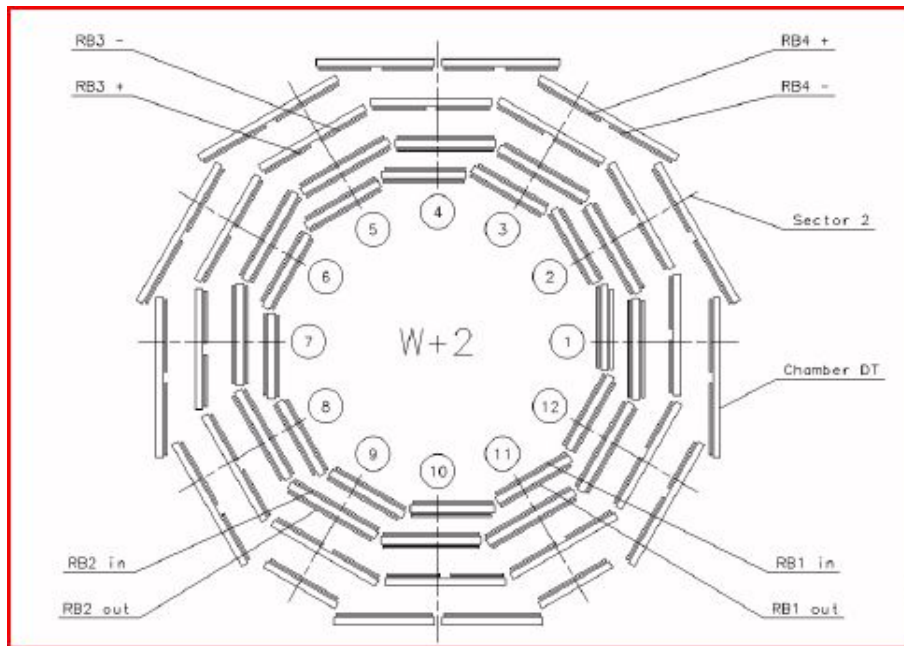
Figure 3.32: Schematic layout of one of the 5 barrel wheels, which are labeled –2, –1, 0, +1, and +2, respectively. Each wheel is divided into 12 sectors that are numbered as shown.

3.2.6 The CMS Trigger System

One of the most daring challenges LHC poses from the experimental point of view is related to the amount of information which is produced: LHC proton-proton operation forsees a design bunch crossing rate of 25 ns, corresponding to a frequency of 40 MHz. For each bunch crossing several collisions occur at each crossing of the proton bunches (approximately 20 simultaneous pp collisions at the nominal design luminosity of $10^{34} cm^{-2} s^{-1}$). For each event, all detector information necessary for physics reconstruction has to be stored, leading to ~ 1 MB per bunch collision. Is by far impossible to store and process an amount of data of the magnitude produced at LHC with any of the current technologies, therefore a drastic rate reduction has to be achieved. This reduction has to be performed in such way not to lose the most interesting physics events, discriminating them from the huge uninteresting hard and soft QCD background events. This is the task of the trigger system. The trigger is therefore also the start of the physics event selection process. The rate is reduced in two steps called Level-1 (L1) Trigger [49] and High-Level Trigger (HLT) [50], respectively. The Level-1 Trigger consists of specifically designed electronics, whereas the
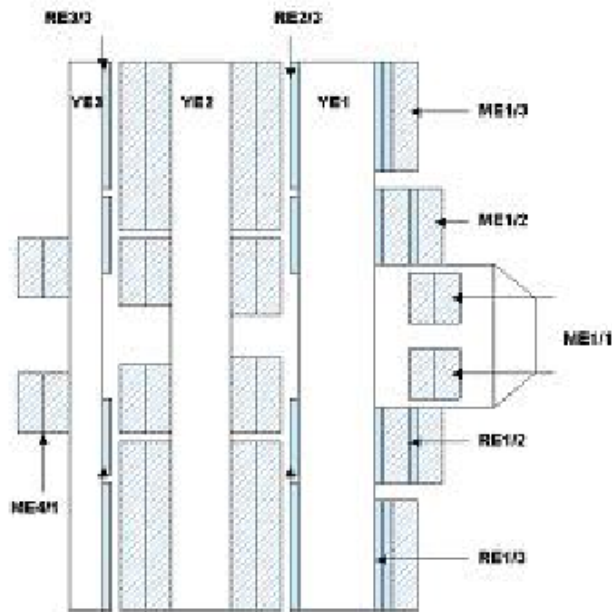
Figure 3.33: Schematic layout of the CMS endcap for the initial muon system

HLT is a software system implemented in a filter farm of about one thousand commercial processors. The trigger is designed so to reduce the rate of at least a factor of 10^6 overall (between L1 and HLT). The design output rate limit of the L1 Trigger is 100 kHz, however a safety factor of ∼3 is assumed, leading to a in practice to a calculated maximal output rate of 30 kHz. The L1 Trigger uses data from the calorimeters and the muon system, while holding the high-resolution data in pipelined memories in the front-end electronics. Figure 3.34 shows a scheme of the overall architecture of the CMS Trigger system. The L1 Trigger is divided in local, regional and global triggers. The Local Triggers, (also called Trigger Primitive Generators or TPG), are based on simple objects like energy deposits in calorimeter trigger towers and track segments or hit patterns in muon chambers. The information from regional triggers is combined using pattern logics to determine trigger objects (electron, photon or muon candidates) and to rank and sort them based on physical quality criteria. Such candidates are searched for in limited spatial regions. Ranking criteria are the function of energy or momentum reconstructed by the electronics trigger algorithm and a quality flag, which reflects the level of confidence attributed to the L1 parameter measurements, and is based based on detailed knowledge of the detectors and trigger electronics and on the amount of information available. The Global Calorimeter and Global Muon Triggers (said GCT and GMT respectively) determine the higher rank calorimeter and muon objects combining the trigger information from in different regions of the detector. GMT and GCT then send information to the Global Trigger, at the top of the Level-1 hierarchy, which ultimately takes the decision whether to accept or reject the event at L1. The decision is based on algorithm calculations and on the readiness of the sub-detectors and the DAQ, which is determined by the Trigger Control System (TCS). The Level-1 Accept (L1A) decision is communicated to the sub-detectors through the Timing, Trigger and Control (TTC) system. The architecture of the L1 Trigger is depicted in figure 3.35. The L1 Trigger has to analyze every bunch crossing. The allowed L1 Trigger latency, between a given bunch crossing and the distribution of the trigger decision to the detector front-end electronics, is 3.2 μs. The processing must therefore be pipelined in order to
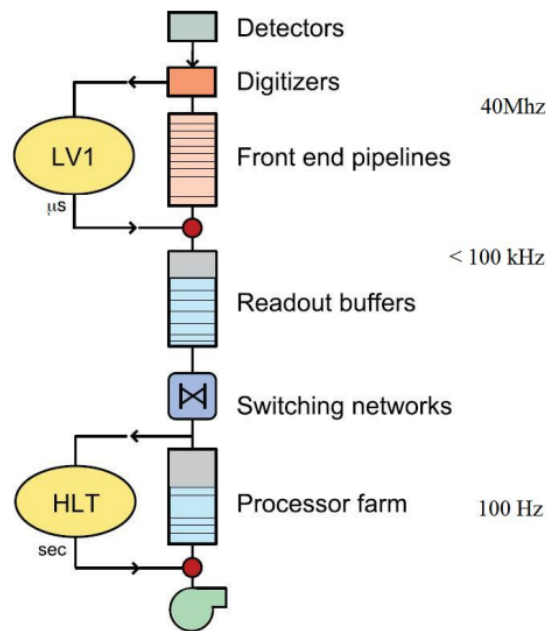
Figure 3.34: Architecture of the CMS trigger system, including the ingoing/rates relative to each step.
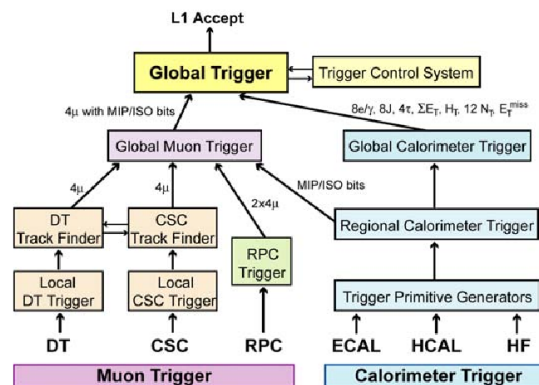
Figure 3.35: Architecture of the CMS Level-1 Trigger.

enable a quasi-deadtime-free operation. The L1 Trigger electronics is housed partly on the detectors, partly in the underground control room located at a distance of approximately 90 m from the experimental cavern. If the event gets the L1A it is then sent to the HLT for further scrutiny.

3.2.6.1   The Muon Trigger

All three detector in the muon system take part in the Muon trigger, providing trigger primitives in the barrel and encap covering the region up to $|\eta| < 2.1$ in this phase of the experiment. The design coverage is $|\eta| \leq 2.4$. The barrel DT chambers reconstruct local trigger track segments in the ϕ-projection and hit patterns in the η-projection. The endcap CSCs deliver 3-dimensional track segments. All chambers also assign unambiguously the trigger bunch crossing and pass it to the GMS The Regional Muon Trigger has one part consisting of the DT and CSC Track Finders, which join segments together in track candidates including physical parameters and position on a reference layer. The RPC trigger system delivers an independent set of track candidates based on regional hit patterns recognition with excellent time resolution. The Global Muon Trigger then combines the information from the three sub-detectors, achieving an improved momentum resolution and efficiency compared to the stand-alone systems. Follows a short description of the L1 Regional Muon Trigger candidates algorithms.

DT Level-1 Trigger

The electronics of the DT local trigger consists of four basic components : Bunch and Track Identifiers (BTI), Track Correlators (TRACO), Trigger Servers (TS) and Sector Collec- tors (SC). While the SCs are placed on the sides of the experimental cavern, all other trigger and read-out electronics is housed in minicrates on the front side of each chamber. All devices are im- plemented in custom-built integrated circuits. The BTIs are interfaced to the front-end electronics of the chambers. Using the signals from the wires they generate a trigger at a fixed time after the passage of the muon. Each BTI searches for coincident, aligned hits in the four equidistant planes of staggered drift tubes in each chamber superlayer. The association of hits is based on a meantimer technique [51], which uses the fact that there is a fixed relation between the drift times of any three adjacent planes. From the associated hits, track segments defined by position and angu- lar direction are determined. The spatial resolution of one BTI is better than 1.4 mm, the angular resolution better than 60 mrad.

CSC Level-1 Trigger

The hardware of the CSC local trigger consists of seven types of electronics boards. Cathode and anode front-end boards (CFEB and AFEB) amplify and digitize the signals. Anode LCT- finding boards (ALCT) latch the anode hits at 40 MHz, find hit patterns in the six chamber layers that are consistent with having originated at the vertex, and determine the bunch crossing. They send the anode information to the Cathode LCT-finding plus Trigger Motherboard (CLTC/TMB) cards. The CLCT circuits look for strip hit patterns consistent with high-momentum tracks. The TMB circuits perform a time coincidence of cathode and anode LCT information. If a coincidence is found, they send the information to the Muon Port Cards (MPC). The TMB selects up to two LCTs based on quality cuts. In order to cancel out ghosts a coincidence with RPC hits is established if two or more LCTs are found.

RPC Level-1 Trigger

The RPC trigger is based on the spatial and temporal coincidence of hits in several layers. It is segmented in 33 trigger towers in η, which are each subdivided in 144 segments in ϕ. As opposed to the DT/CSC, there is no local processing on a chamber apart from synchronization and cluster reduction. The Pattern Comparator Trigger (PACT) logic [195] compares strip signals of all four muon stations to predefined patterns in order to assign pT and electric charge, after having es- tablished at least three coincident hits in time in four planes. Spatially the PACT algorithm requires a minimum number of hit planes, which varies depending on the trigger tower and on the pT of the muon. Either 4/6 (four out of six), 4/5, 3/4 or 3/3 hit layers are minimally required. A quality parameter reflects the numbers of hit layers. For six planes there are typically 14 000 possible patterns. More detailed description will be given in Chapter 5.

Figure 3.36 shows the organization of L1 muon system
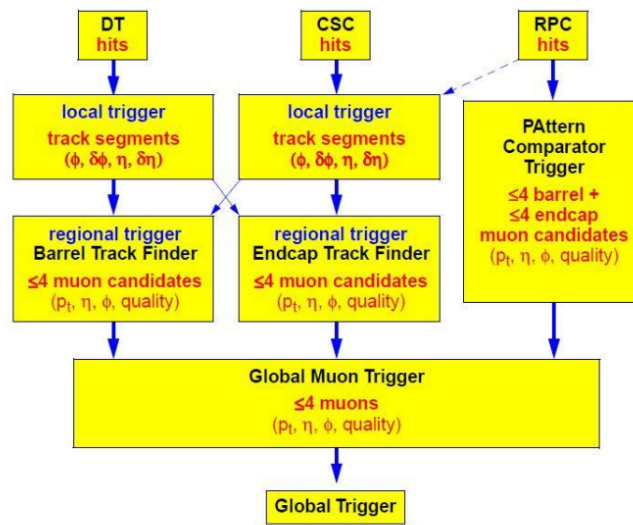
Figure 3.36: Architecture of the muon CMS Level-1 Trigger.

Chapter 4

CMS event reconstruction

In this chapter we give a short description of the CMS offline event reconstruction and we introduce some common concepts for offline analyses in CMS.

4.1   Event Data Model

The central concept of the CMS data model is the Event, hence the acronym Event Data Model (EDM) used to refer to it. The Event provides access to the recorded data from a single triggered bunch crossing, and to new data derived from it. This may include raw digitised data, reconstructed products, or high-level analysis objects, for real or simulated crossings. The Event also contains information describing the origin of the raw data, and the provenance of all derived data products. The inclusion of provenance information allows users to unambiguously identify how each event contributing to a final analysis was produced; it includes a record of the software configuration and conditions / calibration setup used to produce each new data product. Events are physically stored as persistent ROOT files [52]. The Event is used by a variety of physics modules, which may read data from it, or add new data, with provenance information automatically included. Each module performs a well-defined function relating to the selection, reconstruction or analysis of the Event. Several module types exist, each with a specialised interface. The execution of modules in a sequence allows the reconstruction of physics objects up to the highest level which is used for analyses.

The modularity of the CMS EDM allows to make use of several event formats with differing levels of detail and precision, allowing to achieve the necessary level of data reduction for each analysis. Other specialised event formats are used for heavy-ion data. The process of data reduction and analysis takes place in several steps, typically carried out at different computer centres. The most important data tier are:

- *RAW* RAW events contain the full recorded information from the detector, records of the trigger outputs, and other metadata necessary to have the full inormation on the event. RAW data is accepted into the offline system at the HLT output rate (300 Hz for pp collisions). RAW data format is extended to store the output of CMS Monte Carlo simulation tools additional information. The RAW data is permanently archived in safe storage, usually occupy around 1.5 MB/event (2 MB/event for simulated data, due to additional Monte Carlo truth information).

- *RECO* Reconstructed (RECO) data is produced by applying several levels of pattern recognition and com- pression algorithms to the RAW data. These algorithms include: detector-specific filtering and correction of the the digitised data; cluster- and track-finding; primary and secondary vertex recon- struction; and particle ID, using a

variety of algorithms operating on cross-detector information. RECO events usually to occupy around 0.5 MB/event.

- *AOD* AOD (Analysis Object Data) is the compact analysis format, designed to allow a wide range of physics analyses whilst occupying sufficiently small storage so that very large event samples may be held at many centres. AOD events contain the parameters of high-level physics objects, plus sufficient additional information to allow kinematic refitting. This format requires order of 100 kB/event, small enough to allow a complete copy of the experimental data in AOD format to be held at computing centres outside CERN.As for RECO and RAW, additional information is stored when managing Monte Carlo simulated events.

4.1.1 Non-Event data

In addition to event data recorded from the detector, a variety of non-event data is required in order to interpret and reconstruct events. Four types of non-event data are defined in CMS: construction data, related to the construction features of the detector; equipment management data; configuration data, including programmable parameters related to detector operation; and conditions data, including calibrations, alignments and detector status information. For instance, calibration constants for a given run may be derived from prompt reconstruction of a subset of recorded events, and then used both by the HLT system and for subsequent reconstruction and analysis.

4.2 Physics objects reconstruction

Data collected in each of the CMS sub-detectors are used to reconstruct physics object through offline software algorithms which allow the identification of particles passing through CMS and identify its physics parameters of interest, like charge and 4-momentum. The original algorithms developed in the design phase of the experiment were updated taking into account the knowledge of the detector and have constantly been tuned and upgraded to improve the performances. The main physics objects used in CMS are: Muons, Electrons, Jets, Photons, Missing Energy and to a lesser extent b-tagged jets and taus. Figure 4.1 shows a pictorial view of the different objects reconstructed in CMS and of the signature they give in the different CMS subdetectors.

In the next part of this chapter we describe the standard reconstruction of such objects with CMS and some of the more advanced tools that are used for the analyses described in this thesis.

4.2.1 Charged particles track reconstruction

Charged particles are detected in the inner tracking system. Their trajectory bends in the CMS magnetic field: a charged particle moves along an helix whose pace is related to the transverse momentum. One finds:

$$p_T \propto B \cdot r_{curl} \tag{4.1}$$

where B is the magnetic field and r_{curl} is the curling radius of the circumference obtained projecting the helix in the $x - y$ plane. Therefore a precise reconstruction of the tracks is crucial for precise momentum measurements. The tracks in CMS inner tracking system are reconstructed with a fit using as input the position of the strips or pixel fired ("hits") in
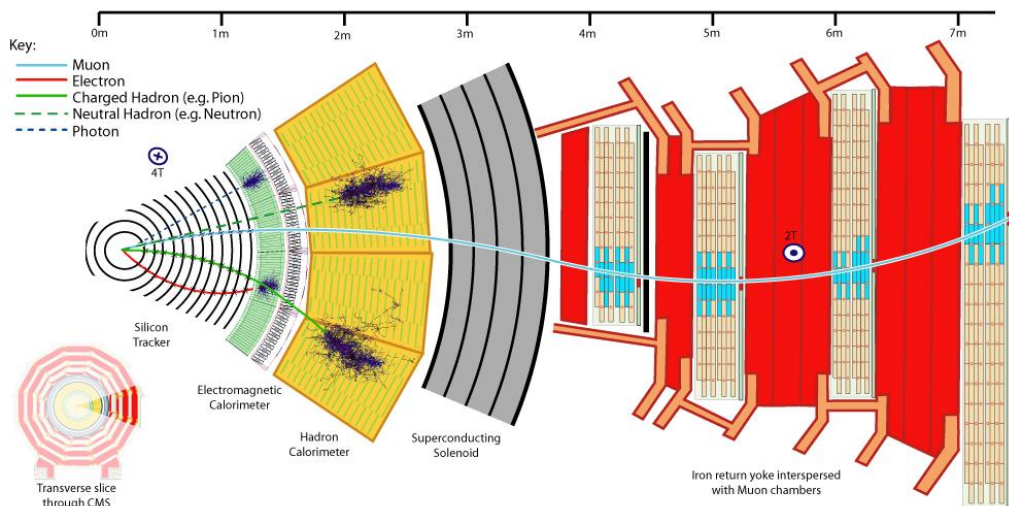
Figure 4.1: Side view CMS slice and detail of the physics objects signatures in the different sub-detectors.

the detectors. A pattern recognition is performed based on the Kalman filter method [53]. First of all a starting point ("seed") is found looking at all hits in the tracker. Each seed is composed of a small subset of the position measurements in the Tracker itself. Since five parameters (including the trajectory curvature) are needed to start trajectory building, at least 3 hits, or 2 hits and a beam constraint, are necessary to properly define a seed. The Kalman filter then proceeds iteratively from the layer where the seed is locate,d starting from a coarse estimate of the track parameters provided by the trajectory seed, and includes the information of the successive detection layers one by one. On each layer, i.e. with every new measurement, the track parameters are known with a better precision, up to the last point, where they include the full tracker information.

The Kalman filter is initialized at the location of the innermost hit with an estimate obtained during seeding. The corresponding covariance matrix is scaled by a large factor in order to avoid any bias. The fit then proceeds in an iterative way through the full list of hits. For each valid hit the position estimate is re-evaluated again using the current values of the track param- eters. This first filter is complemented with the smoothing stage: a second filter is initialized with the result of the first one (except for the covariance matrix, which is scaled with a large factor) and is run backward toward the beam line.

This filtering and smoothing procedure yields optimal estimates of the parameters at the sur- face associated with each hit and, specifically, at the first and the last hit of the trajectory. Es- timates on other surfaces, e.g., at the impact point, are then derived by extrapolation from the closest hit.

On top of the standard Kalman filter, an iterative tracking procedure [55] has been developed in CMS to preserve high tracking efficiency while minimizing the fake rate. For each iteration, the following steps are applied:

- A subset of reconstructed hits is selected by removing hits used in previous iterations. the first iteration the complete set of reconstructed hits is available for reconstructing tracks. In the following iterations, hits associated with a track reconstructed in an earlier iteration are removed. The hits are only removed if they are associated with a highPurity track and pass a (configurable) χ^2 cut of 30.

- Seed finding is performed on the available hits. The seeding configuration is the main difference between iterative steps.

- Track reconstruction (building, filtering, fitting, smoothing) is performed using the avail- able hits. Parameters in each stage can be tuned separately at each iteration to improve performance.

- The track collection is cleaned according to quality criteria and the collection of tracks which pass the cleaning stage is stored.

4.2.2 Muons

Muons are the charged particles that are best reconstructed in the Tracker. They mainly interact with the silicon detector through ionization and their energy loss by bremsstrahlung is generally negligible, except when muons are produced with an initial energy higher than about 100 GeV. Therefore these particles usually cross the whole volume of the tracking system, pro- ducing detectable hits on all the sensitive layers of the apparatus. Finally, muon trajectories are scattered exclusively by multiple-scattering, whose effects are straightforward to include inside the Kalman filter formalism. To identify muons, informations from the outer CMS Muon System are used in combination with the tracker information. Hits within each DT and CSC chamber are matched to form "segments" (track stubs). The segments are collected and matched to generate seeds that are used as a starting point for the actual track fit of DT, CSC and RPC hits. Fr track reconstruction a pattern of segments in the stations is searched for, using a rough geometrical criteria, so that it can be used as a seed for fitting. The track is extended using an iterative algorithm which updates the trajectory parameters at each step and, in order to reduce the possible bias from the seed, a pre-filter can be applied before the final filter. Once the hits are fitted and the fake trajectories removed, the remaining tracks are extrapolated to the point of closest approach to the beam line. In order to improve the pT resolution a beam-spot constraint is applied. Muon reconstructed tracks are classified in three categories, depending on the detectors used for muon reconstruction:

- *StandAlone Muons*: the track is reconstructed only in the muon detector. If the ansatz cosmic muons is made in reconstruction, they are called *Cosmic Muons*.

- *Global Muons*: Those muons are reconstructed both in the Tracker and in the Muon System. a matching criteria is adopted to match inner tracks to tracks in the Muon System, and then the Kalman Filter is applied again on hits from both tracks to get a better estimate of muon parameters.

- *Tracker Muons*: Those muons are reconstructed in the inner Tracker and then matched to a segment in either the DT or the CSC. The matching criteria between the inner track and the muon is tighter than for Global Muons since the MS segment lacks the robustness of a full track reconstruction.

4.2.3 Electrons and photons

Electrons and photons energies are measured in the CMS HCAL. To collect the photons and electrons energy in the ECAL, local deposits ("basic clusters") are summed into superclusters (SCs) which are extended in ϕ . After applying small energy corrections the superclusters are used to reconstruct photons and electrons, and to seed electron track reconstruction. *Electron reconstruction* uses two complementary algorithms at the track seeding stage: 'tracker driven' seeding, more suitable for low p_T electrons as well as performing better for electrons inside jets and 'ECAL driven' seeding. The 'ECAL driven' algorithm starts by the reconstruction of ECAL "superclusters" of transverse energy $E_T > 4$ GeV and is optimized for isolated electrons in the p_T range relevant for Z or W decays and down to $p_T \sim 5~GeV/c$.

A "supercluster" is a group of one or more associated clusters of energy deposits in the ECAL constructed using an algorithm which takes account their characteristic narrow width in the η coordinate and their characteristic spread in ϕ due to the bending in the magnetic field of electrons radiating in the tracker material. As a first filtering step, superclusters are matched to track seeds (pairs or triplets of hits) in the inner tracker layers, and electron tracks are built from these track seeds. Trajectories are reconstructed using a dedicated modeling of the electron energy loss and fitted with a Gaussian Sum Filter (GSF) [54]. The filtering performed at the seeding step is complemented by a preselection. For candidates found only by the 'tracker driven' seeding algorithm, the preselection is performed based on is based on a multivariate analysis. For candidates found by the 'ECAL driven' seeding algorithm, the preselection is based on the matching between the GSF track and the supercluster in η and ϕ. The few 'ECAL driven' electron candidates ($\sim 1\%$ for isolated electrons) not accepted by these matching cuts but passing the multivariate preselection are also kept.

Photons are reconstructed from the energy corrected superclusters, assigning the candidate momentum to the location of the reconstructed primary vertex. The energy of each photon candidate is estimated based on an observable called $r9$ which is the ratio of the energy contained within the 3×3 array of crystals centered on the seed crystal of the photon candidate's supercluster to the total energy contained in the supercluster. This quantity is used to determine if the photon is converted or unconverted. If the $r9$ of the candidate is above 0.94 (0.95) in the barrel (endcap), the energy of the 5×5 crystals ($E_{5\times5}$) around the highest energy crystal is used. Otherwise, the supercluster energy is used. The $r9$ threshold is larger in the endcap because the crystals are larger than in the barrel.

4.2.4 Jets

Jets stem from color charged particles fragmentation as indicated in Section 2.5.1. Jets reconstruction algorithms therefore have to be designed to best exploit the inner structure of the hadronic shower, while at the same time being robust against pile-up contamination and flexible enough to be applicable on Monte Carlo truth level as well as on objects reconstructed from the HCAL, ECAL and even the tracker. In fact, althought a crucial role is played by the HCAL in order to measure the fraction of jets energy from neutral hadrons, jet reconstruction often requires the use of ECAL to measure the fraction of jets energy due to bremsstrahlung of charged particles in the ECAL, which would otherwise be lost. Jets reconstructed through calorimetric informations only are referred to as "CaloJets". More sophisticated reconstruction tools apply jet reconstruction algorithms including also tracks reconstructed in the inner tracking system (said "Jet Plus Track" or "JPT"), or in general objects in the detector as a whole (Particle Flow Jets or "PFJets"). One of the most important properties for jets algorithms is infrared safety [56], which means that the number of jets must be insensitive to:

- *Soft radiation*: adding any number of infinitely soft particles (zero-energy) should not affect jet reconstruction.

- *Collinear radiation*: Splitting an existing particle up into two comoving particles (conserving the total momentum and energy) should not affect jet reconstruction.

We proceed to describe the most important jet algorythms used in CMS:

4.2.4.1 Jet reconstruction algorythms

- *Iterative Cone Algorithms*: Calorimeter towers or particles with $E_T(p_T) \geq T$, with T a given threshold (e.g. 1 GeV), are considered in descending order as starting

points (seeds) for an iterative search for stable cones such that all inputs with $(\Delta\eta)^2 + (\Delta\phi)^2 \leq R$ from the cone axis are associated with the jet, R being the cone size parameter. A cone is considered stable if its geometric center agrees with the (η, ϕ) location of the sum of the constituent four vectors within a certain toler- ance. Once a stable cone is found, it is declared a jet and its constituents are removed from the remaining inputs. The algorithm is neither soft radiation- nor infrared-safe. An infrared-safe variation of the Cone algorithms are the Seedless Cone algorithms: cones are tested for stability against variation of the seed and and merged/split up to get the final jet list [58].

- *kt and Anti-kt Algorithms*: (Anti-)kt algorithms [59] work in the momentum space and allow a good reproduction of the jet structure. Calorimeter towers or particles with $E_T(p_T) \geq T$, with T a given threshold (e.g. 1 GeV) are taken and for each of those seeds $d_i = p_{T,i}^{2k}$ and $d_{ij} = min(p_{T,i}^{2k}, p_{T,j}^{2k}) \frac{(\eta_i - \eta_j)^2 + (\phi_i - \phi_j)^2}{D} = min(p_{T,i}^{2k}, p_{T,j}^{2k}) \frac{R_{ij}^2}{D}$ are defined, where $D \sim 1$ is a parameter of the algorithm. d_{ij} is is the minimal relative transverse momentum between i and j, and k is 1 for kt and -1 for Anti-kt algorithms. Therefore, the minimum d_{min} between all the d_i and d_{ij} is calculated. If d_{min} is a d_{ij}, the ith and j^{th} objects are merged, removed from the seeds list and a new iteration is performed. If d_{min} is a d_i, the ith object is taken as jet and removed from the seeds list. This is iterated up to the depletion of the seeds list. For Anti-kt, soft particles will tend to cluster with hard ones long before they cluster among themselves. If a hard particle has no hard neighbours within a distance $2R$, then it will simply accumulate all the soft particles within a circle of radius R, resulting in a perfectly conical jet.

4.2.5 Vertices and pile up

Using information from the tracks reconstructed in the detector it is possible to determine the 3D position of the primary interaction point and of the secondary vertices using the prompt tracks reconstructed in the tracker (see Section 4.2.1). In the primary vertex reconstruction [57], the measurements of the location and uncertainty of an interaction vertex are computed from a given set of reconstructed tracks. The prompt tracks originating from the primary interaction region are selected based on the transverse impact parameter significance with respect to the beam line, defined as the distance of closest approach to the beam line, number of strip and pixel hits, and the normalized track χ^2. An adaptive vertex fit is performed, where each track in the vertex is assigned a track weight between 0 and 1 based on its compatibility with the common vertex. For a track consistent with the common vertex, its weight is close to 1. The number of degrees of freedom is defined as $n_{dof} = 2\Sigma_{i=1}^{n_T racks} w_i - 3$, where w_i is the weight of the ith track. It is thus strongly correlated to the number of tracks compatible with the primary interaction region. For this reason, the number of degrees of freedom of the vertex can be used to select real proton-proton interactions. The fit considers all reconstructed tracks and iteratively repeat the fit with tracks that were not compatible with the vertices obtained in previous iterations. This procedure is repeated until the list of tracks is exhausted or the vertex fit fails.

4.2.6 b-Tagging

Several algorithms are defined at CMS with the purpose to tag jets stemming from b quarks hadronization, or b-jets. Such jets usually contain B-hadrons which present several characteristics which allow to discriminate between b-jets and jets stemming from light quark hadronization (also referred to as light jets). First of all, the tracks produced by long lived particle decays (such as B-hadrons) are expected to have a non negligible impact

parameter(IP), defined as Section 4.2.5. The IP is invariant with respect to changes of the long lived particle kinetic energy, this is due to the cancellation of the boost effects on the flight path (scaling as $\sim \gamma$) and the average angle of the decay products with respect to the flight direction (scaling as $\sim 1/\gamma$). The typical scale of the IP is the one of the decaying particle $c\tau$; for a B-hadron this corresponds to about $450\mu m$. In CMS the IP can be measured with a precision between $30\mu m$ and few hundreds μm. Given that the uncertainty can be of the same order of magnitude as the IP, a better observable for b-tagging is the impact parameter significance defined as

$$S = \frac{IP}{\sigma_{IP}}.$$
(4.2)

The IP in CMS is "life time signed": tracks orginating from the decay of particles travelling in the same direction of the jet are signed as positive, while those in opposite direction are tagged as negative. This is obtained by using the sign of the scalar product of the IP segment with the jet direction. On the other hand, it is possible to reconstruct the secondary vertices from B hadron decays inside of jets. To do this an adaptive vertex fit is performed (see also Sec. 4.2.5 and Ref. [57]). $b-$jet tagging algorithms can be divided in the following categories:

- *Impact parameter based algorithms*: The first simple way of producing a discriminator based on track impact parameters is an exten- sion of the so-called Track Counting algorithm used in past experiments. The track counting approach identifies a jet as a "b-jet" if there are at least N tracks each with a significance of the impact parameter exceeding S. Currently two algorithms are defined: Track Counting High Purity, for N = 3, and Track Counting High Efficiency, with N = 2. Another way is the one defined in the so-called jet-probability algorithm: it combines the information coming from all selected tracks in the jets instead of using only the first N tracks. A probability to originate from the primary vertex is assigned to each track, and a combination of jet probabilities P_{jet} is defined as a combination of the track probabilities and used as discriminator.

- *Secondary vertices based algorithms*: The first vertex method, called Simple Secondary Vertex, is based upon the reconstruction of at least one secondary vertex, and uses either the 3D distance from the primary vertex as discriminant or its significance. A second method is called Combined Secondary Vertex, where the combination of different jet variables is performed in order to extract the maximum information out of the jets. Several vertex definitions(or categories) are included, and for each definition a different set of probabilities is assigned to the vertex characteristic variables. All variables and vertices categories are combined appropriately to get a single discriminant.

- *Lepton based algorithms*:Algorithms based on the presence of a lepton stemming from the B-hadron decay close to the jet's axis are present for both muons and electrons. the "Soft Muon" tagger takes into account the presence of a GlobalMuon (see Sec 4.2.2) close to the jet's axis and uses as discriminator variable either the $p_{T,rel}$ of the muon with respect to the jet axis ("soft muon by $p_{T,rel}$") or the muon IP significance. the Soft Electron tagger checks the presence of an electron close to the jet's axis and uses as discriminator a Neural Network variable based on the electron IP significance, the electron $p_{T,rel}$ with respect to the jet axis, the ΔR between the electron and the jet, and the ratio between the electron momentum, as reconstructed in the tracker, and the calorimetric jet energy.

- *Combined algorithms*:The reults of algorithms can be combined in a multivariate discriminant called "combined MVA". It takes as input the "Jet Probability", "Combined

Secondary Vertex", "Soft Muon", and "Soft Electron" taggers and returns a single discriminang variable.

Figure 4.2 shows the performances of the different b-tagging algorithms.

4.2.7 Particle Flow

Particle Flow (PF) [60] is the name of an algorithm which aims at reconstruction of all stable particles in an event, i.e., electrons, muons, photons, charged hadrons and neutral hadrons, thorough a combination of CMS sub-detectors. This aims to increase the performances in determination of particles momentum, energy and to get an even more robust identification. While the electrons and muons Particle Flow reconstruction increases, it is generally driven by the resolution of the robust standard algorithms. Jets reconstruction algorithms, however, take great advantage from the fact that particle flow reconstructs the single particles of a jet, allowing to use the list of Particle Flow reconstructed individual particles (as if it came from a Monte Carlo event generator) to build jets. With this algorithm the general jet energy resolution improves and and jet energy scale uncertainties are reduced. Also this PF approach allows a more precise determination of the missing transverse energy $\not{E}_T$ as well as a to reconstruct and identify taus from their decay products, to quantify charged lepton isolation with respect to other particles, to tag b jets, etc. The CMS detector factorized and essential design is well suited for the use of Particle Flow. The particle reconstruction and identification is performed with a combination of the information from each CMS sub-detector, under the form of charged-particle tracks, calorimeter clusters, and muon tracks. These building bricks, or "elements", of the Particle Flow are reconstructed individually, and they include inner tracks, electrons, photons, muons whose description can be found in the previous part of this chapter, charged and neutral hadrons reconstructed through their tracks plus their deposits in the electromagnetic and hadronic calorimeters. Blocks of elements are identified and then altogether used as input in the Particle Flow algorithm. For each block, the algorithm proceeds as follows. First, each global muon gives rise to a "Particle Flow muon", if its combined momentum is compatible with that determined from the sole tracker within three standard deviations. The corresponding track is removed from the block. After muons electron are the next particle to be reconstructed and identificatied. Each track of the block is submitted to a pre-identification stage which exploits the tracker as a pre-shower: electrons tend to give rise to short tracks, and to lose energy by Bremsstrahlung in the tracker layers on their way to the calorimeter. Pre-identified electron tracks are refit with a Gaussian Sum Filter trying to follow their trajectories to the ECAL. A final identification is performed with a combination of a number of tracking and calorimetric variables. Each identified electron gives rise to a "Particle Flow electron". The remaining elements may give rise to charged hadrons, photons or neutral hadrons, and more rarely to additional muons. A track can be directly connected to a number of ECAL and HCAL clusters. The detection of the neutral particles in the block (photons and neutral hadrons) involves a comparison between the momentum of the tracks and the energy detected in the calorimeters (after the latter has been properly calibrated). The process stops either when all tracks with a p_T uncertainty in excess of $1\ GeV/c$ have been examined, or when the removal of a track would render the total track momentum smaller than the calibrated calorimetric energy. Each of the remaining tracks in the block gives rise to a "Particle Flow charged hadron", the momentum and energy of which are taken directly from the track momentum, under the charged pion mass hypothesis. Once Muons, Electrons, Photons are reconstructed, the Particle Flow jets are produced. The jet algorythm of choice (See Section 4.2.4.1) is applied: all particles reconstructed with the Particle Flow algorithm, without distinction of type and without any energy threshold, are clustered into Particle Flow jets. Particle Flow

$\not{E}_T$ is reconstructed at the end of event reconstruction: it consists in forming the transverse momentum-vector sum over all reconstructed particles in the event and then taking the opposite of this azimuthal, momentum two-vector. The missing transverse energy is the modulus of this vector.

Figure 4.3 shows a comparison between CaloJets, JPT, and PF jets resolution.

Figure 4.4 shows a comparison between resolutions on Particle Flow missing energy ("PFMET"), calorimetric only missing energy ("CaloMET") and Calorimetric Missing energy corrected by the tracks momentum ("TCMET").
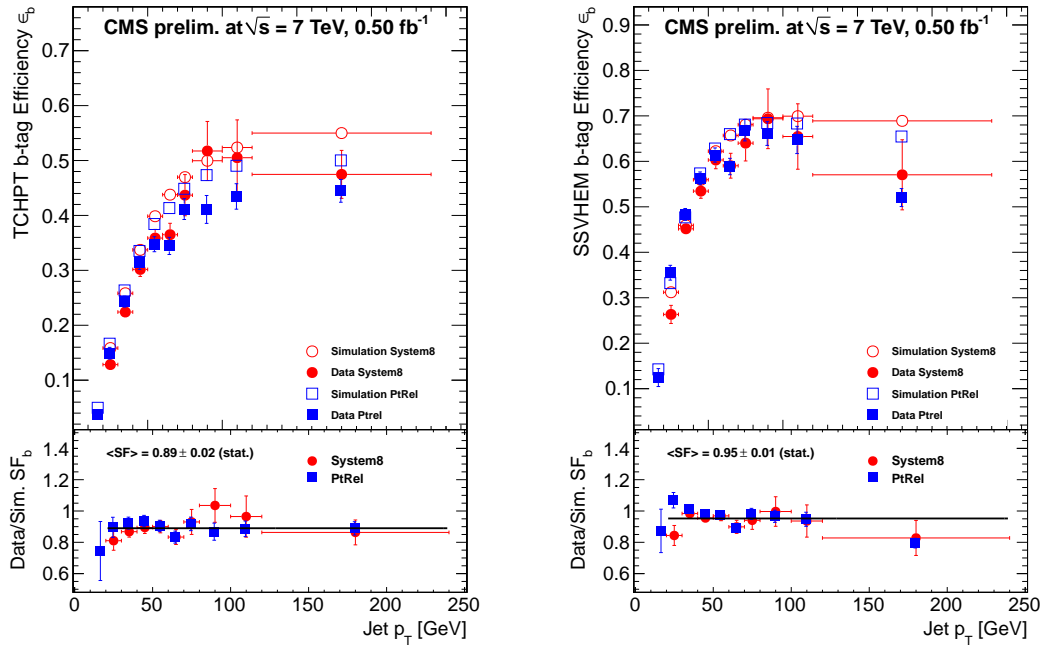
(a)

(b)
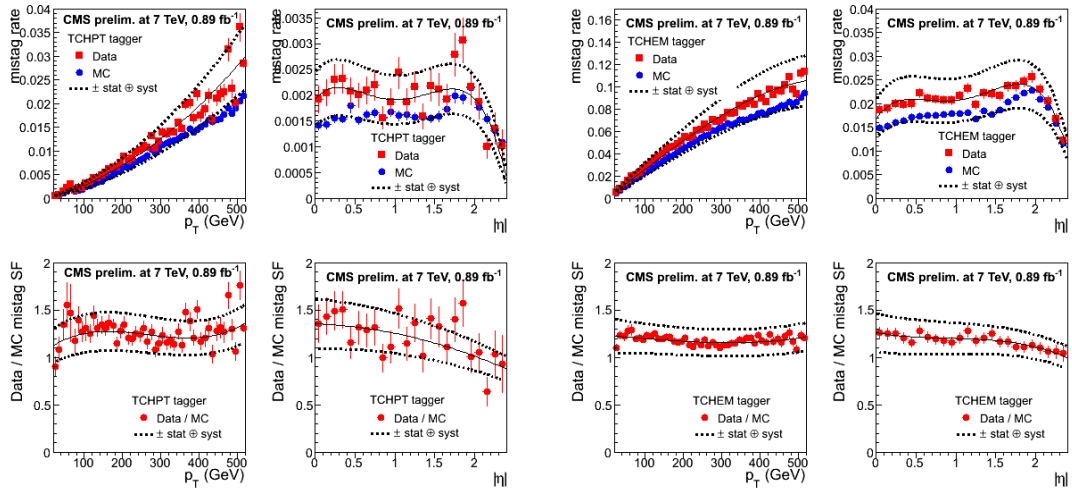
(c)

(d)

Figure 4.2: b-jet tagging efficiency and light jet mis-tagging efficiency for two widely used algorithms: Track Counting High Purity ($N_{tracks} = 3$) with tight threshold of 3.41 on the discriminator, and Simple Secondary Vertex High Efficiency with a middle threshold of 3.3 on the discriminator. TCHPT(SSVHEM) efficiency: a(b). TCHPT(SSVHEM) mistag: c(d) set of plots

.
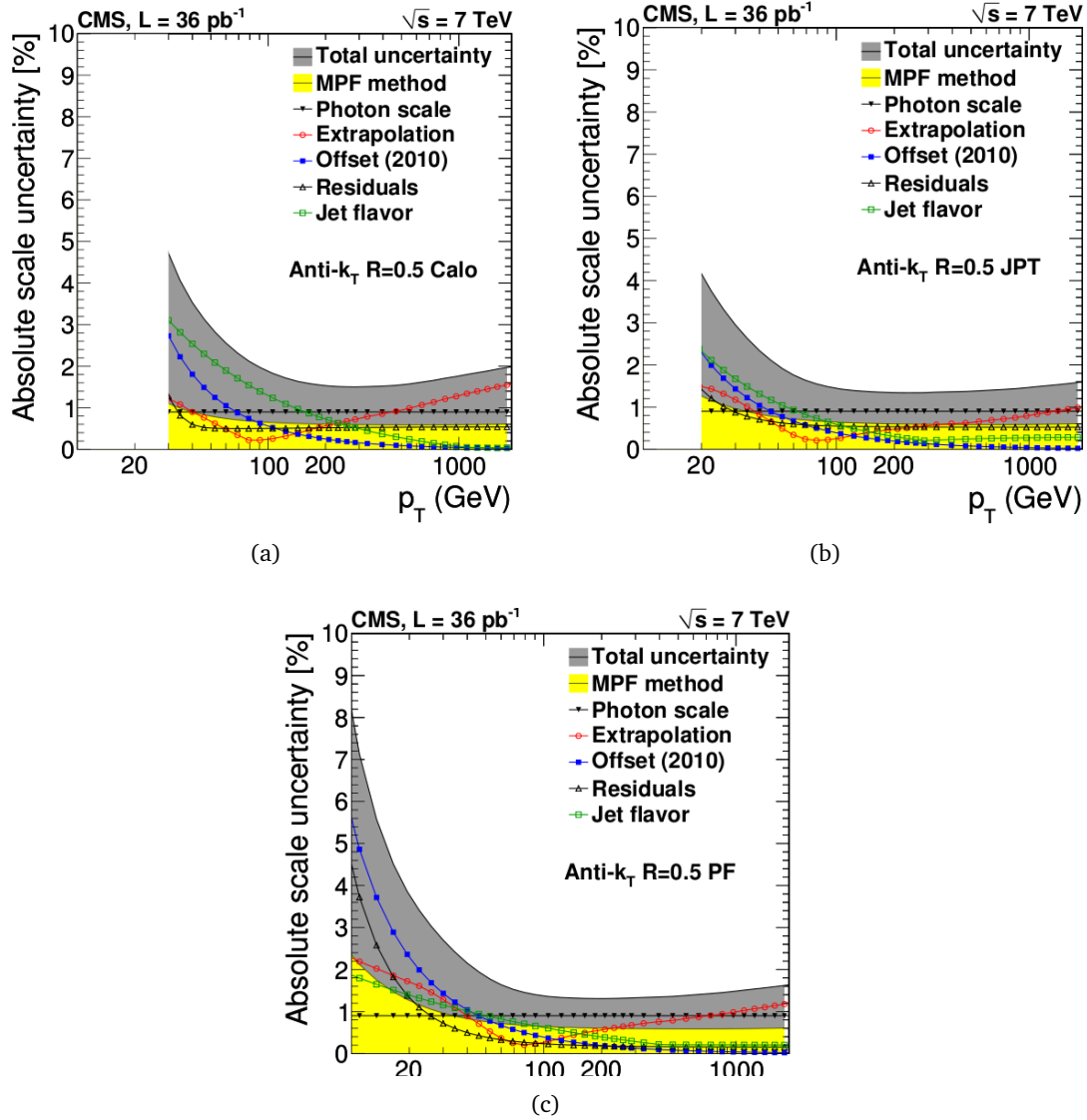
Figure 4.3: Absolute jet energy scale uncertainty as a function of jet p_T for Calo, JPT and PF jets respectively, measured with CMS 2010 data

.
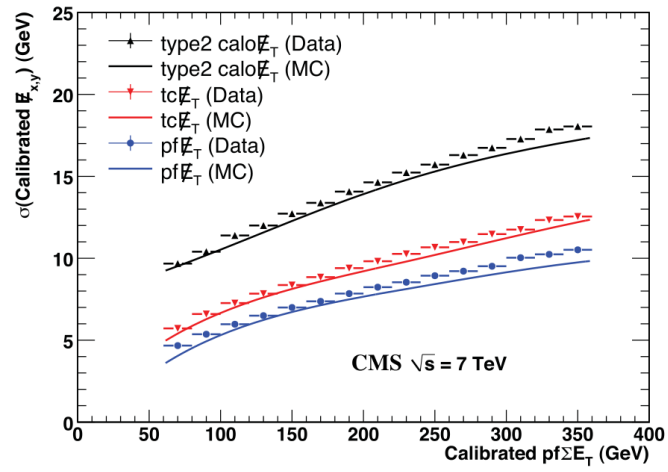
Figure 4.4: Calibrated $\not{E}_T$ resolution versus calibrated $\not{E}_T$ for Calo $\not{E}_T$, TC $\not{E}_T$, and PF $\not{E}_T$ in data and in simulation.

.

Chapter 5

The Resistive Plate Chambers detector and the Level-1 trigger

Muons play a crucial role in both precision measurements of the standard model and in searches for the Higgs boson and for new physics. They are the objects with the cleanest signature in the detector: high p_T muons can penetrate through the CMS ECAL and HCAL losing a little fraction of their energy and therefore can be detected in the Muon System located outside the CMS magnet. As described in Sec.3.2.2, the return yoke allows to have a roughly constant magnetic field outside the CMS Solenoid, with an intensity of 1.8 Tesla and opposite verse with respect to the inner field. In this chapter I describe the workings of the RPC detector, the Level-1 RPC trigger system and the studies performed as part of this thesis work.

5.1   The working principle of the RPCs

Resistive Plate Chambers (RPC) are charged particles gas detectors. The working idea is the same as all gas detectors: a incident charged particle on the detector causes ionization of the gas molecules in the active volume of the detector. Electrons stemming from ionization will be accelerated through an electrical field and will cause ionization of other gas particles themselves. Photons emitted in the ionization can also generate new avalanches themselves. Depending on the applied voltage, different regimes of the amplification can be distinguished (See Fig. 5.1).

RPCs are characterized by a plane geometry, which generally ensures a good time resolution, with two flat resistive electrodes which allow the generation of a continuous electrical field in between. Electrodes are usually made from phenolic resins, like bakelite, and are coated with a conductive substance like graphite. The gas is located in the gap between the electrodes and usually contains a mixture of a strongly electronegative gas to allow a good rate of primary and secondary ionizations, and a second "quenching" gas which has a good UV photons absorbing properties, in order to prevent the formation of secondary avalanches due to photons produced in the ionizations.

Usually, the charge is collected through strips on the graphite coating.

A sketch of a generic RPC detector can be found in figure 5.2

Usually RPCs are kept in streamer mode, with a gain (ratio between the charge produced in the avalanche and the primary ionization charge) $> 10^8$. However, since RPCs in this configuration can sustain an incident flux of about 100 Hz/cm^2, streamer mode is not suitable for the LHC scenario. Therefore RPCs at LHC work in the so called avalanche mode, where streamers are not produced as long as the gain stays $\lesssim 10^8$. In this mode, rates of kHz can be sustained. Considering a generic RPC in this mode, the charge developed in
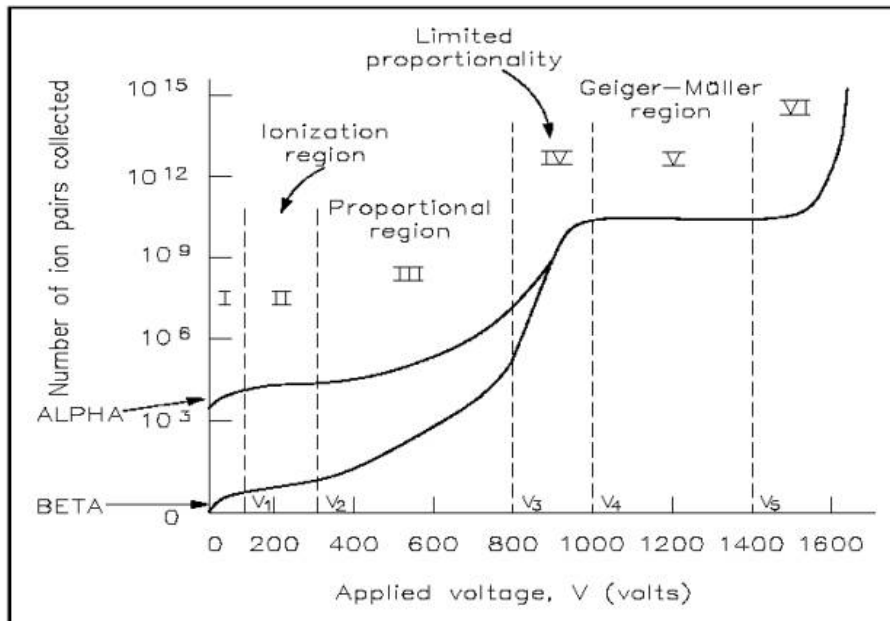
Figure 5.1: Gas ionization curves: the number of electron-ion pairs collected when a charged particle traverses a gaseous counter of average size, plotted against the voltage applied between two electrodes. The curves are for α-particles (He nuclei) and β-particles (electrons). Regions: (I, Recombination) Electron-ion recombine before causing new ionization ;(II, Ionization chamber) Amplification is constant in this region; (III, Proportionality)Charge produced is proportional to the voltage in this region. (IV, Limited proportionality)For amplification greater than 10^8, avalanche degenerates to a streamer (ion-electron plasma); (V, Geiger-Muller) Streamers eventually connect the electrodes. (VI, Continuous discharge) Secondary avalanches produced by photons keep the detector in a continuous discharge status.
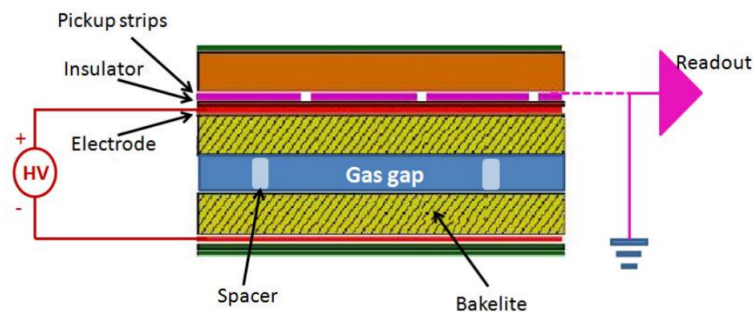
Figure 5.2: Sketch of an RPC detector

the avalanche as a funnction can be written as:

$$q_e = q_{ele} \sum_{j=0}^{n_{cl}} n_{0j} F_j e^{\eta(x-x_{0j})} \tag{5.1}$$

where the sum is performed over the total number of clusters produced in the interaction, $q_e le$ is the charge of the electron, n_{0j} is the initial number of ion-electron pairs produced in the j-th cluster, x_{0j} is the point where the first ionization occurred, x is the distance covered by the shower, η is the effective ionizing coefficient, and F_j is a probability distribution to weight the total number of electrons at a given point. The current generated can therefore be evaluated as

$$i(t) = q_e E_w v_d \tag{5.2}$$

where q_e comes from Eq. 5.1, v_d is the drift velocity which depends on the electromagnetic field, the pressure of the gas and a characteristic parameter of the gas through the relation $v_d = \mu\mathbf{E}/P$, and E_w is the normalized weighted electromagnetic field, which can be simply calculated as:

$$E_w = k/d = \frac{C_b}{C_b + C_g} \cdot \frac{1}{d} = \frac{\epsilon_r \frac{d}{s}}{\epsilon_r \frac{d}{s} + 2} \cdot \frac{1}{d} \tag{5.3}$$

Where C_b and C_g are the capacitors of the bakelite and the gas respectively, S is the RPC surface, d is the width of the gap and ϵ_r is the relative dielectric constant of the gas.

5.1.1 RPCs at CMS

CMS RPCs are made by parallel resistive plates of bakelite treated with linseed oil as electrodes. The plates are separated by a gas gap of 2 mm, mounted in a rigid plastic frame and separated by spacers made of Poly-Vinyl Chloride. CMS RPCs use a double-gap configuration, shown in figure 5.3. Two single gaps are mechanically coupled and signals
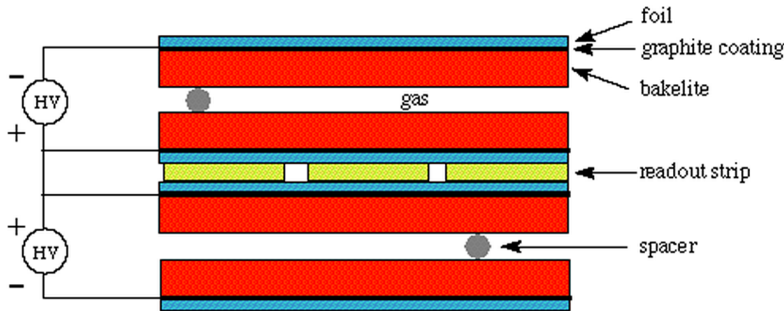
Figure 5.3: Sketch of CMS double-gap RPCs

are extracted from a plane of strips located in the middle. This allows to operate each single gap at lower gas gain with exploiting the OR of the two gaps to increase the efficiency It also maximizes the induced signal which is the analogue sum of the two independent signals developed in each chamber. Figure 5.4 shows the behavior of the RPC efficiency as a function of the voltage applied.
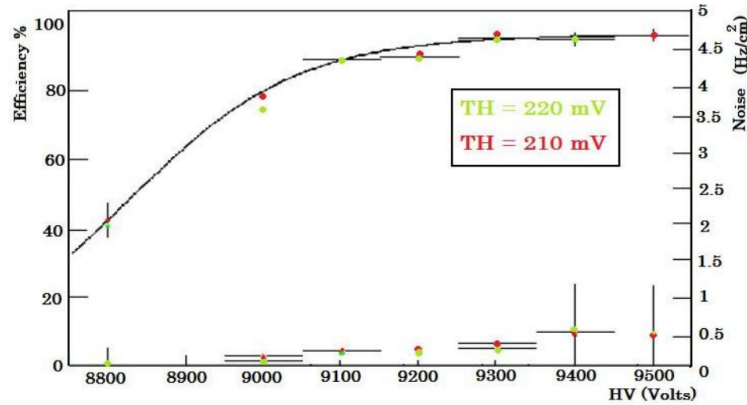
Figure 5.4: High voltage (HV) and threshold (TH) scan for a specific RPC roll during 2009 cosmic ray data taking. In this case, plateau is reached at 9.3 kV. Noise rates are also shown.

5.2 The RPC Level-1 trigger at CMS

From the point of view of the L1 trigger, the RPC system volume is logically partitioned into sections. L1 trigger candidates are searched for independently in each section. Sections in the η view are referred as *towers*, and for each tower the partitions in the r-ϕ view will are referred as *cones*.

5.2.1 Layout of the Barrel RPC system

As described in chapter 3, and shortly repeated here for convenience, the Barrel Muon System is composed of 5 Wheels along the z direction, named W−2, W−1, W0 (the central one), W+1, W+2. Each wheel is divided into twelve sectors (with approximately dodecagonal geometry in the r-ϕ view), from sector S01 to sector S12. For each sector there are 4 DT stations, inserted in the iron gaps of the Barrel Yoke, from MB1 (the inner one) to MB4 (the outer one).

The RPC stations are mounted on one or both sides of the DT stations. Station MB1 is provided with RPC stations on bottom and top sides (RB1In and RB1Out stations), same for MB2 (RB2In and RB2Out stations). Stations MB3 and MB4 are provided with RPC stations on the bottom side only (RB3 and RB4 stations). With this design, a total of six concentric RPC layers are available in the Barrel Muon System. The inner layers can provide up to four coordinate measurements also for low momentum tracks crossing only MB1 and MB2 stations.

For each RPC station, pick-up strips running parallel to the beam axis provide coordinate measurement in the r-ϕ view, thus allowing p_T measurement of the track. Segmentation in the η view is obtained by sectioning a plane of strips in two or three parts. The η partitions are called *rolls*. An RPC station can be segmented into two rolls (named Backward and Forward) or three rolls (named Backward, Middle, and Forward). RPC stations 3 and 4 present also a segmentation along ϕ in two partitions (named + and -). RPC Station 4 sector 4 is segmented in 4 ϕ partitions.

5.2.2 Trigger towers and trigger cones

The definition of the η boundaries of towers (see Fig. 5.5) is based on a set of reference layers. In the Barrel, the reference layers are: layer RB2In for W+1, W0, and W−1, and layer RB2Out for W−2 and W+2.
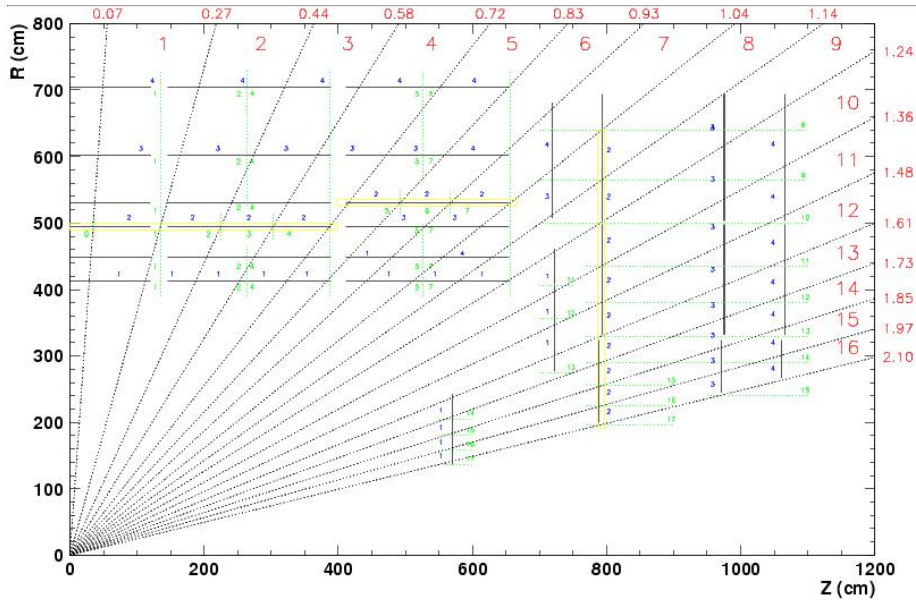
Figure 5.5: Trigger eta towers.

Each tower must contain only one entire roll of a reference layer. On the other hand, a roll of a non-reference layer can belong to adjacent towers, thus in this case the association of roll to towers is not univocally defined. The RPC trigger logic has a total of 17 towers. A total of 5+5+1 towers are entirely contained in the Barrel.

On the reference layers, the strips are grouped in non-overlapping sets of 8 adjacent strips called *segments*. Each segment subtends a ϕ angle of $2.5°$, for a total of 144 segments (12 segments for each sector). Each cone must contain only one segment of a reference layer. On the other hand, in non-reference layers a larger number of strips is grouped into a segment, so that a segment covers more than $2.5°$ in those layers. Thus adjacent segments overlap in the non-reference layers and the association of a strip to those segments is not univocally defined.

5.2.3   The L1 PACT logic

The PAttern COmparator Trigger (PACT) logic collects RPC hits from all stations and searches for spatial and time coincidences independently in each cone. The η and ϕ coordinate of the trigger objects are assigned on the reference station. By comparison with predefinite patterns of hits, also a p_T value is assigned to the candidate trigger object.

Due to the overlap of adjacent cones, *ghost* trigger objects in a certain η tower can appear. Ghosts can also appear in adjacent towers due to the sharing of the rolls in non-reference stations. For this reason, trigger candidates are processed by a proper ghost identification and removal logic, and the remaining ones are sorted according to quality criteria. More details can be found in Ref. [49].

Finally, the 4 highest p_T muons from the Barrel and the 4 highest p_T muons from the Endcap are sent to the Global Muon Trigger.

5.2.4   Cosmic patterns in PACT

In order to increase the trigger efficiency for cosmic muons, which are not constrained to come from the interaction vertex, a looser pattern definition has been adopted with respect to collision runs. A cosmic pattern is defined as a time coincidence of hits on at least 3

different RPC stations in a cone (3/6 majority). No different patterns as a function of p_T are defined, thus the system is not able to assign a p_T value to the track.

5.3   RPC level-1 trigger fficiency studies with cosmic ray data

The whole CMS detector has undergone a commissioning during the cosmic ray data taking of 2008 and 2009. In particular the Muon System detectors including the RPC and the relative triggers systems [3], [61] could be commissioned with cosmic ray muons, so that performances of the chambers as well as of the Level-1 trigger system could be measured in an almost background free condition with respect to the LHC environment. This effort allowed to understand many fundamental aspects of the detector behavior. As part of the work of this thesis, we present the study which was performed on cosmic ray data in 2008 and 2009, which allowed to understand the general behavior of RPC L1 trigger system, ultimately measuring its efficiency as function of p_T, η, and ϕ. In this section we describe the method used for trigger efficiency measurements and the observed performances on cosmic ray data taken by CMS. Cosmic ray data were taken through 2008 and 2009 in both configurations with and without nominal magnetic field being active. All runs taken with 3.8 Tesla nominal field are indicated under the acronym CRAFT08(09) standing for Cosmic Runs At Four Tesla 2008(09).

5.3.1   Analysis method

We start from a sample of reconstructed tracks in the Muon System which are matched to a DT trigger object. In this way we reject fakes and define a sample of muons tracks that have not been triggered exclusively by RPCs.

If the number of tracks in the sample is N_{match}^{DT}, and under the assumption that RPC and DT triggers are uncorrelated, the RPC trigger efficiency ϵ_{L1}^{RPC} is given by the fraction of tracks in the sample that are matched also to an RPC trigger object:

$$\epsilon_{L1}^{RPC} = N_{match}^{RPC\&DT}/N_{match}^{DT} \ . \tag{5.4}$$

5.3.2   Tracks selection

For the analysis we use a collection of tracks reconstructed in the Muon System only, also referred to as CosmicMuons, from the name of the collection in the CMS framework. The two legs of a muon which traverses the Tracker System are reconstructed as two separate CosmicMuon tracks. In order to prevent an eventual bias due to tracks that would not have been reconstructed without RPC hits, we re-run the reconstruction using DT only.

We select cosmic tracks pointing to the p-p interaction region by requiring that the track passes through a cylinder centered in the interaction point, with the height parallel to the z axis $h = 260cm$ and a radius $r = 90cm$. In addition, we apply the following cuts:

- p_T at the innermost point $> 5GeV/c$

- N_{hits} in the DT > 20;

- χ^2 of the track fit < 20.

The p_T cut removes tracks which are bending in the transverse plane due to the magnetic field. The last two cuts ensure good quality of the DT reconstruction and prevent an eventual bias due to tracks that would not have been triggered without RPC hits. Figures 5.6 and 5.7 show the distributions of these variables for typical pointing CosmicMuon tracks.
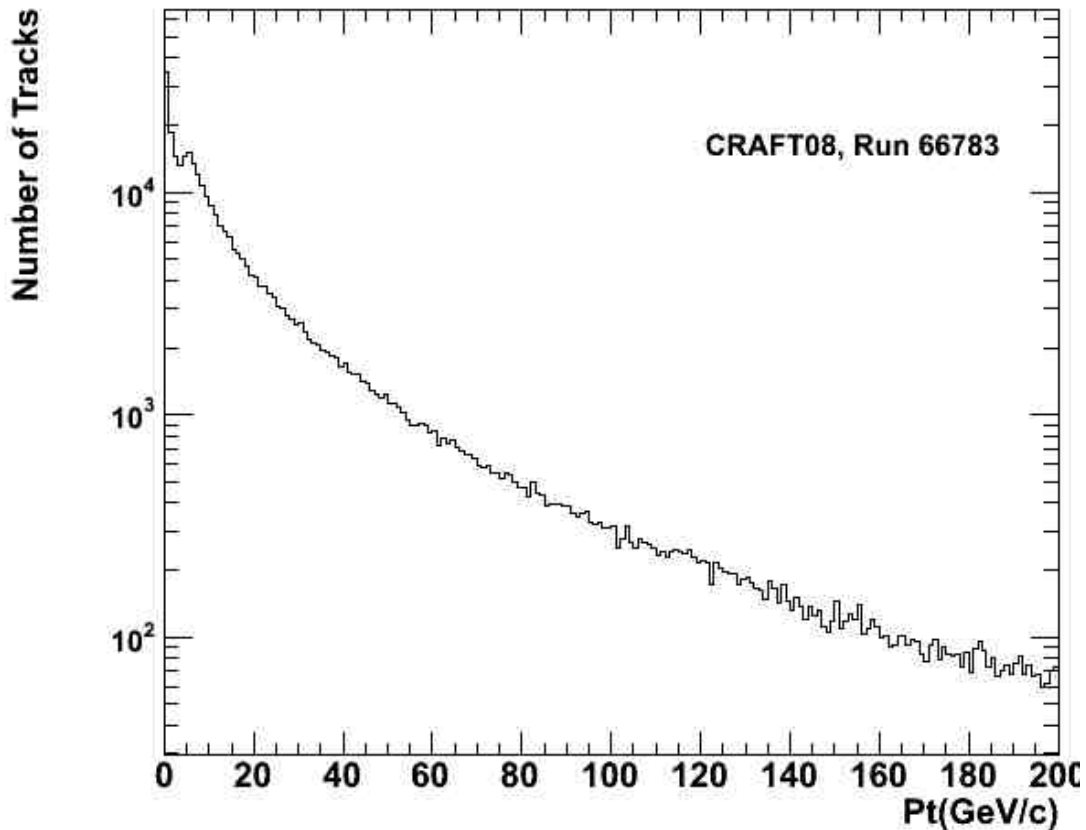
Figure 5.6: Distribution of the p_T of the cosmic muon tracks (CRAFT08, Run 66783).
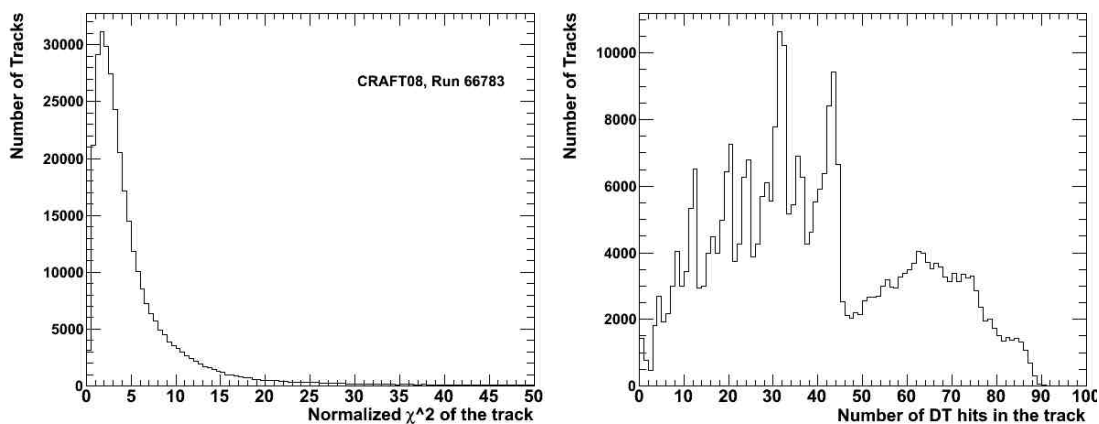
Figure 5.7: Distribution of the normalized χ^2 (left) and number of DT hits (right) of the cosmic muon tracks. The tracks with < 5 hits are reconstructed through the CSCs chambers. The structures in the number of track hits around $n = 12, 24, 36, 44$ are related to the way the seeding is performed for the selected tracks: in general two DT/CSC local reconstructed segments are required or one DT/CSC segment plus one RPC hit. Thi makes it more likely to start the seeding when one or more well reconstructed segments are present. All distributions are taken before the cuts were applied (CRAFT08, Run 66783) and on inclusive tracks reconstructed with all detectors.

5.3.3   Track matching with trigger objects

The position in $\eta - \phi$ of the L1 trigger for both DTs and RPCs is defined on the reference layer. The RPC reference layers have been described in Sec. 5.2.2. The DT reference layer is Station 2 of each wheel. Thus, in order to match the track to a DT trigger candidate, the track is extrapolated to MB2. The extrapolation is done by taking the last point of the track and propagating backwards to the reference layer.taking into account the magnetic field, the energy loss in the detector material and the multiple scattering.The track-trigger matching is performed in the ϕ coordinate only, which is the most accurate coordinate measured by both DT and RPC trigger systems. It was not possible to use a matching in η with the L1 DT trigger candidates since the η part of the algorithm was not commissioned yet during CRAFT08 data taking and most of CRAFT09 data taking. The ϕ distributions for DT and RPC trigger objects are shown in Fig. 5.8.
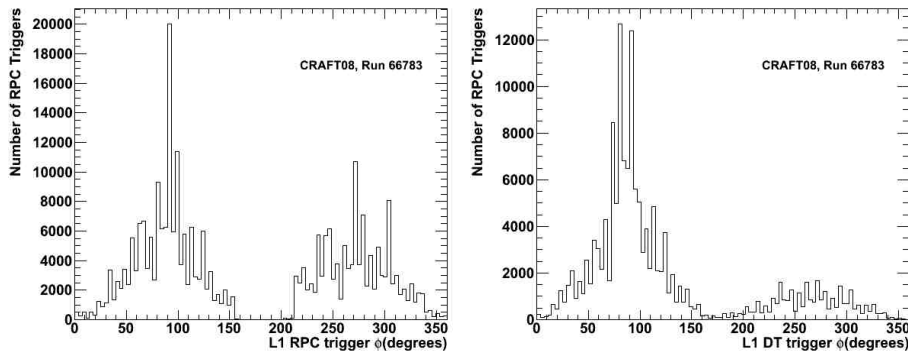
Figure 5.8: Phi distribution of the RPC (left) and DT (right) triggers (CRAFT08, Run 66783).

The matching requirement is $|\Delta\phi_{t-DT}| < 30°$, where $\Delta\phi_{t-DT}$ is the difference between the ϕ of the track at the reference layer and the ϕ of the DT trigger. This loose requirement provides a high matching efficiency.

If a match with a DT trigger is found, a RPC trigger that matches the track is looked for. Figure 5.9 shows the overall $\Delta\phi_{t-RPC}$ as measured using both cosmic patterns and collision patterns (the last one obtained by running the trigger emulator). The second peak at $\Delta\phi_{t-RPC} \approx -0.06$ for the residuals distribution of cosmics patterns is due to the fact that the cosmics pattern configuration cannot identify the p_T of the track. In case of two candidates with the same quality then the one with the smaller ϕ is selected.

The matching requirement is $|\Delta\phi_{SA-RPC}| < 30°$, where $\Delta\phi_{sA-RPC}$ is the difference between the ϕ of the track at the reference layer and the ϕ of the RPC trigger.

5.3.4   Data samples

Only cosmic tracks which mimic muons from collisions have been considered for this study. In order to be suitable for trigger studies, the runs taken from CRAFT08 and CRAFT09 datasets needed to have satisfactory statistics and stable data taking conditions. Also the analysis required DT chambers to be active in that particular run. From the point of view of the Event Data Model (see Section 4.1), an hybrid RAW-RECO format is used which stores all the necessary information for the L1 Trigger analysis and the basic reconstructed objects like tracks, muons, and electrons.

We have filtered the events at the analysis level by applying a requirement for "pointing" CosmicMuons, meaning CosmicMuons passing through the volume of the CMS inner Tracker. This latter requirement consistently reduces the number of muon tracks available
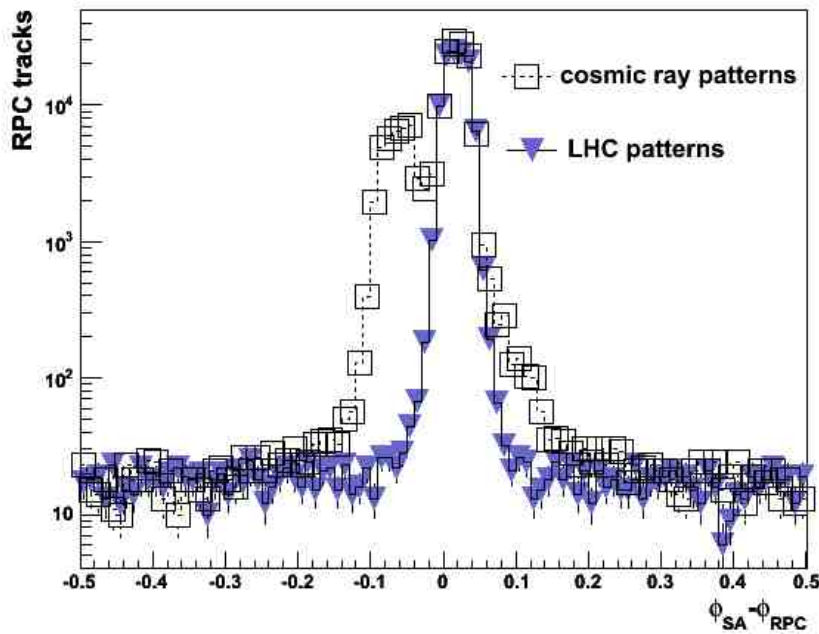
Figure 5.9: adada

in the runs for trigger analysis, but is necessary: muons from cosmic ray data do not have the cylindrical symmetry around the LHC axis collision muons have. This results in a source of inefficiency for the RPC trigger on cosmic muons which is due to the built-in geometry of the RPC trigger system towers and cones, which is explicitly thought and optimized for muons coming from the interaction points. Table 5.1 reports the longest runs analyzed, the average trigger efficiency and the HV working point.

Dataset	Run	RPC HV	Average Barrel RPC eff.
CRAFT08	66783	9.2 kV	82.41%
CRAFT09	110409	9.4 kV	92.05%
CRAFT09	110419	9.4 kV	91.67%

Table 5.1: Analyzed runs from CRAFT08 and CRAFT09 datasets. HV value and average efficiency for the barrel RPCs are also reported.

5.3.5 RPC trigger efficiency on cosmic ray data

We study the trigger efficiency with respect to the p_T of the track and with respect to the position of the track on the reference layer.

5.3.5.1 Results for CRAFT08

Figures 5.10 (a,b),show the RPC trigger efficiency in the Barrel as a function of the $\eta - \phi$ of the track on the reference layer, for the top and bottom part of the detector respectively for one particular run of CRAFT08. Note that sectors 1 and 7 are splitted in half through the two plots, since sector 1 covers the ϕ region from $-15°$ to $15°$.
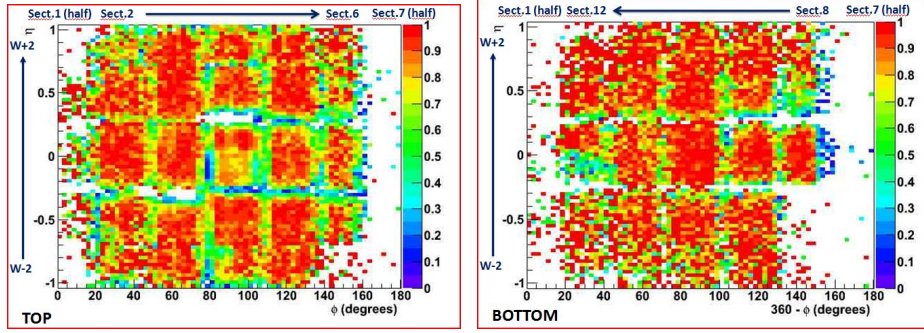
Figure 5.10: RPC trigger efficiency in CRAFT08 as a function of η and ϕ for tracks in top(a) and bottom (b) part of the Barrel detector ($0° < \phi < 180°$). The η and ϕ coordinates are extrapolated to the reference layer. The wheels (sectors) corresponding to different η-ϕ regions are labelled on the left (top) part of the plot.

The efficiency of the trigger drops in the regions of separation between two adjacent sectors or wheels, and in particular it is evident the effect of having shorter chambers in W+1_Sect.4 and W-1_Sect.3 due to chimneys.

There are some less populated regions. This is due to several reasons: cosmic particles distribution which disfavours vertical sectors (sectors 1 and 7), hardware/trigger problems in CRAFT08 such as DT triggers OFF (W-2_Sect.6), masked RPC channels (sectors 6, 7, 8, W-2_Sect.9, W-1_Sect.9). Note also that the loose trigger matching condition of $30°$ gives some statistics in these regions when the RPC/DT trigger object is found in an adjacent sector.

It is also worth to note that in W0_Sect.4 the RB3 layer had low detection efficiency in several runs of CRAFT08 (due to a readout problem), and this reflects in a lower trigger efficiency than other sectors.

In order to determine the trigger efficiency vs. p_T, we introduce geometrical cuts selecting only cosmic tracks in the central regions of the rolls and sectors. Indeed, in the border regions DT and RPC triggers are affected by common inefficiencies due to geometry, which introduces correlations between the two systems. The choice of the fiducial cuts is shown in Table 5.2. Such choice is performed in order to remove inefficiencies due to tracks passing in the cracks between the detectors, which eventually causes the loss of some hits. Moreover, this requirement further increases the number of LHC-like cosmic muons passing close to the interaction point.

$|\phi - \phi_{center}| < 5°$	
$|z| < 100 \, or \, 200 < |z| < 300 \, or \, 450 < |z| < 550$	

Table 5.2: Volume cuts applied to select tracks in the center of the rolls and sectors. ϕ_{center} is the value of ϕ at the center of the sector.

5.3.5.2 Comparison with Tag and Probe method

We have compared the CRAFT08 trigger efficiency measured with the DT vs. RPC method with the efficiency measurement based on the Tag and Probe method ([3]). The comparison was made between the efficiencies measured in the top part of the detector, since in the Tag and Probe technique tracks in the bottom part were used for the tagging. The comparison is shown in Table 5.3.

Tag & Probe	88.02 ± 0.22
DT vs RPC	87.93 ± 0.38

Table 5.3: Overall RPC trigger efficiency in the top part of the Barrel evaluated with the Tag Probe and DT vs. RPC methods.

5.3.5.3 Results for CRAFT09

Figures 5.11 (a,b) show the trigger efficiency in bins of $\eta - \phi$ of the track, extrapolated to the reference layer.
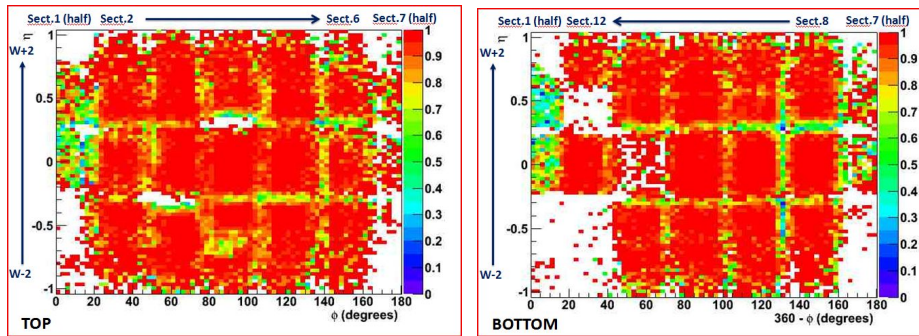
Figure 5.11: RPC trigger efficiency in CRAFT09 as a function of η and ϕ for tracks in the top (a) and bottom (b) part of the Barrel detector ($0° < \phi < 180°$). The η and ϕ coordinates are extrapolated to the reference layer. The wheels (sectors) corresponding to different η-ϕ regions are labelled on the left (top) part of the plot.

In CRAFT09 runs, following up the performance studies on 2008 cosmics data, all the RPCs are in readout and with higher average efficiencies. This reflects in a general improvement of performances. The less populated regions in the plot are related to missing DT trigger matches in those regions.

Figure 5.12 shows the efficiency vs. p_T for cosmics tracks in the fiducial region defined by Table 5.2. The efficiency plateau is reached at around $p_T > 20 GeV/c$ at a value $\epsilon_{09} = 98.01 \pm 0.08\%$.

5.3.5.4 Comparison of CRAFT08 vs. CRAFT09 performances

The results shown in the previous sections show a differece of about 9% between the plateau efficiencies ϵ_{08} and ϵ_{09}. At the same time, as seen from Table 5.1, also the average Barrel RPCs efficiency increases from 82.41% in CRAFT08 to 92.05% in CRAFT09, thanks to the HV increase from 9.2 to 9.4 kV and to the fixing of many problems during the commissioning effort in CRAFT08 (see also [3]).

For a sistematic study of the dependancy of the trigger efficiency from the efficiency of the chambers the detailed geometry of the cones has to be taken into account.
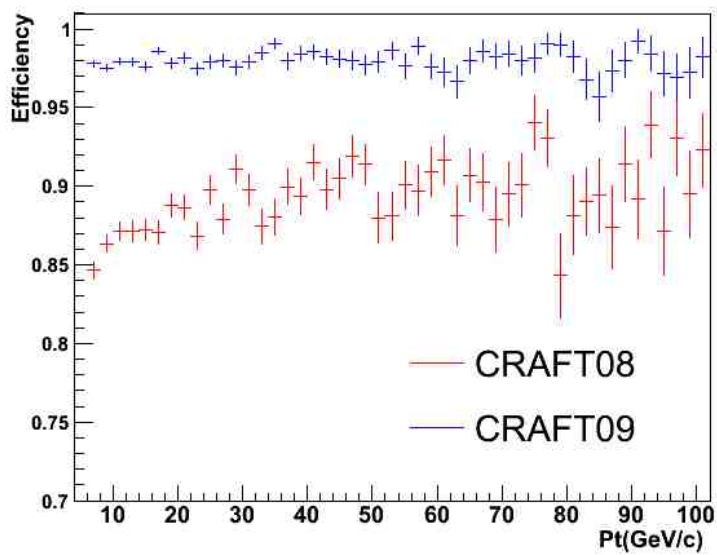
Figure 5.12: Trigger efficiency vs. p_T of the tracks. The efficiency in CRAFT08 is also shown for comparison.

Chapter 6

The physics program at the Large Hadron Collider

Section 2.1 has shown how the standard model gives satisfactory answers to many questions about the electroweak and strong interactions. Nevertheless, it also appears evident how several problems are left unsolved, and of them cannot be faced staying within the boundaries of the standard model (see also 2.6). The physics program at the LHC, and in particular at the CMS and ATLAS experiments, is meant to give insight on all the crucial issues of the particle physics at the TeV scale. Those so called general purpose experiments are therefore designed to probe the TeV energy scale in several directions:

- First of all, as we have previously shown, without the higgs boson the standard model alone cannot introduce a mass term in the lagrangian. Other scenarios are of course possible, but they imply the presence of physics beyond the standard model. The search for the higgs boson therefore is a high-priority objective for the experiments at the LHC.

- On the other hand, the standard model approximations are supposed to break up around the TeV scale, so standard model measurements at the LHC are crucial to spot evidences of new physics. Hint of new particles or of new interactions could reside in the top quark sector, which is by all theoretical expectations the most likely to be influenced from new physics phenomena and where the LHC measurements precision is soon going to surpass, wherever it has not already happened, the precision achieved at Tevatron.

- Besides the search for new physics, standard model precision measurements, challenging the accuracy of theoretical predictions, are possible at the LHC, allowing to gain greater insight on the model itself. Some examples are the universality of the lepton decay, where the LHC yields the greatest precision ever achieved, the $t\bar{t}$ production cross section, where the CMS and ATLAS experiments precision is starting to challenge the accuracy of the predictions, or and top quark mass measurements, where the measurements at Tevatron have been already outperformed. Finally, any model which is supposed to address the issues of the standard model can be probed with the LHC looking for direct evidences of beyond standard model processes. Usually those processes manifest through a peculiar topology that can be exploited to discriminate them from the standard model background.

On the day 27th October 2011, the LHC has successfully concluded the proton-proton collisions data taking for 2011. Since the beginning of circulating 7 TeV beams in march 2010, it has delievered $47.03\ pb^{-1}$ of integrated luminosity in 2010 and $5.73\ fb^{-1}$ 2011, of which $43.17\ pb^{-1}$ and $5.22\ fb^{-1}$ were collected by the CMS experiment in 2010 and 2011

respectively. Thanks to the extraordinary performance of both the accelerator and detectors it was possible to carry on the physics program, which has already successfully achieved the observation at LHC of many standard model particles, progressing up to the determination of exclusion limits on many beyond standard model processes as well as on the standard model higgs boson. This chapter gives a summary of the physics program at the Large Hadron Collider, discusses the measurements already performed with a particular attention to the top quark sector. The final part of the chapter is specifically dedicated to the physics of single top, reviewing the measurements at the Tevatron and phenomenology of single top processes at LHC.

6.1 Standard model physics

The physics program for Standard Model measurements at the LHC is very rich, covering a huge phase space which allows to study QCD processes, J/Ψ production W/Z bosons production, and so on up to the top quark pyhsics and the search for the standard model Higgs boson. There are standard model measurements who serve different purposes: in the first place there are processes which are crucial for all experiments in order to validate the reconstruction algorithms, to understand the behavior of the detectors and the MC simulations. On the other hand there are precision measurements which are either competitive with the accuracy of the SM predictions at the TeV scale or crucial to probe physical quantities which are particularly sensitive to new physics. The cross sections for standard model processes are reported in table 6.1.

The cross sections as a function of center of mass energy are displayed in figure 6.1. The increase of the production cross section for many processes allows for a much higher production rate at the LHC with respect for to Tevatron.

6.1.1 B physics at the LHC

CP-violation is one of the outstanding questions in particle physics. It was first discovered and established in the kaon system. The LEP experiments and CDF have performed many studies of the B-system, but only in the year 2001, with the advent of the SLAC and KEK B-factories, the first significant observation of CP-violation in B-decays has been obtained. The BaBar [28] and Belle [29] experiments, operating at the SLAC and KEKB/KEK e^+e^- machines, respectively, have unambiguously established the non-vanishing value of $\sin 2\beta$, one of the angles of the CKM unitarity triangle (present world average: $\sin 2\beta = 0.736 \pm 0.049$). The most intriguing issue in this field, relevant to both particle physics and cosmology, is that the above experimental measurements confirm, within their uncertainties,

Process	$\sigma_{pp}(7TeV)(pb)$	LHC: $\sigma_{pp}(14TeV)(pb)$	$\sigma_{p\bar{p}}(1.96TeV)\ (pb)$
total cross section	$92 \cdot 10^9$	$100 \cdot 10^9$	$80 \cdot 10^9$
$W\ (\to l\nu)$	$3.1 \cdot 10^4$	$6.8 \cdot 10^4$	$10.8 \cdot 10^3$
Z	$3.05 \cdot 10^3$	$6.6 \cdot 10^3$	
$t\bar{t}$	163	852	7.08
single top, $t-$channel	64.57	246	2.3
single top, $tW-$channel	15.7	66	0.28
single top, $s-$channel	4.6	11	1.08
Higgs, $m_h = 120$	16.6	53	

Table 6.1: Cross sections of some standard model processes at the LHC and at other detectors.
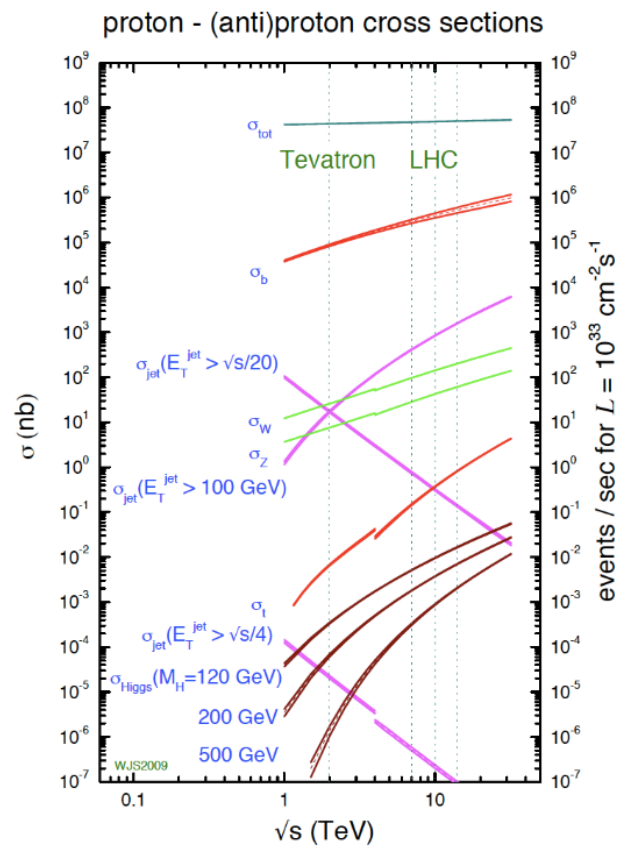
Figure 6.1: Cross sections of some of the main processes at the LHC as a function of the center-of-mass energy

the CP-violation predicted by the Standard Model, which is a consequence of the quark mass generation and of a phase in the quark-mixing CKM matrix. The problem is that this amount of CP-violation is insufficient to explain baryogenesis and the ensuing matter-antimatter asymmetry in the universe, which calls for additional contributions from new physics. The task of present and future B-physics experiments is therefore to clarify this puzzle, by performing precise, comprehensive, and redundant studies of CP-violating effects in the B-system, which should test the internal coherence of the Standard Model (and disclose possible inconsistencies), shed some light on the origin of CP-violation, and probe the existence of new physics. In the field of b-physics, LHC benefits from a very large bb production cross section. The main interest is the study of the neutral B meson, and in particular of CP violation in the systems. The LHC had great benefit from the high production cross section of $b\bar{b}$ pairs, which allowed early measurements already with the first data of 2010, for example decay channels like $pp \rightarrow b\bar{b} \rightarrow \mu\mu\Upsilon$. Figures 6.2 and 6.3 show the measurement of the total and differential in rapidity cross section for J/Ψ and Υ production at the LHC, which shows a good agreement with the standard model predictions.
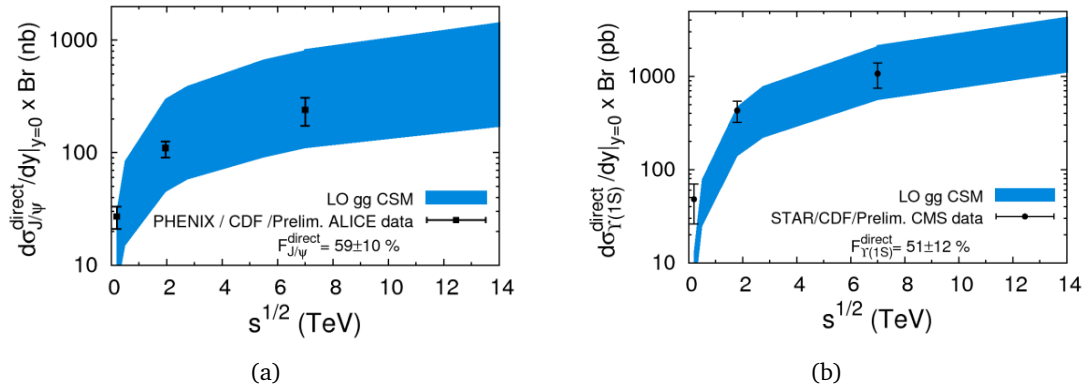
Figure 6.2: $d\sigma^{direct}_{J/\psi}/dy|_{y=0}$ (a) and $d\sigma^{direct}_{\Upsilon}/dy|_{y=0}$ (b) from gg fusion in pp collisions for $\sqrt{s}$ from 200 GeV up to 14 TeV. compared to (a) PHENIX [63], CDF [64], ALICE [66], and to (b) STAR [71], CMS [67], CDF [65].
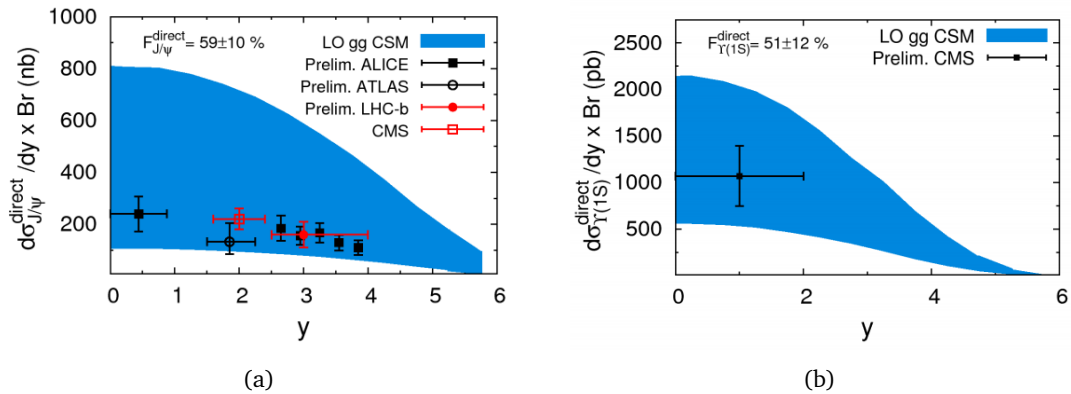
Figure 6.3: $d\sigma^{direct}_{J/\psi}$ (a) and $d\sigma^{direct}_{\Upsilon}/dy$ (b) from gg fusion in pp collisions for $\sqrt{s}$ from 200 GeV up to 14 TeV compared to (a) LHCb[70], ATLAS [69], ALICE [66], CMS [68] and (b) to CMS [67].

6.1.2 The W/Z bosons at the LHC

Standard model W and Z boson productions are charachterized by a relatively high cross section with respect for example to the top and higgs production or to any other channel of physics beyond standard model. They can count on accurate theoretical prediction and very precise measurements performed at other accelerators (like LEP). In particular, the channels where W/Z bosons decay in association to jets they also constitute an important background for many other physics processes of interest, amongst which we can mention also the $t\bar{t}$ and single-top processes. Precise determination of the production cross sections and their ratios, like the ratio of W^+/W^- or Z^+/Z^- events, provide an important test of the standard model, as well as a chance to measure the Parton Distribution Functions at the LHC. The $Z \rightarrow ll$ is often used as "candle" to measure lepton reconstruction and triggering efficiencies, thanks to their extremely clean signature. An understanding of those processes is therefore crucial for precision measurements in the standard model as well as for new physics searches. The signature for Z decaying to leptons is one of the cleanest to be found in a detector at a hadron collider, since it is characterized by two isolated, high p_T leptons of opposite sign, whose 4-momentum add up to the reconstructed Z boson 4 momenta, with an invariant mass peaked around the Z boson mass. On the other hand the
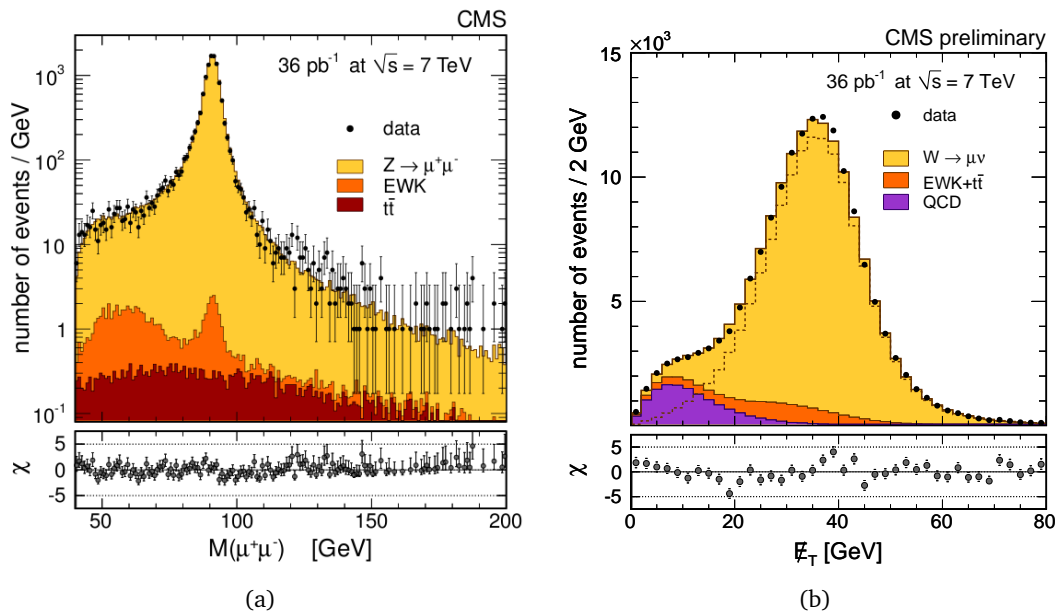
Figure 6.4: The invariant mass of dimuon pairs reconstructed in CMS $m_{\mu\mu}$ (a), and $\not{E}_T$ distribution for the CMS $W \rightarrow l\nu$ candidates (b) with $36.1\ pb^{-1}$ of collision data.

W decaying to a lepton neutrino pair has in general a bigger QCD contamination, due to the presence of a single well-defined and isolated lepton instead of two, but it is possible in this case to infer the neutrino transverse momentum assuming the kinematic closure of the event and counting the missing energy $\not{E}_T$ necessary for all transverse momenta with respect to the beam axis in the detector to sum to zero. Several physical measurements of interest have been performed at the LHC, for example the measurement of the leptonic branching ratios of the W, $B(W \rightarrow l\nu)$, as well as the measurement of the width of the W: $\Gamma(W)$. Figures 6.4 (a) and (b) show respectively the distribution of the reconstructed invariant mass of muon-antimuon pairs, and the distribution of the $\not{E}_T$ for events with one electron reconstructed in the event, at at the CMS experiment with $36.1\ pb^{-1}$ of data collected during 2010. Those figure show clearly how it is possible to discriminate the W/Z from the background. Figure 6.5 shows the summart of the results from the CMS

experiment vs the theoretical predictions, and figure 6.6 shows the measurements of inclusive W and Z production cross sections times branching ratios as a function of the center-of-mass energies.
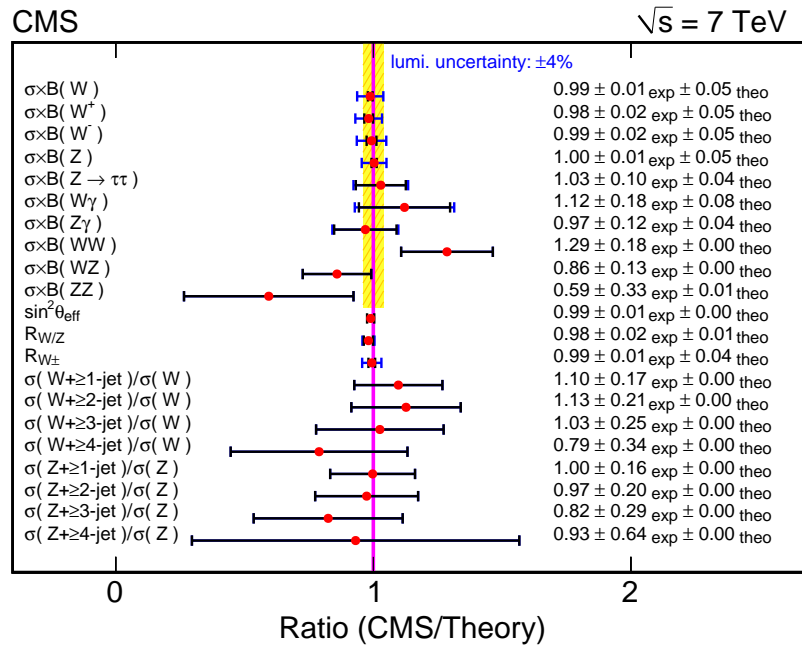
Figure 6.5: Ratio of CMS measurement to theory expectations. The experimental uncertainty is the sum in quadrature of the statistical and the systematic uncertainties not including the uncertainty on the extrapolation to the full acceptance due to parton density functions. Obtained with $36.1\ pb^{-1}$ 2010 and 2011 $1.1\ fb^{-1}$ of collision data [72].

6.1.3 The Standard Model Higgs search

6.1.3.1 The LEP scenario

The Large Electron Positron collider has searched for the Higgs boson in the low mass range, as well as extracted constraints on the mass itself by performing precision measurements on all the standard model parameters. The direct search of LEP-II has excluded at 95% Confidence Level the higgs with mass $m_H < 114 GeV/c^2$. The measuremenets on radiative corrections to the mass of the W boson m_W have put a constrain on the higgs mass very close to the excluded mass range. Figure 6.7 show the fitted value of the Higgs boson mass resulting of of the simultaneous fit to all SM parameters.

6.1.3.2 The Higgs search at the LHC

The main production channels for the Standard Model Higgs boson are:

- gluon fusion via top loop.

- vector boson (W/Z) fusion.

- $t\bar{t}$ fusion.

- W/Z associated production.

The corresponding Feynman diagrams are shown in Figure 6.8 and the production cross section the LHC as a function of the the Higgs mass m_H [74] are shown in Figure 6.9.
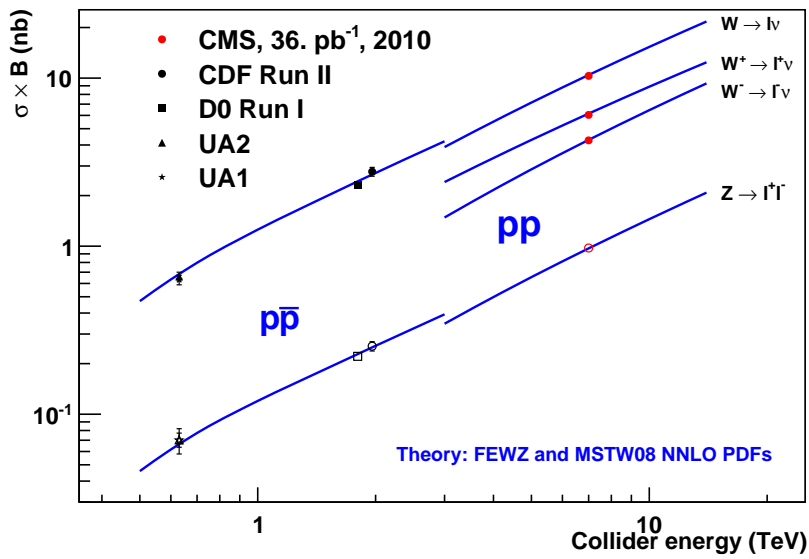
Figure 6.6: Measurements of inclusive W and Z production cross sections times branching ra- tios as a function of center-of-mass energy for CMS and experiments at lower-energy colliders. The lines are the NNLO theory predictions [73].
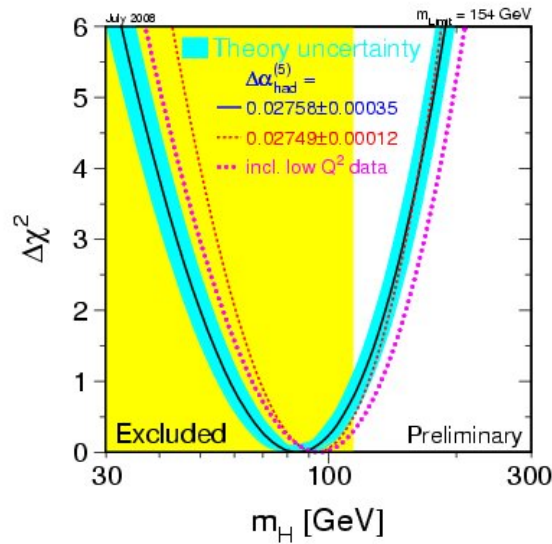
Figure 6.7: LEP fit to data: $\Delta\chi^2$ vs m_H, including the fit using the evaluation of $\Delta\alpha_{had}^{(5)}(m_Z)$ (dashed curve) and using low Q^2 data (dotted curve). The best fit central value for all the fits is within the region excluded by direct searches, indicated by vertical yellow bands, giving possible indication of a Higgs boson with a mass close to the excluded region.
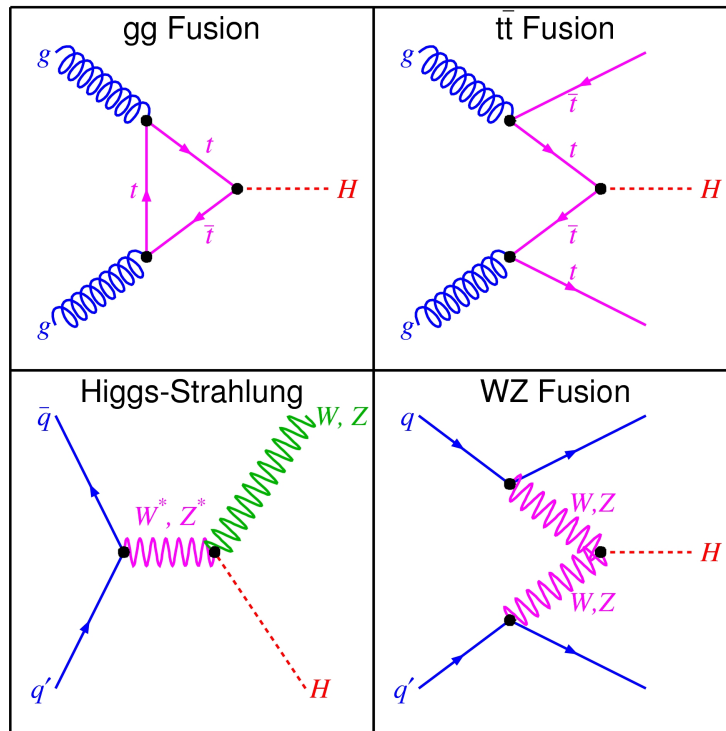
Figure 6.8: Feynman graphs for Higgs boson production modes.
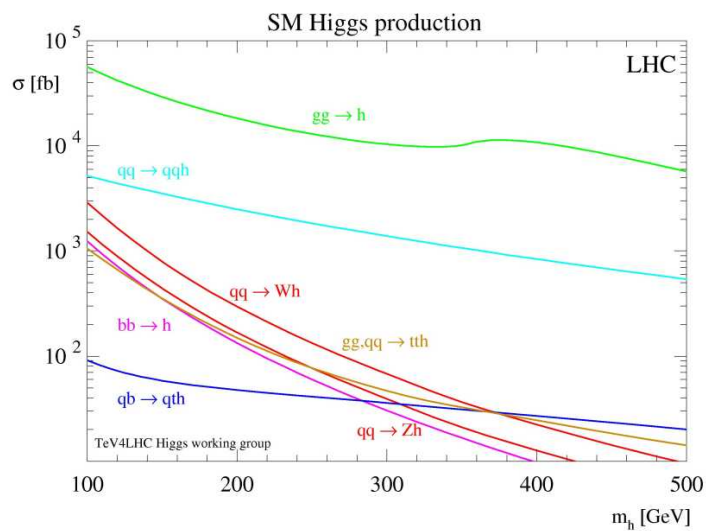
Figure 6.9: Cross section for boson production modes as a function of M_H

For the entire range of the Higgs masses below 1 TeV, the production via gluon fusion dominates. The number of events expected is shown on the vertical scale on the right hand side of the graph. The Standard Model Higgs boson is searched for at the LHC in various decay channels, the choice of which is given by the signal rates and the signal-to-background ratios the various mass regions. The higgs boson essentially couples to any massive particle, therefore a great variety of decays is possible, keeping also in mind that the phase space available for such decays depends also on the mass of the higgs boson, so for example some of them might not be kinematically accessible or highly suppressed in the case of a low mass higgs. Figure 6.10 shows the different decay channels for the higgs boson.
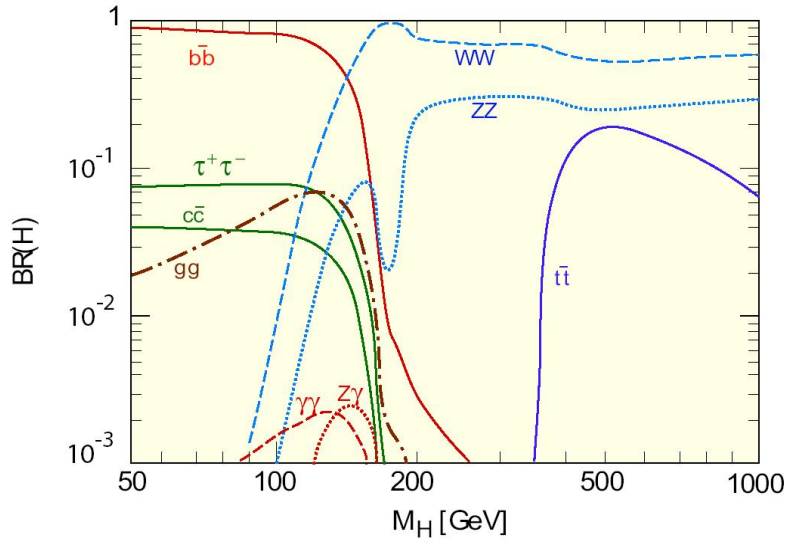
Figure 6.10: SM Higgs Decay Branching Fractions.

Both the CMS and the ATLAS detector searched the higgs boson through several decay modes, having as lower bound the LEP exclusion limit and as upper bound 1 TeV which is the scale for the higgs mass at which the WW diagrams are not renormalizable anymore. Actually, due to the limited statistics in the very high mass range, the search extended up to 600 GeV of higgs mass:

- $H \to \gamma\gamma$: very important channel for low mass higgs, limited by the huge cross section of the background.

- $H \to b\bar{b}$: searched for in channel where the higgs is associated to a W/Z boson, so that the final state is $l\nu b\bar{b}$ or $l^+l^-b\bar{b}$. Also important for low mass searches.

- $H \to \tau\tau$: the final state looked for in the detector is either $\tau\tau \to l^+l^- + 4\nu$ or $\tau\tau \to l + 3\nu + \tau_{hadronic}$. Also optimal for low mass searches.

- $H \to WW \to l^+\nu l^-\nu$: this channel is dominant in the range $m_H > 2M_W$. It has also been explored at Tevatron.

- $H \to ZZ \to 4l$: this channel is the cleanest and it is important for the high mass higgs in the range $m_H > 2M_Z$.

- $H \to ZZ \to 2l2jets$: as for the $ZZ \to 4l$ channel, this is important range $m_H > 2M_Z$ and althought charchterized by a less striking signature, it is competitive with the previous thanks to the hightest branching ratio of $Z \to qq$ with respect to $Z \to ll$.

- $H \rightarrow ZZ \rightarrow 2l2\nu$: this search has a similiar signature to the $WW \rightarrow l\nu l\nu$ but it is orthogonal to it.
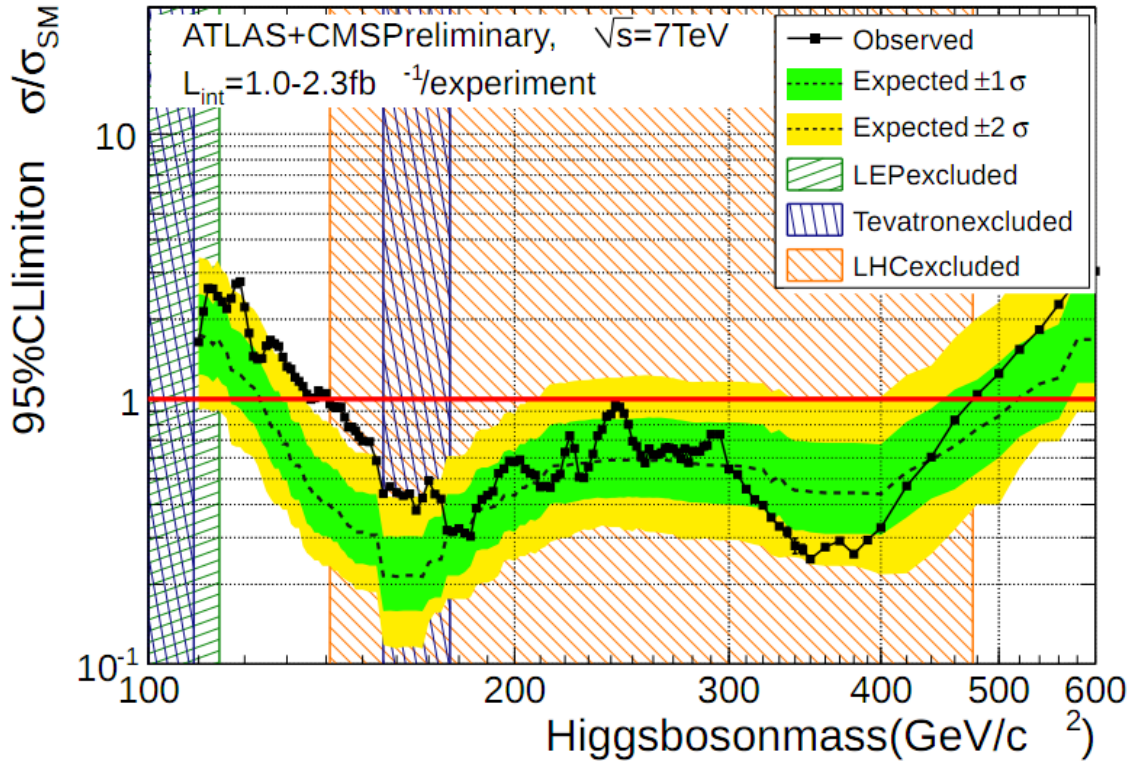
Figure 6.11: The combined 95% C.L. upper limits on the signal strength modifier $\mu = \sigma/\sigma_{SM}$, obtained with the CLs method, as a function of the SM Higgs boson mass in the range $110 - 600 GeV/c^2$. The observed limits are shown by solid symbols. The dashed line indicates the median expected $\mu^{95\%}$ value for the background-only hypothesis, while the green (yellow) bands indicate the ranges expected to contain $68\%(95\%)$ of all observed limit excursions from the median. The SM Higgs boson mass ranges excluded by LEP, by Tevatron and by this combination are shown as hatched areas.

The combined CMS + ATLAS measuremetns allowed to gain greater power in the search [75]. The SM Higgs boson is currently excluded 95% C.L. in the mass range $141 - 476 GeV/c^2$, with the largest excess observed having an estimated significance of about 1.6 standard deviation from the no-signal hypothesis. Figure 6.11 shows the excluded regions for the higgs mass range up to November 2011.

6.1.4 The top quark sector

The LHC is often regarded as a top quark factory, and in general is even more suited for top quark studies than the Tevatron itself, where the top quark production was first observed. The main standard model physics process involving top production at the LHC are top-antitop pair production ($t\bar{t}$), mostly through strong interactions, and the top production in association to a non-top quark or a W boson through electroweak interactions, namely the s, t, and tW channels. All those processes at LHC are favoured with respect to Tevatron: for $t\bar{t}$ production we find the cross section ratio $\sigma_{t\bar{t},LHC}/\sigma_{t\bar{t},Tevatron} \simeq 23$. For single top channels, this is even more evident, $t-$channel: $\sigma_{t-channel,LHC}/\sigma_{t-channel,Tevatron} \simeq 28$ and $\sigma_{t-channel,LHC}/\sigma_{t-channel,Tevatron} \simeq 57$. We are now going to describe separately the physics of $t\bar{t}$ and single-top processes.

6.1.4.1 $t\bar{t}$ processes

The production of top-antitop pairs $t\bar{t}$ is by far the dominant one amongst the top production processes. The feynman diagrams for $t\bar{t}$ production are shown in figure 6.12, where the dominant contribution is the one from gluon fusion $gg \to t\bar{t}$.
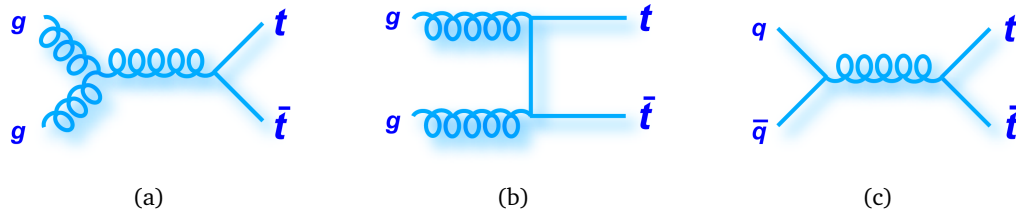
Figure 6.12: SM $t\bar{t}$ pair main production mechanisms.

The first important characteristic of top quarks is that their mass is much higher than, the other quarks, including the b quark, its partner in the $SU(2)_{is}$ doublet. This has several implications: first of all, it implies a very short lifetime for the top quark. This allows tops to decay through an electroweak processes into $t \to Wq'$, with $q' = (b, s, d)$. Nevertheless, the mixing between the top and other families is so small that it is in most cases neglected when it comes up to determine the topologies of top quark decay. So since $|V_{tb}| >> |V_{ts(d)}|$, one generically only considers $t \to Wb$ decay channels. This causes essentially two types of decay for the top quark: the leptonic decays $t \to Wb \to l\nu b$ and the hadronic decays $t \to Wb \to q\bar{q}'b$.

For $t\bar{t}$ processes this leads several to essentially three different categories of decays: so called fully leptonic or di-leptonic decays, where both tops decay through $t \to Wb \to l\nu b$, fully hadronic, where both tops decay through $t \to Wb \to q\bar{q}'b$, and semi-leptonic, where there is one leptonic and one hadronic decaying top quark. Figure 6.13 shows an example of a diagram for a top quark semi-leptonic decay. Figure 6.14 shows the branching ratios of the top quark in the different categories.
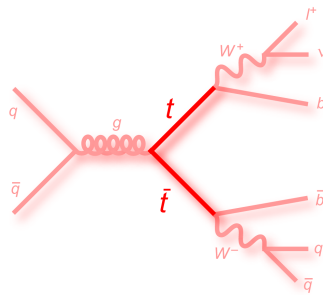
Figure 6.13: Example of a diagram for $qq \to t\bar{t} \to l\nu bq\bar{q}'b$.

The measurement of $t\bar{t}$ cross section has been performed both in CMS and ATLAS and the results up to date are reported in Figure 6.15.

Also, differential $t\bar{t}$ cross section measurements can probe the standard model even more precisely scanning for deviations from the predicted behavior.

Besides the precision measuremnt of the $t\bar{t}$ cross section, which is starting to challenge the accuracy of the theoretical predictions, several other measurements are possible exploiting the very well defined $t\bar{t}$ topology. First of all, the measurement of the mass of the top quark is of great interest since it is a parameter of the standard model, so the most precise is its knowledge, It is noteworthy that since the higgs boson couples with the mass of the particles, the measurement of the top mass is important for accurate precisions on

Top Pair Decay Channels

(a)

Top Pair Branching Fractions

(b)

Figure 6.14: Decay charts of the $t\bar{t}$ events. (a) Shows the decay modes of the top quark as a consequence of the W decay modes: the branching ratio for each channel in fact is the combinatorics between the branching ratios of the two W bosons decay modes. (b) Shows the branching ratio of each mode.
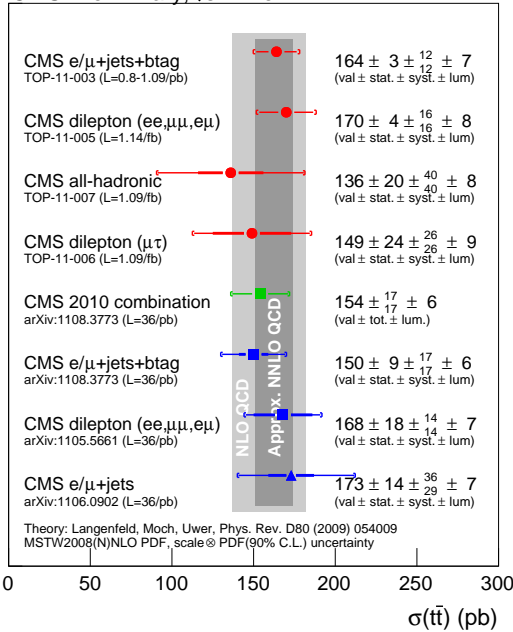
(a)
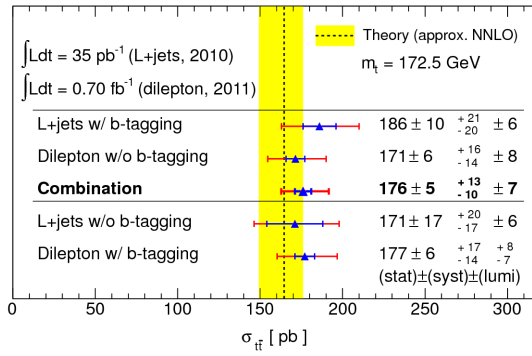
(b)

Figure 6.15: Measured $t\bar{t}$ cross section for (a) CMS with $36.1~pb^{-1}$ and all decay channels [76] [78], (b) ATLAS with $0.7~fb^{-1}$ and leptonic and dileptonic channels [77].

(a)

(b)
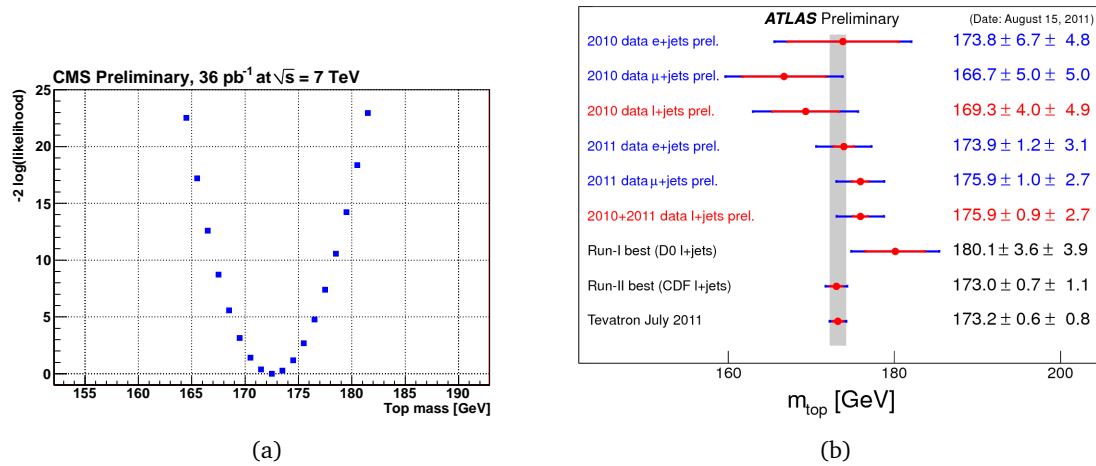
Figure 6.16: (a): maximum likelihood fit to the top quark invariant mass at CMS with $36.1\ pb^{-1}$ in the $t \to Wb \to l\nu b$ channels, yielding $m_t = 173.1 \pm 2.1(stat)^{+2.8}_{-2.5}(syst)$ [78]. The CMS combination with the di-leptonic channel measurement yields $m_t = 173.4 \pm 1.9(stat) \pm 2.7(syst)$. (b) ATLAS summary with $0.7\ fb^{-1}$ integrated luminosity [79].

the physics of the higgs. The mass of the top quark has been measured at the LHC by both the ATLAS and the CMS experiments, and the up-to-date results are reported in Figure 6.16

Other examples of important measurements on the $t\bar{t}$ pair production top quark charge asymmetry measurements, which allow to search for unknown top quark production mechanisms which invisible in the invariant mass spectrum. Different vectorial and axial couplings of new resonances to top and anti-top quarks or interferences with Standard Model (SM) production processes will lead to an emission of the top quark preferably either in the direction of the incoming quark or in the direction of the anti-quark in case of quark-antiquark annihilation in the initial state. On the other hand helicity measurements on the polarisation of the W bosons in top quark decays is sensitive to the structure of the Wtb-vertex the measurements were used to set limits on anomalous contributions to the Wtb-vertex. Figure 6.17 shows the measurement of top quark helicity as well as the differential cross section measurement as a function of the reconstructed top transverse momentum.

Also, a direct search of beyond standard model processes decaying through $t\bar{t}$ pairs is possible reconstructing the invariant mass of the whole system composed of the decay products of the top and the anti-top. Figure 6.18 shows the exclusion bands for such processes for CMS and ATLAS

6.1.4.2 The single top processes

The standard model forsees production of single-top quarks through three electroweak processes in the LHC and Tevatron energy reach: the s, t, and tW channels. The Feynmann diagrams for such processes are shown in Figure 6.19.

Single top processes are classified in function of the virtuality of the W boson involved in the interactions: for the $s-$channel the transferred four momentum squard module is $Q^2 - m_w^2 > 0$, for the $t-$channel $Q^2 - m_w^2 < 0$, while the $tW-$channel sees the production of a real, on-shell W boson in the final state. All those processes cross section at LHC and at the Tevatron are reported in table 6.1. All channels of single top are related to the Kabibbo Kobayashi Maskawa matrix element V_{tb}, in particular each single top process includes an electroweak vertex where V_{tb} is present. This feature is very important because it allows a

(a)   (b)
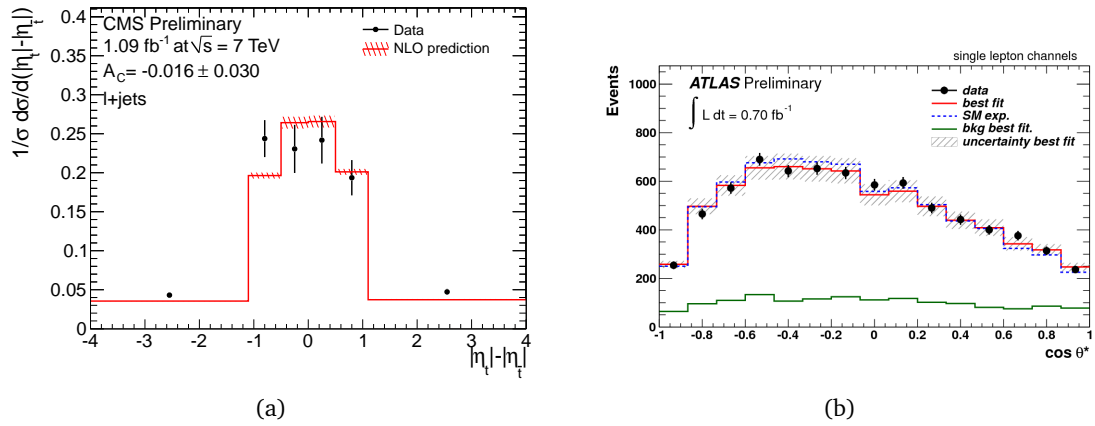
Figure 6.17: (a) Distribution of the unfolded $|\eta_t| - |\eta_{\bar{t}}|$ spectrum measured by CMS with $36.1 \ pb^{-1}$ [80]. (b) Distributions of the angle $\cos \theta^*_{lj}$ between the lepton and the b quarks from top decay mode $t \to Wb \to l\nu b$ in the reconstructed top quark rest frame, for data measured by ATLAS with $0.7 \ fb^{-1}$ [81].

(a)   (b)
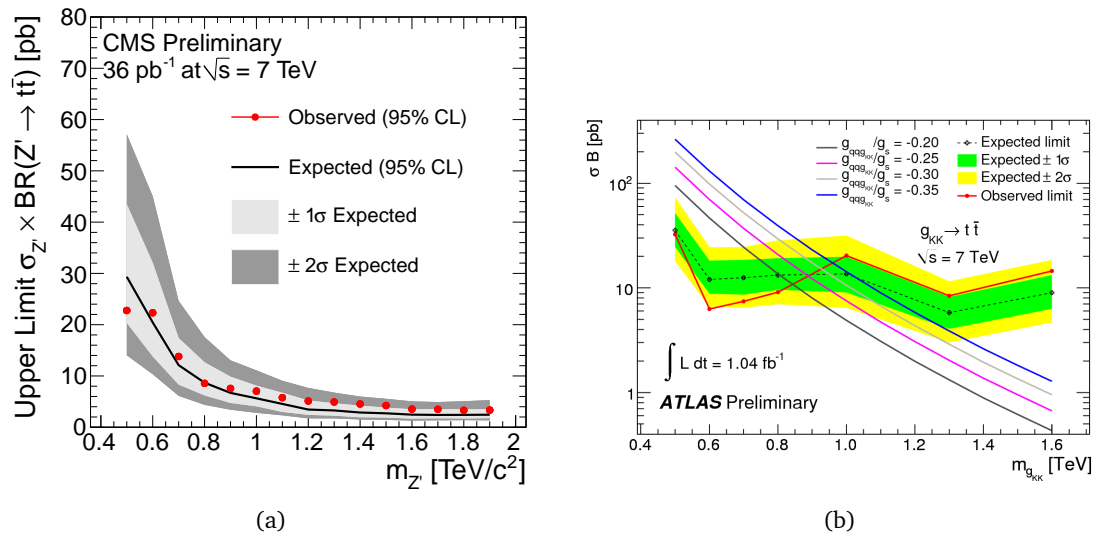
Figure 6.18: (a) CMS Expected and observed limits from Bayesian integration using Markov chain Monte Carlo for $\sigma(pp \to Z') \times BR(Z' \to t\bar{t})$ for $36.1 \ pb^{-1}$ of data as a function of Z' mass [82]. (b) Expected and observed limits on cross section times branching ratio at 95% C.L. and expected cross section for a Randall-Sundrum KK-gluon gKK [83].
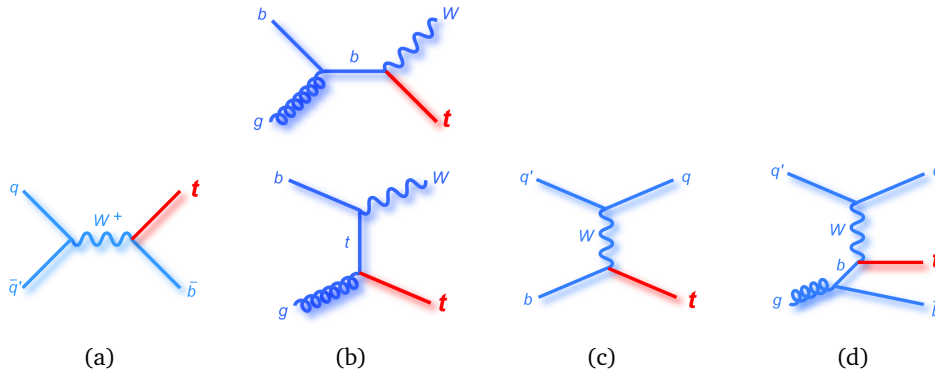
Figure 6.19: SM single top top quark main production mechanisms: $s-$channel (a), $tW-$channel (b), and $t-$channel respectively in the so-said $(2) \to (2)$ scheme (c), and $(2) \to (3)$ scheme (d).

direct measurement of V_{tb}. On the other hand, the polarization of top(antitop) quarks is almost 100% left(right) handed, resulting in a very clear angular distribution of the top quark's decay products. In fact, considering top quarks decaying through: $t \to Wb \to l\nu b$ one can write:

$$\frac{1}{\Gamma} \frac{d\Gamma}{dcostheta^*} = \frac{1}{2}(1 + Acos\theta^*) \tag{6.1}$$

Where A depends on the decay product and is $+1$ for the lepton, -0.4 for the b quark and -0.33 for the neutrino, and $cos\theta^*$ is the angle with respect to the top quark spin axis in the top quark rest frame. Figure 6.20 shows the distribution of $\cos\theta^*_{lj}$ one obtains taking as spin axis the direction of the four momentum of the light quark recoiling against the top (see Fig. 6.19 c, and d). Other important properties of those channels are for example the
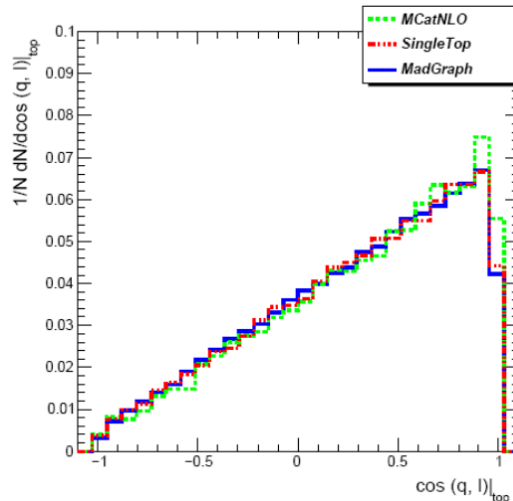
Figure 6.20: Distribution of $\cos\theta^*_{lj}$ from 6.1 on monte carlo truth. Here θ^* is the angle between the lepton momentum and the light quark momentum in the top quark rest frame, tested using different Monte Carlo models(See also [99], [105])
.

asymmetry in production of tops-antitops for t and s channels. Standard model predictions for separate $t(\bar{t})$ processes are reported in Table 6.2. For comparison, the asymmetry between W^+ and W^- is added. The only measurements prior to the ones presented in this thesis about single top $t-$channel and $s-$channel are the ones at Tevatron, which

Process	σ_{top} (pb)	$\sigma_{anti-top}$ (pb)	asymmetry $\frac{\sigma_{top}-\sigma_{anti-top}}{\sigma_{top}+\sigma_{anti-top}}$
$t-$channel (†)	$41.92^{(+1.59)}_{(-0.21)} \pm 0.83$	$22.65 \pm 0.50^{(+0.68)}_{(-0.91)}$	0.298
$s-$channel (†)	$3.19 \pm 0.20^{(+0.55)}_{(-0.10)}$	$1.44 \pm 0.01^{(+0.06)}_{(-0.07)}$	0.38
Process	σ_{W+} (pb)	σ_{W-} (pb)	asymmetry $\frac{\sigma_{W+}-\sigma_{W-}}{\sigma_{W+}+\sigma_{W-}}$
$W + X \to l\nu + X (\diamond)$	6.04 ± 0.26	4.26 ± 0.18	0.173

Table 6.2: Cross sections for $t-$channel and $s-$channel separated by top-antitop processes. $W^{+(-)} + X \to l\nu + X$ processes measured cross sections are also shown.†: NNLO prediction,$\diamond$: from CMS measurement.

confirm the standard model, but have a wide margin for improvement at the LHC. Also in $p\bar{p}$ colliders like Tevatron, the top-antitop production asymmetry in t and s channels production is not present. Figure 6.21 shows the cross section measurements at Tevatron in the $t-$channel and in the $2D$ plane for $t-$channel and $s-$channel.
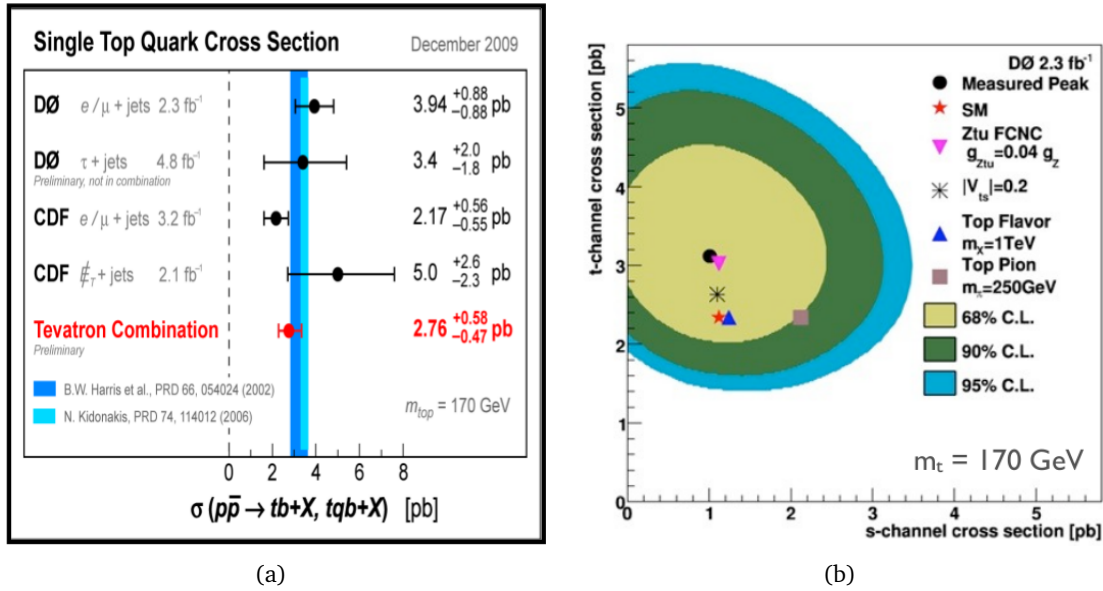
Figure 6.21: (a) Tevatron combined $t-$channel cross section measurement. (b) Tevatron combined $s-$channel vs $t-$channel cross section in the assumption of $m_T = 170 GeV/c^2$ [84]

.

The precision measurement of $t-$channel cross section allows to measure the Kabibbo Kobayashi Maskawa matrix element V_{tb}. Figure 6.22 shows the measurement of $|V_{tb}|$ at the Tevatron experiment $D0$ and the determination of a lower bound bound with a bayesian technique. This technique is also implemented in the analysis described in chapter 7,and the results are shown in chapter 9.3.

It is also possible to perform searches for anomalous couplings of the electroweak current in single top channels: Figures in 6.23 show the measurements performed at $D0$ of the left handed and right handed components of the current, parametrized as components of V_{tb} decomposing the current in a vector and a 2D tensor component. Finally, due to the extremely low production cross section, the $tW-$channel could not be observed, nevertheless it is a very important check for the SM consistency. LHC is a far more promising machine for studies on the $tW-$channel. The main challenge for this channel is that it is difficult to discriminate it from the $t\bar{t}$ processes, since already at next to
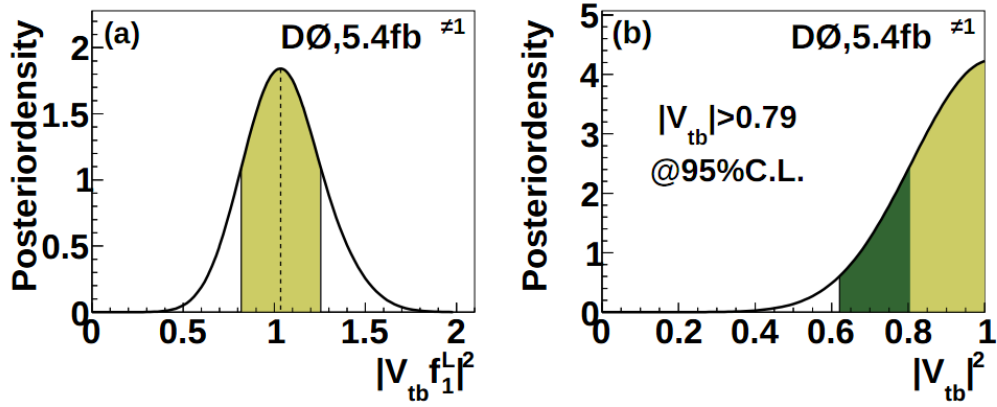
Figure 6.22: (a) Tevatron D0 measurement of $|V_{tb}|$: no assumption on $|V_{tb}| \leq 1$. (b) Lower limit at 95% CL in the assumption $|V_{tb}| \leq 1$ [85] [86].
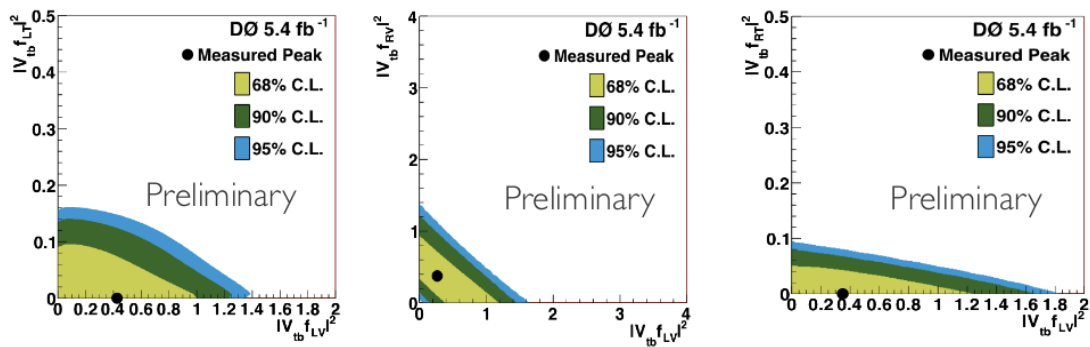
Figure 6.23: Tevatron measurements of the components of the vector and tensor currents: L(R)V = Left(Right)-Handed Vector, L(R)T = Left(Right)-Handed Tensor [87].

leading order there are some overlapping diagrams which cause interference. Therefore it is difficult to make a prediction on the cross section of the $tW-$channel unless a way is found to treat those diagrams. One way is to remove them and evaluate the cross section of the remaining ones at LO and NLO. This method, said Diagram Removal, does not preserve gauge invariance. Other more complicated methods (Diagram Subtraction) allow to subtract the diagrams and define a $tW-$channel signal preserving the gauge invariance. However it has been demnstrated that in most cases those methods are in reasonable agreement between each other. The $tW-$channel exactly as the $t\bar{t}$ can be divided in several decay modes, depending on the combination of the decays of the two W bosons in the final state (see also figure 6.14). The most favourable channels for tW search are refer to the semileptonic and dileptonic decay modes, characterized respectively by one top decaying through $t \rightarrow Wb \rightarrow q\bar{q}'b$ and one through $t \rightarrow Wb \rightarrow l\nu b$ or both tops decaying through $t \rightarrow Wb \rightarrow l\nu b$. Figures in 6.24 show the of the results of the first measurement of the $tW-$channel cross section in the dileptonic decay mode, performed at LHC by the CMS experiment with 2011 data.

(a)

(b)

(c)
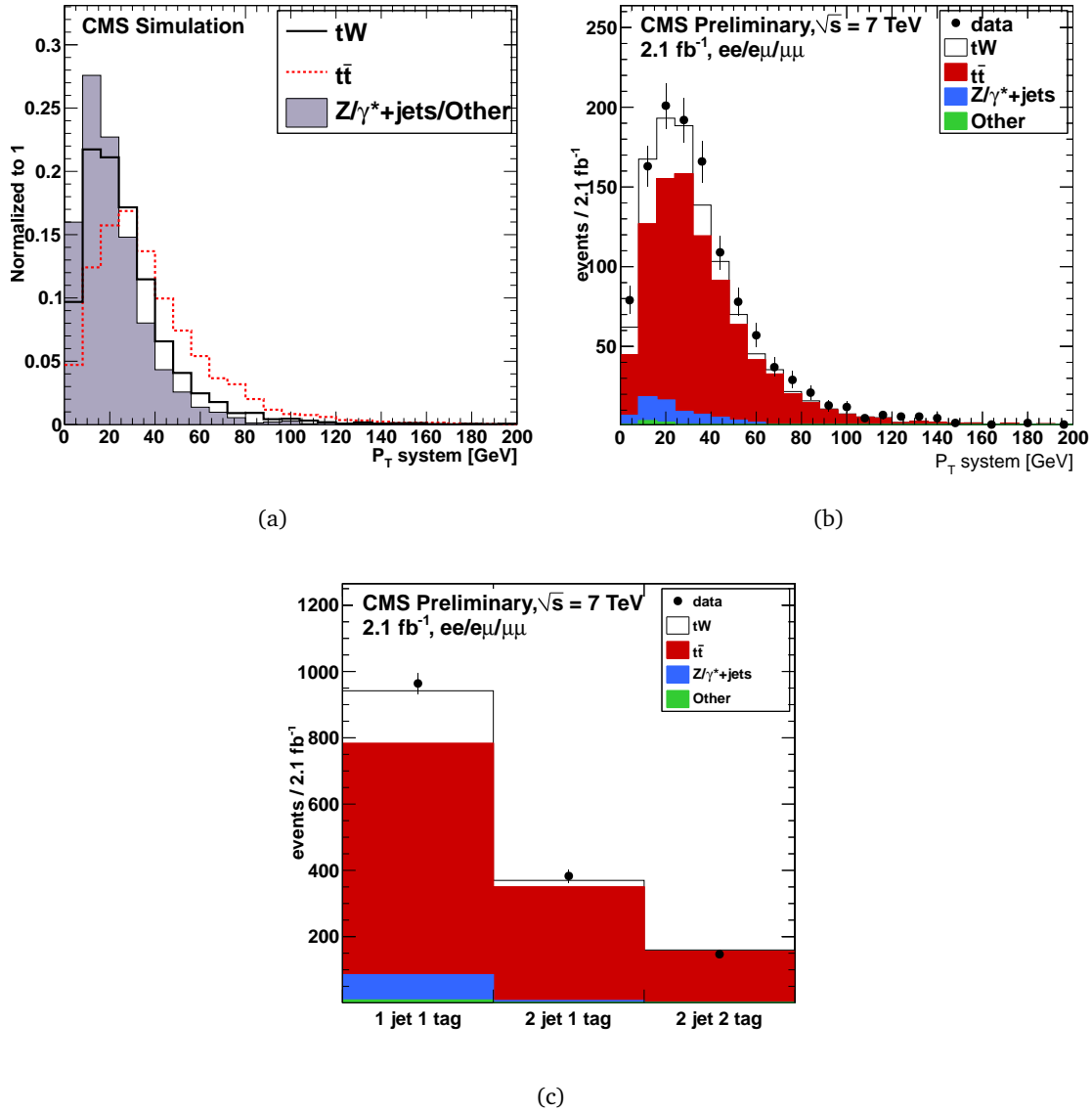
Figure 6.24: CMS measurement of $tW-$channel cross section with $2.1\ fb^{-1}$ in channels with two leptons in the final state [88]: (a) p_T of the system, one of the main variables used for $t\bar{t}$ discrimination, in MC. (b) p_T of the system on data. (c) Overall yield in different jets and b-tagged jets bins after all selection. The first bin is used for signal extraction with a simple event counting.

6.2   The search for physics beyond standard model

The searches for new physics beyond standard model (BDM) complete the panorama of the physics measurements at the LHC. In many cases, such searches have to be performed in channels which have an irreducible background source, for example a standard model process which presents the same final state topology as the BSM process searched for. This also means that often those searches have to rely on peculiar characteristics or angular correlations which are derived from the physics of the BSM process, making them on a certain degree model dependent.

6.2.1   Technicolor

Technicolor [89] is a theory introduced in 1970' as an alternative to the standard Higgs mechanism. introduces a new interaction with a similiar behavior to the strong interaction but which manifests itself at the scale of the TeV. In those models the higgs boson is a composite of techniquarks, and the spontaneous symmetry breaking mechanism as well as the flavour mechanism are explained dinamycally in the context of a technicolor model. Direct searches of technicolor models at CMS and ATLAS are done, allowing to exclude technicolor models. Figure 6.25 shows the results of the analysis performed by CMS on 1.15 fb^{-1} of data, with the corresponding exclusion limit.
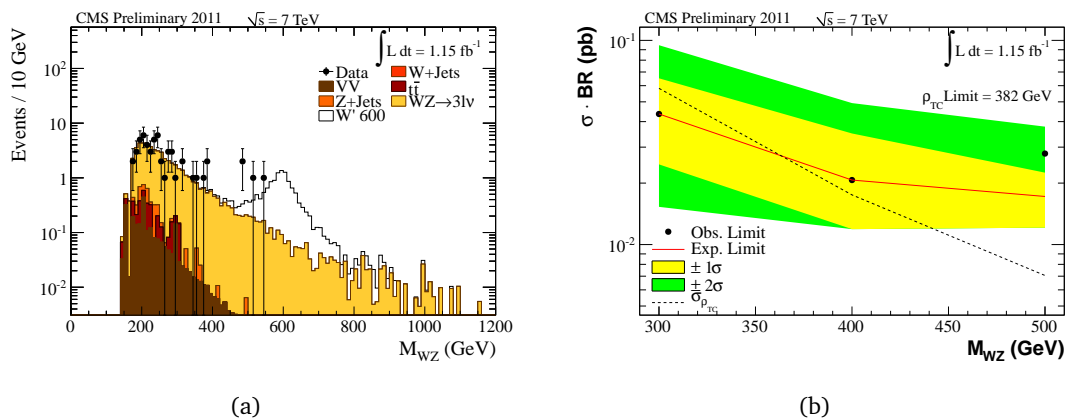
Figure 6.25: (a):WZ invariant mass reconstructed with 1.15 fb^{-1} of CMS data. (b) Expected and observed exclusion limit on $\sigma \times BR(\rho_{TC} \to 3l\nu)$ as a function of the WZ mass, along with the combined $1\sigma(2\sigma)$ statistical and systematic uncertainties depicted with the yellow (green) band (CMS Experiment, 1.15 fb^{-1} of data) [90].

6.2.2   Supersymmetry

One of the most promising theories BSM is supersymmetry (SUSY) [27] [89]. There are several possible SUSY models, but they all predict new physics channels at the scale of energy explored at LHC. SUSY is introduced to solve a problem of Standard Model known as the hierarchy problem. This is not a problem with the Standard Model at the current energy scale, but rather difficulty with the Higgs potential that occours as new BSM particles are introduced. The problem is that the Higgs mass term m_H^2 receives corrections from the virtual effects of every particle that couples to the Higgs field, namely every massive particle. If the Higgs field couples to a fermion f with a term in the Lagrangian

$-\lambda_f$, then the Feynman diagram in Figure yields a correction Δm_H^2 to the Higgs mass:

$$\Delta m_H^2 = \left(\frac{\lambda_f}{16\pi^2}\right)\left[-2\Lambda_{UV}^2 + 6m_f^2 ln\frac{\Lambda_{UV}}{m_f} + ...\right] \qquad (6.2)$$

where Λ_{UV} is the ultraviolet momentum cutoff used to regulate the loop integral. Every particle that couples with the Higgs boson gives therefore a contribution to the Higgs mass term. However, theoretical limits to the Higgs mass predict a value of $m_H < 1000 GeV/c^2$, due to the requirement of renormalizability of WW scattering. This creates an uncomfortable situation where the stability of standard model Higgs mass depends critically on whatever BSM massive particle is present. If corrections to Higgs mass due to BSM particles are too large, it may significantly exceed the expected values, therefore creating an inconsistency in the SM. Since the strength of the coupling increases with the mass of the particles involved and some systematic cancellation has to occur in order to keep the Higgs mass under control, since in principle from the electroweak scale ($O(100)GeV$) up to the Planck scale ($10^{19}GeV$) arbirarily large physics sectors might lie.In order to obtain the sistematic cancellation of all Δm_H^2 terms, supersymmetry postulates the existance of a new symmetry that associates bosons to fermions. The reason for this choice is that the signs of bosonic and fermionic loops corrections to Higgs mass are opposite, thus giving a hint that for each fermion a boson should exist and vice-versa. Particles associated this way are said supersymmetric partners, and they possess identical characteristics except for the spin. Each 1/2 spin fermion has a 0-spin particle, while 1-spin and 0-spin bosons are associated with 1/2 spin fermions. Quarks are associated to squarks, leptons to sleptons, W and Z bosons have Winos and Zinos as their partners. It is noteworthy that, since no supersymmetric particle has yet been observed, the masses of SM particles must differ from those of their supersymmetric partners. In order to preserve intrinsic consistency, Supersymmetry must therefore be spontaneously broken. Supersymmetry searches at the LHC revolve around inclusive studies based on large missing energy and jets. Typical SUSY signatures are squarks and gluinos. Supersymmetry searches have been going on since the beginning of the LHC data taking, and the resulting exclusion limits from CMS and ATLAS respect to the most simple supersymmetric model, the so said Minimal Spersymmetric Standard Model, are displayed in Figures 6.26(a),(b).

6.2.3 Other searches

Many other searches are possible at the LHC, amongst them we can quote:

- W' and Z': many models foresee the presence of a heavy boson which can be spotted through the usual decay channels of W, Z bosons [89]. It is noteworthy that all single top channels are sensitive to the presence of W' bosons. Another example in the top quark sector are the searches for resonances in the $t\bar{t}$ pair invariant mass already mentioned in section 6.1.4.1.

- The search for ultra-compact extra dimensions: to solve the issue of the difference between the Planck and electroweak scale, it was hypothized that extra spacial dimensions with size $< \mu m$ are present, and that gravity force lines travel through such dimensions, while other interactions stay confined in the three dimensional hyperplane. This means that the weakness of gravitational coupling constant is just due to this spread of the gravitational interaction in other dimensions, while the real coupling constant is much higher. This would cause the "real" Planck scale to be closer to the electroweak scale. Several models are possible depending on the number of extra dimensions and on the geometry of such dimensions (flat or warped). A possible signature of such model would be dileptons or in general particle-antiparticle
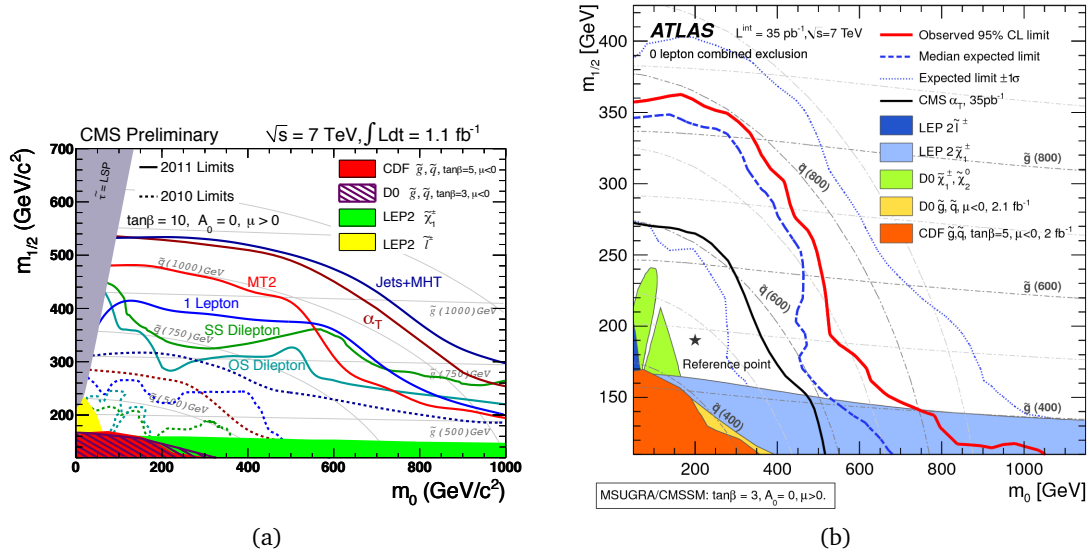
Figure 6.26: (a): Observed limits from SUSY searches plotted in the CMSSM $(m_0, m_{1/2})$ plane, with 1.1 fb^{-1} of CMS data [91]. (b) with 36 pb^{-1} of ATLAS data [92]. m_0 and $m_{1/2}$ are the masses of the superparticles with spin 0 and 1/2, respectively.

pairs arising from gravitons exchanges at the TeV scale, made possible because of the lower the Planck scale predicted by those models.

- The search for short-lived blafck holes: the presence of small, evaporating black holes makes sense if one imagines some mechanism, like the one suggested for the ultra-compact extra dimensions, lowers the Planck scale so that quantum gravity is accessible at lower energies. In such cases, mini-black holes could possibly form. According to Hawkings' theory on quantum black holes, they should evaporate generating thermal radiation. Their characteristic would therefore be an isotropic radiation, without a preferred decay channel.

Up-to date results for the current searches at the LHC ATLAS and CMS experiments can be found at Reff. [93], [94].

Chapter 7

Single top evidence with the CMS detector

In section 6.1.4.2 we described the phenomenology of single top $t-$channel processes. In this chapter we describe the selection we perform on the physics objects reconstructed in the cms detector to obtain an event sample enriched with $t-$channel events, the reconstruction of the top quark four-momentum starting from its decay products, and the variables which allow a clear discrimination between single top and background events, and the analysis performed on LHC collision data collected during 2010 by the CMS experiment and that allowed to achieve the first evidence of single top at the LHC with 7 TeV center of mass energy.

7.1 t-channel topology

Diagrams in Fig:7.1 show the $t-$channel so said $(2) \to (2)$ (a), and $(2) \to (3)$ schemes (b). The final state of single top events is constituted by one top quark, a light (u,d,s) or c quarks and a b quark for the $(2) \to (3)$scheme. One extra final state b quark is also present in the $(2) \to (2)$scheme: since there is no valence b quark it can only come from a sea contribution, therefore only $b\bar{b}$ pairs can be present. Such $b\bar{b}$ pairs in the initial state are produced from the splitting of a sea gluon of the proton. This has two consequences: first of all, event samples generated separately for $(2) \to (2)$and $(2) \to (3)$processes can have a superposition depending on the hadronization cutoff of the perturbative scale. To evaluate the total cross section of $(2) \to (2)$and $(2) \to (3)$the effect of this cutoff has to be taken into account in order to avoid double counting of events. Second, the extra b quark results in an extra b-jet stemming from the quark hadronization, which has to be accounted for in the selection. For this thesis work, we considered events where the top decays through the chain: $t \to Wb \to \mu\nu b$. The branching ratio (BR) of $t \to Wb$ is very close to 1,[9] [10] , while the BR of $W \to l\nu$ is ~ 0.324 and the BR to muons is ~ 0.11.

The final state event topology therefore consists of one muon, one neutrino, one light quark and one or two b quarks. The muon can be directly reconstructed in the detector, while from b and light quarks hadronization stem jets which can eventually be identified as associated to b quarks throught the b-tagging algorithms (see also Chapter 4). The neutrino cannot be directly detected, yet the components of its momentum in the plane transverse to the beam axis can be inferred from the missing energy in the detector to get kinematic closure of the events.

It is notheworthy that we also consider events where W decays to $W \to \tau\nu \to \mu\nu\nu$ as part of our signal. Both our acceptances (rate) and our Monte Carlo simulated distributuons ("shapes") take this fraction of events into account. The effect on the rates is $O(10\%)$ and the distortion of the shapes is in most cases negligible. On the other hand,

to discriminate $W \to \mu\nu$ events to discriminate $W \to \tau\nu \to \mu\nu\nu$ and $W \to \mu\nu$ events would require much complication, which is not necessary considering them inclusively. The longitudinal momentum of the neutrino for single top events can be reconstructed with a special procedure described further on in this chapter. See also chapter 4 for more detail on the description of how leptons, jets and missing energy are reconstructed in the detector. Several physics processes can generate events which reproduce such topology,
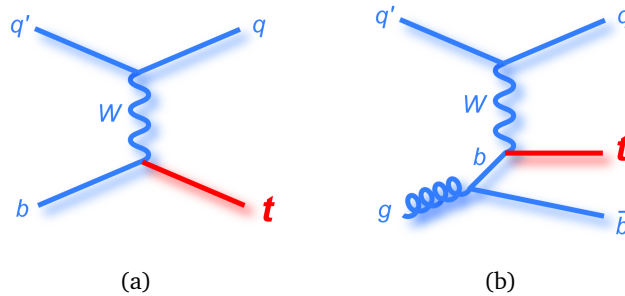
Figure 7.1: SM single top top $t-$channel production mechanisms: the so said $(2) \to (2)$ (a), and $(2) \to (3)$ schemes (b).

thus constituting, background sources for our processes. The most important are:

1. W+jets: The processes where a W boson is produced in association to jets are an important source of background. In particular, processes where W decays through $W \to \mu\nu$ and are associated to a c quark or $b\bar{b}$, $c\bar{c}$ quark pairs could be mis-identified as signal events. Also events where W is associated to light partons (u, d, s and gluons), can mimic signal events, in case one of the jets stemming from a light parton mimics the behavior of a $b-$jet. The low probability for such an event to occur is balanced by the much higher cross section of such processes with respect to $t-$channel cross section.

2. $t\bar{t}$:The processes where a $t\bar{t}$ quark pair is produced are also an important source of background. In particular events where one t quark decays leptonically, namely through the chain $t \to Wb \to l\nu b$, and the other top quark decays hadronically, namely through the chain $t \to Wb \to q\bar{q}'b$, are the most signal like. Such events are also called "semi-leptonic" $t\bar{t}$ events in jargon. The semi-leptonic $t\bar{t}$ jet multiplicity is in general higher than for the $t-$channel, and this reduces the contamination from this background.

3. Multi-jet QCD: Events where a well-isolated muon is present and the jet-environment reproduces the signal topology in hard QCD scatterings are very rare, nevertheless, due to the much higher cross section of such multi-jet QCD processes its contribution to the background is not negligible.

4. s, and tW channels: the other single top processes, in particular the $tW-$channel, can eventually produce a non-negligible contamination in the signal region. Such backgrounds, like the $t\bar{t}$ background, share with the $t-$channel the decay chain of the top quark.

5. VV,Z+jets and others: diboson processes like WW, WZ, and ZZ, or Z+jets processes are also minor sources of backgrounds which can reproduce in some cases the $t-$channel topology. However either the low cross section for VV processes (with $V = W$ or Z), or the extremely narrow phase space for Z+jets processes passing the cuts, consistently limit the contamination from such processes. Other SM possible

background processes (multi-boson production, multi-top production, SM higgs) have a much smaller cross section than the $t-$channel, and in general their countribution is limited to very rare topologies. They are therefore are considered negligible.

7.2   Datasets and triggers

In order to get into further detail in the selection and the description of the different approaches to background estimation, it is necessary to the some detail of the datasets used for the analysis This section describes the datasets used to perform the analysis with 2010 data. Thi measurements allowed to get the first evidence of single top $t-$channel production at the LHC. The statistics collected by the CMS experiment through the year 2010 corresponds to an integrated luminosity of 44.2, known within 4.0 % [96]. However, for the actual analysis a smaller part of the dataset was used: only the luminosity sections (lumisections) which were flagged good by the Data Quality Monitoring (DQM) group of CMS, and the Physics Validation Team (PVT) according to the validations performed by each sub-detector Detector Performance Group (DPG). We make use of the so-called Muon (Mu) Primary Datasets, which have been collected using High Level Triggers (HLT, see also 3) paths fired by muons in the event, reprocessed with the state of the art detector knowledge. We access the muon HLT paths `HLT_Mu15_v1` which is fired by muon candidates whose transverse momentum is measured to be above 15 GeV/c during the online reconstruction, with the exception of early data where this trigger path was not executed, in which case we access `HLT_Mu9`, defined by a 9 GeV/c, and in simulated events we use path `HLT_Mu9` as well; this is expected to make no practical difference for this analysis, as the offline threshold we use is not affected by the turn-on efficiency curve in both cases. The trigger paths used in data are summarized in TabLe 7.1. The

Table 7.1: High level trigger paths used in the analysis.

HLT cut	Run range
$p_{T,\mu} > 9$ GeV	< 147196
$p_{T,\mu} > 15$ GeV	≥ 147196

t-channel events from Monte Carlo simulation used in this study have been generated with the MadGraph event generator [99], and normalized to the NLO cross section of 64.6 pb^{-1} [95] times $3 \cdot BR(t \to \ell\nu b)$ as only leptonic decays are simulated. In order to give a fair approximation of the full next-to-leading order (NLO) properties of the signal, the (2)→(3) diagram (Figure 7.1 (b)), corresponding to the dominant NLO contribution to the t channel, is combined with the leading order (LO) (2)→(2) dominant process (Figure 7.1 (a)) by a special matching procedure based on Ref. [102], giving a merged sample that describes the entire phase space while avoiding double counting. The separately generated sub-samples for the (2)→(2) and (2)→(3) processes are matched in such a way to give a smooth $p_T^{2nd\ b}$ spectrum. The optimal matching threshold is determined under the assumption that the soft transverse momentum region of the additional b quark is best described by the (2)→(2) process, whereas the modeling of the high-p_T tail of the spectrum by the (2)→(3) process. The technical implementation of the matching inside the CMS software is described in detail in Ref. [106]. Several standard model processes are taken into account as background to the analysis. Table 7.2 summarizes the Monte-Carlo data samples for signal and backgrounds, and provides the number of events and cross section for each sample, as well as the MC generator used for the simulation [100] [101] [99].

Process	$\sigma[\text{pb}] \cdot BR$	Generator
single top, t channel ($W \to l\nu, l = e, \mu, \tau$)	20.9 (NLO) [95]	`madgraph`
single top, s channel ($W \to l\nu, l = e, \mu, \tau$)	1.5 (NNLL) [111]	`madgraph`
single top, tW channel (inclusive)	10.6 (NLO) [116]	`madgraph`
$t\bar{t}$	163 (NNLL) [112]	`madgraph-tauola`
$W(\to l\nu) + jets$	31,314 (NNLO)	`madgraph-tauola`
$W(\to l\nu) + c(+jets)$	3,628 (NLO) , (****)	`madgraph-tauola`
$Z/\gamma^*(\to l^+l^-) + jets$ (*)	3,048 (NNLO)	`madgraph-tauola`
$V(\to l\nu, l^+l^-) + Q\bar{Q}(+jets)$ (**)	35.8 (LO) , (****)	`madgraph-tauola`
WW	43 (NLO)	`pythia6-tauola`
WZ	18.2 (NLO)	`pythia6-tauola`
ZZ	5.9 (NLO)	`pythia6-tauola`
μ-enriched QCD (***)	84,679 (LO)	`pythia6`

(*) $m_{ll} > 50$ GeV
(**) $V = W, Z; Q = b, c$
(***) $\hat{p}_T > 20$ GeV, $p_T^\mu > 15$ GeV
(****) scale factors from Ref. [107], see text

Table 7.2: Monte Carlo datasets used in this analysis. The samples are generated either inclusively or with a final state restricted to the leptonic mode, including electrons, muons, and taus. Where no references are given, the cross sections come from the generator itself if LO, from FEWZ [118] if NNLO, and from MCFM 5.8 [117] if NLO. The name specifies the tune used for parton fragmentation model (named Z2 or D6),as well as the Monte Carlo generator used for each particular simulation.

All the cross sections have been taken from the references listed in Table 7.2 or, when no reference is given, from the generator itself.

The $W(Z) + jets$ and the $VQ\bar{Q}$ and Wc samples partially overlap, so a splitting procedure based on the so called "MLM prescription" [109] has been applied: we split and re-merge the events into the categories $W(Z)b\bar{b}$, $W(Z)c\bar{c}$, $W(Z)$+light partons, and Wc; the latter is excluded from the $W + jets$ sample, as we prefer to use the higher statistics of the dedicated dataset.The cross section of $VQ\bar{Q}$ and Wc was extracted by a CMS analysis simultaneously measuring $t\bar{t}$ and its main backgrounds' cross sections [107]. This measurement yields a Scale Factors of

$$SF(VQ\bar{Q}) = 2 \pm 1 \tag{7.1}$$

$$\tag{7.2}$$

for $VQ\bar{Q}$ and

$$SF(Wc) = 1^{+1}_{-0.5} \tag{7.3}$$

$$\tag{7.4}$$

for Wc processes with respect to expectations. The simulation of the full detector response is based on GEANT 4 [98], and assumes realistic alignment and calibration, tuned on data. No pile-up was included in these simulated samples. In the running conditions under which most of these data were taken, on average roughly one pile-up event is present in addition to the event giving the trigger. The impact of pile-up on this analysis is estimated in Sec. 7.7.

For this analysis we use the CMS software [103]: an ad hoc package has been developed for this analysis. The developement and implementation of this package part of the work

for this thesis. This analysis is uses the Physics Analysis Toolkit (PAT) of CMS [104] as a starting point, which performs the standard objects reconstruction as described in 4. Non-event data (see 4.1) were extracted from the CMS condition database [126].

7.3 Selection

The final state topology in the t channel is then characterised by exactly one isolated muon and a b jet from the top quark decay, as well as a light flavour jet produced in the forward region. The event selection process can be conceptually divided in two parts:

1. The physics object definition, including the quality criteria to identify the particles and the kinematic cuts and geometric acceptance cuts.

2. The counting of defined objects, adjusted according to the event topology to reproduce.

The reconstruction of higher level physics observables, like in our case top quark reconstructed four momenta (described further on in section 7.4), is performed in parallel to the selection process. In the following part we present the definition of the selected reconstructed muons and electrons, the requirements on the jets, including the definitions of b-tagged jets we chose. The leptons and jets definitions commonly agreed with the other CMS top group analyses in $t\bar{t}$ semileptonic channels (e.g.: [107]). In order to reject and control the QCD events able to survive the selection chain up to this point, we make use of an additional requirement on the transverse W boson mass: events above the threshold pass the selection, while those below the threshold are used in Sec. 7.5.1 to estimate the QCD contamination in the signal region.

7.3.1 Primary vertex, noise cleaning

Prior to any selection, primary vertex quality cuts and cleaning from events presenting spikes in the calorimeters are performed. At least one primary vertex is required to be reconstructed from at least 4 tracks (fit $n_{\mathrm{dof}} \geq 5$) with $|z_{\mathrm{PV}}| < 24$ cm and $\rho_{\mathrm{PV}} < 2$ cm, where ρ is the transverse distance from the center of the detector. Events with high noise in the HCAL barrel or endcaps are discarded using pulse shape, hit multiplicity, and timing criteria.

7.3.2 Physics object definition

The definition of objects is based on the imposition of general quality criteria and kinematic cuts aiming to minimize the fake rate and to get the best possible measurement of physics objects parameters. The physics objects are defined as follows:

- **Tight muons**: Reconstructed muons with a transverse momentum $p_T > 20\ GeV/c$ within the trigger acceptance range ($|\eta| < 2.1$) are selected. The quality of the candidate has to meet the requirements of both a Global Muon and a Tracker Muon (see Sec: 4.2.2 for such definitions), and furthermore be flagged as a global tight prompt muon, i.e. $\chi^2/ndof < 10$ and at least one valid hit in the muon chambers are required. We tighten this selection by requiring more than 10 valid hits in the silicon tracker, out of which at least one in the pixel detector; at least two segments matched to the global muon object in the muon chambers; a distance $\Delta R = \sqrt{\Delta\eta^2 + \Delta\phi^2}$ larger than 0.3 from any jet passing the standard selection defined further on in this paragraph; an absolute 2D impact parameter smaller than 0.02 cm with respect to the center of the estimated beam spot position; a distance of less than 1 cm between

the z coordinates of the leading primary vertex [1] and of the muon track at the point of closest approach. We add an isolation requirement in order to reject muons coming from QCD events cutting on the "relative isolation" variable $Iso_{rel} < 0.05$, defined as:

$$Iso_{track} = \frac{Iso_{track} + Iso_{calo}}{p_T} \, , \qquad (7.5)$$

where Iso_{track} and Iso_{calo} are the sums of the respectively the transverse momenta of the tracks and the transverse energies of ECAL and HCAL deposits in a cone of size $\Delta R < 0.3$ around the lepton direction, excluding the footprint of the lepton itself in the Tracker or Calorimeter.

- **Loose muons**: An additional muon definition is given, with looser identification and kinematic cuts with respect to to the tight lepton. We define "loose muon" by requiring a reconstructed GlobalMuon with $p_T > 10 \ GeV/c$ within the full muon acceptance range ($|\eta| < 2.5$), and $Iso_{rel} < 0.2$.

- **Loose electrons**: We define a "loose electron" [2] candidate requiring a reconstructed electron $E_T > 15 \ GeV/c$, $|\eta| < 2.5$, and $Iso_{rel} < 0.2$.

- **Jets**: Jets are reconstructed using the anti-k_T algorithm (See also Sec. 4.2.4.1, and Ref. [125]) with a cone size of 0.5, using the particle flow algorithm (PF) described in in Sec. 4.2.7. The jet energy is scaled by a factor that describes the detector response depending on the transverse energy and the pseudo-rapidity of the jet [120]. Technically, we apply MC-derived corrections on both data and simulation, and for data we further apply residual corrections derived from data themselves during the spring of 2010. We perform a cut on the jet calibrated $p_T > 30$ GeV/c, and require $|\eta| < 5$. Other quality requirements are that jets must have more than one constituent, and central jets ($|\eta| < 2.5$, namely within HCAL and ECAL acceptance) they must have neutral hadronic, charged electro-magnetic, and neutral electro-magnetic energy fractions smaller than 99%. Furthermore, charged hadronic energy fraction and charged particle multiplicity is required to be larger than 1%.

Jets are within $\Delta R < 0.1$ of a tight muon candidate (taken before the $\Delta R(\mu, jets) > 0.3$ requirement) are rejected.

- **Missing Transverse Energy**: PF $\displaystyle{\not}E_{\mathrm{T}}$ is the opposite of the vectorial sum of the transverse momenta of the identified PF particles. No explicit cut is applied on $\displaystyle{\not}E_{\mathrm{T}}$ in this analysis. A cut on a higher level reconstructed variable (M_T) will be performed.

- **b-tagging**: Several b tagging algorithms are available in CMS, and an overview is provided in Sec. 4.2.6. We use the track counting algorithm, in the "high purity" and "high efficiency" versions. The b-tagging physics object group (POG) proposes a set of three reference thresholds (tight, medium and loose working points) for each algorithm, and for the track-counting family the tight working point corresponds to using the high-purity algorithm with threshold set to 3.41, while the loose working point requires a threshold of 1.7 on the high-efficiency tagger. The advantage of sticking to these reference points lies mostly in the fact that the data/MC scale factors (and corresponding uncertainties) on efficiencies and mistag rates have been evaluated elsewhere [121]. These have been applied to this analysis, and their uncertainty is taken into account as in Sec. 7.7. The tight working point for TCHP

---

[1]If more than one primary vertex is identified, the one with largest sum of the squared transverse momenta of associated tracks is taken.

[2]The denomination "loose" comes from the naming convention adopted within the selection in common to of the CMS top group, where a "Tight" electron is defined.

algorithm, yields find an efficiency of 43% for jets (defined according to our criteria) matched to b quarks, while in the case of the loose working point for the TCHE algorithm such efficiency is 62%. within $\Delta R < 0.3$, with $p_T > 30$ GeV and within the tracker acceptance (i.e., $|\eta| < 2.5$).

7.3.3 Object counting

We define our signal region selecting event which count the following objects responding to the definitions of Sec.: 7.3.2:

- **Lepton counting** We require the presence of exactly one tight lepton. In order to reduce the contribution of dilepton events, which can come from $t\bar{t}$ or from Drell-Yan processes, we veto events with additional loose muons or loose electrons. Figure 7.2 (a) shows the jet multiplicity after the lepton counting in data and simulation. The signal (red) is still overwhelmed by background, in particular $W+$jets and $t\bar{t}$ events. $W+$jets events contaminate lower jet multiplicity bins, while $t\bar{t}$ events dominate higher jet multiplicity bins. Figure 7.2 (b) shows that in most of the signal events two jets are reconstructed, therefore making this bin the most signal efficient.

(a)   (b)
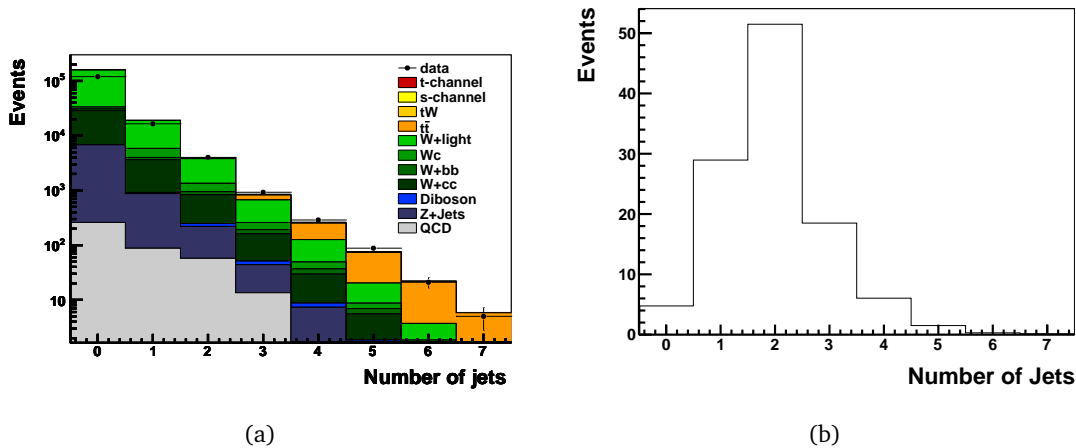
Figure 7.2: Jet multiplicity after the lepton counting in data and simulation (a) and for simulated signal events only (b). Here, and in the following figures, "QCD" is a short-hand notation for multi-jet QCD, $Q = c/b$, and "light" is short-hand for light partons.

- **Jet counting** Sec. 7.3.2, therefore the present study focuses on the 2-jets sub-sample. At this stage of selection the sample is still dominated by $W+$jets processes without b or c quarks, .

- b **counting** The signature of the t-channel single-top production includes 3 partons in the final state, see Fig. 7.1: one light quark recoiling against the virtual W boson, one b quark from the top-quark decay, and a second b quark from the initial gluon splitting. Since the second b quark is most likely produced at very high rapidities, i.e., outside the tracker acceptance of $|\eta| < 2.5$ and thus not allowing b tagging to be performed, we expect most signal events to have only one b-tagged jet. The b-tag multiplicity in 2-jets events is shown in Fig. 7.3 for data and simulation, and in Fig. 7.3(b) for signal and W plus light partons. The contribution of processes without b quarks in the final state is strongly suppressed in the 1-tag sub-sample, showing the largest population of signal events at the same time; the small 2-tags sub-sample is

dominated by $t\bar{t}$. Therefore, selected events are required to have exactly one b-tagged jet. This requirement is further tightened by rejecting the event if the jet which fails the tight b-tagging selection passes the loose one; we call this requirement "b veto" in the following. Figure 7.4 shows the number of b vetoed jets in 2-jets events with one b-tagged.

(a)   (b)
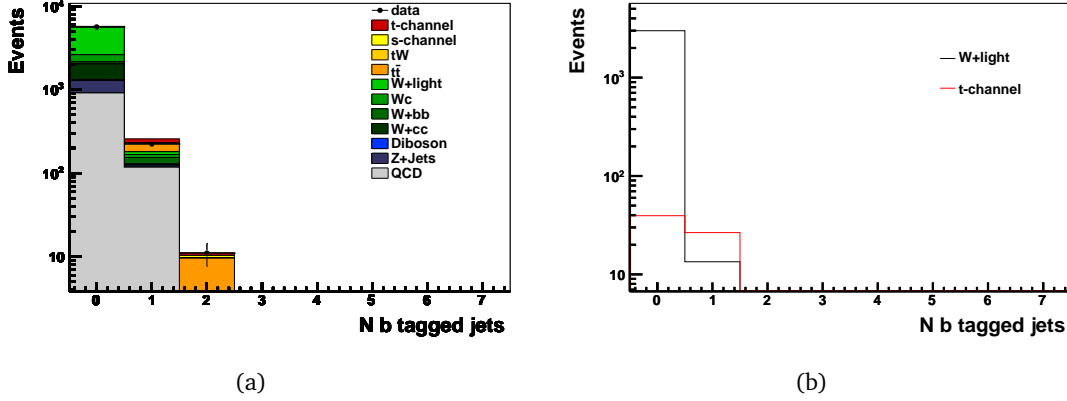
Figure 7.3: Number of tags for $D_{highPur} > 3.41$ for data and simulation (a) and for signal and W plus light partons only (b), after the 2 jets request.

(a)   (b)
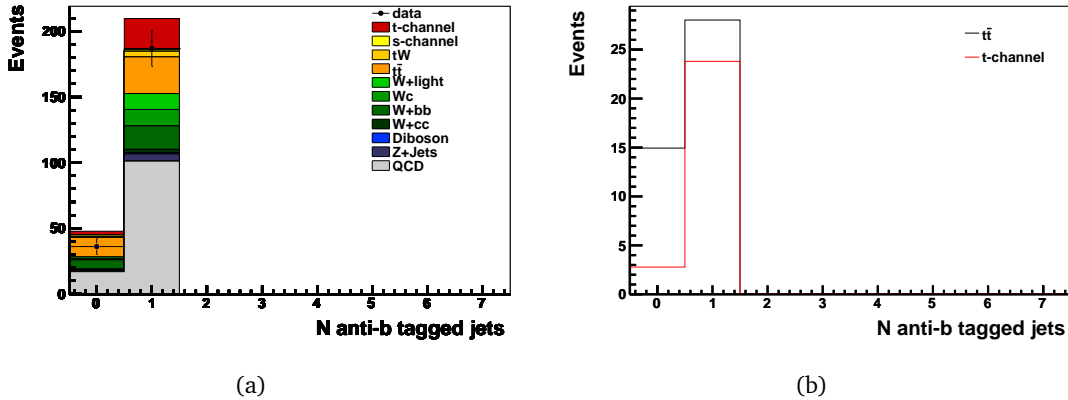
Figure 7.4: Number of anti-tags for $D_{highEff} < 1.7$ for data and simulation (a) and for signal and $t\bar{t}$ (b), after the 2 jets request.

- **Transverse W boson mass** The lepton and neutrino stemming from W boson decay have an invariant mass distribution which is a Breit-Wigner distribution peaked at the W boson mass value. It has to be kept into account that while the transverse momentum components of the neutrino can be reasonably approximated by the components of the missing transverse energy, neutrinos longitudinal momentum is much more difficult to correlate with detector observables, since no reliable estimate of longitudinal energy lost in the beam pipe can be made. A convenient variable to be defined in this situation is the W transverse mass, which is reconstructed out of the transverse components of leptons and neutrino (inferred from $\not{E}_T$):

$$M_T = \sqrt{(p_{T,l} + p_{T,\nu})^2 - (p_{x,l} + p_{x,\nu})^2 - (p_{y,l} + p_{y,\nu})^2} \, , \qquad (7.6)$$

A selection based on the reconstructed transverse W-boson mass is performed. Figure 7.5 b shows the shape of the M_T distribution after the preceding selection. The

QCD background can be nicely distinguished, since the transverse mass of the alleged W bosons accumulates at low values while all processes with real W bosons tend to cluster around the W mass (this feature is known in the literature as "Jacobian peak"). This variable is largely correlated to $\not{E}_T$, so no $\not{E}_T$ cut is performed. We chose

(a)   (b)
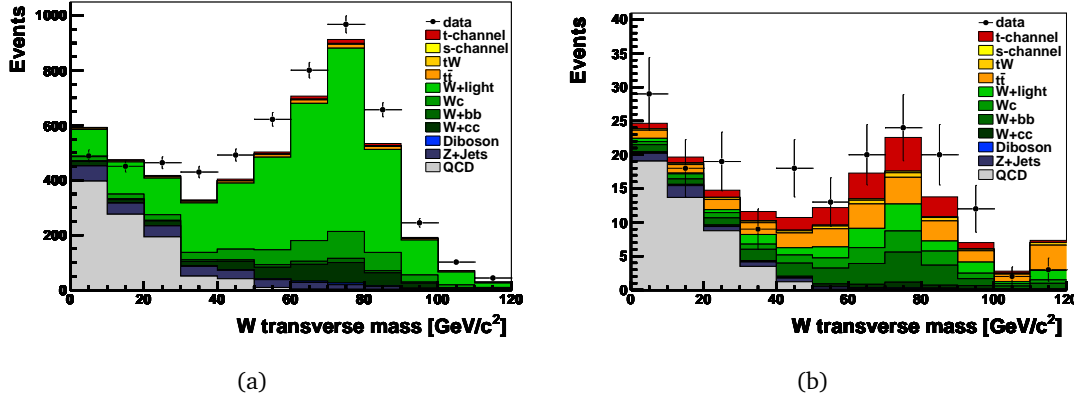
Figure 7.5: Transverse mass after the entire selection minus the M_T cut and the b-tagging requirements (a), and after the b-tagging requirements (b).

this variable over the $\not{E}_T$ since it is more robust against $\not{E}_T$ uncertainty and generally yielding a better discriminating power against QCD events. The M_T distribution is also roughly similar for all non-QCD events, allowing QCD background extraction from data, as presented in Sec. 7.5.1, where the data driven procedure adopted to optimize the M_T threshold is also described.

7.3.4 Selection results

The number of selected events, step by step, in data and simulation is shown in Table 7.3. These number don't take into account the scale factors on leptonic selection derived from data [121]. After the leptonic selection the sample is still dominated by QCD, despite the isolation requirements on the reconstructed muon. This motivates the use of the combined isolation variable Iso_{rel}, and an additional selection on the transverse W-boson mass allows a good QCD reduction. Nevertheless, QCD remains one of the most difficult backgrounds to predict, and Sec. 7.5.1 will be entirely devoted to a data-driven estimation of its contribution. On the other hand, this table shows how the 2-jet requirement reduces both the W+jets and $t\bar{t}$ components of the background, the 1 b-tagged jet requirement reduces the W+light contamination and the loose $b-$jet veto drastically improves the signal to $t\bar{t}$ ratio. An estimation of the light-flavour component will be presented in Sec. 7.5.2. On top of this selection, in Sec. 7.6 the full shapes of two discriminating variables are exploited in order to extract the signal, while minimizing the need of assumptions about the main background processes.

7.3.5 Data-driven scale factors for b-tagging and mistagging

For the tight and loose b-tagging working points used in this analysis ("$TCHPT$" and "$TCHEL$"), respectively for the tagged and veto jets, estimates of the efficiencies of true and fake b-jets identification can be found in Ref. [121], as a function of p_T and η. Only the mistagging rates and their uncertainties were available for 2010 data in the conditions database, therefore a flat b-tagging efficiency scale factor $SF = (90 \pm 15)\%$ was assumed. To correct the simulation mistag rates and b-tagging efficiency each event is weighted by

Process	1 tight muon	2 jets	1 tight b tag	loose b veto	$M_T > 40$ GeV
single top, t channel	145.0	66.9	26.59	23.81	19.37 ± 0.17
single top, s channel	10.07	4.97	2.260	1.128	0.895 ± 0.010
single top, tW	42.16	14.63	5.07	4.29	3.32 ± 0.05
$t\bar{t}$	592.3	103.8	43.0	28.0	22.1 ± 0.3
Wc	5601	483	17.8	17.4	14.0 ± 0.5
$W+$ light partons	147941	3025	17.9	16.7	13.8 ± 1.3
$Z + X$	10659	381	6.6	5.5	1.7 ± 0.3
$V + Q\bar{Q}$	14910	432	19.0	14.3	11.1 ± 0.5
WW	97.29	27.99	0.396	0.363	0.299 ± 0.012
WZ	23.28	6.83	0.484	0.301	0.237 ± 0.006
ZZ	2.622	0.826	0.068	0.0438	0.0182 ± 0.0012
QCD (μ-enriched)	11940	518	55	51	1.3 ± 0.4
Total background	191819	4998	168	139	68.8 ± 1.6
Signal + background	191964	5065	195	163	88.2 ± 1.6
Data	174647	5844	223	187	112

Table 7.3: Number of events surviving each selection step, in data and simulation (normalized to 36.1 pb^{-1}).

the probability of it passing the cuts given the appropriate scale factors. The number of jets N_{BTag}^{data} passing the b-tag cut and the number of jets $N_{AntiBTag}^{data}$ passing the b veto out of a number of jets N corrected by the scale factor is:

$$N_{p,BTag} = \epsilon_{p,data}^{TCHPT} \cdot N = \epsilon_{p,MC}^{TCHPT} \cdot N \cdot SF$$
$$N_{p,AntiBTag} = (1 - \epsilon_{p,data}^{TCHEL}) \cdot N = (1 - \epsilon_{p,MC}^{TCHEL}) \cdot N \cdot SF'$$
(7.7)

where

- $\epsilon_{q,data(MC)}^{TCHPT(TCHEL)}$ is the efficiency ($p = b, c$) or mistag probability ($p = g, u, d, s$) for algorithm *Track Counting High Purity (High Efficiency)* at the tight(loose) working point in data(MC)

- SF_p is the ratio $\epsilon_{p,data}^{TCHPT(TCHEL)}/\epsilon_{p,MC}^{TCHPT(TCHEL)}$

- SF'_p is the ratio $(1 - \epsilon_{p,data}^{TCHPT(TCHEL)})/(1 - \epsilon_{p,MC}^{TCHPT(TCHEL)})$.

- A dependency from η and p_T of the jet is intended but not written explicitly for clarity reasons.

For an event in the 2-jet bin the probability P for an event to pass the full selection is thus calculated as:

$$P(1,2) = P_{b-tag}(1)P_{antib-tag}(2) + P_{b-tag}(2)P_{antib-tag}(1)$$
(7.8)

Where $P_{b-tag}(i)$ is the probability for the i-th jet to be b-tagged and $P_{antib-tag}(i)$ is the probability for the i-th jet to be b-vetoed. From equations 7.7 and 7.8 we find that the corrected number of events N_{corr} is :

$$N_{corr} = \Sigma_{p,q=heavy,light} SF_p SF'_q \cdot N_{(p,q')} + SF'_p SF_q \cdot N_{(p',q)}$$
(7.9)

Where $N_{heavy(light),(light),heavy}$ are the number of events where one heavy(light) flavor jets is passing the b-tag or anti b-tag cut. In order to get the number of events corrected by the scale factors we therefore apply a weight to each jet passing the b (anti b) cut of $SF_{heavy(light)}$ ($SF'_{heavy(light)}$). We assign to each event a weight which is the product of the weight of the jets.

7.4 Discriminating variables

We identified a set of characteristic single top variables in order to further discriminate signal events from background once the baseline selection has been performed.

7.4.1 Light jet pseudorapidity

A firs striking feature of single top events is the presence of a jet generated from the fragmentation of the light quark recoiling against the top quark(see Fig. 7.1). Such jet's characteristic η distribution (Fig. 7.6) stemms from the kinematics properties of the quark scattering against a much more massive object.
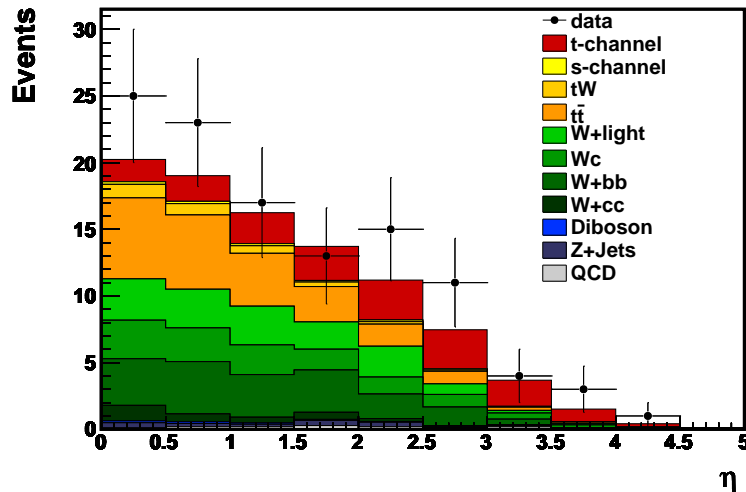
Figure 7.6: Pseudorapidity of the untagged jet (η_{lj}) after the full event selection.

η_{lj} has several advantages that make it an ideal variable for signal discrimination:

- it is a simple kinematic variable, not requiring any high level object reconstruction.
- it has a very characteristic shape for the signal and backgrounds as well, granting a good discriminating power.
- it has low model dependance.

Therefore we use it in a combination with another variable we will describe further on in this chapter (See sec 7.4.5) in an unbinned maximum likelihood fit to extract the signal yield.

7.4.2 Reconstruction of the top quark 4-momentum

We can performing a full reconstruction of top quark 4-momentum reconstruction, which allows us to define discriminating variables reproducing the top quark p_T or invariant mass spectra, as well as to also exploit the $V - A$ nature of the interaction which is

reflected in the top quark polarization and ultimately in the top quark decay products angular distributions. The first step to exploit the the angular properties of single top event topology is to reconstruct the top quark 4-momentum.

7.4.3 W **mass constraint**

We reconstruct the top quark from its decay products, starting from the W boson 4-momentum reconstruction. Starting from the assumption that the x and y components of the missing energy due to undetectable nutrino, we therefore apply a constraint on the invariant mass of the muon-neutrino pair in order to extract the longitudinal component of the neutrino ($P_{z,\nu}$):

$$M_W^2 = (E_\mu + \sqrt{\not{E}_{\mathrm{T}}^2 + P_{z,\nu}^2})^2 - (\vec{P}_{T,\mu} + \vec{\not{E}}_{\mathrm{T}})^2 - (P_{z,\mu} + P_{z,\nu})^2 \ . \tag{7.10}$$

This assumption exploits the fact that the W-boson decay width is smaller than the experimental resolution of the $\not{E}_{\mathrm{T}}$. Equation 7.10 has typically two solutions:

$$P_{z,\nu}^{A,B} = \frac{\mu \cdot P_{z,\mu}}{P_{T,\mu}^2} \pm \sqrt{\frac{\mu^2 \cdot P_{z,\mu}}{P_{T,\mu}^4} - \frac{E_\mu^2 \cdot \not{E}_{\mathrm{T}}^2 - \mu^2}{P_{T,\mu}^2}} \ , \tag{7.11}$$

with

$$\mu = \frac{M_W^2}{2} + \vec{P}_{T,\mu} \cdot \vec{\not{E}}_{\mathrm{T}} \ . \tag{7.12}$$

7.4.3.1   **Complex solutions**

In case of negative discriminant for equation 7.11, which is equivalent to the case where M_T is larger than the W pole mass used in the constraint, the solutions have an imaginary part. This happens in 36.0% of the cases, and is related to the finite resolution of $\not{E}_{\mathrm{T}}$ (and to a much smaller extent, of muon momentum and the non-zero W).

To deal with this situation we remove the imaginary component by modifying the $\not{E}_{\mathrm{T}}$ imposing $M_T = M_W$ and Eq. 7.10 simultaneously: this is done imposing the discriminant in Eq. 7.11 to be zero. This of course implicitly means that neutrino momentum components $p_{x,\nu}$ and $p_{y,\nu}$ are not directly inferred from the components of the $\not{E}_{\mathrm{T}}$. This means that the system of equations loses two constraints on the neutrino momentum componensts and gains one constraint, namely $M_T = M_W$. To choose a solution for the system we chose the solution which minnimizes the distance between $p_{T,\nu}$ and $\not{E}_{\mathrm{T}}$ $\Delta(p_{T,\nu}, \not{E}_{\mathrm{T}})$.

$\Delta(p_{T,\nu}, \not{E}_{\mathrm{T}})$ is a function of both $p_{x,\nu}$ and $p_{y,\nu}$ while the constraint $M_T = M_W$ allows to write $p_{y,\nu} as a function of (p_{x,\nu})$, so the minimization of $\Delta(p_{T,\nu}, \not{E}_{\mathrm{T}})$ can be done analytically writing its derivative with respect to $p_{x,\nu}$:

$$\frac{d\Delta(p_{T,\nu}, \not{E}_{\mathrm{T}})}{dp_{x,\nu}} = 0; \tag{7.13}$$

This results in a third order equation which can be solved and whose solutions multiplicity can be reduced to 1 easily ruling out the unphysical cases.

7.4.3.2   **Ambiguity resolution and event interpretation**

In the case of two real solutions for $P_{z,\nu}$ we choose the solution with the smallest absolute value of $P_{z,\nu}$.

A similar two-fold ambiguity is however always present in when reconstructing a top-quark hypothesis, since two jets are selected. The ambiguity is resolved by assigning the b-tagged jet to the top-quark decay.

The b-tagged jet matches the true b quark from top-quark decay in 43% of the selected signal events, using as matching criterion a distance of $\Delta R < 0.3$ from the parton.

7.4.4 Reconstructed top-quark mass
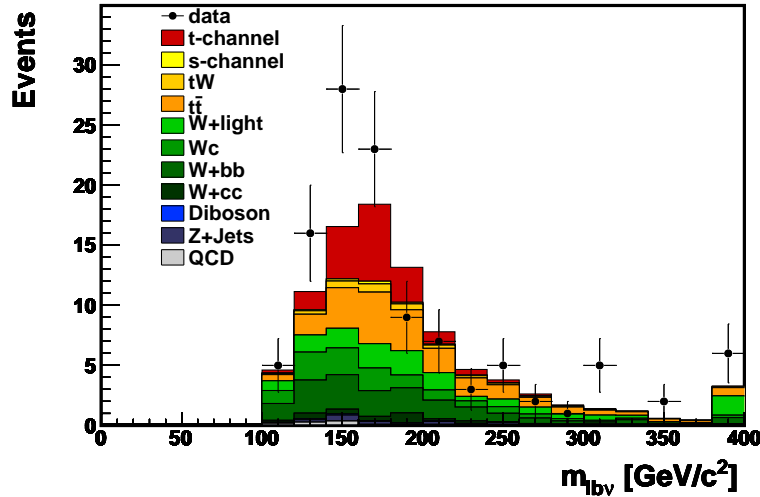
Figure 7.7: Reconstructed top-quark mass after the full selection. The last bin also contains events with $M_{bl\nu} \dot{\iota} 400 \ GeV/c^2$.

Figure 7.7 shows the mass of the reconstructed top quark ($M_{bl\nu}$) for events passing the baseline selection. $t\bar{t}$ events present a peak at top mass which is broader with respect to signal events. In semileptonic $t\bar{t}$ events this is mainly due to the fact that two b quark from top quark decay are present, so the b-tagged used for top reconstruction jet has roughly 50% chance to stem from the same top quark decay as the lepton. On the other hand in $t\bar{t} \rightarrow 2l$ events (including tauons) the missing energy gets contributions by more than one neutrino.

7.4.5 Top quark polarization angle

The $V - A$ structure of the weak interaction, causes the top(anti-top) quark to have an almost 100% left(right)-handed polarization with respect to the spin axis [123]. Angular correlations in the top quark decay products keep track of the top quark spin direction. We can write:

$$\frac{1}{\Gamma}\frac{d\Gamma}{d\cos\theta^*} = \frac{1}{2}(1 + A\cos\theta^*) , \qquad (7.14)$$

where θ^* is the angle between the direction of the outgoing particle and the spin axis, in the top-quark rest frame. A is a coefficient of spin asymmetry, which depends on the identity of the particle and is equal to $+1$ for charged leptons.

We make use of the "spectator basis" (see, e.g., Ref. [123]), where θ^* the angle θ^*_{lj} between the lepton momentum and the light quark momentum, in the top quark rest frame. We reconstruct this observable taking the direction of the untagged jet is chosen as spin axis and the boost in the top quark rest frame is performed taking the 4-momentum of the top from our reconstruction.
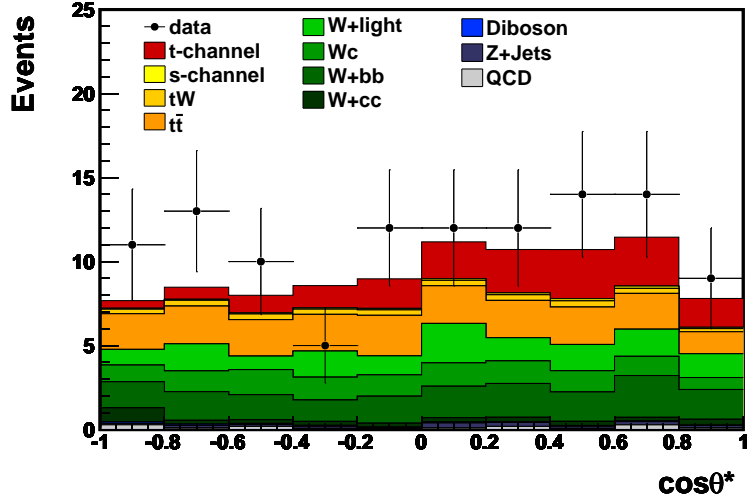
Figure 7.8: Cosine of the angle between charged muon and untagged jet, in the
reconstructed top rest frame after the full event selection.

Figure 7.8 shows the distribution of the $\cos\theta^*_{lj}$ variable. The dip at $\cos\theta^*_{lj} \approx 1$ is mainly
due to the particular muon requirements: the distance ΔR in the $\eta - \phi$ plane between the
muon and the light jet in fact cannot be $\Delta R < 0.3$ due to explicit selection requirements
and to Iso_{rel} cuts. The sensitivity of the shape of this variable to some modeling effects,
have been studied at generator level in Ref. [110], and after full reconstruction in previous
Monte Carlo studies.

7.5 Background description

7.5.1 QCD

Monte Carlo estimations of the QCD contamination have to be considered particularly
unreliable for the purposes of our analysis, because only extreme kinematical regions pass
this kind of selection, and tail effects are the most difficult to simulate properly. These
arguments lead to the conclusion that only *in situ* data-driven estimations will give the
needed confidence on the amount of this background.

We use the M_T distribution, after all other cuts have been applied, to estimate QCD
with an unbinned maximum likelihood template fit. The word "template" will be used
hereafter to indicate a probability distribution function taken from a simulated or real data
distribution, after it has been properly normalized. In order to reduce to the minimum
the dependence on simulated QCD we make use of a control sample to extract template
extracted from data and a single template for the sum of "signal-like" processes. Here and
in the following, when we refer to QCD extraction with signal-like events we mean all
events where the lepton comes from the decay of a W boson, including for example $t\bar{t}$ and
W+jets. We fit the formula

$$F(M_T) = a \cdot S(M_T) + b \cdot B(M_T) \, , \tag{7.15}$$

where $S(M_T)$ and $B(M_T)$ are the assumed templates for signal-like and QCD events
respectively, letting only a and b fluctuate in the fit. Since we wish to avoid, as much
as possible, model dependent assumptions for QCD, we extract $B(M_T)$ from a control
sample designed to have high statistics and to be kinematically similar to the selected
sample. Figure 7.9(a) shows that the M_T distribution for QCD is not dramatically affected

Process	$N_{evtpre-tag}$	$N_{evtfullselection}$
QCD	$15.3 \cdot 10^4$	$15.1 \cdot 10^2$
$signal$	1.1	0.044
$t\bar{t}$	1.7	0.029
$W + X$	61.2	0.29
Data	$8.05 \cdot 10^4$	$9.05 \cdot 10^2$

Table 7.4: Event yield for the main processes in the QCD-enriched selection before the b-tagging requirements and after full selection for muon channel

by isolation requirements for the muon channel. The observed difference difference in the tail goes in the "conservative" direction. This suggests the idea of removing or inverting this cuts in order to enlarge the statistics for control samples. In particular, in order to extract a QCD-enriched sample, we apply a dedicated selection which differs from the standard one by the absence of b-tagging requirements and by an anti-isolation cut ($Iso_{rel} > 0.2$ for muons) intended to get rid of most of the signal-like events. The event yields for this selection are given in Table 7.4, and the M_T distribution shown in Fig. 7.9(b) is used as a template for the $B(M_T)$ shape. In order to test the stability of the fit we changed the range of the fit and check the consistency of the results. The systematics uncertainty is then conservatively estimated as the maximum between 50% and the maximum shift from the central value. Table 7.5 shows the results for the fit in the different fit ranges.

(a)   (b)
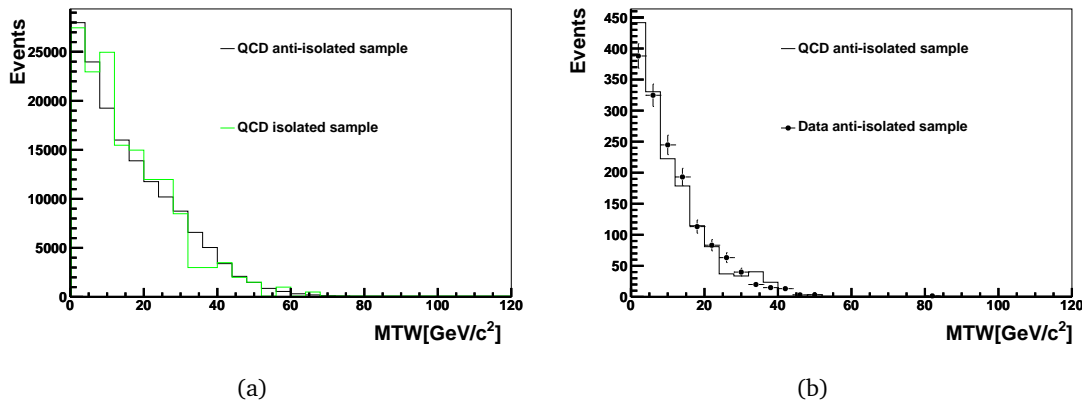
Figure 7.9: a: M_T distributions for simulated QCD samples obtained removing the b tagging from the standard selection, after an anti-isolation cut, $Iso_{rel} > 0.2$ (green) and after the standard isolation cut (black). b:M_T distribution for the QCD-enriched control sample, in data and simulation.

Figure 7.10 demonstrates that the M_T shape is almost the same for signal and $W + jets$ events, and still quite similar for $t\bar{t}$ despite the occasional presence of events with two final-state neutrinos which broaden the distribution. However, since this QCD estimation can afford a certain degree of approximation, and since the modeling of the signal-like components turns out to be uncritical for this study we consider all the non-QCD processes in the same cathegory and take the $S(M_T)$ shape from simulation. In a couple of alternatives have been tested in the past, (Ref. [124]) for the data-driven extraction of $S(M_T)$ as well, based on a W- and Z-enriched sample, in order to further robustify the analysis against possible problems in $\not{E}_T$ reconstruction. The stability of the fit, the good degree of control over this variable and the low impact on the final result (see Sec 7.7) are such that it is not necesary to perform a shape extractions for the signal.

The fit has also been exploited to choose the optimal M_T threshold without using
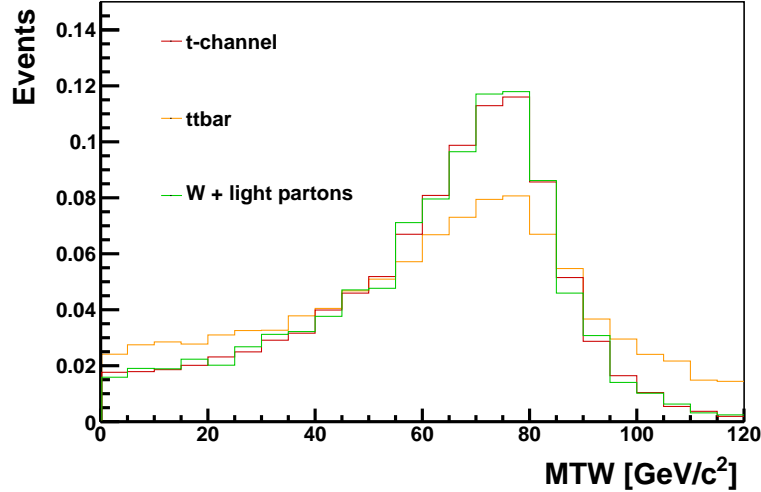
(a)

Figure 7.10: M_T distributions for some signal-like processes: signal (red), $t\bar{t}$ (yellow) and W + light partons (orange). The events have passed a selection that differs from the standard one only for the anti-isolation requirement.

simulation. With the first 15.1 pb^{-1} we have used a data-driven method to choose the threshold on M_T. We selected 72 events in this sample passing the single-muon selection and the request of exactly two jets. When the isolation cut is inverted, 2408 events are selected. Figure 7.11 show the result of a template fit to the M_T distribution, taking the signal-like shape from W+jets simulation and the QCD shape from the anti-isolated sample. We obtain an estimation of 18 QCD events and 54 W+jets events. As a figure of merit we
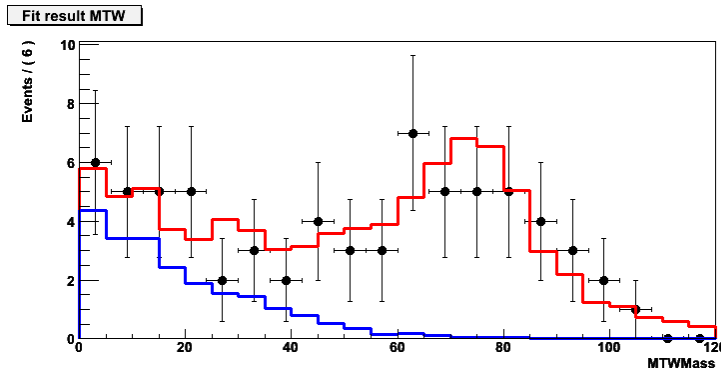
Figure 7.11: M_T fits for QCD with the data-driven template for 15.1 pb^{-1}.

chose

$$FOM = S/\sqrt{S + B + (kB)^2}, \tag{7.16}$$

where kB is the expected uncertainty on the QCD estimation, put at 50% as conservative estimate. This figure of merit is chosen in order to keep into account in a simple way QCD background fluctuation due to the systematics uncertainty. Figure 7.12 shows how this figure of merit is maximised by a 40 GeV/c^2 threshold. The prediction for QCD contamination in the signal region is calculated as $b \cdot \int_{cut}^{\infty} B(M_T) dM_T$, where *cut* is $40 GeV/c^2$. The result in this study is based on the $B(M_T)$ shape extracted from the QCD-enriched sample, and the $S(M_T)$ shape from simulation, yielding a prediction of $43 \pm 9(57 \pm 11)$ events after full selection apart from the M_T cut, and $0.62 \pm 0.12(2.6 \pm 0.6)$ events above the cut. To check the stability of the fit with respect to variation of the background model we also
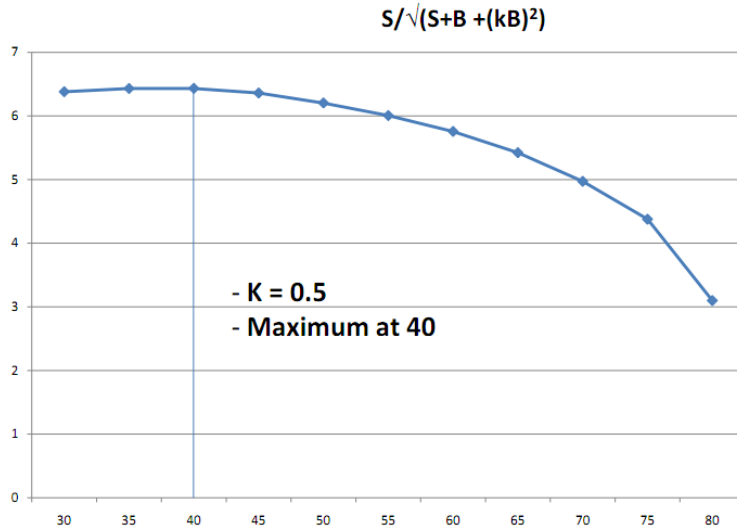
Figure 7.12: M_T fits: scan of the figure of merit $S/\sqrt{S+B+(kB)^2}$ as a function of the threshold for the cut.

perform the fit using the Monte Carlo distribution of the QCD-isolated pre-tag sample in Figure 7.13 . With this background model the fit yields a result of $0.70 \pm 0.13(2.6 \pm 0.6)$ events in the muon decay channel passing the selected cut for M_T, see Table 7.5. The absolute value of the difference between the results of the fits with the two models is reported as systematic uncertainty on the QCD yield and summed to the statistical uncertainty from the fit procedure.

(a)   (b)
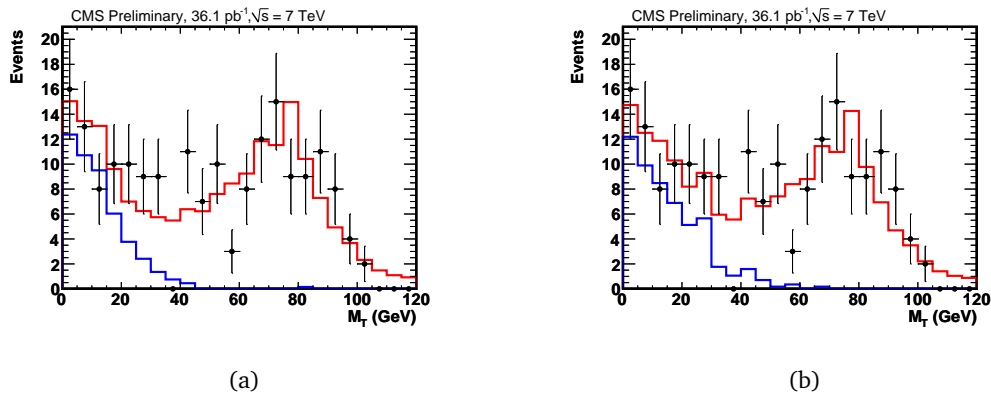
Figure 7.13: M_T fits for QCD with the data-driven template for QCD (a), and Monte Carlo template extracted from pre-tag isolated sample (b). The difference of those values is summed to the statistics uncertainty on the fit and used as systematics on the QCD prediction.

This procedure yields the following predictions for the number of QCD events passing the M_T threshold in the 2D analysis:

$$N_{qcd} = 0.62 \pm 0.12(stat.) \pm 0.08(shape) \pm 0.15(stability) \qquad (7.17)$$

where "$shape$" indicates the systematic uncertainty coming from the $B(M_T)$ model, estimated by comparing with the result of a fit performed with an M_T shape taken from simulated QCD events with no b-tagging requirement (in order to enhance the available statistics of simulated events) but with the standard isolation request; "$stability$" indicates the maximum variation between the results when variating the fit range ($10 < M_T < 200\,GeV/c^2$,

QCD Model	N_{qcd}, full fit range	N_{qcd}, M_T cut
data-driven	43 ± 9	0.62 ± 0.12
MC pre-tag	49 ± 11	0.70 ± 0.13
data-driven range 10-200	24 ± 7	0.77 ± 0.2

Table 7.5: Result of the fits on W transverse mass using the QCD model from the anti-iso sample (data-driven) or from the Monte Carlo pre-tag sample.

taking the maximum variation as a symmetric uncertainty).We make hereafter use of the central values of these predictions, while the uncertainties on these values are conservatively taken as $max(50\%, stat \oplus shape \oplus stability)$, therefore $\pm 50\%$.

For the template fits we will consider the shape of the discriminating variables obtained by the QCD control sample, after having checked that it is consistent with the Monte Carlo expectation for it, normalized to the prediction obtained in this section.

7.5.2 $W+$**light partons**

$W+$jets events surviving the baseline selection result from a mixture of W + light partons (u, d, s, g) events and W + heavy partons (c, b) events. We alro refer to W + light (heavy) partons as W + light (heavy) flavours. An accurate simulation of $W+$light and $W+$HF events is crucial for signal extraction, therefore ad hoc Monte Carlo samples are used for the W + heavy flavor channels. We use the already mentioned MLM prescription to remove double counting and allow for a coherent sum of all contributions. Jets are matched with the closest partons in the $\eta - \phi$ plane. The events where there are two jets associated to c, b partons from the Matrix Element(ME) are taken from the $VQ\bar{Q}$ ($Q = c, b$) sample. The events where there are two jets associated to c, b partons from Parton Shower (PS) are taken from the $W + jets$ sample. Events where there is one jet is associated to a c quark are taken from the Wc sample if the c quark comes from the ME, and from the $W + jets$ sample if the c quark comes from the PS. The W + light flavor events are entirely extracted from the $W + jets$ sample, vetoing all the heavy flavor components. The relative contribution of light and heavy flavour is then fixed and the samples are normalized to the NLO cross section. The normalization to the NLO cross section is taken from the $W + Jets$ sample: we normalize to take the event yield of the $W + Jets$ sample scaled to NLO without any flavor requirement. W + light flavour events surviving our selection are constrained to extreme kinematic regions, therefore to have a reliable template for signal extraction procedure we use a partially data-driven method to extract the shape of $W+$light variables. The $W+$light flavors processes events are the most abundant in the 2 jet bin from Fig. 7.2, i.e. after the lepton selection and before the tagging requirements. To constrain the $W+$light and $W+$HF backgrounds we define two control samples in the 2 jet bin:

- control sample "A" is defined by having the highest-TCHP jet failing the tight TCHP threshold;

- control sample "B" is a sub-set of A, where the highest-TCHP jet fails the tight TCHP threshold but passes the loose TCHE threshold.

Those samples are both orthogonal to the signal region. Table 7.6 report the number of events in sample A from MC and data. We extract the shape of η_{lj} and $\cos \theta_{lj}^*$ for $W+$light partons from sample A. This is done under the assumption that the b-tagging requirements do not critically affect the kinematics of $W+$light jets or the $\cos \theta_{lj}^*$ reconstruction and that other background contributions do not significantly affect the shape of such sample. For events passing the selection in sample A we apply the top reconstruction described

Process	$N_{evt,\mu}$
$W+$ light partons	2476
Wc	408
$Wc\bar{c}$	584
$Wb\bar{b}$	118
$t\bar{t}$	81
QCD	57
signal	54
MC total	3774
Data	4010

Table 7.6: Event yield for the main processes in the W-enriched selection "A".

Process	SF from region A	SF from region B
μ channel	1.02 ± 0.03	1.27 ± 0.09

Table 7.7: Scale factors for W+light partons predicted by the fits in control regions A and B. Uncertainties are statistical only.

in Section 7.4.2. We use the jet with the highest value of the b-tag TCHE algorithm to reconstruct the top quark momentum. Figures 7.15 (a,b) and show the distribution of $\cos\theta_{lj}^*$ and η_{lj} for data and Monte Carlo in theis control sample. Figures 7.16, 7.17, 7.18, and 7.19 show the two variables $\cos\theta_{lj}^*$ and η_{lj} for the W+light,$W + bb$,$W + cc$,and $W + c$ channels in the W-enriched sample and after full selection. Figures 7.14 shows the $\cos\theta_{lj}^*$ and η_{lj} distributions for W+light partons in Monte Carlo compared with the distribution extracted from control sample A in data. The shapes for W+bb,W+cc and Wc with this selection are then used as templates for the same variables in the signal region for the signal yield extraction procedure.

(a)   (b)
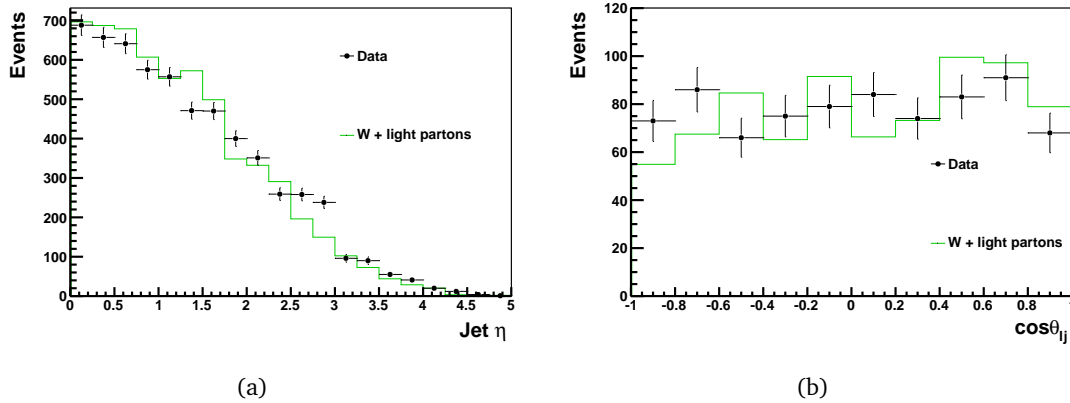
Figure 7.14: Distributions of η_{lj} (a) and $\cos\theta_{lj}^*$ (b) in the W-enriched sample A for data and W + light flavors Monte Carlo.

We perform an unbinned maximum likelihood fit to M_T distribution in both control samples A and B to estimate the QCD contamination, in the same way it is described in Section 7.5.1 for the signal region. We take the template for QCD distribution from the selection of samples A and B with inverted isolation cut (as in Sec. 7.5.1). The results of the fit in both control regions are shown in Figure 7.20 and in Table 7.7.

(a)   (b)
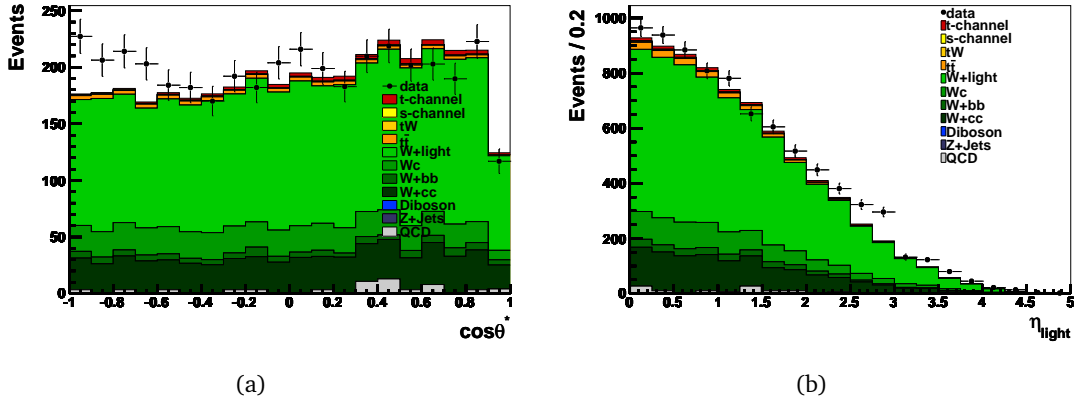
Figure 7.15: Distributions of η_{lj} (a) and $\cos\theta_{lj}^*$ (b) in the W-enriched sample A for data and Monte Carlo, normalized to the luminosity of the sample.

(a)   (b)
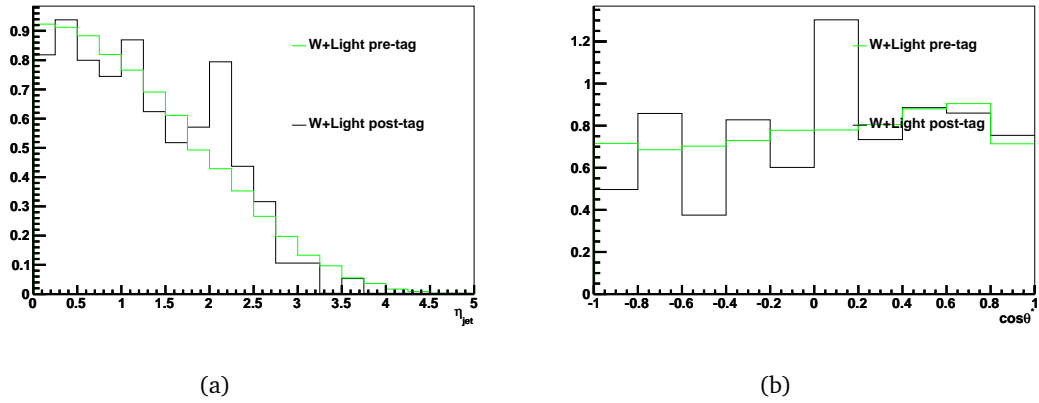
Figure 7.16: Distributions of η_{lj} (a) and $\cos\theta_{lj}^*$ (b) in the W-enriched sample A and after full selection for W + light flavors Monte Carlo.

(a)   (b)
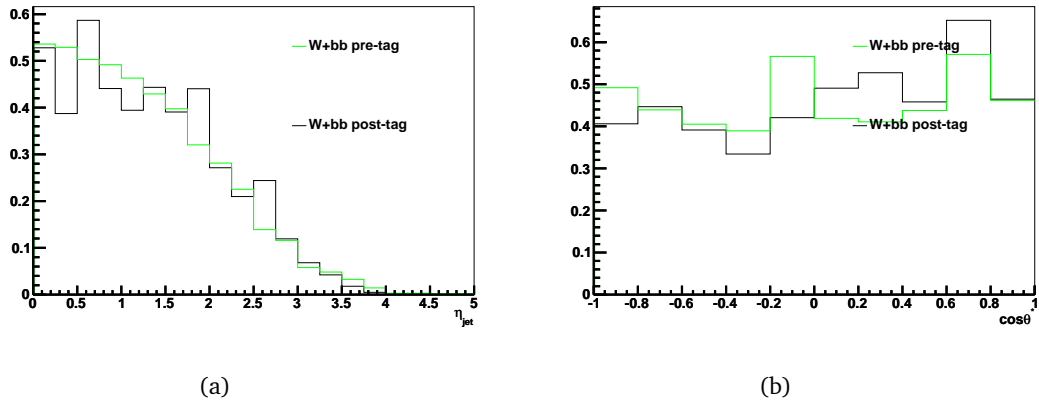
Figure 7.17: Distributions of η_{lj} (a) and $\cos\theta_{lj}^*$ (b) in the W-enriched sample A and after full selection for $Wb\bar{b}$ Monte Carlo. The parton showering component taken from the W+jets sample is also shown in this plot and is the main responsible for the statistical fluctuation. The shape of the variables for the fit are thus taken from W-enriched sample.

We take as central predictions those from control sample B, upon the argument that it is closer to the signal region, obtaining an expectation of 18.2 W+light parton events

(a)   (b)
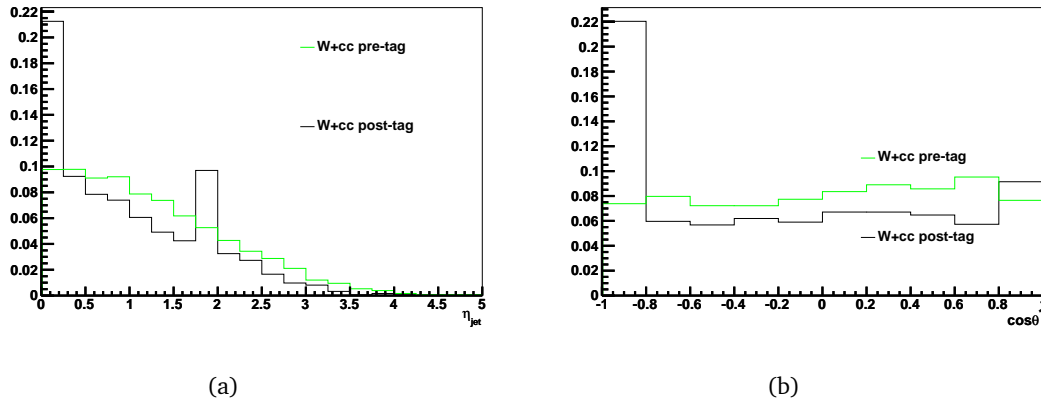
Figure 7.18: Distributions of η_{lj} (a) and $\cos\theta^*_{lj}$ (b) in the W-enriched sample A and after full selection for $Wc\bar{c}$ Monte Carlo. The parton showering component taken from the W+jets sample is also shown in this plot and is the main responsible for the statistical fluctuation. The shape of the variables for the fit are thus taken from W-enriched sample.

(a)   (b)
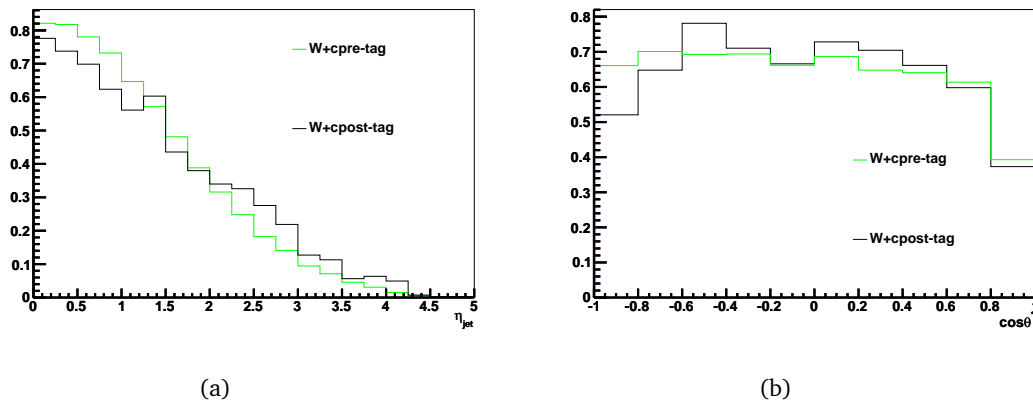
Figure 7.19: Distributions of η_{lj} (a) and $\cos\theta^*_{lj}$ (b) in the W-enriched sample A and after full selection for W + c Monte Carlo.

(a)   (b)
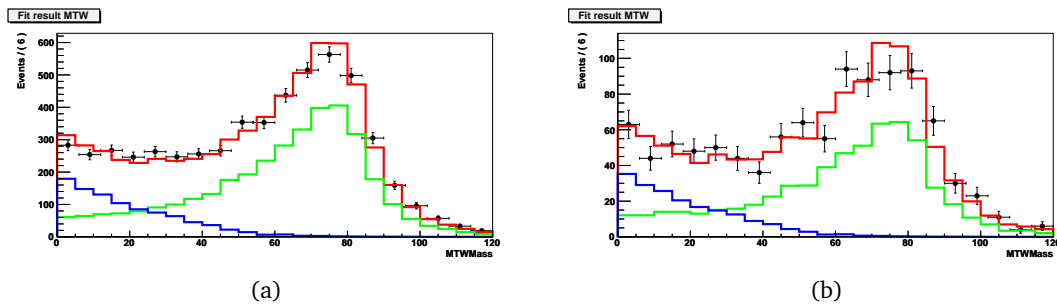
Figure 7.20: M_T fits in control region A (a) and in control region B (b).

in the signal region, and we assign a $\pm 30\%$ uncertainty to these numbers, which by far covers both the statistical uncertainty from the fit and the difference between A and B predictions, therefore it is a conservative assumption. This is taken into account as a rate systematic in section 7.7. The same scale factors are applied to Z+jets.

7.5.3 $W+$ **heavy flavours**

As already anticipated an estimation of the heavy flavour component of $W + X$ was taken from an independent measurement [107], including the corresponding range of variation. We doubled the uncertainties of Ref. [107] to keep conservatively into account the fact that we propagated the $VQ\bar{Q}$ and Wc Scale Factors obtained in a different phase space region for such processes. The central values plus uncertainties that we assign to such Scale Factors are therefore:

$$SF(VQ\bar{Q}) = 2 \pm 2 \tag{7.18}$$
$$SF(Wc) = 1^{+2}_{-1.} \tag{7.19}$$

We get confidence in the adequacy of this hypothesis by comparing data and Monte Carlo in both the signal region and in the W-enriched control sample A of the previous subsection with and without these scale factors, see Figure 7.21. We conclude that the application of these scale factors improves the agreement between data and Monte Carlo in the control region, although it does not impact enough the signal region to explain the observed excess of data, which we attribute to an excess of signal with respect to the Standard Model expectation.

(a)

(b)
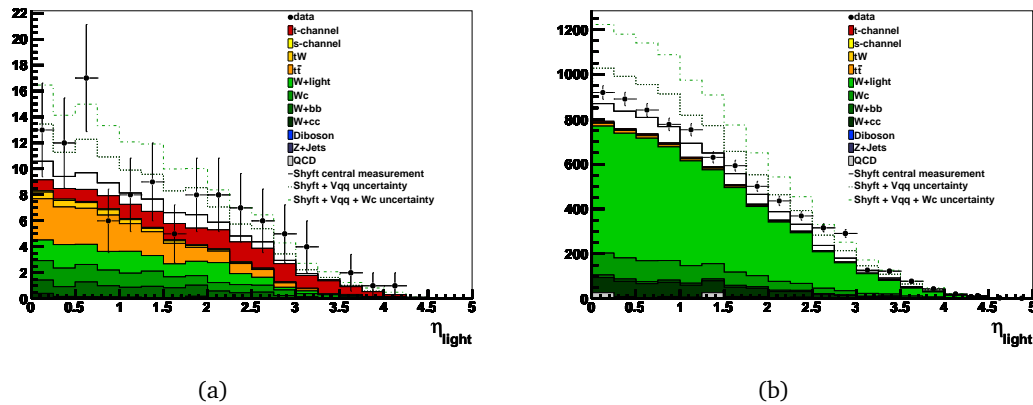
Figure 7.21: Distribution of η_{lj} in the signal region (a) and in the W-enriched control sample A (b), with and without the scale factors from Ref. [107].

7.5.3.1   Backgrounds summary

In the rest of this document the QCD and $W+$ light partons backgrounds are normalized to the predictions of the data-driven procedures described in this section. The normalization of $Z+$ jets (irrespective of the flavour of the associated partons) is scaled by the same factor as $W+$ light partons. The $VQ\bar{Q}$ and Wc components are scaled to LO values and, on top of this correction, by further factors 2 ± 1 and $1^{+1}_{-0.5}$, respectively, in order to take into account the results of the $t\bar{t}$ cross section measurement exploiting b-tagging [107], from which we also take the $t\bar{t}$ cross section itself. The theory prediction is used for VV [118] and single top in s [111] and tW [116] channels. The uncertainties on these values are considered as components of the systematic uncertainty, see Sec. 7.7.

Table 7.8 summarizes the event yields used as input in the analysis, corrected for all the Data/MC scale factors.

Process	
single top, t channel	17.6 ± 0.7 *
single top, s channel	0.9 ± 0.3
single top, tW	3.1 ± 0.9
WW	0.29 ± 0.09
WZ	0.24 ± 0.07
ZZ	0.018± 0.005
$W+$ light partons	18.2 ± 5.5
$Z + X$	1.7 ± 0.5
QCD	0.6 ± 0.3
$VQ\bar{Q}$	20.4 ± 10.2
Wc	$12.9\,^{+12.9}_{-6.5}$
$t\bar{t}$	20.3 ± 3.6
Total background	78.6 ± 15.2
Signal + background	96.2 ± 15.3
Data	112

Table 7.8: Event yields summary, including data-driven estimations and b-tagging scale factors. The signal (*) in this table is normalized to the 5-flavour computation with the corresponding uncertainty [113]. Background uncertainties are discussed in Sec. 7.7.

7.6 Signal extraction

A 2D unbinned maximum likelihood fit is performed to $\cos\theta^*_{lj}$ and η_{lj} distributions to determine the signal cross section. Our free parameters are the signal and background yield, where the individual components of the overall background are constrained but the sum is not. The idea behind this choice is to be maximally robust against background uncertainties, taking advantage of the small difference in shape for the individual background components in the two observables considered.

7.6.1 Likelihood function

We define the unbinned likelihood function given by:

$$L(cos\theta^*_1, ..., cos\theta^*_n, \eta_1, ..., \eta_n | N_s, N_b) =$$

$$e^{-(N_s+N_b)} \cdot (N_s + N_b)^n \prod_{k=1}^{n} \frac{1}{N_s + N_b}\left(N_s \cdot P_s(cos\theta^*_k, \eta_k) + N_b \cdot P_b(cos\theta^*_k, \eta_k) \right)$$

$$(7.20)$$

where N_s, N_b are the signal and background yields, n is and number of observed events, and P_s, P_b are the signal and background distribution functions. Since $\cos\theta^*_{lj}$ and η_{lj} are weakly correlated variables (we estimated, with Monte Carlo, a correlation of 6% for signal and 2% for the overall background), we factorize P_s and P_b into the product of separated functions: $P_s = F_s(cos\theta^*) \cdot G_s(\eta)$ and $P_b = F_b(cos\theta^*) \cdot G_b(\eta)$. The extended maximum likelihood fit gives us the best estimation of N_s and N_b, with the model distributions considered fixed and taken from Monte Carlo templates. To be more specific, the background term in equation 8.10 is given by:

$$N_b \cdot F_b(cos\theta^*) \cdot G_b(\eta) = \sum_i N_{b_i} \cdot F_{b_i}(cos\theta^*) \cdot G_{b_i}(\eta) \qquad (7.21)$$

where i runs over all the backgrounds (whose relative normalizations are taken from Monte Carlo). The fit results are shown in Fig. 7.22 and the estimated yields are:

$$N_s = 27.2 \pm 11.2 \quad N_b = 84 \pm 14$$

(a)
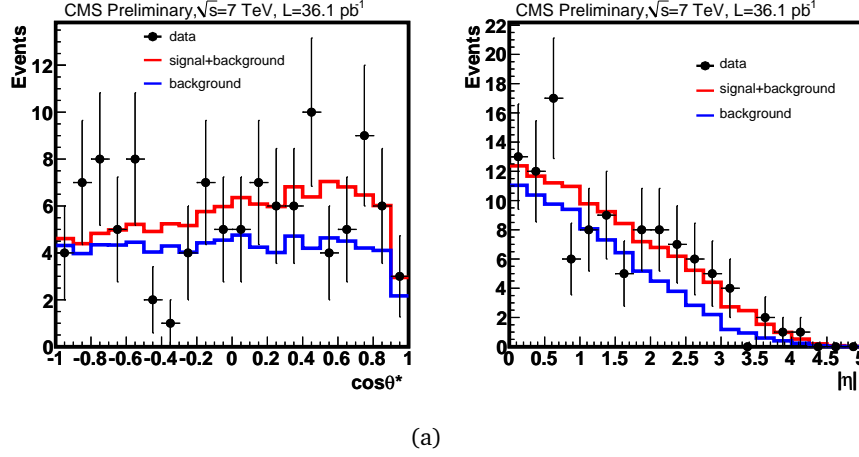
Figure 7.22: Fit to $\cos\theta^*_{lj}$ and η_{lj} and profile likelihood plot.

7.6.2 Significance estimation

Our sensitivity to the single top signal has been computed using two methods: profile likelihood and CL_b method.

Profile likelihood method

We define the test statistics λ as:

$$-2\ln\lambda(N_s) = -2\ln\left(\frac{L(N_s, \hat{\hat{N}}_b)}{L(\hat{N}_s, \hat{N}_b)}\right) \tag{7.22}$$

where $L(\hat{N}_s, \hat{N}_b)$ is the maximum likelihood value obtained from the best fit to the data, while $L(N_s, \hat{\hat{N}}_b)$ is the maximum value obtained by fixing N_s and fitting N_b. By varying the signal hypothesis N_s we obtain the profile likelihood function from which we can extract the significance of our single top signal. Using Wilks' theorem, $-2\ln\lambda(N_s)$ is asymptotically distributed as a $\chi^2(1)$ (that is, profile likelihood curve has a parabolic shape) so that:

$$-2ln\lambda(N_s) = -2(lnL(N_s) - lnL(\hat{N}_s)) = n_\sigma^2 \quad \text{with} \ n_\sigma = \frac{N_s - \hat{N}_s}{\sigma} \tag{7.23}$$

where σ represents the Gaussian standard deviation of the parameter N_s.

As a test for reliability of the profile likelihood estimator of significance, we perform 2,000 pseudo-experiments that are diced according to the background-only hypothesis. The significance obtained from such experiments is plotted in Figure 7.23 (a), and shows a good agreement with a one-tailed Gaussian distribution. As further check, the agreement with a Gaussian distribution is observed as well for a set of pseudo-experiments diced in the signal + background hypothesis (as shown in Figure 7.23 (b)). The mean and RMS of significance distribution for signal + background hypothesis is:

(a)   (b)
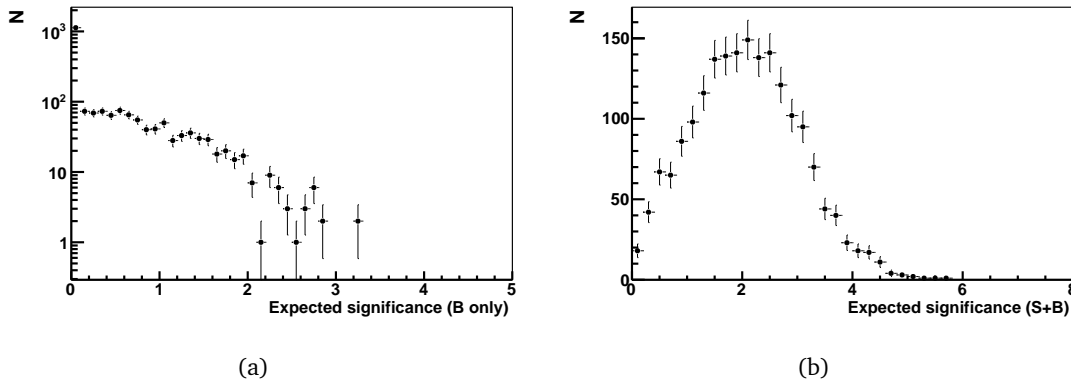
Figure 7.23: Expected significance for the background-only (a) and signal + background (b) hypothesis in terms of Gaussian standard deviations for 2,000 pseudo-experiments (systematics not included in this plot).

$$\sigma = 2.0 \pm 1.1 \tag{7.24}$$

The estimated significance for our signal is:

$$n_\sigma = 2.83 \tag{7.25}$$

whereas the expected significance is

$$n_{\sigma,exp} = 2.0; RMS_{n_{\sigma,exp}} = 1.1 \tag{7.26}$$

To keep into account the systematic uncertainties in the significance calculation we use the CL_b method.

CL_b **method**

The fraction of signal events in the selected data set is estimated by means of a binned likelihood fit. Simultaneously, also the contributions of the main background processes are fitted. In a binned likelihood fit the number of expected events μ_i in each bin i of the distribution of the variable of choice is compared to the observed number of events in this bin (n_i).
The number of expected events in bin i is given by:

$$\mu_i = \sum_k \beta_k \cdot \alpha_{ik} \ , \tag{7.27}$$

where the fit parameters β_k give the ratio between the fitted fraction and the expected fraction of events for component k,

$$\beta_k = \frac{\sigma_k}{\sigma_k^{\text{pred}}}. \tag{7.28}$$

α_{ik} is the predicted number of events for bin i of process k. For fixed k, this is a template, normalized to the expected number of events.

For the CL_b method, the fit has two components and thus k takes only two values to denote signal or background.

Measured	Median	68% range
2.83	1.9	0.9 - 3.0

Table 7.9: Measured, and expected median and central 68% range of the expected significance values in the signal + background hypothesis.

To test the signal + background hypothesis against the background only (null) hypothesis we define a likelihood ratio test statistic Q as:

$$Q = -2ln\left(\frac{L_{s+b}}{L_b}\right) \tag{7.29}$$

Here L_{s+b} is the likelihood function defined in equation 7.20, while L_b is the background only likelihood (with $N_s = 0$). We generate hundreds of thousands of pseudo-experiments and evaluate the test statistics Q with best fit values for N_s and N_b on a toy background sample (Q_b). For each pseudo experiment, data is fluctuated according to a Poisson distribution around the mean expected value. Systematic uncertainties are included via a prior-predictive technique using template morphing. This is discussed in more detail in section 7.7. Then we calculate Q on data and define the confidence level CL_b:

$$CL_b = N_{Q_b > Q_{obs}} \tag{7.30}$$

where $N_{Q_b > Q_{obs}}$ is the number of the generated experiments which have a Q value greater than the measured one, and express the compatibility of the observation with the background only hypothesis. The sensitivity of the analysis (in terms of Gaussian n_σ) is related to the confidence level CL_b by the formula:

$$n_\sigma = \sqrt{2} \cdot \mathrm{erf}^{-1}(2 \cdot CL_b - 1) \quad \text{with} \quad \mathrm{erf}(z) = \frac{2}{\pi} \int_0^z e^{-t^2} dt \tag{7.31}$$

We implement the method with the use of the *theta* framework [127]. The median and central 68% range of the expected significance distribution for signal + background hypothesis are shown in Table 7.9. Figure 7.24 shows the Q distribution for the signal-only and signal+background hypotheses. Table 7.9 and Figure 7.24 do not yet keep into account the systematic uncertainties, whose treatment will be described in 7.7.
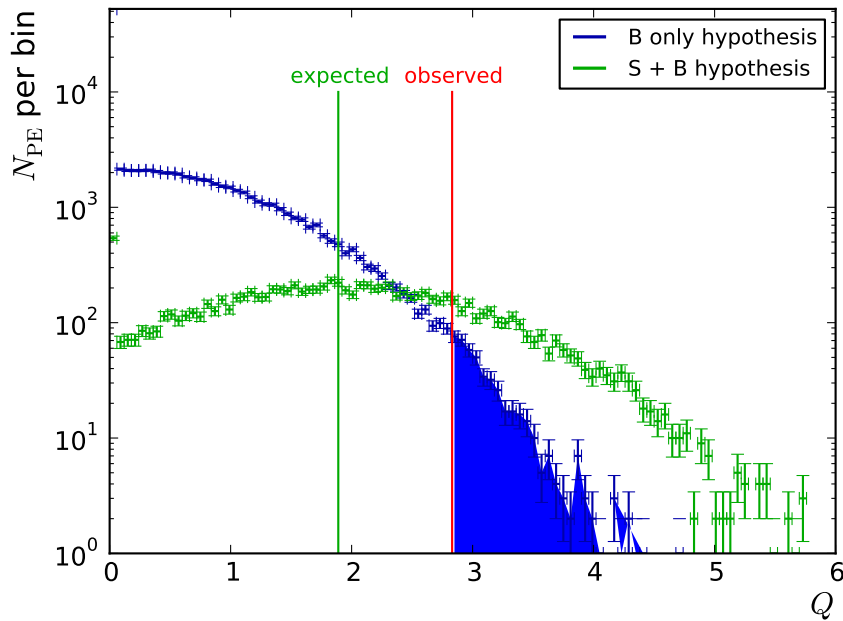
(a)

Figure 7.24: Q distribution for 2,000 pseudo-experiments in background-only and signal + background hypotheses.

7.7 Systematic uncertainties

This section considers the sensitivity of the analysis to systematic uncertainties of instrumental or physics origin.

7.7.1 Backgrounds normalization

Although this analysis makes no assumption on the overall background rate, which is derived simultaneously with the signal, a variation in the relative rates of different background processes can in principle affect the shape of the overall background. We consider:

- $t\bar{t}$: $\pm 18\%$, motivated by the quadratic sum of all the statistical and systematic uncertainties of Ref. [107], but this choice is conservative as the main systematic uncertainties of that measurement are shared by the present analysis;

- VV, single top in s channel and tW: $\pm 30\%$, motivated by the theory uncertainty;

- QCD, and $W+$ light partons: their variation ranges are taken from the data-driven procedures described in Sec. 7.5.1 and 7.5.2;

- $Z+$ light partons: variated coherently with $W+$ light partons;

- Wc: $^{+100\%}_{-50\%}$ [107];

- $VQ\bar{Q}$: $\pm 50\%$ [107].

7.7.2 Jet Energy Scale (JES) and $\not{E}_{\mathrm{T}}$ scale uncertainty

To take into account the jet energy scale uncertainty we apply a simultaneous variation of $1 \pm \alpha$ on all jet 4-momenta, where α comes from the quadratic sum of the uncertainties on the data-driven corrections derived as a function of the transverse energy and the pseudo-rapidity of the jet [120], which are better than $\pm 3.5\%$ in all the interesting range, added in quadrature to additional terms that take into account specific corrections for b-jet scale and pile-up. For each variation in jet energy scale, the missing transverse energy is recalculated accordingly.

An additional and independent source of systematic uncertainties affecting the missing transverse energy is estimated by an uncorrelated shift of the "unclustered energy" component of $\not{E}_{\mathrm{T}}$.

We define as "unclustered" the energy which is not associated to physics objects, and thus the component of the missing energy that is associated to this. The uncertainty on the measurement of the unclustered energy is propagated considering vectorially the uncorrected four-momenta of all jets in the event (without any additional kinematic or identification requirement) and the four-momenta of all leptons which are not clustered in jets. Then, a shift of $\pm 10\%$ is applied to $\vec{\not{E}}_{\mathrm{T}}$ and leptons and jets are added back to the unclustered energy.

No uncertainty on jet energy resolution is considered in this analysis, because estimated to be a minor one in the $t\bar{t}$ analyses with one lepton in the final state [107].

7.7.3 b tagging and mistagging uncertainties

We variate the scale factors of Sec. 7.3.5 by their data-driven uncertainties [121], propagating these variations to the formulas 7.7 and 7.8. At the time of writing only the mistagging rates and their uncertainties are available in the conditions database, and for the b-tagging efficiency a flat scale factor $SF = (90 \pm 15)\%$ is assumed here (to be updated as soon as the dedicated measurements are finalized).

It must be noted that with this procedure we completely neglect any possible distortion of the $\cos\theta^*_{lj}$ and η_{lj} shapes due to the η and p_T dependence of the efficiency uncertainties, while these are taken into account for mistagging.

7.7.4 Signal modeling

As explained in Sec. 7.2, we model the signal by matching the $(2) \to (2)$ and $(2) \to (3)$ diagrams at Leading Order, and we normalize to the NLO cross section. To estimate an uncertainty on signal modeling we compare with a private production with the SingleTop generator [102]; the same matching procedure is applied, but the Matrix Element part of the simulation is different, and also the Parton Shower and Underlying Event models are different because of a different tuning ($D6T$ for SingleTop, $Z2$ for MadGraph).

Statistically significant differencies in the total selection efficiency were observed. In the muon channel the efficiencies are $(2.56 \pm 0.02)\%$ for MadGraph and $(2.385 \pm 0.02)\%$ for SingleTop. The observed difference is believed to origin from the different tune (D6T is used, while it is Z2 in the MadGraph case) and not from disagreement between the two generators. This is motivated by the comparison between two SingleTop signal samples with only muon decays, generated with different tunes. The total selection efficiencies are $(8.06 \pm 0.10)\%$ with the Z2 tune and $(7.00 \pm 0.04)\%$ with D6T. W+jets MadGraph samples are also avaailible with both Z2 and D6T tunes, and the total selection efficiencies are $(2.53 +/- 0.13) \times 10^{-5}$ for Z2 and $(2.35 +/- 0.13) \times 10^{-5}$ for D6T. Thereby the selection efficiency is greater with the Z2 tune comparing to D6T in all the observed cases. We assign a rate systematic of -6.8%. We also consider a shape systematic.

(a)   (b)
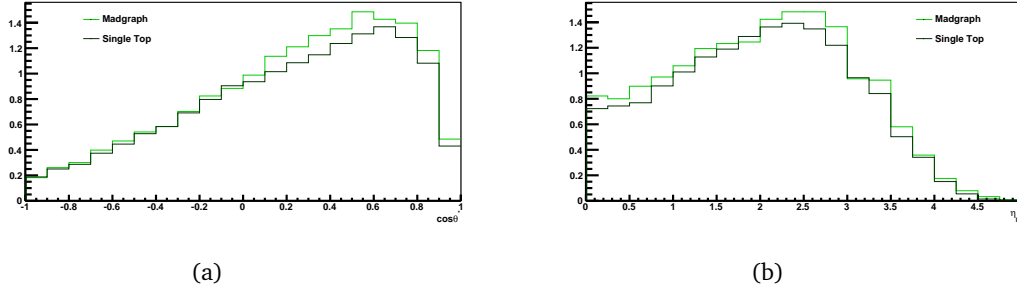
Figure 7.25: $\cos\theta_{lj}^*$ and η_{lj} (right) distributions for the signal changing using the Madgraph and Single Top generator.

7.7.5 $t\bar{t}$ and $W/Z + X$ modeling

The uncertainty on the $t\bar{t}$ and $W/Z + X$ models is estimated by comparing simulated samples with variated Q^2 scale (within half and double the nominal value, independently for $t\bar{t}$ and for $W/Z + X$), initial- and final-state radiation parameters, and fragmentation models (the latter by comparing simulations with the D6T and Z2 tunes).

7.7.6 W+light jet η_{lj} modeling

The W+light jet shapes in η_{lj} and $\cos\theta_{lj}^*$ are extracted from data, see Sec. 7.5.2, and we checked with simulated events that the shapes extracted from our control sample are statistically consistent with those in the signal region for the same process. Nevertheless, we found a small difference in the η_{lj} shapes in the two selections for the Wc process. As a shape systematic, therefore, we consider a reweighting of the W+light partons shape in η_{lj} and take the weights from the comparison of the two samples for Wc.

7.7.7 Pile up

We estimate the impact of pile-up by comparing the standard Monte Carlo samples, with no pile-up, with dedicated samples where minimum bias interactions are superimposed to the process of interest with a probability distribution corresponding to the average over the 2010 data.

7.7.8 W branching ratio

The uncertainty on the W branching ratio into leptons, and thus of $t \to \ell\nu b$ (with $\ell = e, \mu, \tau$), is taken as $\pm 0.8\%$. This value is taken from the uncertainty on the world wide average [128].

7.7.9 η_{lj}-$\cos\theta_{lj}^*$ correlation

We consider a conservative systematic uncertainty on the degree of correlation between η_{lj} and $\cos\theta_{lj}^*$ (estimated as 6% from the MadGraph simulation) by comparing an extraction where this correlation is included (a true 2D template is used) with one where the 2D template for signal is factorized by the product of uncorrelated individual 1D templates.

7.7.10 Luminosity uncertainty

The luminosity determined from dedicated measurements [96] is known within a 4.0 % uncertainty. This uncertainty is propagated directly to the formula 7.34.

7.7.11 Effect on signal extraction

The distributions of $\cos\theta^*_{lj}$ and η_{lj} for each channel is affected by rate and shape uncertainties due to systematics. The shape of the overall background distribution is affected by the relative normalization of background events.

Figures 7.28, 7.26, 7.29, 7.27, 7.29, and 7.30 show the effect of the most relevant systematics on the signal and background model functions.

(a)   (b)
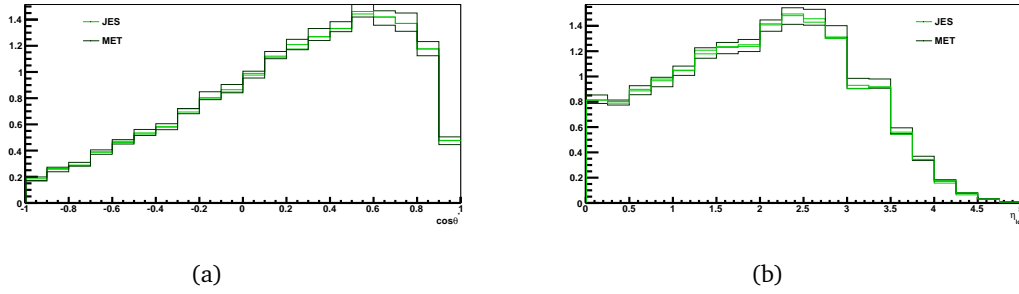
Figure 7.26: $\cos\theta^*_{lj}$ and η_{lj} (right) distributions for the signal changing the JES.

(a)   (b)
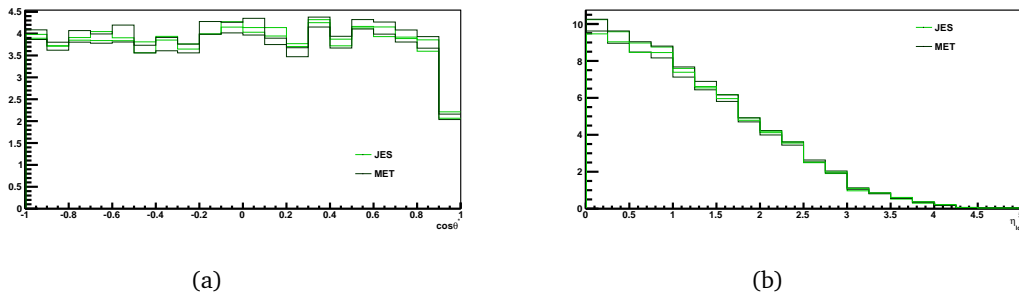
Figure 7.27: $\cos\theta^*_{lj}$ and η_{lj} (right) distributions for the overall background changing the JES.

(a)   (b)
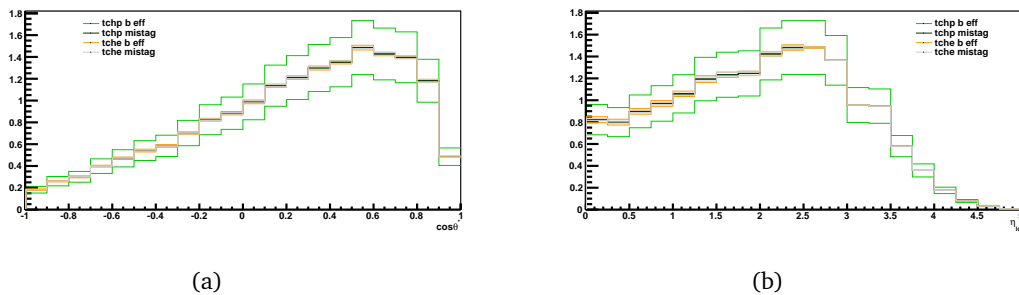
Figure 7.28: $\cos\theta^*_{lj}$ and η_{lj} (right) distributions for the signal changing the b tagging efficiencies.

Procedure used with the profile likelihood method

To check the consistency of the results, the fit procedure is repeated using the two variables separately. Table 7.12, reports the results of the fits and the uncertainties. $\cos\theta^*_{lj}$ alone has not the statistical power to "re-discover" single top, but that its addition improves the statistical power with respect to η_{lj} alone.

(a)   (b)
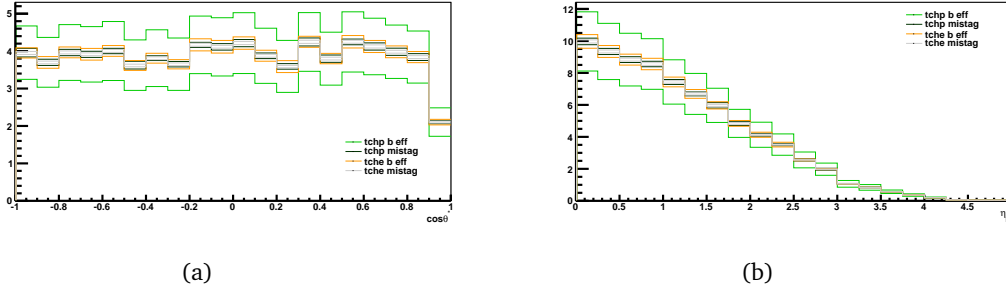
Figure 7.29: $\cos\theta^*_{lj}$ and η_{lj} (right) distributions for the overall background changing the b tagging efficiencies.

(a)   (b)
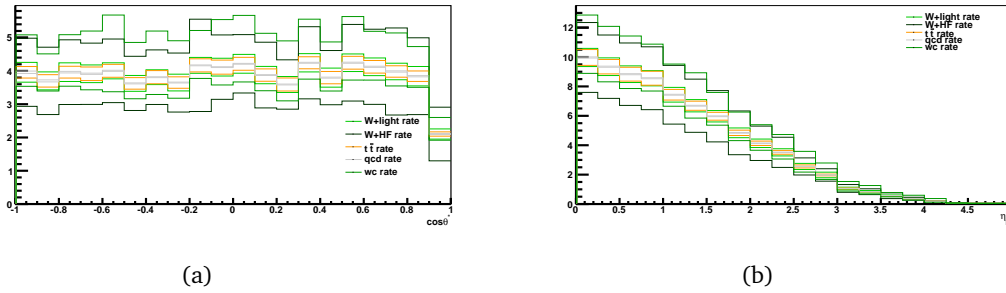
Figure 7.30: $\cos\theta^*_{lj}$ and η_{lj} (right) distributions for the overall background changing the rates of $t\bar{t}$, $W+X$ and QCD.

In Table 7.10 the effect of the main systematics uncertainties on the signal yield is reported. Here and in the next tables the total systematics contribution is calculated using the program at [129], which combines asymmetric systematic errors in a consistent way, assuming a non-linear dependence of the measurement result on the nuisance parameter (which the systematic error comes from). It involves the convolution of Gaussian functions describing each nuisance parameter and the calculation of three quantities that simply add under convolution (the semi-invariant cumulants of Thiele), from which it is possible to obtain the overall asymmetric errors σ_+ and σ_-; more details can be found in Ref. [130].

Table 7.11 reports the effect on the cross section and on the significance of the measurement.

Procedure used with the CL_b method

To estimate the effect of the systematic uncertainties on the signal extraction with the CL_b method a different approach was used with respect to the profile likelihood method. For each uncertainty u, a nuisance parameter, called strength parameter, $\delta_{\mathrm{syst},u}$ is introduced. Such parameter represents how much the parameter corresponding to systematics u deviates from the nominal value: each strength parameter is assumed to have a gaussian distribution with mean value 0 and RMS equals to 1. $\delta_{\mathrm{syst},u} = 0$ corresponds to the nominal value of the systematics parameter (e.g.:0.9 for the b-tagging efficiency Scale Factor of Sec. 7.7.3), $\delta_{\mathrm{syst},u} = \pm 1$ corresponds to the systematics parameter variated of $\pm$ the value from its prescription (e.g.: 0.9$\pm$0.15 for the b-tagging efficiency Scale Factor). Therefore, pseudo-experiments for CL_b procedure are diced keeping the of all systematic uncertainties into account. Template histograms are variated applying a template morphing procedure that we will briefly describe.

Systematics	yield up,down
Central value (stats)	27.2 ± 11.2 (41.2 %)
W+light rate	-1.4 +1.9 %
$W + qq$ rate	-1.4 +5.4 %
$W + c$ rate	-6.3 +3.8 %
$t\bar{t}$ rate	+1.7 -1.6 %
QCD	-0.07 +0.06 %
$b - tag$	+2.2 -2.1 %
$mistag$	+0.6 -0.8%
JES (+ corr. $\not{E}_T$)	-3.6 +7.2 %
Unclustered $\not{E}_T$	+0.08 -2.0 %
Z+jets rate	-0.02 +0.05 %
VV rate	$\pm$ 0.15 %
Single top s channel rate	$\pm$ 0.3 %
Single top tW channel rate	$\pm$ 0.8 %
Signal pdf not factorized	-1.5 %
MadGraph vs SingleTop	-0.8 %
WLight model	-10.2 %
Pile up	+6.6 %
Q^2	+15.0 -2.4 %
$pdf\,ISR/FSR$	-1.44 -0.13 %
$D6 - Z2$	+2.3 %
Total Systematics	-13.1 +17.0 %

Table 7.10: Effect of systematics for the muon channel on the signal yield measured by the fit. The "yield up, down" notation indicates the effect of varying the systematics parameter up or down according to the prescriptions indicated in the text

Systematics	σ up,down	significance (stats only)
Central value (stats)	104.1 $\pm$ 42.3 (40.4 %)	2.83
W+light rate	-1.4 +1.9 %	
W+qq rate	-1.4 +5.4 %	
W+c rate	-6.3 +3.8 %	
$t\bar{t}$ rate	+1.7 -1.6 %	
QCD	-0.07 +0.07 %	
$b-tag$	-14.7 +20.8%	
$mistag$	-0.4 +0.4%	
JES (+ corr. $\not{E}_{\mathrm{T}}$)	-1.8 +8.7 %	
Unclustered $\not{E}_{\mathrm{T}}$	-2.8 +2.7 %	
Z+jets rate	-0.02 +0.05 %	
VV rate	$\pm$ 0.15 %	
Single top s channel rate	-0.3 +0.3 %	
Single top tW channel rate	+0.8 -0.8 %	
Signal model not factorized	-0.5 %	
MadGraph vs SingleTop	+6.4 %	
W+light model	-10.2 %	
Pile up	+6.6 %	
Q^2	+15.0 -2.4 %	
$pdf\,ISR/FSR$	-1.4 -0.13 %	
$D6-Z2$	+2.3 %	
Total Systematics	-21.0 +26.3 %	2.56

Table 7.11: Effect of systematics on the cross section and on the significance of the measurement. The "σ up, down" notation indicates the effect of varying the systematics parameter up or down according to the prescriptions indicated in the text (same convention as table 7.10).

Fit variables	Signal yield $\pm$ statistics	cross section $\pm$ stat (pb)
$\cos\theta^*_{lj}, \eta_{lj}$	27.2 $\pm$ 11.2	104.1 $\pm$ 42.3
$\cos\theta^*_{lj}$	19.7 $\pm$ 20.7	71.6 $\pm$ 75.2
η_{lj}	28.8 $\pm$ 13.3	104.3 $\pm$ 48.3

Table 7.12: Results for 2D, $\cos\theta^*_{lj}$ only and η_{lj} only fits in the muon channel.

Measured	Median	Central 68%
2.5	1.7	0.7 - 2.8

Table 7.13: Expected and observed significance with the CL_b method on the $\cos\theta_{lj}^*$-η_{lj} fit, where the expected significance is the calculated using the median result, assuming Standard Model cross section, and the range is given by the 16% and 84% quantiles.

Template morphing procedure

To formally describe the effect of a systematic uncertainty on the number of expected events in each bin of the template histograms i, μ_i, an interpolation procedure is adopted. The templates α_{ik}, which are used in equation 7.27 to calculate the expected number of events, are written as function of $\delta_{\text{syst},u}$ such that the nominal template is reproduced for $\delta_{\text{syst},u} = 0$ and the altered templates for $\pm 1\sigma$ uncertainty for $\delta_{\text{syst},u} = \pm 1$. The linear interpolation is therefore:

$$\alpha_{ik}^{\text{syst}}(\vec{\delta}_{\text{syst}}) = \alpha_{ik} + \sum_u |\delta_{\text{syst},u}| \cdot (\alpha_{iku,\text{sign}(\delta_{\text{syst},u})}^{\text{syst}} - \alpha_{ik}) \ . \tag{7.32}$$

Therein, u runs over all sources of systematic uncertainties and $\alpha_{iku,\pm 1}^{\text{syst}}$ is the prediction for bin i of process k affected by $+1\sigma$ or -1σ of uncertainty u. They are obtained by running the same analysis procedures on samples which have been altered to include the respective uncertainty at a strength of $\pm 1\sigma$. For some uncertainties, the nominal samples have been altered as described in the following sections, for other uncertainties, dedicated samples have been produced.

In order to prevent unphysical negative predictions for a process, the linear interpolation is cut off at a bin content of zero: whenever $\alpha_{ik}^{\text{syst}}(\vec{\delta}_{\text{syst}})$ calculated according to equation 7.32 has a value below zero, zero is used instead in equation 7.27 to calculated μ_i.

The modified templates according to equation 7.32 are used to dice the pseudo data used to determine the p-value and the significance as explained in section 7.6. The modified template are only used for dicing pseudo data; the definition of the test statistic Q remains unchanged.

Table 7.13 shows the expected and observed significance with the CL_b method after the inclusion of all systematics.

7.8   Results and combination with the electron channel

Equation 7.33 summarizes the results of the bidimensional likelihood fit to $\cos\theta_{lj}^*$ and η_{lj} distributions:

$$27.2 \pm 11.2(stats)_{-3.6}^{+4.7}(syst) \tag{7.33}$$

The single top cross section is related to the signal yield by the formula:

$$\sigma = \frac{N_s}{\epsilon \cdot B(t \to \ell\nu b) \cdot L} \tag{7.34}$$

Assuming the efficiencies estimated from Monte Carlo, and $\epsilon_{mu} = 2.33$ %, $B(t \to \ell\nu b) = 0.1080$ [128], and the luminosity of 36.1 pb^{-1} we measure:

$$\sigma = 104.1 \pm 42.3(stat.)_{-21.8}^{+27.2}(syst) \pm 4.2 \text{ pb} \tag{7.35}$$

with a significance of 2.5 standard deviations.

Systematics	"σ up,down"
Central value	124.2 $\pm$ 33.8 (stats) (27 %) pb
W+light rate	+1.2 -1.0 %
W+qq rate	-1.6 +4.0 %
W+c rate	-4.7 +3.3 %
$t\bar{t}$ rate	+0.9 -0.9 %
QCD	+3.2 -1.7 %
$b-tag$	-15 +21%
$mistag$	-0.4 +0.4%
JES (+ corr. $\not{E}_{\mathrm{T}}$)	-1.9 +6.2 %
Unclustered $\not{E}_{\mathrm{T}}$	-2.3 +5.5 %
Z+jets rate	$\pm$ 0.2 %
VV rate	$\pm$ 0.1 %
Single top s channel rate	-0.2 +0.2 %
Single top tW channel rate	+0.5 -0.5 %
Signal model not factorized	-0.5 %
MadGraph vs SingleTop	+9.0 %
W+light model	-6.4 %
Pile up	+3.5 %
Q^2	+11 -3.4 %
$pdf\,ISR/FSR$	+0.06 -0.7 %
$D6-Z2$	+5.8 %
Total Systematics	-19.9 +25.2 %

Table 7.14: Effect of systematics on the cross section measurement from the combined fit. The σ up, down notation indicates the effect of varying the systematics parameter up or down according to the prescriptions indicated in the text (same convention as table 7.10).

7.8.1 Combined cross section measurement

A combination with a measurement performed in the electron channel is performed in order to increase the precision and the significance of both measurements. A simultaneous fit to the signal and backgrounds yields is performed in both channels. The final result is obtained applying exactly the same statistical inference described in Sections 7.6, 7.7 to the simultaneous fit of muons + electrons. The fit stays a two parameter fit for the muon+electron combination. Table 7.14 shows the break-up of the different systrematics contributions:

The resulting cross-section measurement is therefore:

$$\sigma = 124.2 \pm 33.8(stat.)^{+25.2}_{-19.9}(syst) \pm 4.2 \text{ pb} \qquad (7.36)$$

With a significance of 3.7, obtained with the C_{lb} method described in 7.7.

Figure 7.31 shows the combined significance of 3.7 σ obtained with the fit.
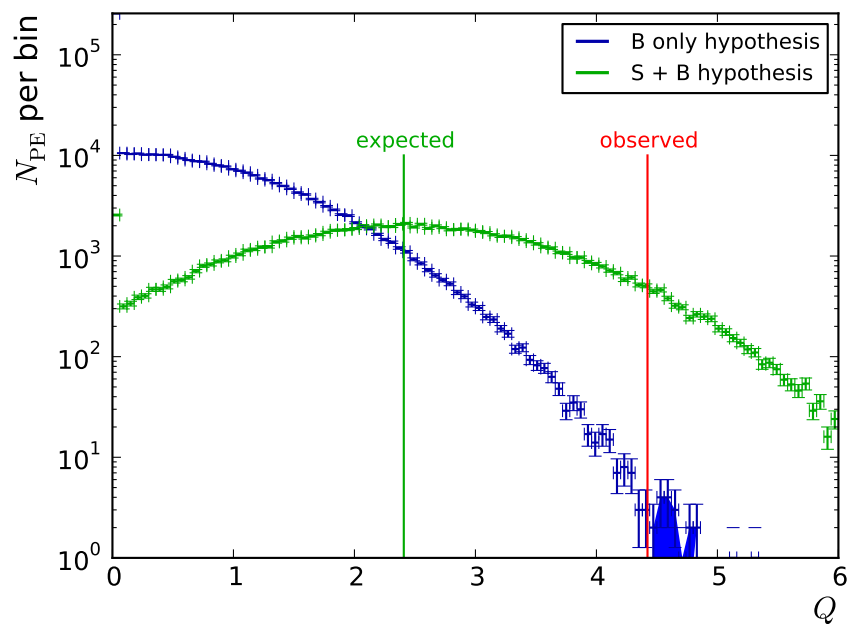
(a)

Figure 7.31: Q distribution for 2,000 pseudo-experiments in background-only and signal + background hypotheses for the combined muon + electrons fit (systematics not included in this plot).

Chapter 8

The single top precision measurements with 2011 data

The data taking conditions significantly changed between 2010 and 2011. The steeply increasing instantaneous luminosity delievered by the machine also directly increased the rate of primary interactions and the multiplicity of events piling-up in the detector. To cope with the ever-growing rate, the trigger conditions changed accordingly to keep the number of recorded information manageable. At the same time, the reconstruction algorythms were and tuned in order to take into account the new pile up scenario. On the other hand, the increased statistics and the know-how acquired by the community during the 2010 data taking allowed to increase the insight on the behavior of the detector, so that more precise measurements of the b-tagging efficiency the Jet Energy Scale or the lepton momenta resolution. From the prospective of the analysis of the single top, the increased statistics opens up a new set of possibilities for single top $t-$channel measurements. It is possible to perform a precision measurement of the $t-$channel cross section, as well as to measure the asymmetry in single top production or the polarization of the top quark from the shape of $\cos\theta^*_{lj}$. However, it is noteworthy that with the increasing statistics, any of those measurements is deemed to be limited by systematics uncertainty. The measurement with 2010 data was performed with a luminosity of $36.1 \ pb^{-1}$had comparable systematics and statistical uncertainties. It is intuitive to understand that collecting a statistics of O(100) times greater than the 2010 dataset, single top analyses will enter a regime where the systematics contributions to the uncertainties dominate over the statistical one. To cope with this a new strategy is needed. In particular, the uncertainty on the modeling of $W+$light and $W+$HF background proved itself to be one of the greatest sources of uncertainty during 2010: summing up the uncertainties for the wjets yields one finds a contribution of about $^{+15}_{-10}\%$ to the overall muon uncertainty. To reduce this uncertainty, we introduce a cut on the $M_{bl\nu}$variable as defined in Section 7.4.2 in order to define a Signal Region and a SideBand Region and to extract the shape and the rate of $W+$HF directly from this sample. The uncertainty on this data-driven method will mitigate or superseed all uncertainties on $W+$HF and $W+$light modeling. The other main source of uncertainty comes from the b-tagging efficiency scale factors. This uncertainty is reduced with the use of the latest measurement performed by CMS [122], which allow for a reduced uncertainty (see Sec 8.4.3). In order to further decrease our dependance on the b-tagging, the b-veto is removed from the selection described in Sec 7.3. Furthermore in order to allow for this analysis to be able to perform polarization measurement, and since with higher statistics the effect of the correlation between $\cos\theta^*_{lj}$ and η_{lj} could become relevant, we perform a one dimensional fit to η_{lj} only. The measurement of 2010 shown how η_{lj} gave the most discriminating power to the analysis.In this chapter we describe the detail of the new trigger and selection strategies, the new data driven methods applied to extract the $W+$HF

backgrounds, and the preliminary results on the cross section and $|V_{tb}|$ measurements.

8.1   Datasets and triggers

This study is based on an integrated luminosity of 1299 pb^{-1} known within an 4.5 % [97]. We make use of the dataset consisting of all the events that have fired a trigger characterized by the presence of at least a muon. Those triggers have different p_T, η and isolation requirements, so a more specific trigger requirement must be applied in order to precisely know the muon rate. For the 2011 measurements the MC $s, t,$ and tW channels events have been generated with the POWHEG event generator [131] [132], which provided separately events where a single top or a single anti-top is produced. $t-$channel MC simulated datasets are normalized to the NLO cross section of 41.9 (22.6) pb for events with top(antitop) [114]. $tW-$channel processes at NLO need some specific prescription to be distinguished from $t\bar{t}$ process at matrix element level. Two different approaches are possible : diagram removal (used as a default in our analysis) and diagram subtraction (more details in Ref [133]). The standard model processes taken into account as background to the analysis are the same as Chapter 7, but the corresponding simulated datasets have been reprocessed taking with different statistics, taking into account the insight gained on the detector and on the physics of processes at $\sqrt{s} =$7 TeV. Also, the effect of pile-up of QCD events was taken into account, simulating up to 25 extra vertices in the events. Table 8.1 summarizes the Monte-Carlo data samples for signal and backgrounds, as well as the Monte Carlo generators used, and provides the number of events and cross section for each sample. All the cross sections have been taken from the references listed in Table 8.1 or, when no reference is given, from the generator itself. The MC W/Z samples in 8.1 are divided in the $W/Z + (u, d, s, g) +$ (light flavours) and the $W/Z + c, b$ components. To each jet is associated the flavour of the quark that is within $\Delta R = \sqrt{(\Delta\phi^2 + (\Delta\eta)^2)} < 0.5$. An event is classified as $W/Z + b$ if at least 1 b-flavoured jet is present, as $W/Z + c$ if no b-flavoured jet is present, but at least 1 c-flavoured jet is present, and finally $W +$light flavour if none b or c are present. Since in such samples a flat pile up distribution is simulated: a data-driven procedure has been used to take into account the difference between the MC and Data pile-up distribution.

We used one specific muon trigger High Level Trigger path for all the run 160404-169141, which is fired by isolated muon candidates whose transverse momentum is measured to be above 17 GeV/c during the online reconstruction. Besider that, an extra isolation requirement is made at HLT level.

Process	$\sigma[\text{pb}] \cdot BR$	Dataset name
single top, t channel (t, inclusive)	41.9 (NNLO) [114]	`powheg-tauola`
single top, t channel ($\bar{t}$, inclusive)	22.6 (NNLO) [114]	`/powheg-tauola`
single top, s channel (t, inclusive)	3.19 (NNLL) [115]	`powheg-tauola`
single top, s channel ($\bar{t}$, inclusive)	1.44 (NNLL) [115]	`powheg-tauola`
single top, tW channel (t, inclusive) (***)	7.9 (NNLO) [116]	`powheg-tauola`
single top, tW channel ($\bar{t}$, inclusive) (***)	7.9 (NNLO) [116]	`powheg-tauola`
$t\bar{t}$	163 (NNLL) [112]	`madgraph-tauola`
$W(\to l\nu) + jets$	31,314 (NNLO)	`madgraph-tauola`
$Z/\gamma^*(\to l^+l^-) + jets$ (*)	3,048 (NNLO)	`madgraph-tauola`
WW	43 (LO)	`pythia6-tauola`
WZ	18.2 (LO)	`pythia6-tauola`
ZZ	5.9 (LO)	`pythia6-tauola`
μ-enriched QCD (**)	84,679 (LO)	`pythia6`

(*) $m_{ll} > 50$ GeV
(**) $\hat{p}_T > 20$ GeV, $p_T^\mu > 15$ GeV
(***) diagram removal (DR) samples taken as dafault, see text

Table 8.1: Monte Carlo datasets used for the 2011 analysis. The samples are generated either inclusively for s, t, and tW channels, for $t\bar{t}$ and Z+jets and for WW, WZ, and ZZ processes, in the leptonic decay channels only for W+jets processes. Where no references are given, the cross sections come from the generator itself if LO, from FEWZ [118] if NNLO, and from $MCFM$ 5.8 [117] if NLO.

8.2 Selection

One of the most important differences in the event selection with respect to the one described in Sec 7.3 is that Particle Flow algorythms have been used for reconstruction of all physics objects including muons and electrons, whereas in selection from Sec. 7.3 the standard muons and electrons were used. The lepton selection criteria and the quality cuts for central jets are taken equal to those agreed for $t\bar{t}$ analyses in the single-muon channels [108]. The topology of the events we search for with 2011 data is the same as the ones described in chapter 7.3: we look for exactly 1 "tight" lepton, we veto "loose" leptons and select exactly 1 b-tagged jet passing the tight threshold of the track counting high efficiency algorythm. We do not apply the loose TCHE veto.

Follows the physics objects definition, in most aspect similar to the one in 7.3.

8.2.1 Object definition

- **Leptons**: Tight muons and loose muons and electrons are defined with the same kinematic cuts as 7.3.2. There are two main differences: the first is that they are reconstructed through particle flow algorythm. The secons is in the definition of isolation, which is done according to particle flow algorythm: We define the "particle flow relative isolation" (Iso_{PF}) of a lepton as

$$Iso_{PF} = \frac{Iso_{photon} + Iso_{charged} + Iso_{neutral}}{p_T} \ , \tag{8.1}$$

Where Iso_{photon} ($Iso_{charged}$, $Iso_{charged}$) is the sum of the transverse energies associated by the particle flow algorythm to photons, charged, and neutral hadrons respectively in a cone of size $\Delta R < 0.4$ around the lepton direction. In particular,

Process	1 iso μ, 0 e	2 jets	$M_T > 40$ GeV	1 tight b tag
single top, t channel	5251	2368	1916	804 ± 3
single top, s channel	353	159.4	126.2	$59,0 \pm 0.9$
single top, tW	2120	702	547	194.8 ± 1.6
$t\bar{t}$	21783	4325	3364	1438 ± 9
W+jets	5344899	142638	125852	2040 ± 32
Z+jets	335021	14790	6908	163 ± 4
VV	6734	1825	1453	42.6 ± 0.6
QCD (μ-enriched)	287319	11794	923	75 ± 17
Total background	5998228	176232	139174	4012 ± 38
Signal + background	6003479	178600	141089	4816 ± 38
Data	7083990	212297	145847	5342 ± 73

Table 8.2: Number of events surviving each selection step, in data and simulated datasets (normalized to 1299 pb^{-1}), in the muon decay channel.

to define a muon, a maximum Iso_{PF} of 0.2 is required during reconstruction. Tight muons are selected by the requirement $Iso_{PF} < 0.1$. Loose muons and electrons are defined with $Iso_{PF} < 0.2$.

- **Jets and $\not{E}_T$:** The definitions and cuts used to define jets are the same as 7.3.2. We apply MC-derived corrections on both data and simulation and update and for data we further apply residual corrections derived from data in 2011.

- b**-tagging**: We use the same TCHP tight threshold to define a tight b-jet selection a TCHE loose threshold to define a loose b-jet selection.

8.2.2   Object counting

Our baseline signal enriched region is defined as in 7.3.3:

- **Lepton counting**:We require the presence of exactly one tight muon and we veto events with additional loose muons or loose electrons.

- **Jets counting**:We require the presence of 1 jet passing the kinematic and quality requirements.

- b**-jets** As in 7.3.3, we require exactly 1 jet passing the track counting high purity threshold of 3.41. In this case however we do not require a loose b veto on the second jet. The motivation for this is to reduce the impact of the mistag efficiency uncertainty.

- M_T **cut** We keep the cut on $M_T > 40$ GeV, performing the QCD extraction.

8.2.3   Selection results

The number of selected events, step by step, in data and simulated datasets is shown in Table 8.2. Again the dominating background sources for this selection are the W+jets and $t\bar{t}$, and the QCD is taken into account performing a fit whose details are shown in Section 8.3. With the removal of b-veto, the cut in jet multiplicity now is the most important for cutting out the $t\bar{t}$ background. Figure 8.1(a) shows the jet multiplicity after the lepton counting in data and simulation after the M_T cut. Figure 8.1(b) shows the jet multiplicity of $t-$channel vs $t\bar{t}$. The treatment of W+light and W+HF at MC level is different than the

(a)   (b)
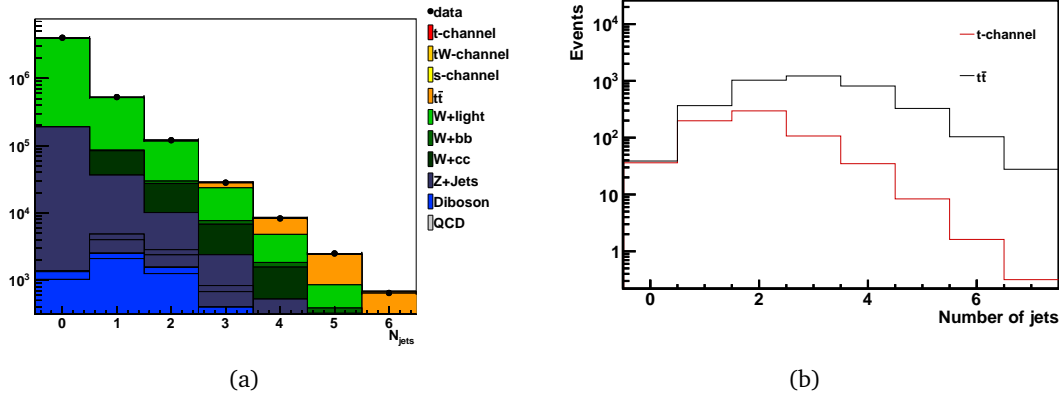
Figure 8.1: Jet multiplicity after the lepton counting in data and simulation and
for signal and $t\bar{t}$ events only.

one applied on 2010 data and will be explained in the detail in section One can clearly notice a discrepancy between data and MC yields even after all cuts have been performed. To better understand this difference, control samples for W+jets and $t\bar{t}$ are taken into account and a study of tagged jets multiplicity is made. On top of this selection, further data driven techniques will be introduced in 8.3 in order to understand the composition of the signal sample and finally to extract the total yield. 8.3

8.2.4 Data-driven scale factors for b-tagging and mistagging

For the tight and loose b-tagging working points used in this analysis ("$TCHPT$" and "$TCHEL$"), respectively for the tagged and veto jets, estimates of the efficiencies of true and fake b-jets identification can be found in Ref. [122], as a function of p_T and η. To correct the simulation mistag rates and b-tagging efficiency each event is weighted by the probability of it passing the cuts given the appropriate scale factors. We define:

- $\epsilon_{q,data(MC)}^{TCHPT(TCHEL)}$ is the efficiency ($p = b, c$) or mistag probability ($p = g, u, d, s$) for algorithm *Track Counting High Purity (High Efficiency)* at the tight(loose) working point in data(MC)

- SF_p is the ratio $\epsilon_{p,data}^{TCHPT(TCHEL)}/\epsilon_{p,MC}^{TCHPT(TCHEL)}$. A dependence from η and p_T of the jet is intended but not written explicitly for clarity reasons.

The scale factors for b jets tagging and mistagging are taken from the CMS database. For a jet the probability to be tagged and not to be tagged varies as follows:

$$\epsilon_{b-tag(mistag)} \rightarrow SF \cdot \epsilon_{btag(mistag)}$$
$$\epsilon_{b-tag(\not{mistag})} \rightarrow (1 - SF) \cdot \epsilon_{btag(\not{mistag})} = \tag{8.2}$$

Where $P_{b-tag}(i)$ is the probability for the i-th jet to be b-tagged. We apply the full combinatorics in order to get the weight of the event. For the 2011 analysis, due to the complications that arise defining the different jet multiplicity bins, we usa a more general approach with respect to the one adopted in 2010. Given the number of jets stemming from light quarks nl , from c quarks nc, and from b quarks nb, the probability P for an event to pass the b tagging requirements is:

$$P^{MC} = \Sigma_{tl}^{nl}\Sigma_{tc}^{nc}\Sigma_{tb}^{nb}C \cdot \epsilon^{tl}(1-\epsilon)^{tl}\epsilon^{tc}(1-\epsilon)^{tc}\epsilon^{tb}(1-\epsilon)^{tb}S \tag{8.3}$$

where S is a 0 if the event does not pass the selection, 1 otherwise, and C is the combinatorics factor. A scale factor is then applied on each event to recalculate the probability on MC taking into account. Such scale factor is derived substituting Eq. 8.2 in Eq.8.3 to get P^{Data}. Finally we define a weight as:

$$b - weight = P^{Data}/P^{MC} \qquad (8.4)$$

All events are weighted accordingly and this weight is factorized with other weights, like the ones from luminosity normalization and pile up (see Sec 8.2.5)

8.2.5   Data-driven scale factors for pile up

To take into account the effect of the pile up on the analysis and to keep in consideration the different pile up condition between the data and simulation, data-driven scale factors are taken into account according to CMS prescriptions:The pile up distribution is measured on data, while the pile up distribution used in simulation is known. Therefore for each simulated proccess, an appropriately defined function remodels the generated pile-up distribution to take the shape of the data distribution. The weights for each simulated event are therefore assigned according to this function, which is given as input the number of pile-up interactions for that event. Fig. 8.2 shows the distribution of the number of vertices in data, in MC $t-$channel and in MC after the reweighting procedure is applied.
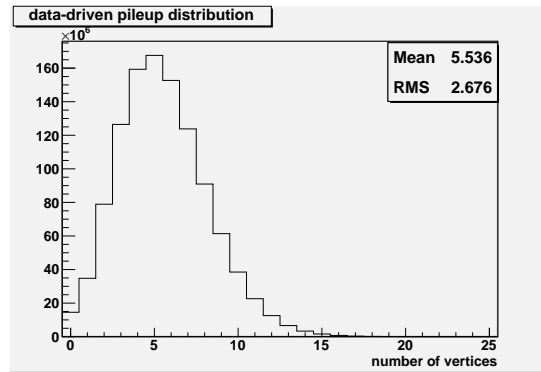
(a)
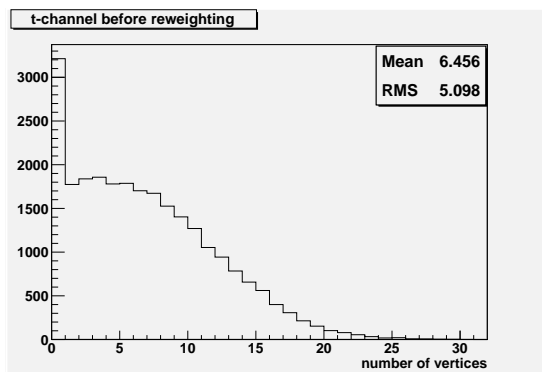
(b)
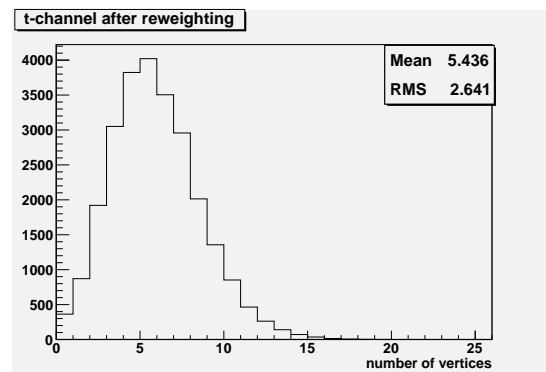
(c)

Figure 8.2: Number of vertices for 1299 pb^{-1}data (a). $t-$channel MC events (b), $t-$channel MC events after the reweighting procedure (c)

Process	entries
t-channel	399.9
tW-channel	163.3
s-channel	8.4
$t\bar{t}$	619.9
$W+$ light partons	82665.8
$Z+$ jets	4705.9
$Wc(\bar{c})$	13501.3
$Wb(\bar{b})$	714.0
Diboson	1027.3
QCD	554.7
Total	104361
Data	99916

Table 8.3: Event yield for the main processes in Sample A, MC vs Data. QCD is extracted from the M_TT fit.

8.3 Background description and 2011 data driven procedures

8.3.1 Control samples definition

8.3.2 $W+$ light flavor enriched sample

Sample A is defined exactly as in 7.5.2: 2 jets are selected, and both fail the TCHP loose threshold. Table 8.3 shows the yield for MC and Data in control sample A. The qcd yield is determined with a fit to the M_T distribution (Figure 8.3 described in section 8.3.6.1. sample is contaminated by non-qcd events which are subtracted accordingly MC normalized to number of events in this plots. This procedure yields the following predictions for the
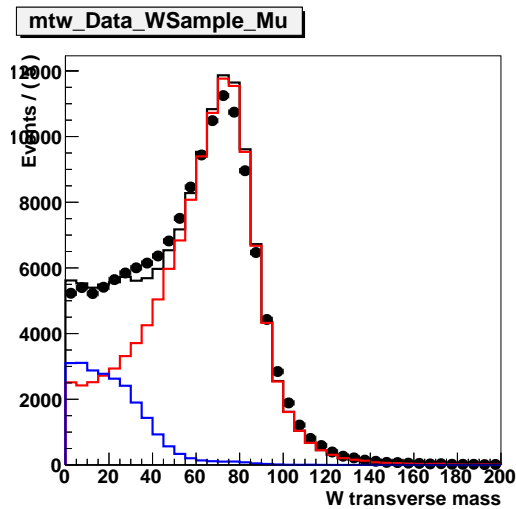
(a)

Figure 8.3: Plot of M_T fits for (run range 160404-169141, 1299 pb^{-1}) with the data-driven template for QCD.

number of QCD events passing the M_T threshold:

$$N_{qcd} \quad = 2682.8 \pm 29.6584(stat) \tag{8.5}$$

$$\tag{8.6}$$

Figures 8.5, 8.6,and 8.7 show the $\cos\theta_{lj}^*$, η_{lj} and $M_{bl\nu}$in the control sample A, where
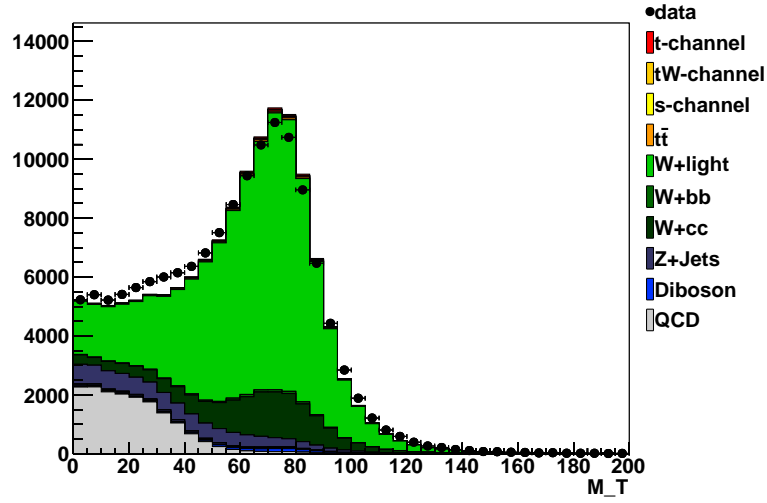
(a)

Figure 8.4: Plot of M_T after the fits for (run range 160404-169141, 1299 pb^{-1}) with the data-driven template for QCD.

the shape for QCD is extracted from the anti-isolated sample. This sample is not directly

(a)
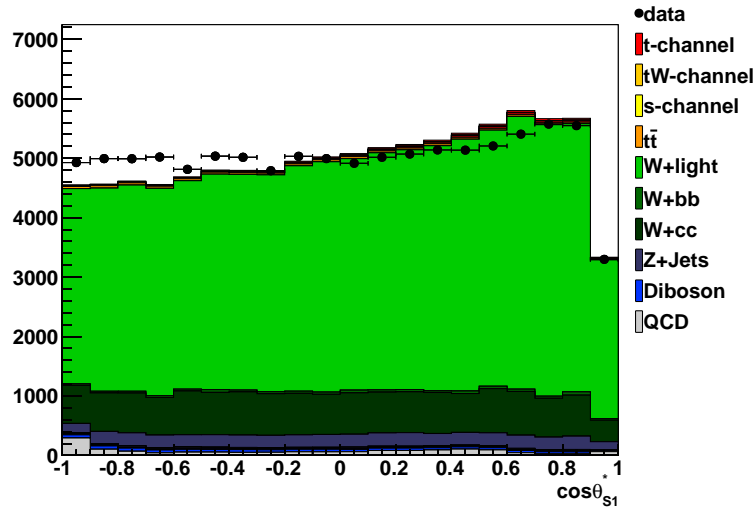
Figure 8.5: $\cos\theta_{lj}^*$ in Sample A, for run range 160404-169141, 1299 pb^{-1}.

used in the measurement to extract the W+jets scale factors, but only to find out potential disagreement in data-mc comparison. After the qcd extraction procedure, the data-mc yield agrees within order of 5%. The data-mc agreement is reasonable for the main variables except for $\cos\theta_{lj}^*$. This does not constitute a problem for the signal extraction procedure, since $\cos\theta_{lj}^*$ is not used to measure the signal yield.

8.3.3 $t\bar{t}$ enriched samples

A $t\bar{t}$ enriched control sample is defined in the following way: Lepton selection is the same as Sec 8.2. we select the 3 jets as in 8.2.1 and we require that 2 of them pass the TCHP

(a)
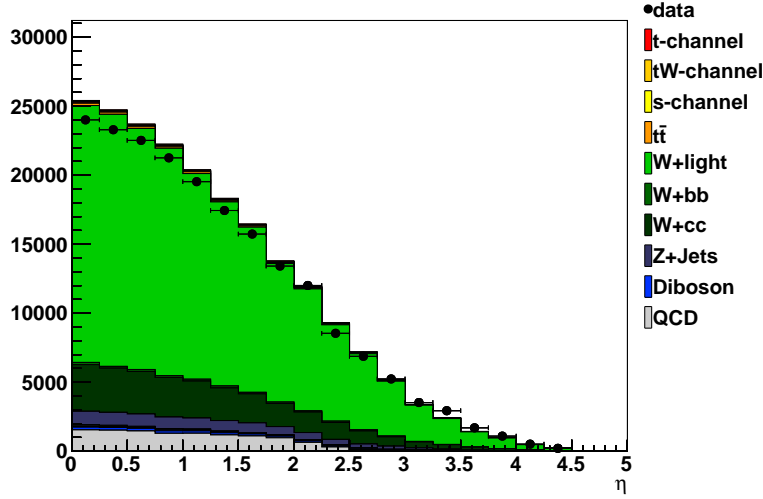
Figure 8.6: η_{lj}, in this sample taken from the sum of both jets eta for run range 160404-169141, 1299 pb^{-1}.
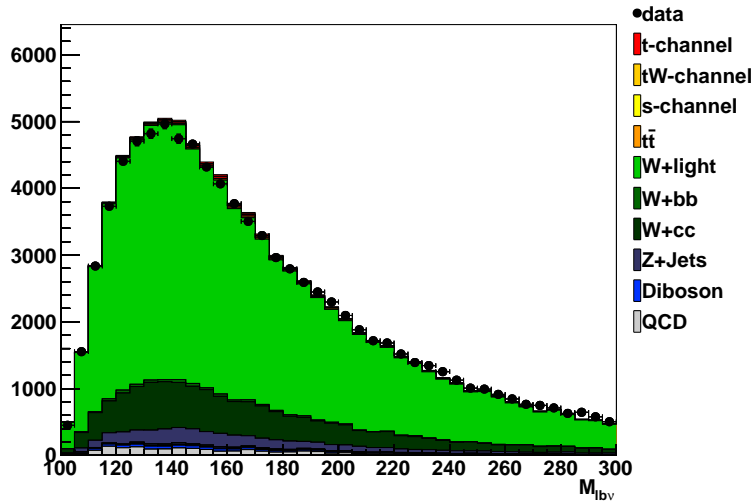
(a)

Figure 8.7: $M_{bl\nu}$ in Sample A, run range 160404-169141, 1299 pb^{-1}.

tight threshold. We also refer to this sample as 3-Jet 2-Tags bin. The highest TCHP tagged jet is used for top quark hypothesis. Table 8.4 shows the yield for MC and Data in this control sample.

The qcd yield here is taken from MC. This sample is enriched in $t\bar{t}$ events, to keep in check both the yield and the shapes of the variables, in particular η_{lj} and $M_{bl\nu}$. Figures (8.8, 8.9, 8.10) show the $\cos\theta_{lj}^*$, η_{lj} and $M_{bl\nu}$ data-mc comparison. The shape comparison of $M_{bl\nu}$ has a reasonable agreement, as reflected in the Kolmogorov Smirnov test value, also the tail regions seem to be well reproduced. Therefore we assume that we can reasonably trust at least the acceptance for $M_{bl\nu}$ variable.

Performing a Kolmogorov-Smirnov test between the data-MC distributions yields a p-value of 85%. There it can be seen that the shape of $\cos\theta_{lj}^*$ is well reproduced for $t\bar{t}$ events. This is particularly important for our purposes since that $M_{bl\nu}$ shape is similiar

Process	entries
t-channel	52.2
tW-channel	15.2
s-channel	3.1
$t\bar{t}$	532.3
$W+$ light partons	0.76
$Z+$ jets	2.51
$Wc(\bar{c})$	0.65
$Wb(\bar{b})$	36.9
Diboson	1.58
QCD	0
Total	645.1
Data	761

Table 8.4: Event yield for the main processes 3-Jets 2-Tags ($t\bar{t}$) Sample, MC vs Data.

(a)
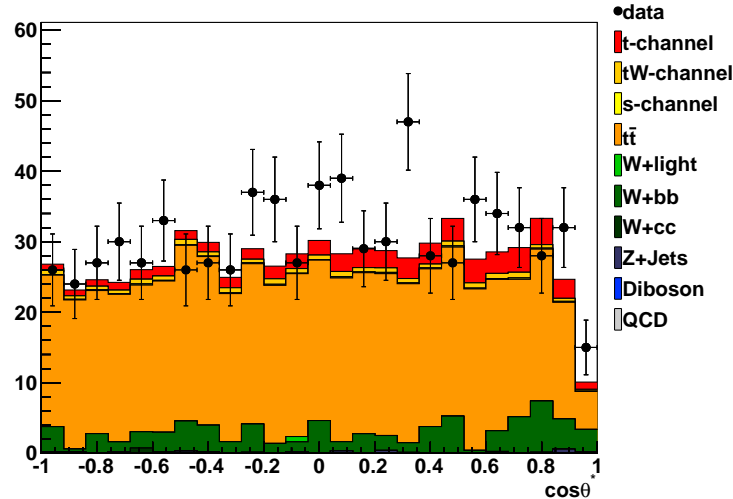
Figure 8.8: $\cos\theta_{lj}^{*}$ in $t\bar{t}$ sample for run range 160404-169141, 1299 pb^{-1}.

between $t\bar{t}$ and signal events for the cases where the correct b-tagged jet is taken for reconstruction of the top.

8.3.4   Signal region and $W + HF$ sideband region

The results of the selection shown in table (8.2) show a discrepancy in the yield between data and mc. To understand this difference, we look at the b-tagged jet multiplicity plots: figure 8.12 clearly shows that there is an excess of data wherever W processes are present, while $t\bar{t}$ enriched regions are under control. Since also control samples explicitly conceived for $t\bar{t}$ and $W+$ light flavours find an excellent agreement in yield and W processes in 8.12 are dominated by $W+$ heavy flavours, we infer that the main reason behind this discrepancy is the $W+$ heavy flavours.

Another group independently obtained sscale factors with a simultaneous extraction of $t\bar{t}$ and of its main background [108], and the corresponding range of variation finding for

(a)
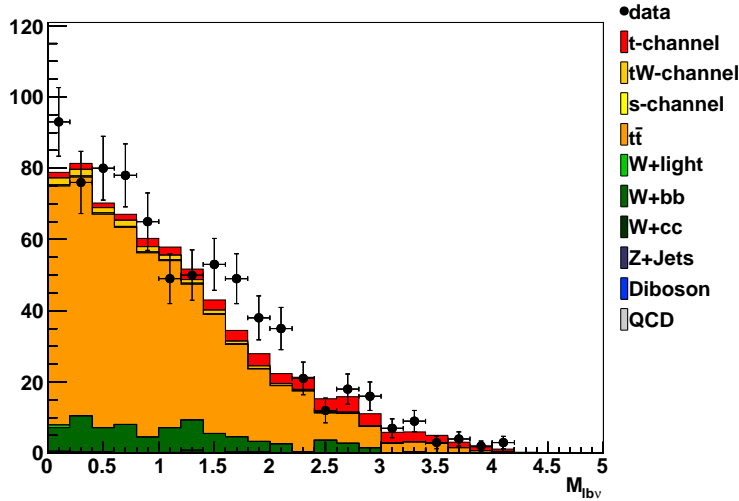
Figure 8.9: η_{lj} in $t\bar{t}$ sample for run range 160404-169141, 1299 pb^{-1}.
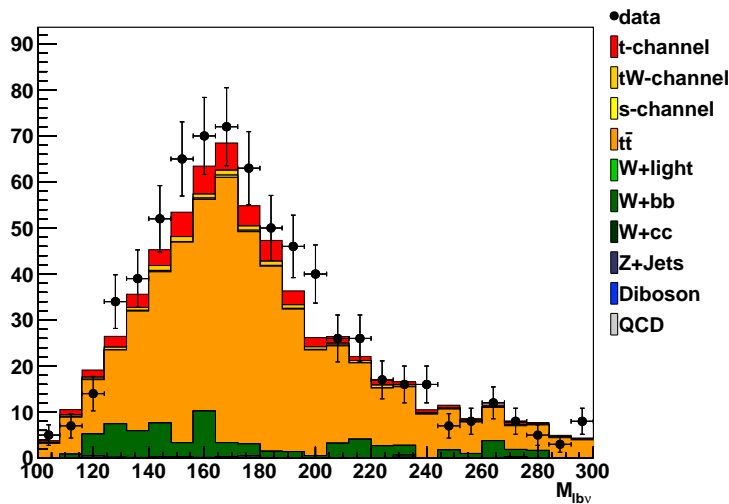
(a)

Figure 8.10: $M_{bl\nu}$ in $t\bar{t}$ sample for run range 160404-169141, 1299 pb^{-1}.

example for the 2 jets bin:

$$SF(WcX) = 1.21^{+0.28}_{-0.27} \qquad (8.7)$$

$$SF(WbX) = 1.66 \pm 0.6 \qquad (8.8)$$

Where X stands for any other final state object. Such scale factors would require an extrapolation the kinematic region of our interest. Such procedure is not straightforward. Several attempts have been made in the past defining different control samples, nevertheless it was not possible to find a satisfactory strategy for dealing with $W + b$ in particular. To avoid this we define a different "*in situ*" strategy for W+HF estimation: The $M_{bl\nu}$ variable has a big discriminating power between the signal and W backgrounds. We therefore perform a cut on $M_{bl\nu}$ to separate a signal enriched region and a W (and $t\bar{t}$) enriched region. We chose the cut as $130 < M_{bl\nu} < 220$. We cut both on the lower and the upper value in order to reduce any kinematic bias. We define the off peak region the Sideband

u
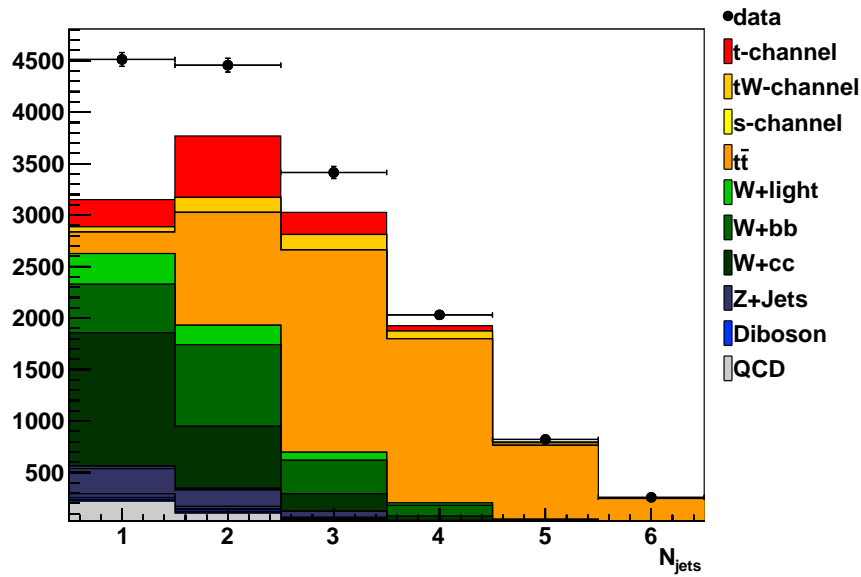
(a)

Figure 8.11: Jet multiplicity in events with 1 jet passing the TCHP tight (3.41)
threshold for run range 160404-169141, 1299 pb^{-1}.

u
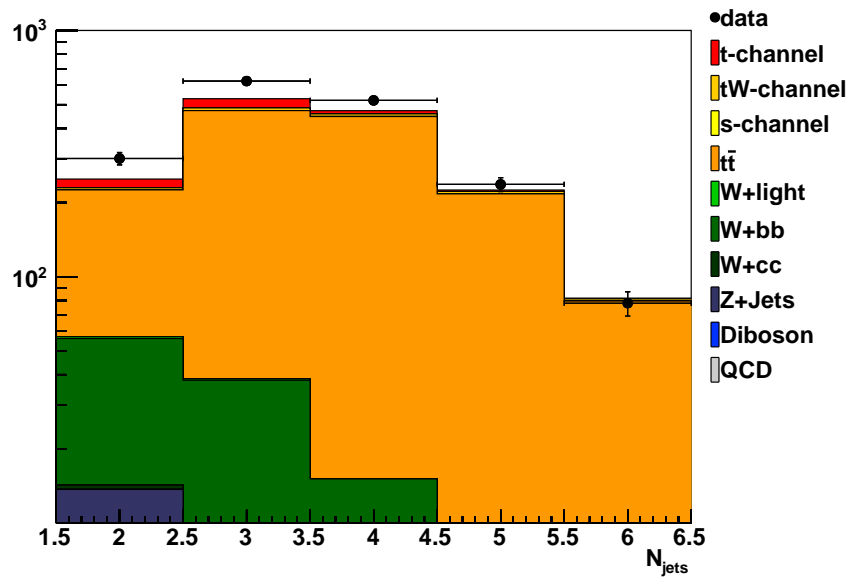
(a)

Figure 8.12: Jet multiplicity in events with 2 jets passing the TCHP tight (3.41)
threshold for run range 160404-169141, 1299 pb^{-1}.

Region (SB) and the region inside the cuts the Signal Region. We refer to the sample after
the selection in section 8.2 and before the $M_{bl\nu}$cut simply as 2-Jet,1-Tag bin. Table 8.5
shows the yield for MC and Data in the Sideband and Signal Region. Due to the difficulty
of the modeling of the $M_T(MET)$ in this region , we perform a fit to the M_T distribution
described in section 8.3.6.1 on the whole 2 jet, 1 tag sample. Then the amount of QCD in

Process	entries signal region (SR)	entries sideband (SB)
t-channel	618.938	87.7135
tW-channel	125.995	58.6537
s-channel	25.9128	9.70259
$t\bar{t}$	908.309	442.344
$W+$ light partons	104.553	121.866
$Z+$ jets	87.145	58.2034
$Wc(\bar{c})$	417.086	307.301
$Wb(\bar{b})$	538.302	443.323
Diboson	22.6551	17.4847
QCD	52.8255	24.8479
Total	2901.72	1571.44
Data	3529	1884

Table 8.5: Event yield for the main processes in Signal Region and Sideband, MC vs Data. QCD is extracted from the M_T fit.

the SB and SR is determined taking the corresponding Anti-Isolated sample in the 2 jet , 1 tag bin and applying the cut. On MC, we ensured that this introduces no bias. The qcd fit to the $M_T(MET)$ cannot be performed in the SR and SB separately, due to poor mc statistics which introduces big uncertainties in the signal modeling. Instead we perform the fit on the 2 jet 1 tag bin, shown in (Figure 8.13) and take the acceptance from the anti-isolated
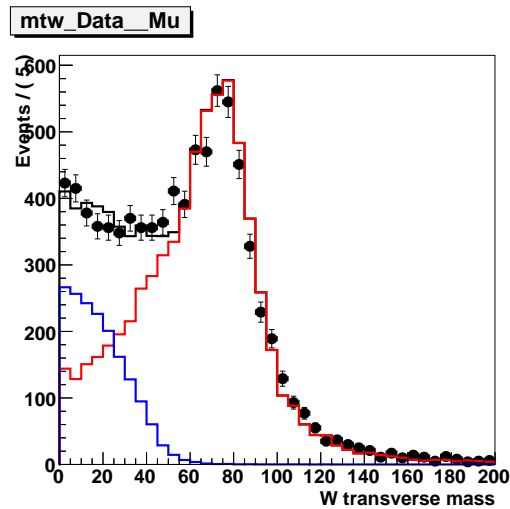
(a)

Figure 8.13: $M_T(MET)$ fits for QCD run range 160404-169141, 1299 pb^{-1}.

sample $M_{bl\nu}$ distribution. The shape for the qcd variables is extracted from the anti-isolated sample. We assume that the acceptance on the signal is reliable the comparisons performed in 8.3.3.

8.3.5 Anti-isolated Samples

For each of the samples previously described, we define a corresponding qcd-enriched sample thanks to anti-isolation and anti-ID requiremenets. For such samples the jet, M_T and $E\!\!\!/_T$ object definition is the same as 8.2.1. For such control samples, it is not necessary to apply special triggers. The tight muon definition is the same as 8.2.1, except for the

relative isolation requirements. The tight muon $pfRelIso$ cut, defined in section 8.2.1, is released.Relative isolation is required to be between 0.3 and 0.5 for the tight muon. We require exactly one tight muon and drop any second lepton veto. Therefore we define an Anti-isolated sample for: 2Jet-1Tag and A samples samples. In such samples the jet and b-tagging requirements are the same as the samples defined respectively for the 2jet 1 tag bin, and for the selection of Sec.: 8.3.2.

8.3.6   Background estimations

8.3.6.1   Multi-jet QCD estimation strategy

Monte Carlo estimations of the QCD contamination have to be considered particularly unreliable for the purposes of our analysis, because only extreme kinematical regions pass this kind of selection, and tail effects are the most difficult to simulate properly. These arguments lead to the conclusion that only *in situ* data-driven estimations will give the needed confidence on the amount of this background.

We use the M_T distribution for muons, after all other cuts have been applied, to estimate QCD by fitting a QCD template extracted from data and a single template for the sum of "signal-like" according to simulation, yielding N_{qcd}^{tot} in the fitted region. Using the same QCD template, N_{qcd}^{SR} is the prediction in the signal region ($M_T > cut$).

We fit the formula

$$F_\mu(M_T) = a_e \cdot S_\mu(M_T) + b_\mu \cdot B_\mu(M_T) \ , \tag{8.9}$$

where $S_\mu(M_T)$ and $B_\mu(M_T)$, are the assumed templates for signal-like and QCD events, letting only a_μ and b_μ fluctuate in the fit. Such fit is performed in 2j1t Sample and in Sample A. The result and the details of such fits are given in the 2-Jet 1-Tag bin defined in 8.2, and in sample A (see Sec. 8.3.2). The QCD shape for M_T is taken from the Anti-isolated samples described in detail in section 8.3.5, where the tight muon is required to have relative isolation : $0.3 < Iso_{PF} < 0.5$.
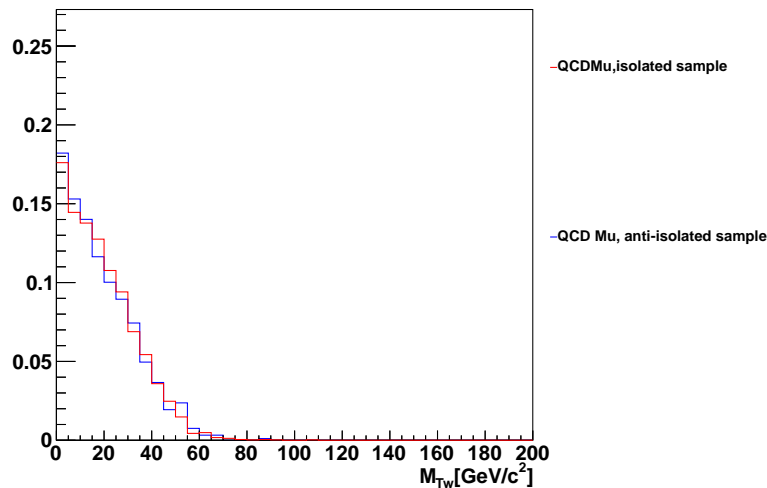
(a)

Figure 8.14: M_T distributions for Monte Carlo QCD samples obtained after an anti isolation cut (red) and after the standard isolation cut (blue). In order to get more MC statistics, the b-requirements were dropped and the presence of 1 jet of $p_T > 30 GeV$ and at least 1 other jet with $p_T > 20 \ GeV$ was required .

Figure 8.14 shows that the $M_T(MET)$ distribution for QCD is not dramatically affected by isolation requirements for the muon channel.The results for the fits in each sample are described in detail in the respective sections. The systematics uncertainty is then conservatively estimated to be 50%. Since we want to take the shape of the QCD discriminating variables from data, we confront the distribution of eta and top mass in the isolated and anti-isolated sample to check that no significant bias is introduced (Figures 8.15(a,b)).

(a)   (b)
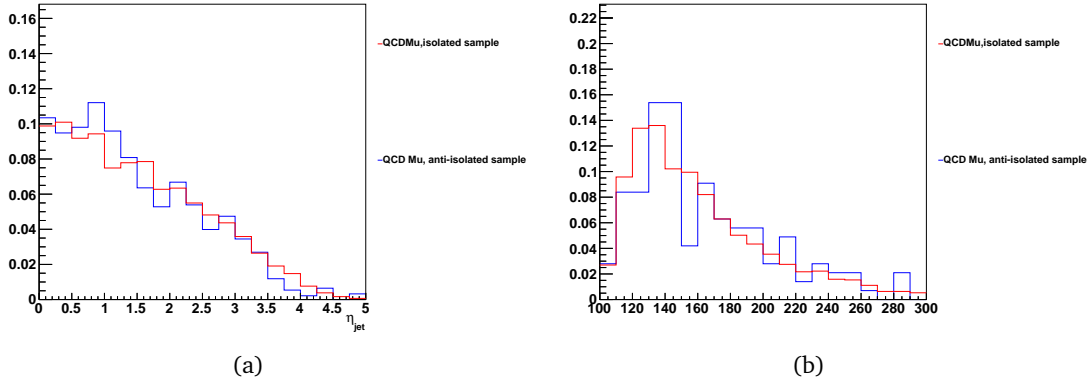
Figure 8.15: η_{lj} (a) and $M_{bl\nu}$(b) distributions for Monte Carlo QCD samples obtained after an anti isolation cut for the muon, (red) and after the standard isolation cut (blue).

8.3.6.2 $W + HF$ extraction strategy

In this section we describe the shape extrapolation procedure to get the shape of $M_{bl\nu}$and η_{lj} for W components of the background. Section 8.3.4 define a W+HF enriched region, where the signal contamination is small. Plots 8.12 and sections 8.3.2,8.3.3 allow us to understand the behavior of $W+$ light and $t\bar{t}$ components of the background. We extract a scale factor and a data-driven shape for the modeling of η_{lj} from the sideband region. For this procedure, the yields in signal and sideband region for $t\bar{t}$, single top tW, s channels, VV processes is taken from the Monte Carlo. QCD is extracted from the SB and SR with the procedure described in section 8.3.4. The extraction proceeds as follows:

Step 1: Sideband W+X extraction First we extract the shape and scale factor and the η_{lj} shape for W/Z+X. We take the data η_{lj} and subtract the data driven QCD shape, the Standard Model $t\bar{t}$, single top tW, s, and VV. Finally we subtract also the standard model t channel. What remains is taken as the data driven W/Z+X η_{lj}.

Step 2: W+X in the signal region we apply the scale factor and η_{lj} from the sideband to the signal region. This is used for the fit described later on in section 8.4.

Figure 8.16 shows the comparison of η_{lj} for the W/Z+X in the Signal Region vs SideBand. After the extraction has been performed we use as a conservative estimate of the uncertainty $\pm100\%$ the t channel cross section to keep into account the effect of the ansatz made on the signal yield. Figure 8.17 shows the effect of this assumption on the extracted shape of W/Z+X. Table in 8.6 show the distribution for $W + b, W + c$, and the overall W/Z+X in Signal and Sideband region.

However, the extracted shape depends on the statistics of the sample. Therefore we perform pseudo-experiments where we repeat the subtraction procedure on simulated datasets. Such datasets are obtained summing η_{lj} Monte Carlo distributions for all channels assuming the standard model yields except for W/Z+HF, which is scaled by a factor 2
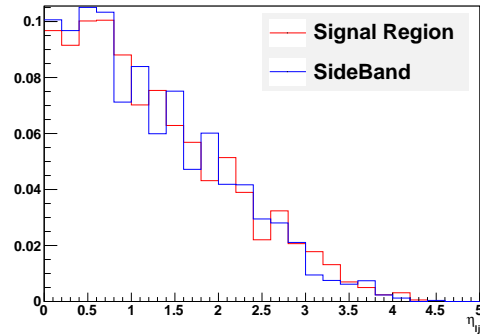
(a)

Figure 8.16: comparison of η_{lj} fpr the $W/Z+$X in the Signal Region vs SideBand region, normalized to 1.
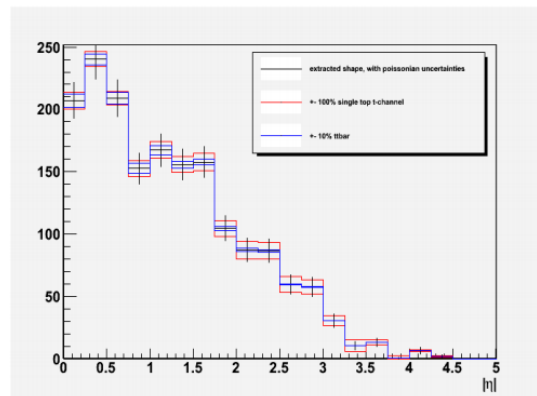
(a)

Figure 8.17: Effect of varying the $t-$channel yield of $\pm$ 100 and the $t\bar{t}$ yield of $\pm$ 20 % in the SideBand region on the data driven extracted shape.

Process/Observable	KS(shape only) η_{lj} comparison in the SR/SB: muon
$W + cX$	0.99
$W + bX$	0.98
$W+$HF	0.98

Table 8.6: KS probability of η_{lj} in the Signal and Sideband regions for $W + b, c$ and overall $W, Z+$X

Process	entries
t-channel	706.651
tW-channel	184.649
s-channel	35.6153
$t\bar{t}$	1350.65
$W+$ light partons	226.419
$Z+$ jets	145.348
$Wc(\bar{c})$	724.386
$Wb(\bar{b})$	981.625
Diboson	40.1398
QCD	77.6734
Total	4473.16
Data	5413

Table 8.7: Event yields summary for the muon channel, including data-driven estimations and b-tagging scale factors.

to get a realistic scenario. Such results show so far that this procedure is consistent. Yet the quantitative effect on the final result have to be evaluated. It turns out the statistical fluctuations in the SideBand affect the final extraction procedure, resulting in additional systematics uncertainty. Such effects are discussed in the detail in section 8.4.3.

8.3.6.3 Backgrounds summary: scale factors and qcd fit in the 2j1t bin

The QCD yield is obtained performing the fit described in section 8.3.6.1 in the signal sample. Figure 8.13 shows the result of the fit.

8.4 Signal extraction

A likelihood fit is performed to η_{lj} distribution to determine the signal cross section in the Signal Region. Our free parameters are the signal yield, the electroweak background yield($W/Z + X, WW, WZ, and ZZ$), and the top background yield($t\bar{t}$, tW, and s single top channels), while the QCD is costrained to the value obtained from the fit and the uncertainty on QCD is considered in systematics. Individual components of the overall background are constrained but the sum is not. The idea behind this choice is to be maximally robust against background uncertainties, taking advantage of the difference in shape while grouping together the channels. Also, we exploit the fact that electroweak backgrounds ($W/Z + X$) should scale together, and the relative uncertainties on their shape only affect the shape of the overall pdf.

8.4.1 Likelihood function

We define the unbinned likelihood function given by:

$$L(\eta_1, ..., \eta_n | N_s, N_b) =$$

$$= e^{-(N_s + N_{ewk} + N_{top} + N_{qcd})} \cdot (N_s + N_{ewk} + N_{top} + N_{qcd})^n \prod_{k=1}^{n} \left(\frac{1}{N_s + N_{ewk} + N_{top} + N_{qcd}} \right)$$

$$\cdot (N_s \cdot P_s(\eta_k) + N_{ewk} \cdot P_{ewk}(\eta_k) + N_{top} \cdot P_{top}(\eta_k) + N_{qcd} \cdot P_{qcd}(\eta_k))$$

$$(8.10)$$

where N_s, N_{ewk}, N_{top}, N_{qcd} are the signal and background yields. The parameter group together channels which have similiar η_{lj} distributions from MC studies:

- **top**: $t\bar{t}$, s, and tW channels.

- **ewk**: W+jets, Z+jets, WW, WZ, and ZZ.

- **QCD**: QCD.

$t\bar{t}$, respectively. n is and number of observed events, and P_s, $P_{b=(ewk,top,qcd)}$ are the signal and background distribution functions. The ewk component is fitted separately in the muon and electron channel, because different we want to make the minimum possible assumption on such background. The extended maximum likelihood fit gives us the best estimation of N_s and $N_{b=ewk,top,qcd}$, with the model distributions considered fixed and taken from Monte Carlo or data driven templates. To be more specific, the background term in equation 8.10 is given by:

$$N_{b=ewk,top,qcd} \cdot G_b(\eta) = \sum_i N_{b_i} \cdot G_{b_i}(\eta) \tag{8.11}$$

where i runs over all the backgrounds (whose relative normalizations are taken from Monte Carlo) which compose the b template. It is convenient to define the signal strength S_{signal}, ewk strength S_{ewk} and top strength S_{top} as the ratio

$$S_{i=signal,ewk,top} = N_{measured,i}/N_{expectation,i} \tag{8.12}$$

Whenever the fit results will be expressed in terms of S_i, they will refer to Table 8.7 for $N_{expectation,i}$. Figure 8.18 shows the result obtained normalizing the simulated datasets yields to the fitted values and the estimated yields are:

$$S_{signal} = 1.15 \pm 0.204 \quad S_{ewk} = 1.21 \pm 0.109 \quad S_{top} = 1 \pm 0.109 \tag{8.13}$$

Which in terms of number of events becomes for the signal:

$$N_{signal} = 671 \pm 119 \tag{8.14}$$

The results reported up to here, however, still has to take into account systematics effects on the data driven estimation of the W+HF, which has been discussed in detail in Sec. 8.3.6.2.

8.4.2   Results

We use formula in Eq. 7.34, taking $\epsilon_{mu} = 0.84$ %, $B(t \rightarrow \ell\nu b) = 0.1080$ [128], and the luminosity, L, is equal to 1299 pb^{-1} to measure the cross section. We find the results reported in Table 8.8.

N_s	σ (pb)
671 ± 119	74.3 ± 7.16

Table 8.8: Fit results.
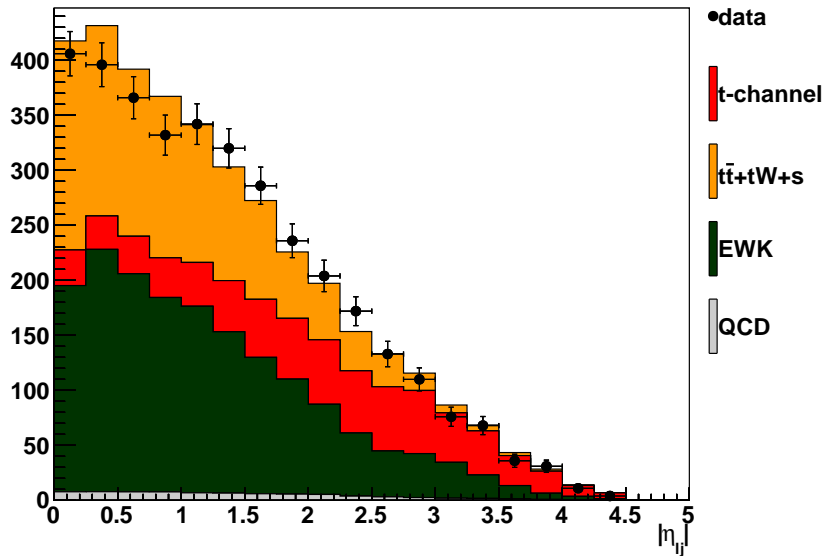
Figure 8.18: η_{lj} distribution for Data and simulation normalized

8.4.3 Systematic uncertainties

This section considers the sensitivity of the analysis to systematic uncertainties of instrumental or physics origin. Many of them have been already discussed in the detail in Sec. 7.7, here we list them shortly:

- $t\bar{t}$ **normalization**: $\pm 11\%$, taking the uncertainty from [112];

- QCD **normalization**: QCD variation is taken conservatively as $\pm 50\%$

- $W, Z+$ **light partons and heavy flavours component and modeling**: we use data driven shape extraction and derive the yield from the fit.

- **Jet Energy Scale (JES))**: To take into account the JES variation, the official CMS Jet Energy Corrections are taken from DataBase, which include a new 10% for jets with $|\eta| > 3$ due to large HCAL response in the forward region. This is particularly important since in that region the signal to bacground ratio is most favorable, so it reflects clearly in our analysis. For each variation in jet energy scale, the missing transverse energy is recalculated accordingly.

- $\not{E}_T$ **scale uncertainty** : An additional and independent source of systematic uncertainties affecting the missing transverse energy is estimated by an uncorrelated shift of the "unclustered energy" component of $\not{E}_T$. The unclustered energy is calculated by subtracting vectorially the uncorrected four-momenta of all jets in the event (without any additional kinematic or identification requirement) and the four-momenta of all leptons which are not clustered in jets. Then, a shift of $\pm 10\%$ is applied to $\vec{\not{E}_T}$ and leptons and jets are added back to the unclustered energy.

- **Jet Energy Resolution (JER)**: An uncertainty on jet energy resolution is considered in this analysis: we impose a variation of $\pm 15\%$ on the difference between the generated parton p_T and the reconstructed jet for MC samples.

- b **tagging and mistagging uncertainties** We variate the scale factors of Sec. 8.2.4 by their data-driven uncertainties [122], propagating these variations to the formula

8.3. Mistagging and B-Tagging scale factors are varied independently according to errors measured by independent cms measurement [122].

- **Pile up** The effect of the pile up is taken into account in the analysis though a reweighting procedure summarized in section 8.2.5. The systematics uncertainty in the Pile-Up is taken into account by varying the overall pile-up distribution considered in such procedure of ± 1.

- W **branching ratio** The uncertainty on the W branching ratio into leptons, and thus of $t \to \ell \nu b$ (with $\ell = e, \mu, \tau$), is taken as $\pm 0.8\%$ [128].

- **Luminosity uncertainty** The luminosity determined from dedicated measurements [97] is known within a 4.5 % uncertainty.

8.4.4   Effect on signal extraction

The distributions η_{lj} for each channel is affected by rate and shape uncertainties due to systematics. The shape of the overall background distribution is affected by the relative normalization of background events. η_{lj} is quite stable under variations of JES, $\not{E}_{\mathrm{T}}$, b tagging, mistagging, while for instance $M_{bl\nu}$ is much more affected. We consider those uncertainties in the definition of the signal and sideband regions, as well as in the data driven extraction procedure described in Section 8.3.6.2

8.4.5   Data driven procedure

The data driven procedure described in Sec 8.3.6.2 has the advantage that incorporates all W/Z rate and modeling uncertainties (Q^2,ISR/FSR,hadronization mode), but on the other hand is dependent on the statistics of the Signal Region and the Sideband Region. To evaluate this effect pseudo experiments have been performed: using the standard model prediction for all samples except for $W + c.b$, where a scale factor of 2 has been applied, a pseudo-dataset has been built. This dataset was hence divided in Signal Region and the Sideband , and pseudo experiments were drawn in the SB region in order to simulate the random extraction of the sample and the of the template for the fit. The distribution of the resulting fits is shown in Figure 8.19(μ). This distribution has a non-negligible RMS (in short we call it "spread") and a difference in the mean value with respect to the generation central value (in short we call it "bias") for all three cases. We expect that both of those quantities are The effect of the spread is taken into account as a systematics. To take into account the bias we define a simple scale factor:

$$SF_{bias} = s_{generation}/s_{meanvalue} \tag{8.15}$$

where $s_{generation}$ is 1 and $s_{meanvalue}$ is the bias. To get the result, we scale of this SF_{bias} the values we get from the fits.

8.4.6   Results

In Table 8.9 the effect of the main systematics uncertainties on the signal strenght is reported. The systematics uncertainty is evaluated dicing pseudoexperiments with the variated templates using template morphing technique with the theta software [127]. Since this procedure gives us the relative uncertainties, they are afterwards scaled to take into account the SF_{bias}.

Therefore the result after the correction is:

$$\sigma = 71 \pm 6.84 (stat.) \, ^{10.6}_{10.6} (syst.) \, \mathrm{pb} \tag{8.16}$$
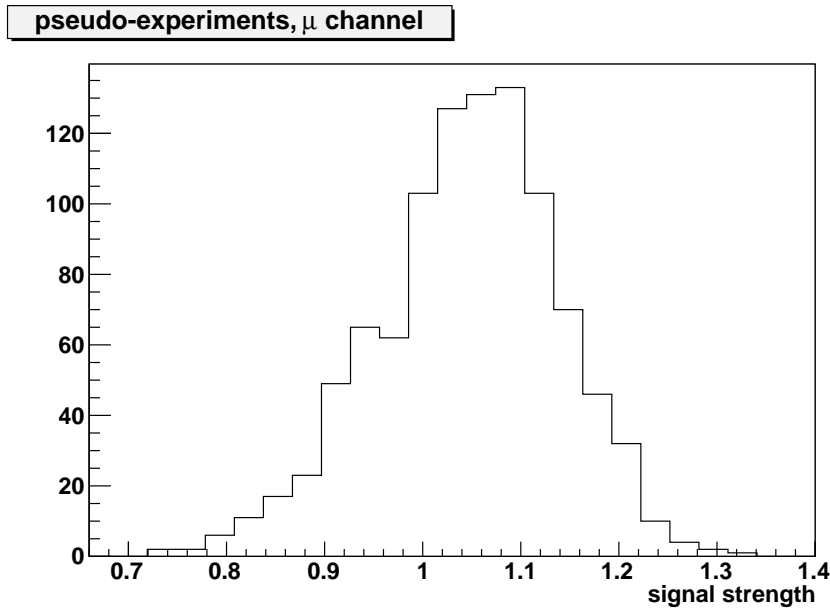
Figure 8.19: Result of the fits on one pseudodataset in the Signal Region, drawing random Pseudo Experiments in the SideBand region

8.4.7 Results and combination with the electron channel

A combination with a measurement performed in the electron channel is performed in order to increase the precision of both measurements. A simultaneous fit to the signal and backgrounds yields is performed in both channels. The final result is obtained applying exactly the same statistical inference described in Sections 8.4, 8.4.3 to the simultaneous fit of muons + electrons. Table 8.10 shows the break-up of the different systrematics contributions: The resulting cross-section measurement is therefore:

$$\sigma = 69.5 \pm 6.03(stat.)^{+9.92}_{-9.92}(syst) \pm 3.7 \text{ pb}$$

(8.17)

With a significance > 5 standard deviation, obtained with the C_{lb} method described in 7.7 . This preliminary measurement has however has to be finalized adding uncertainties on the parton Distribution Functions and on the factorization scale Q^2 as well as pdf initial and final state radiation uncertainties, in particular for the latter two extra Monte Carlo simulated samples are needed.

SignalStrength: 1.15	± 0.11 (stats)
DD stats error	± 0.09
Systematics	up/down variation
$BTag$	+0.08 -0.08
JES	+0.07 -0.10
JER	-0.013 -0.024
$MisTag$	+0.0006 -6.41$\cdot 10^{-5}$
$UnclusteredMET$	-0.012 -0.0028
$TTBar$	-0.04 +0.04
PU	+0.04 +0.0019
total systematics:	$\pm$ 0.17
total syst+stats:	$\pm$ 0.20
Corrected by SF_{bias}:	1.10 ± 0.20(stats + syst)

Table 8.9: Effect of systematics on the signal strength measured .

SignalStrength: 1.15	± 0.10 (stats)
DD stats error	± 0.08
Systematics	up/down variation
$data$	+0.14 +0.14
$BTag$	+0.08 -0.08
JES	+0.07 -0.09
JER	+0.005 -0.04
$MisTag$	-4.3 $\cdot 10^{-5}$ -0.00019
$UnclusteredMET$	-0.012 -0.003
$TTBar$	-0.04 +0.04
PU	+0.04 +0.002
total systematics:	± 0.16
total syst+stats:	± 0.19
Corrected by SF_{bias}:	1.08 ± 0.18(stats + syst)

Table 8.10: Effect of systematics on the signal strength measured by the combined muon-electron channel fit.

Chapter 9

Results, combination and Conclusions

The results from 2010 have been combined with an independent multivariate analysis measuring the single top cross section, based on the use of a Boosted Decision Tree, called for simplicity bdt. In the following sections we report the result of the combination and the extraction of the Cabibbo Kobayashi Maskawa matrix element V_{tb}.

9.1 Combined 2010 results

The measurement with 2010 data (Sec.7) yields a cross section of :

$$\sigma = 124.2 \pm 33.8(stat.)^{+25.2}_{-19.9}(syst) \pm 4.2 \text{ pb}$$

(9.1)

combining muon and electron channels. The BDT analysis held a result of: The measurement with 2010 data (Sec.7) yields a cross section of :

$$\sigma = 78.7 \pm 25.2(stat.)^{+13.2}_{-14.6}(syst) \pm 3.1 \text{ pb}$$

(9.2)

in order to combine the above results, the following steps have been made:

- **Uniformation of the systematics treatment**: since the two analyses used different treatments for systematics, a common treatment was decided, which consisted in generating pseudo-experiments in the different systematics scenarios, repeating the extraction procedure and taking the mean difference as systematics uncertainty. This is done using as probability distribution function the simulated MC datasets, with and without each systematics variation, and generating according to those distributions to obtain simulated datasets. This is more conservative than the single methods adopted by the two analyses and was easily reproductable in both cases.

- **Statistical correlation evaluation**: the datasets of the two analyses were partially overlapping. The statistical correlation is not 100% despite the use of the same 2010 data collected by CMS. This is due to several differences in the cuts and in the reconstruction algorithms used in the analyses. This was performed taking the datasets passing the selection for both the analyses, then considering the subset of events which was in common to both selection and generating random pseudo-datasets where a subset in common was generated only once per pseudo-experiment from the common subset and used for both analyses. For each analysis then the

extraction was performed and the correlation of the two results was evaluated. The correlation evaluated in this way is 51%.

- **Systematics correlation**: Most of the systematics were considered correlated except the ones that were analysis specific, in particular the $W+$light partons normalization and shape (data-driven in our analysis and taken from theory in the BDT analysis), the QCD normalization. The correlation of the latter component is poorly known, therefore we consider a 50% correlation and treat the uncertainty on this correlation as an additional systematic (within 0% and 100%), whose impact is found to be negligible.

- **BLUE technique**: the Best Linear Unbiased Estimator was used to evaluate the central value and the uncertainty. Hereby is assumed that all uncertainties are Gaussian and symmetric [134] .

  Although these are rough approximations for many systematic uncertainties, the dominant uncertainties fulfill these assumptions.

Table 9.1 shows the correlated sources of uncertainty evaluated, and the result of the application of BLUE technique is:

$$\sigma = 83.6 \pm 29.8(stat. + syst) \pm 3.3 \text{ pb}$$

$$(9.3)$$

 All uncertainties fully correlated with the following exceptions (see Table 9.1). Figure 9.1 shows the comparison of the combination and the single measurement with the SM expectations. Figure 9.2 compares the combined measurement with the dedicated t-channel cross section extractions at Tevatron , demonstrating the large increase due to the higher centre-of-mass energy.

uncertainty	correlation	impact on			
		2D		BDT	
		−	+	−	+
statistical only	60	52		39	
shared shape/rate uncertainties:					
ISR/FSR for $t\bar{t}$	100	−1.0	+1.5	< 0.2	< 0.2
Q^2 for $t\bar{t}$	100	+3.5	−3.5	+0.3	−0.4
Q^2 for V+jets	100	+5.7	−12.0	+2.6	−4.5
Jet energy scale	100	−8.8	+3.6	−5.1	+1.2
b tagging efficiency	100	−19.6	+19.8	−15.2	+14.6
MET (uncl. energy)	100	−5.7	+3.7	−3.9	−0.5
shared rate-only uncertainties:					
$t\bar{t}$ ($\pm 14\%$)	100	+2.0	−1.9	+0.5	−0.6
single top s ($\pm 30\%$)	100	−0.4	+0.5	−0.4	+0.4
single top tW ($\pm 30\%$)	100	+1.1	−1.0	< 0.2	< 0.2
$Wb\bar{b}$, $Wc\bar{c}$ ($\pm 50\%$)	100	−3.0	+2.9	+1.7	−1.9
Wc ($^{+100\%}_{-50\%}$)	100	−3.0	+6.1	−2.4	+4.4
Z+jets ($\pm 30\%$)	100	−0.6	+0.7	+0.4	−0.2
electron QCD (BDT: $\pm 100\%$, 2D: $^{+130\%}_{-100\%}$)	50	+2.9	−3.7	−1.7	+1.7
muon QCD (BDT: $\pm 50\%$, 2D: $\pm 50\%$)	50	< 0.2	< 0.2	−2.1	+2.1
signal model	100	−5.0	+5.0	−4.0	+4.0
BDT-only uncertainties:					
electron efficiency ($\pm 5\%$)	0	—	—	−1.4	+1.4
muon efficiency ($\pm 5\%$)	0	—	—	−3.6	+3.5
V+jets ($\pm 50\%$)	0	—	—	−1.5	< 0.2
2D-only uncertainties:					
muon W+light ($\pm 30\%$)	0	−1.4	+1.4	—	—
electron W+light ($\pm 20\%$)	0	−0.6	+0.7	—	—
W+light model uncertainties	0	−5.4	+5.4	—	—

Table 9.1: Relative impact of the uncertainties on the combined cross section measurement ($e + \mu$) in the two analyses, in percent of the standard model cross section, estimated with pseudo-data. The table includes the correlation assumed for the final combination.
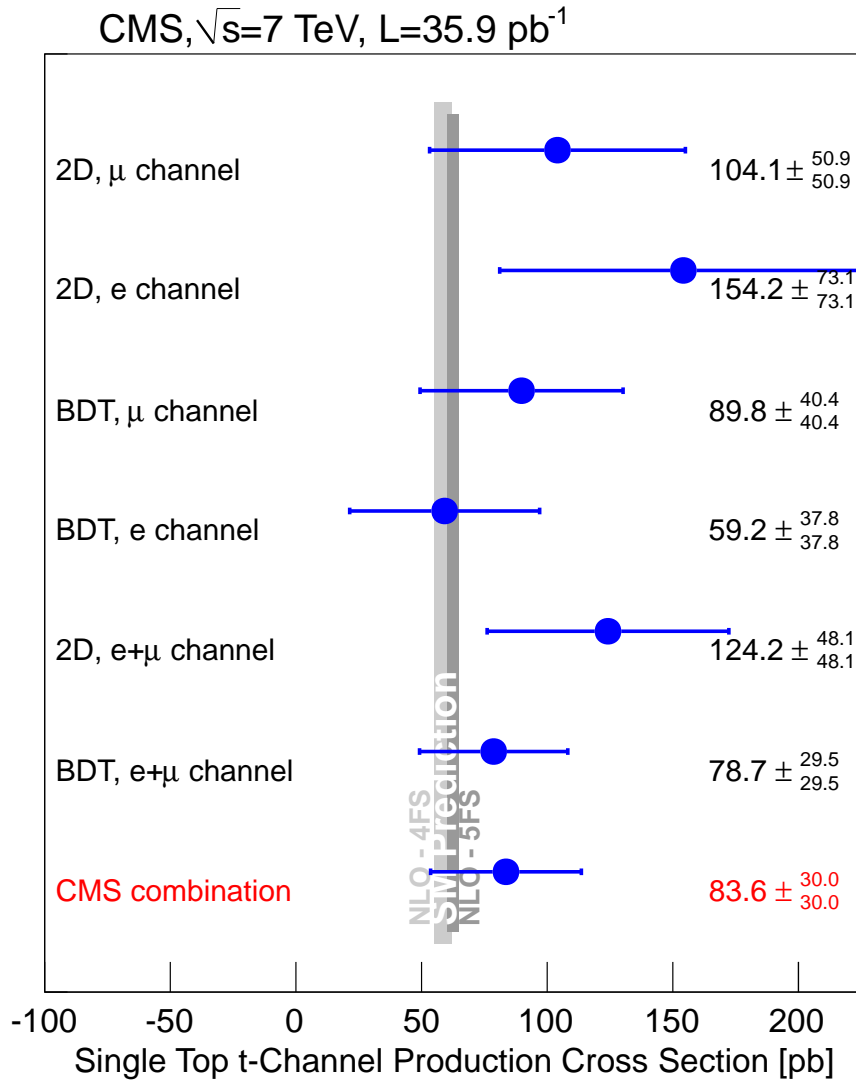
Figure 9.1: Comparison of the cross section measurements in all channels in the 2D and BDT analyses, and theoretical calculations under the standard model assumption.
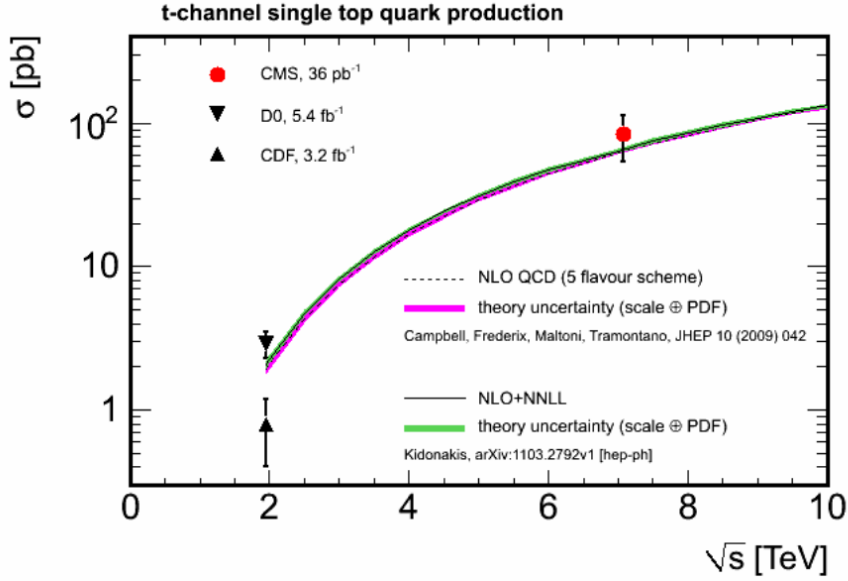
Figure 9.2: Single top cross section in the $t-$channel versus centre-of-mass energy, comparing our measurement with the dedicated t-channel cross section measurements at Tevatron and with the NLO QCD expectation computed with MCFM in the 5-[U+FB02]avour scheme [113]. The error band (width of the curve) is obtained by varying the top mass within its current uncertainty , estimating the PDF uncertainty according to the HEPDATA recommendations, and varying the factorization and renormalization scales coherently by a factor two up and down.

9.2 V_{tb} extraction

Under the assumption that $|V_{td}|$ and $|V_{ts}|$ are much smaller than $|V_{tb}|$, we extract the latter quantity as

$$|V_{tb}| = \sqrt{\frac{\sigma^{exp}}{\sigma^{th}}} \qquad (9.4)$$

where σ^{exp} is taken from (9.2) and $\sigma^{th} = 64.6^{+2.3}_{-2.4}$ pb is the NLO prediction .

Within the framework of the standard model, V_{tb} is a diagonal element of a unitary matrix and $|V_{tb}|$ can therefore never exceed unity.

Therefore, making the SM assumption that $0 \leq |V_{\mathrm{tb}}|^2 \leq 1$, we use a Bayesian method to extract a 95% C.L. lower limit on $|V_{tb}|$. We use a flat prior probability distribution function for the single top cross section which correponds to a flat prior in $|V_{tb}|^2$. The posterior in the model parameters is (up to an overall normalization) given by

$$p(\beta_s, \beta_{b,\mu}, \beta_{b,e}, \delta_i | \text{data}) = \prod_{i=1}^{400} \text{Poisson}(n_i | \mu_i) \pi(\delta_u). \qquad (9.5)$$

The index i runs over all the bins of the two-dimensional template used in the fit, n_i is the number of observed events in this bin and Poisson$(n|\lambda)$ is the Poisson probability to observe n events, given mean λ. The expected number of events μ_i depends on the scaling factors β_i and the shape-changing nuisance parameters δ_u as given in equations 7.27 and 7.32. $\pi(\delta_u)$ denotes the prior used for the shape-changing nuisance parameters δ_u. As priors, we choose to use independent Gaussian functions around 0 with width 1, motivated by the template interpolation (see eq. 7.32) which yields the $\pm 1\sigma$ modified templates for values $\delta_u = \pm 1$.

To include the uncertainty on the cross section, the term in the sum on the right hand side of equation 7.27 which corresponds to the signal content, $\beta_s \cdot \alpha_{is}$, is modified by an

additional factor $\beta_{\text{vtb-xs}}$:

$$\mu_{i,s} = \beta_s \cdot \beta_{\text{vtb-xs}} \cdot \alpha_{is}.$$

This additional parameter $\beta_{\text{vtb-xs}}$ encodes the imprecise knowledge of the single top t-channel cross section, assuming a perfect knowledge of $|V_{tb}|$. As prior of this parameter, a Gaussian around 1.0 with a width if 3.9% is used. This corresponds to the uncertainty of the most precise cross section calculation for single top available.

From the full posterior given in Eq. 9.5, we obtain the marginal posterior for β_s by marginalization, i.e., integration over all other parameters. Technically, this is done using a Markov-Chain Monte-Carlo technique, more details can be found in Ref. [127] and references therein. From the marginal posterior in β_s, the 5% quantile is the 95% C.L. lower limit on $|V_{tb}|$.

At the 95% confidence level we infer the lower bound $|V_{\text{tb}}| > 0.62$ from the our analysis only.

If we release the SM assumption that $0 \leq |V_{\text{tb}}|^2 \leq 1$, we get the following measurements of $|V_{tb}|$

$$|V_{tb}| = 1.16 \pm 0.22(exp) \pm 0.02(th) \tag{9.6}$$

with 2010 data, and

$$|V_{tb}| = 1.04 \pm 0.09 \,(\text{exp}) \pm 0.02(\text{th}) \tag{9.7}$$

adding 2011 data.

9.3   Conclusions

The CMS experiment has been collecting 7 TeV proton-proton collision data since March 2010, resulting in a total integrated luminosity of $36.1 \ pb^{-1}$ and $5.22 \ fb^{-1}$ taken in 2010 and 2011 respectively. The physics program at CMS has quickly evolved to its more mature stages where precision standard model measurements aiming to constrain new physics models are possible. In this respect, the top quark physics represents a true testing ground for our knowledge of particle physics, pioneering the search for new physics through measurements of Standard Model parameters and helping to constrain BSM scenarios, in some analogy, mutatis mutandis, with the role the b-quark physics played at the great b-factories like $BaBar$ or $Belle$. In particular, the single top offers a vast array of opportunities for physics measurements aiming to explore the electroweak sector of top quark physics. The measurement of single top $t-$channel processes properties prior to LHC were only possible at the Tevatron, but their precision was limited by the disadvantageous signal to background ratio and the statistics available. On the other hand, LHC is perfectly suited for single top measurements: the very fact that the first evidence of single top at the LHC in 7 TeV proton-proton collisions, presented in this thesis, was possible one year after the start of the data taking, a result that took Tevatron more than ten years to achieve. The measurements of single top $t-$channel cross section in good agreement with the standard model predictions provided a crucial check of the validity of the theory, and with the increasing statistics and knowledge of systematics effects it will soon challenge the theoretical uncertainties stemming from extrapolation of the Parton Distributin Functions to the LHC energy scale and from the matrix element calculations. The electroweak nature of single top $t-$channel couplings makes it straightforward to extract a measurement on the Kabibbo Kobayashi Maskawa matrix element V_{tb}. For the first measurement of the single top $t-$channel cross section was performed in the $t \rightarrow Wb \rightarrow \mu\nu b$ channel, a strategy was chosen to maximize the significance, based on a maximum likelihood fit to two characteristics variables of single top $t-$channel topology: the pseudorapidity η_{lj} of the light jet stemming from hadronization of the quark recoiling against the top, and the cosinus of the angle between the muon and the top quark spin axis in the top quark rest

frame $\cos\theta^*_{lj}$, whose distribution is a consequence of the $V - A$ nature of the electroweak current. This allowed to extract the value for the cross section of

$$\sigma = 124.2 \pm 33.8(stat.)^{+25.2}_{-19.9}(syst) \pm 4.2 \text{ pb} \tag{9.8}$$

that was combined with other CMS measurements obtaining:

$$\sigma = 83.6 \pm 29.8(stat. + syst) \pm 3.3 \text{ pb} \tag{9.9}$$

and resulting in a lower bound on the CKM matrix element V_{tb} of:

$$|V_{tb}| = 1.16 \pm 0.22(exp) \pm 0.02(th) \tag{9.10}$$

The 2011 marked the transition to the systematics-dominated regime for single top measurements, which resulted in a modified approach to the cross section measurement, foreseeing a 1-dimensional fit to η_{lj}, allowing a more model independent measurement and at the same time a new data-driven procedure to extract the rate and shape of the most troublesome background, the $W+$ heavy flavour, from a sideband of the signal region. Preliminary results with 1299 $pb^{-1}$of 2011 CMS data allowed to measure:

$$\sigma = 71 \pm 6.84(stat.)\,^{10.6}_{10.6}(syst.) \pm 3.72 \text{ pb} \tag{9.11}$$

Which combined with the 2011 complementary electron channel resulted in a cross section of:

$$\sigma = 69.5 \pm 6.03(stat.)^{+9.92}_{-9.92}(syst) \pm 3.7 \text{ pb} \tag{9.12}$$

and a measurement of V_{tb}:

$$|V_{tb}| = 1.04 \pm 0.09 \text{ (exp) } \pm 0.02(\text{th}) \tag{9.13}$$

The latter result will be finalized taking into consideration other sources of systematic uncertainty. All the performed measurements confirm the standard model predictions at the NNLO. An update to the current measurements will be possible, aiming both to increase the precision of the current cross section measurements and to study the many other properties of the $t-$channel. Dedicated studies on charge asymmetry will allow to effectively probe the Parton Distribution Functions at the LHC. Moreover, thanks to the modified analysis strategy, allowing for instance to measure the polarization of the top quark through studies of the the $\cos\theta^*_{lj}$ variable, which is a sensitive observable to detect to beyond standard model production mechanisms of top quark, e.g. through Flavour Changing Neutral Currents or through exchange of an exotic W' in the $t-$channel process.

Bibliography

[1] The CMS Collaboration, Measurement of the t-channel single top quark production cross section in pp collisions at $\sqrt{(s)} = 7$ TeV, Phys. Rev. Lett. 107, 091802.

[2] The CMS Collaboration, Measurement of the single-top t-channel cross section in pp collisions at $\sqrt{s} = 7$ TeV, 2011, CMS PAS TOP-10-008.

[3] The CMS Collaboration, Performance of the CMS Level-1 Trigger during Commissioni ng with Cosmic Ray Muons, JINST 5 (2010) T03002.

[4] A. O. M. Iorio on behalf of The CMS Collaboration, Expectations for first single-top studies in CMS in proton-proton collisions, 2010, CMS-CR-2010-108; CERN-CMS-CR-2010-108.

[5] A. O. M. Iorio on behalf of The CMS Collaboration, Study of the RPC Level 1 Trigger efficiency of the Compact Muon Solenoid at LHC with cosmic ray data, CMS-CR-2010-064.

[6] S.Glashow, Nucl. Phys. 22 579 (1961).

[7] S.Weinberg, Phys. Rev. Lett. 19 1264 (1967)

[8] A.Salam, Elementary particle Theory , Ed. N. Svarholm (1968).

[9] N. Cabibbo, Phys. Rev. Lett. 10, 531 (1963).

[10] M. Kobayashi and T. Maskawa, Prog. Theor. Phys. 49, 652 (1973)

[11] Gell-Mann, Murray (1995). The Quark and the Jaguar. Owl Books. ISBN 978-0805072532.

[12] P. Langacker, Introduction to the Standard Model and Electroweak Physics, arXiv:0901.0241 [hep-ph].

[13] .J.R. Aitchison, A.J.G. Hey, Gauge Theory in Particle Physics (Vol 1), Institute of Physics Publishing, Bristol and Philadelphia. I.J.R. Aitchison, A.J.G. Hey, Gauge Theory in Particle Physics (Vol 2), Institute of Physics Publishing, Bristol and Philadelphia.

[14] P. Langacker, Introduction to the Standard Model and Electroweak Physics, arXiv:0901.0241 [hep-ph].

[15] P.W. Higgs, Phys. Lett. 12,132 (1968)

[16] S. Dawson, the Standard Model intermediate Higgs Boson,in the prospective on Higgs Physics II, Ed. Gordon L.Kane, World Scientific (1997)

[17] The UA1 Collaboration, Phys. Lett. B166, p. 484 (1986).

[18] The UA2 Collaboration, Phys. Lett. B186, p. 440 (1987).

[19] R.P. Feynman: Very High-Energy Collisions of Hadrons. Phys. Rev. Lett. 23, 1415-1417 (1969); The behavior of hadron collisions at extreme energies, in Stony Brook 1969, Proceedings, Conference On High Energy Collisions, ed C.N. Yang, et al, (Gordon and Breach, New York 1969), 237-258.

[20] J.D. Bjorken et al., Inelastic Electron-Proton and γ-Proton Scattering and the Structure of the Nucleon. Phys. Rev. 185, 1975-1982 (1969).

[21] G. Altarelli, G. Parisi, and R. Petronzio. Transverse momentum in drell-yan processes. Phys. Lett., B76:351, 1978.

[22] T. Sjostrand, Computer Physics Commun. 82 (1994) 74.

[23] G. Marchesini et al., Comp. Phys. Commun. 67, 465 (1992)

[24] B. Andersson, The Lund Model, Cambridge University Press, 1998.

[25] R. D. Field and S. Wolfram, Nucl. Phys. B 213 (1983) 65.; T. D. Gottschalk, Nucl. Phys. B 214 (1983) 201 and B 239 (1984) 349.

[26] For a review and a list of references, see, for example, J. Hewett and M. Spirop- ulu, Ann.Rev.Nucl.Part.Sci. 52, 397 (2002), hep-ph/0205196.

[27] S.P. Martin, "A Supersymmetry Primer", hep-ph/9709356 (1997).

[28] The BABAR Collaboration, The BABAR detector, Nucl. Instrum. Meth. A 479 (2000) 1.

[29] The Belle Collaboration The Belle detector, NIM A479,117 (2002).

[30] LHC Machine Lyndon Evans and Philip Bryant (editors) 2008 JINST 3 S08001, doi: 10.1088/1748-0221/3/08/S08001

[31] The ATLAS Collaboration, The ATLAS Experiment at the CERN Large Hadron Collider, 2008 JINST 3 S08003 (http://iopscience.iop.org/1748-0221/3/08/S08003)

[32] The CMS Collaboration, The CMS experiment at the CERN LHC, 2008 JINST

[33] The ALICE Collaboration, The ALICE experiment at the CERN LHC, 2008 JINST 3 S08002 (http://iopscience.iop.org/1748-0221/3/08/S08002)

[34] The LHCb vollaboration, The LHCb Detector at the LHC, 2008 JINST 3 S08005

[35] The LHC Study Group, Design study of the Large Hadron Collider (LHC), CERN 91-03, May 1991 (Pink Book).

[36] F. Kircher et al., Final design of the CMS solenoid cold mass, IEEE Trans. Appl. Supercond., 10 (2000) 407.

[37] The CMS Collaboration, The CMS tracker system project: technical design report, CERN-LHCC-98-006, http://cdsweb.cern.ch/record/368412.

[38] The CMS Collaboration, The CMS tracker: addendum to the technical design report, CERN-LHCC-2000-016, http://cdsweb.cern.ch/record/490194.

[39] The CMS Collaboration, Performance and operation of the CMS electromagnetic calorimeter, Journal of Instrumentation 5 (2010). doi:10.1088/1748-0221/5/03/T03010.

[40] The CMS Collaboration, Electromagnetic calorimeter calibration with 7 TeV data, CMS PAS EGM-10-003. 2010.

[41] M. Anfreville et al., Laser monitoring system for the CMS lead tungstate crystal calorimeter, CMS Note 2007/028 (2007).

[42] The CMS collaboration, The hadron calorimeter project: technical design report, CERN-LHCC-97-031, http://cdsweb.cern.ch/record/357153.

[43] A. Panagiotou et al., CASTOR engineering design report, CMS Note in preparation (2008).

[44] N. Akchurin et al., Quartz fibers as active elements in detectors for particle physics, Rev. Sci. Instrum. 74 (2002) 2955.

[45] CMS collaboration, The CMS muon project, technical design report, CERN-LHCC-97-032, http://cdsweb.cern.ch/record/343814.

[46] G. Charpak et al., High-accuracy, two-dimensional read-out in multiwire proportional chambers, Nucl. Instrum. Meth. 113 (1973) 381.

[47] M. Abbrescia et al., The simulation of resistive plate chambers in avalanche mode: charge spectra and efficiency, Nucl. Instrum. Meth. A 431 (1999) 413.

[48] M. Abbrescia et al., Local and global performance of double-gap resistive plate chambers operated in avalanche mode, Nucl. Instrum. Meth. A 434 (1999) 244.

[49] The CMS collaboration, The TriDAS project, technical design report. Volume 1: The level-1 trigger, CERN-LHCC-2000-038, http://cdsweb.cern.ch/record/706847.

[50] The CMS collaboration, The TriDAS project, technical design report. Volume 2: Data acquisition and high-level trigger technical design report, CERN-LHCC-2002-026, http://cdsweb.cern.ch/record/578006.

[51] RD5 collaboration, F. Gasparini et al., Bunch crossing identification at LHC using a mean-timer technique, Nucl. Instrum. Meth. A 336 (1993) 91.

[52] R. Brun et al., ROOT — An object oriented data analysis framework, Nucl. Instrum. Meth. A 389 (1997) 81, see also http://root.cern.ch.

[53] P. Billoir, et al., Nucl Instr. Meth. A241 (1985) 115.

[54] W. Adam et al., "Reconstructions of Electrons with the Gaussian-Sum Filter in the CMS Tracker at the LHC", J. Phys. G: Nucl. Part. Phys. 31 (2005) N9–N20.

[55] M. Pioppi, "Iterative Tracking", CMS Internal Note 2007/065 (2008).

[56] G. C. Blazey et al., Run II jet physics: Proceedings of the Run II QCD and Weak Boson Physics Workshop, hep-ex 0005012 (2000).

[57] R. Fruewirth et al., Adaptive Vertex Fitting, CMS Note 2007/008 (2007)., W. Waltenberger et al., Adaptive Vertex Fitting, J. Phys. G: Nucl. 434 Part. Phys. 34 (2007), no. 12, N343. doi:10.1088/0954-3899/34/12/N01.

[58] G. P. Salam et al., A practical seedless infrared-safe cone jet algorithm,JHEP05(2007)086 (2007).

[59] S. Catani et al., Longitudinally invariant kt clustering algorithms for hadron hadron collisions, Nucl.Phys.B406:187-224 (1993).

[60] The CMS Collaboration, Particle–Flow Event Reconstruction in CMS and Performance for Jets, Taus, and E_T^{miss}, CMS PAS PFT-09-001 (2009).

[61] The CMS Collaboration, Performance Study of the CMS Barrel Resistive Plate Chambers with Cosmic Rays, JINST 5 (2010) T03017 [arXiv:0911.4045

[62] R. Trentadue on behalf of the CMS Collaboration, CMS RPC trigger and detector performance during the 2009 Cosmic Run At Four Tesla (CRAFT09), 2009 IEEE Nuclear Science Symposium Conference Record N13-178 (2009).

[63] A. Adare et al., Phys. Rev. Lett. 98 (2007) 232002. C. L. da Silva,Nucl. Phys. A 830 (2009) 227C; L. Linden Levy, Nucl. Phys. A 830 (2009) 353C

[64] The CDF Collaboration, Phys. Rev. D 71 (2005) 032001.

[65] The CDF Collaboration, Phys. Rev. Lett. 88 (2002) 161802.

[66] The ALICE Collaboration, Talk at RQW 2010, Oct. 25-28 2010, Nantes, France

[67] The CMS Collaboration, PAS BPH-10-003 (2010)

[68] The CMS Collaboration, Prompt and non-prompt J/psi production in pp collisions at $\sqrt{(s)}$ = 7 TeV, (2010) arXiv:1011.4193 [hep-ex].

[69] The ATLAS Collaboration, ATLAS-CONF-2010-062 (2010).

[70] The LHCb Collaboration, LHCb-CONF-2010-010 (2010).

[71] The STAR Collaboration, Phys. Rev. D82 (2010) 012004.

[72] For a collection of CMS results in the Electroweak Standard Model sector see also https://twiki.cern.ch/twiki/bin/view/CMSPublic/PhysicsResultsEWK

[73] The CMS Collaboration, Measurements of Inclusive W and Z Cross Sections in pp Collisions at $\sqrt{s}$= 7 TeV, J. High Energy Phys. 01 (2011) 080.

[74] LHC Higgs Cross Section Working Group, S. Dittmaier et al.. Handbook of LHC Higgs cross sections: 1. Inclusive observables. CERN-2011-002, CERN, Geneva, 2011, All the numbers can be obtained at https://twiki.cern.ch/twiki/bin/view/LHCPhysics/CrossSections.

[75] The ATLAS Collaboration, The CMS Collaboration, Combined Standard Model Higgs boson searches with up to 2.3 inverse femtobarns of pp collision data at $\sqrt{s} = 7$ TeV at the LHC, CMS PAS HIG-11-023.

[76] The CMS Collaboration, Measurement of ttbar Pair Production Cross Section at $\sqrt{s} = 7$ TeV using b-quark Jet Identification Techniques in Lepton + Jet Events, CMS PAS TOP-11-003, The CMS Collaboration, Top pair cross section in e/mu+jets, CMS PAS TOP-11-005; The CMS Collaboration, Measurement of the ttbar production cross section in the dilepton channel in pp collisions at $\sqrt{s} = 7$ TeV with a luminosity of 1.14 fb^{-1},, CMS PAS TOP-11-005; The CMS Collaboration, Measurement of the ttbar production cross section in the fully hadronic decay channel in pp collisions at 7 TeV, CMS PAS TOP-11-007; The CMS Collaboration, First measurement of the top quark pair production cross section in the dilepton channel with tau leptons in the final state in pp collisions at $\sqrt{s} = 7$ TeV, CMS PAS TOP-11-007; The CMS Collaboration, Measurement of the ttbar Production Cross Section in pp Collisions at 7 TeV in Lepton + Jets Events Using b-quark Jet Identification, CERN-PH-EP-2011-085, arXiv:1108.3773; The CMS Collaboration, Measurement of the Top-antitop Production Cross Section in pp Collisions at sqrt(s)=7 TeV using the Kinematic Properties of Events with Leptons and Jets , Eur. Phys. J. C71 (2011) 1721; The CMS Collaboration, First Measurement of the Cross Section for Top-Quark Pair Production in Proton-Proton Collisions at sqrt(s) = 7 TeV, Phys. Lett. B695 (2011) 424.

[77] The ATLAS Collaboration, Measurement of the Top Quark Pair Production Cross Section in pp Collisions at $\sqrt{s} = 7$ TeV in Dilepton Final States with ATLAS, arXiv:1108.3699 , CERN-PH-EP-2011-103; The ATLAS Collaboration, Measurement of the top quark pair production cross-section based on a statistical combination of measurements of dilepton and single-lepton final states at $\sqrt{s}$ = 7 TeV with the ATLAS detector, ATLAS-CONF-2011-108.

[78] The CMS Collaboration, Measurement of the ttbar production cross section and the top quark mass in the dilepton channel in pp collisions at sqrt(s) = 7 TeV, JHEP 07 (2011) 049.

[79] The ATLAS Collaboration, Measurement of the top quark mass from 2011 ATLAS data using the template method, ATLAS-CONF-2011-120.

[80] The CMS Collaboration, Measurement of the Charge Asymmetry in Top Quark Pair Production, CMS PAS TOP-11-014.

[81] The ATLAS Collaboration, Measurement of the W boson polarisation in top quark decays in 0.70 fb-1 of pp collisions at sqrt(s)=7 TeV with the ATLAS detector, ATLAS-CONF-2011-122.

[82] The CMS Collaboration, Search for Resonances in Semi-leptonic Top-pair Decays Close to Production Threshold, CMS PAS TOP-10-007.

[83] The ATLAS Collaboration, A Search for $t\bar{t}$ Resonances in the Lepton Plus Jets Channel in 200 pb^{-1} of pp Collisions at $\sqrt{s} = 7$ TeV, ATLAS-CONF-2011-087

[84] The CDF Collaboration, The D0 Collaboration, Combination of CDF and D0 Measurements of the Single Top Production Cross Section, http://arxiv.org/abs/0908.2171.

[85] The D0 Collaboration, Measurements of single top quark production cross sections and $|V_{tb}|$ in ppbar collisions at $sqrts = 1.96$ TeV, arXiv:1108.3091.

[86] The D0 Collaboration, Model-independent measurement of t-channel single top quark production in $p\bar{p}$ collisions at $\sqrt{s} = 1.96$ TeV, arXiv:1105.2788.

[87] The D0 Collaboration, Search for anomalous top quark couplings with the D0 detector, http://arxiv.org/abs/0901.0151.

[88] The CMS Collaboration, Search for single top tW associated production in the dilepton decay channel in pp collisions at $\sqrt{s} = 7$ TeV, CMS PAS TOP-11-022.

[89] Michael E. Peskin, Beyond the Standard Model (1997), arXiv:hep-ph/9705479v1.

[90] The CMS Collaboration, Search for W'(or techni-rho) to WZ, CMS PAS EXO-11-041.

[91] The CMS Collaboration, summary plots of CMS results, can be found at: https://twiki.cern.ch/twiki/bin/view/CMSPublic/PhysicsResultsSUS.

[92] The ATLAS Collaboration, summary plots of ATLAS results, can be found at: https://twiki.cern.ch/twiki/bin/view/AtlasPublic/SupersymmetryPublicResults.

[93] The ATLAS Collaboration, Exotics results page: https://twiki.cern.ch/twiki/bin/view/AtlasPublic/ExoticsPublicResults.

[94] The CMS Collaboration, Exotica results page: https://twiki.cern.ch/twiki/bin/view/CMSPublic/PhysicsResultsEXO.

[95] N. Kidonakis, Higher-order soft gluon corrections in single top quark production at the LHC, Phys.Rev. D75 (2007) 071501, arXiv:hep-ph/0701080

[96] CMS Collaboration, "Absolute Calibration of the Luminosity Measurement at CMS",CMS DP-2011/002 (2011).

[97] The CMS Collaboration, "Absolute Calibration of Luminosity Measurement at CMS: Summer 2011 Update", CMS-EWK-11-001. 2011.

[98] J. Allison et al., "Geant4 developments and applications", IEEE Transactions on Nuclear Science 53 No. 1 (2006) 270-278

[99] F. Maltoni et al., MadEvent: Automatic event generation with MadGraph, JHEP 0302 (2003) 027

[100] T. Sjostrand et al., "PYTHIA 6.4 physics and manual", JHEP 05 (2006) 026.

[101] S. Jadach et al., TAUOLA - a library of Monte Carlo programs to simulate decays of polarized τ leptons, Comput.Phys. Commun. 64 (1991) 275.

[102] E. Boos and others, Method for simulating electroweak top-quark production events in the NLO approximation: SingleTop event generator, Phys.Atom.Nucl. 69 8 (2006) 1317

[103] The cms software CMSSW, http://cmssw.cvs.cern.ch/cgi-bin/cmssw.cgi/CMSSW/

[104] A. Adam et al. PAT: the CMS Physics Analysis Toolkit,J. Phys.: Conf. Ser. 219 032017, doi:10.1088/1742-6596/219/3/032017

[105] Frixione, Stefano and Webber, Bryan R., Matching NLO QCD computations and parton shower simulations, JHEP 06 (2002) 029, hep-ph/0204244.

[106] J. Bauer, Prospects for the Observation of Electroweak Top-Quark Production with the CMS Experiment, Ph.D. thesis Karlsruhe (2010), http://www-ekp.physik.uni-karlsruhe.de/pub/web/thesis/iekp-ka2010-08.pdf, IEKP-KA/2010-8.

[107] The CMS Collaboration, Measurement of the tt-bar Production Cross Section in pp Collisions at 7 TeV in Lepton + Jets Events Using b-quark Jet Identification, CMS PAS TOP-10-003 (2010).

[108] The CMS Collaboration, Measurement of the tt-bar Pair Production Cross Section at p $\sqrt{s}$ = 7 TeV using b-quark Jet Identification Techniques in Lepton + Jet Events, CMS PAS TOP-11-001 (2011).

[109] J. Alwall et al., Comparative study of various algorithms for the merging of parton showers and matrix elements in hadronic collisions, Eur.Phys.J.C53 (2008) 473-500

[110] P. Motylinski, Angular correlations in t-channel single top production at the LHC, Phys. Rev. D 80 (2009) 074015, arXiv:hep-ph/0905.4754, doi: 10.1103/PhysRevD.80.074015.

[111] N. Kidonakis, NNLL resummation for s-channel single top quark production, Phys. Rev. D 81 (2010) 054028, arXiv:hep-ph/1001.5034, doi: 10.1103/PhysRevD.81.054028.

[112] N. Kidonakis, Higher-order corrections to top-antitop pair and single top quark production, 2009, arXiv:hep-ph/0909.0037.

[113] J. Campbell et al., NLO predictions for t-channel production of single top and fourth generation quarks at hadron colliders, JHEP 10 (2009) 042, arXiv:hep-ph/0907.3933, doi: 10.1088/1126-6708/2009/10/042

[114] N. Kidonakis, Phys. Rev. D 83, 091503(R) (2011), arXiv:1103.2792

[115] N. Kidonakis, Phys. Rev. D 81, 054028 (2010), arXix:1001.5034

[116] N. Kidonakis, Phys. Rev. D 82, 054018 (2010), arXiv:1005.4451

[117] J. Campbell et al., MCFM - Monte Carlo for FeMtobarn processes, http://mcfm.fnal.gov/.

[118] R. Gavin et al., FEWZ 2.0: A code for hadronic Z production at next-to-next-to-leading order, (2010) arXiv:hep-ph/1011.3540

[119] Pumplin, P. and others, New Generation of Parton Distributions with Uncertainties from Global QCD Analysis, JHEP 0207 (2002 012

[120] The CMS Collaboration, Determination of the Jet Energy Scale in CMS with pp Collisions at $\sqrt{s}$ = 7 TeV, CMS-PAS JME-10-010.

[121] The CMS Collaboration, Commissioning of b-jet identification with pp collisions at sqrt(s) = 7TeV, CMS-PAS BTV-10-001.

[122] The CMS Collaboration, Performance of b-jet identification in CMS, CMS-PAS BTV-11-001.

[123] G. Mahlon et al., Improved Spin Basis for Angular Correlation Studies in Single Top Quark Production at the Tevatron, Phys.Rev. D55, 7249 (1997), arXiv:hep-ph/9611367

[124] The CMS Collaboration, Prospects for the measurement of the single-top t-channel cross section in the muon channel with 200 pb^{-1} of CMS data at 10 TeV, CMS-PAS TOP-2009-005.

[125] M. Cacciari et al., The anti-k_T jet clustering algorithm, JHEP 04 (2008) 063.

[126] CMS collaboration, CMS: The computing project. Technical design report, CERN-LHCC-2005-023.

[127] Muller, Th. and Ott, J. and Wagner-Kuhr, J.,Theta - a framework for template based modelling and inference, CMS Internal Note, 2010, CMS-IN 2010/017. Further documentation: http://www-ekp.physik.uni-karlsruhe.de/ ott/theta/html/index.html

[128] K. Nakamura, et al., Particle Data Group,Review of particle physics, J. Phys. G37 (2010) 075021, doi = 10.1088/0954-3899/37/7A/075021.

[129] R. Barlow, http://www.slac.stanford.edu/ barlow/java/statistics1.html

[130] R. Barlow, .Asymmetric Systematic Errors, arXiv:physics/0306138v1.

[131] S. Alioli et al., Single-top production in the s- and t-channel, , JHEP 0909 (2009) 111, arXiv:0907.4076

[132] E. Re, Single-top production associated with a W boson, Eur. Phys. J. C71 (2011) 1547, arXiv:1009.2450

[133] S. Frixione et al., Single-top hadroproduction in association with a W boson, JHEP 07 (2008) 029, arXiv:0805.3067. doi:10.1088/1126-6708/2008/07/029.

[134] L. Lyons et al., How to combine correlated estimates of a single physical quantity, Nucl. Instrum. Meth. A 270 (1988) 110.